PhD

3rd CYCLE

FCUP
UA
UM
2026

U.PORTO

The 3D Ising Model as a Laboratory for Nonperturbative Quantum Field Theory

José Guilherme Boura de Matos

FC

U.PORTO
FACULDADE DE CIÊNCIAS
UNIVERSIDADE DO PORTO

universidade de aveiro

Universidade do Minho

The 3D Ising Model as a Laboratory for Nonperturbative Quantum Field Theory

José Guilherme Boura de Matos
Programa Doutoral em Física

Faculty of Sciences of the University of Porto, University of Aveiro and University of Minho
2026

U.PORTO
FACULDADE DE CIÊNCIAS
UNIVERSIDADE DO PORTO

universidade de aveiro

Universidade do Minho

The 3D Ising Model as a Laboratory for Nonperturbative Quantum Field Theory

José Guilherme Boura de Matos
Thesis carried out as part of the Programa Doutoral em Física
Department of Physics
2026

Supervisor
João Manuel Viana Parente Lopes, Professor Auxiliar, FCUP

Co-supervisor
João Miguel Augusto Penedones Fernandes, Associate Professor, EPFL

Thesis Submitted in Fulfilment of the Requirements for the Degree of *PHILOSOPHIÆ DOCTOR* in PHYSICS

The 3D Ising Model as a Laboratory for Nonperturbative Quantum Field Theory

José Guilherme Boura de Matos

September 22, 2026



Universidade do Porto

Departamento de Física e Astronomia, Faculdade de Ciências

Centro de Física das Universidades do Minho e do Porto

Chair:

Prof. Miguel Sousa da Costa (Universidade do Porto, Porto, Portugal)

Supervisors:

Prof. João Manuel Viana Parente Lopes (Universidade do Porto, Porto, Portugal)

Prof. João Miguel Augusto Penedones Fernandes (EPFL, Lausanne, Switzerland)

Referees:

Dr. Joan Elias Miró (International Centre for Theoretical Physics (ICTP), Trieste, Italy)

Prof. Michele Caselle (Torino University, Torino, Italy)

Prof. António de Aguiar e Pestana de Morais (Universidade do Minho, Braga, Portugal)

Dr. Vasco David Fonseca Gonçalves (Universidade do Porto, Porto, Portugal)

To the people who were there,
and without whom this would not have been possible.

And to the Ising model,
for hiding so much behind so little.

Contents

Acknowledgments i

Abstract iii

Resumo v

Published Work vii

Introduction ix
Brief overview of the thesis . . . xii
References . . . xiv

1. Overview of the Effective String Theory 1
1.1. Long flux tubes as effective Goldstone theories . . . 2
1.1.1. Gauge choices . . . 4
1.1.2. Lüscher term . . . 5
1.1.3. Open-closed duality . . . 6
1.1.4. Higher-order bulk terms . . . 8
1.1.5. Boundary terms . . . 11
1.2. Nambu-Goto as the minimal geometric completion . . . 12
1.2.1. Beyond Nambu-Goto: geometric invariants and the end of universality . . . 14
1.3. Modern effective string theory: Integrability and the $T\bar{T}$ deformation . . . 15
1.3.1. The structure of the scattering amplitude . . . 17
1.3.2. Thermodynamic Bethe ansatz for effective strings . . . 19
1.4. Lattice developments and the worldsheet axion . . . 21
References . . . 22

2. Lattice realization of the domain wall and Monte Carlo 27
2.1. Lattice ensembles and observables . . . 28
2.1.1. Lattice model and boundary conditions . . . 28
2.2. Markov chain Monte Carlo . . . 29
2.2.1. Importance sampling . . . 29

2.2.2. Markov chains . . . 30
2.2.3. Detailed balance and ergodicity . . . 31
2.2.4. Thermalization, autocorrelation, and statistical errors . . . 31
2.3. Monte Carlo updates . . . 32
2.3.1. The Metropolis update . . . 32
2.3.2. The Wolff cluster update . . . 32
2.3.3. Algorithmic efficiency . . . 33
2.4. Free-energy differences . . . 33
2.4.1. Bias reconstruction: the flat histogram sampling . . . 35
2.4.2. Continuous plus residual flat-histogram bias . . . 37
2.4.3. Jarzynski method . . . 38
2.5. Observables: Continuum/Lattice correspondence . . . 41
2.5.1. Microscopic operators . . . 42
2.5.2. Connection between lattice and continuum . . . 42
2.5.3. Correlation functions . . . 43
References . . . 44

3. Effective string theory on a torus: the 3D Ising domain wall **47**
3.1. Summary . . . 48
3.2. Effective string theory on a toroidal worldsheet . . . 49
3.2.1. Universal contribution and Gaussian normalization . . . 49
3.2.2. Leading non-universal correction . . . 53
3.3. Non-universal free energy from the thermodynamic Bethe ansatz . . . 56
3.3.1. Spectrum . . . 56
3.3.2. Partition function and its large-area expansion . . . 59
3.3.3. Higher order corrections . . . 60
3.4. MC simulations . . . 61
3.4.1. A dilute gas of domain walls versus a single domain wall . . . 61
3.4.2. The string tension . . . 61
3.4.3. Area-independent contribution . . . 64
3.4.4. Measuring γ_3 . . . 64
3.5. Effective string tension . . . 67
References . . . 70

4. Branon-Glueball interactions **73**
4.1. Summary . . . 74
4.2. Effective field theory for particle-wall interactions . . . 75
4.2.1. Regime of validity . . . 76
4.2.2. Wall fluctuations and Gaussian smearing . . . 76
4.2.3. Finite transverse-volume correction to the wall tension . . . 78
4.2.4. Particle scattering across the wall . . . 80
4.2.5. Correlation functions in the wall sector . . . 81
4.2.6. Flux tube profile . . . 83
4.3. Geometric approximation for Ising correlators . . . 86
4.3.1. $\mathbb{Z}_2$-odd operators . . . 86
4.3.2. $\mathbb{Z}_2$-even operators . . . 88

4.4. Monte Carlo simulations of domain walls in 3D Ising . . . 89
4.4.1. One-point functions . . . 89
4.4.2. Two-point functions . . . 91
4.4.3. Free energies . . . 94
References . . . 96

5. Twisted Sectors in the thermal 3D Ising CFT **97**
5.1. Summary . . . 98
5.2. Twisted-sector free energy and scaling . . . 99
5.2.1. Scaling at criticality and corrections to scaling . . . 99
5.3. Monte Carlo method and results . . . 100
5.3.1. Two-dimensional benchmark . . . 100
5.3.2. Three-dimensional analysis . . . 102
References . . . 108

6. Conclusions and Outlook **111**
6.1. Extensions to $SU(N)$ and $3+1$ dimensions . . . 112
6.2. Future directions . . . 113
6.3. Open questions . . . 115
References . . . 116

A. Modular functions and Eisenstein series **117**

B. Two-dimensional Ising **121**
B.1. Finite-volume corrections . . . 122
B.1.1. Lattice corrections and irrelevant operators . . . 122
B.1.2. Exponential corrections from the cylinder spectrum . . . 123
B.1.3. Mixed terms . . . 124

C. Three-dimensional finite volume corrections **125**
C.1. One-particle transverse corrections . . . 125
C.2. Slab power corrections . . . 126
C.3. Sector difference of $\mathbb{Z}_2$-even one-point functions . . . 127
C.4. 3D Ising analysis . . . 129

Acknowledgments

I would first like to thank my supervisors, João Viana and João Penedones, for their guidance, patience, and support throughout these years. Their advice shaped both the scientific direction of this thesis and the way I learned to approach research. I am especially grateful to João Viana for his continued support and encouragement since my bachelor's degree, and for the many ways in which he has helped me grow as a researcher.

I am especially grateful to João Pires and António Antunes, who patiently helped me through many things I did not yet understand. I am very grateful for their time, their explanations, and their willingness to help, often far beyond what I could reasonably have asked of them. More than that, I am grateful for their friendship.

I also want to thank my close friends, Jéssica Gonçalves and Gonçalo Roboredo. Their importance to these years is difficult to separate from life itself. They were there through the ordinary days, the difficult ones, and the moments worth celebrating, providing companionship and perspective beyond work. For the conversations, meals, trips, distractions, arguments, jokes, and many small moments in between, I am grateful. These years would have been different without them.

I also want to thank the people I met along the way. At schools, conferences, workshops, visits, and other events, I met people whose ideas and company contributed to my experience of the PhD. Some encounters led to collaborations, some to friendships, and others were brief conversations that I nevertheless remember. I am grateful to all of them. They reminded me that doing science also involves the people one meets along the way.

Finally, I want to thank my family for their support throughout these years. They have been a constant source of encouragement and stability, and their support extended beyond anything related to this thesis. They stood by me through the uncertainties, frustrations, and changes that came with these years. I am grateful for the confidence they placed in me and for always giving me a place to return to. None of this would have been the same without them.

Abstract

Confining strings are the emergent extended objects that capture the long-distance interaction between external color sources in confining gauge theories. At sufficiently large length scales, their dynamics is described by an effective theory, whose low-energy sector is universal because it is fixed by symmetry. Beyond this universal regime, however, the string can retain information about the microscopic quantum field theory in which it is embedded. This includes worldsheet Wilson coefficients, the interaction between the string and massive bulk excitations, and finite-temperature or finite-volume observables probing the RG flow from the CFT to the effective string description. In this thesis, we study these questions analytically and numerically, through dedicated Monte Carlo simulations, using the 3D Ising model as a laboratory. We also develop an effective field theory for branon-glueball interactions, describing the leading coupling between the fluctuating wall and the lightest massive bulk excitation, and test its predictions against Monte Carlo. In the broken phase, antiperiodic boundary conditions select the sector with a non-trivial $\mathbb{Z}_2$ twist, which at large volume is dominated by a single fluctuating domain wall, whose infrared fluctuations are governed by the same effective theory as the confining string in 3D $\mathbb{Z}_2$ gauge theory. From the toroidal domain-wall free energy we determine the first non-universal worldsheet Wilson coefficient, $\gamma_3 = -0.00106(20)$, which lies near the lower bound from the worldsheet S-matrix bootstrap. At criticality, the same $\mathbb{Z}_2$ twist defines thermal finite-volume observables of the 3D Ising universality class. We measure the twisted-sector thermodynamic Casimir difference $\Delta_{\mathbb{Z}_2} = 0.327(2)$, the thermal screening mass $\kappa_{\text{eff}} = m_{\text{scr}} L_z = 0.71(4)$, and the lowest $\mathbb{Z}_2$-odd energy gap on the square transverse torus $\kappa_\sigma = 1.230(3)$.

Resumo

As cordas confinantes são objetos extensos emergentes que capturam a interação a longas distâncias entre fontes externas de cor em teorias de gauge confinantes. A escalas de comprimento suficientemente grandes, a sua dinâmica é descrita por uma teoria efetiva, cujo setor de baixas energias é universal por ser fixado pela simetria. Para além deste regime universal, contudo, a corda pode reter informação sobre a teoria quântica de campos microscópica na qual está inserida. Isto inclui coeficientes de Wilson da folha de mundo, a interação entre a corda e excitações massivas do volume, e observáveis a temperatura finita ou volume finito que sondam o fluxo de RG desde a CFT até à descrição em termos da teoria efetiva de cordas. Nesta tese, estudamos estas questões analítica e numericamente, através de simulações de Monte Carlo dedicadas, utilizando o modelo de Ising tridimensional como laboratório. Desenvolvemos também uma teoria efetiva de campos para as interações entre branons e glueballs, que descreve o acoplamento dominante entre a parede flutuante e a excitação massiva mais leve do volume, e testamos as suas previsões através de simulações de Monte Carlo. Na fase quebrada, condições de fronteira antiperiódicas selecionam o setor com um twist $\mathbb{Z}_2$ não trivial que, no regime de grande volume, é dominado por uma única parede de domínio flutuante, cujas flutuações no infravermelho são governadas pela mesma teoria efetiva que descreve a corda confinante na teoria de gauge $\mathbb{Z}_2$ tridimensional. A partir da energia livre da parede de domínio num toro, determinamos o primeiro coeficiente de Wilson não universal da folha de mundo, $\gamma_3 = -0.00106(18)$, que se encontra próximo do limite inferior obtido pelo bootstrap da matriz S da folha de mundo. No ponto crítico, o mesmo twist $\mathbb{Z}_2$ define observáveis térmicos a volume finito da classe de universalidade do modelo de Ising tridimensional. Medimos a diferença de Casimir termodinâmica no setor com twist, $\Delta_{\mathbb{Z}_2} = 0.327(2)$, a massa térmica de screening, $\kappa_{\text{eff}} = m_{\text{scr}} L_z = 0.71(4)$, e o menor gap de energia ímpar sob $\mathbb{Z}_2$ no toro transversal quadrado, $\kappa_\sigma = 1.230(3)$.

Published Work

This thesis is based in part on the following publications. For each work, I indicate the chapters in which its results are used.

Papers included in this thesis

1. David Lima, J. M. Viana Parente Lopes, **José Matos**, and Joao Penedones. "Effective String Theory on a Torus: The 3d Ising Domain Wall." In: *Journal of High Energy Physics* 2026.7 (July 29, 2026), p. 267. ISSN: 1029-8479. DOI: 10.1007/JHEP07(2026)267
   Material from this work is used mainly in Chapter 3.
2. J. M. Viana Parente Lopes, **José Matos**, and Joao Penedones. *Effective Strings and Particles Interacting in 3D: The Ising Model*. Apr. 9, 2026. DOI: 10.48550/arXiv.2604.08670. arXiv: 2604.08670 [hep-th]
   Accepted in JHEP. Material from this work is used mainly in Chapter 4.
3. **José Matos**. *Monte Carlo Reconstruction of Symmetry-Twisted Partition Function Ratios: The Critical 3D Ising*. June 30, 2026. DOI: 10.48550/arXiv.2607.00106. arXiv: 2607.00106 [hep-lat]
   Material from this work is used mainly in Chapter 5.

Papers not included in this thesis

1. Gabriel Cuomo, J.M.Viana Parente Lopes, **José Matos**, Júlio Oliveira, and João Penedones. "Numerical Tests of the Large Charge Expansion." In: *Journal of High Energy Physics* 2024.5 (May 14, 2024), p. 161. ISSN: 1029-8479. DOI: 10.1007/JHEP05(2024)161

Introduction

Quantum field theory is one of the basic frameworks of modern physics, providing a common language for a diverse range of phenomena, from interactions of elementary particles to the collective behaviour of many-body systems. Its importance lies not only in describing microscopic interactions, but also in explaining how complex macroscopic behaviour can emerge from many simple local degrees of freedom. In high-energy physics it is the paradigm on which the Standard Model is built, while in statistical physics it captures the universal behaviour of systems near continuous phase transitions. A central insight of quantum field theory is that very different microscopic systems can exhibit the same long-distance physics, governed primarily by field content and symmetries rather than by their detailed microscopic structure.

A major difficulty is that many physically important examples are strongly coupled, beyond the regime in which perturbation theory based on Feynman diagrams is predictive. In quantum chromodynamics, confinement prevents quarks and gluons from existing as isolated particles at low energies. In statistical systems close to a critical point, fluctuations occur on all length scales and simple mean-field descriptions break down. In such regimes there is no simple description in terms of weakly interacting particles. Non-perturbative methods are therefore essential to understand how emergent collective phenomena arise.

Lattice field theory gives one of the few controlled ways to study quantum field theory beyond perturbation theory. At finite volume and lattice spacing, the path integral becomes a finite-dimensional statistical system, making non-perturbative observables amenable to numerical simulation. Nonetheless, their interpretation requires effective descriptions and/or symmetry principles that identify the relevant infrared degrees of freedom and separate universal behaviour from microscopic details. This thesis combines these two perspectives: lattice simulations make non-perturbative observables accessible, while effective descriptions provide the language needed to interpret them.

One of the central examples considered in this thesis is the confining flux tube, which can be studied both through lattice simulations and through an infrared effective description. Flux tubes are intrinsically tied to confinement, and their dynamics provides a concrete probe of its long-distance physics. At sufficiently large distances, a flux tube behaves as a fluctuating string whose low-energy dynamics is governed by effective string theory. The same infrared framework also applies to fluctuating domain walls with the same symmetry-breaking pattern, despite their different microscopic origin. More

generally, it describes the Goldstone sector of sufficiently long and stable two-dimensional extended objects in a gapped theory, provided that no additional gapless worldsheet degrees of freedom are present.

In three dimensions, this relation is particularly direct for the system studied in this thesis. The Ising model is dual to $\mathbb{Z}_2$ lattice gauge theory, under which an Ising domain wall can be identified with a confining-string worldsheet. The lattice domain walls studied below therefore provide a microscopic realization of the same long-distance worldsheet dynamics. The shared infrared EFT separates universal long-distance behaviour from non-universal corrections that retain information about the microscopic theory.

Several observations support this string description. In lattice gauge theory, the strong-coupling expansion gives an area law for Wilson loops, with a surface representation that motivates a fluctuating-worldsheet interpretation [1]. Direct lattice measurements of the field distribution between static color sources show a tube-like excess in the gauge-field energy density [2]. Experimentally, approximately linear Regge trajectories suggest a string-like organization of strongly interacting hadronic states, which motivated the early dual-resonance models [3–6].

Effective string theory (EST) is the resulting infrared framework. In the following, we introduce the aspects of this framework that will be needed throughout the thesis: the universal Goldstone sector, its non-universal higher-derivative corrections, finite-volume observables, and the possible appearance of additional worldsheet or bulk degrees of freedom. Most progress has been made in the isolated long-string regime, where the flux tube is treated independently of string breaking, junctions, and the existence of an embedding medium. In this limit the worldsheet Goldstone modes have been identified, the universal terms have been identified, higher-derivative worldsheet and boundary corrections have been classified, and several complementary formulations of the theory are available [7–13].

On the numerical side, lattice studies of the static interquark potential have provided evidence for the effective-string description through the linear potential and the universal Lüscher correction [7, 8, 10]. Complementary studies of open and closed flux-tube spectra have revealed the expected string-like pattern of low-lying excitations [7, 8, 11–13].

A notable development was the identification, in lattice studies of the closed flux-tube spectrum in 3+1-dimensional Yang-Mills theory, of a relatively light massive pseudoscalar excitation. This state has been interpreted as an additional worldsheet degree of freedom, commonly referred to as the flux-tube axion [1] [14, 15]. Its existence is not predicted by the universal Goldstone-sector EST, which constrains only the low-energy dynamics of the transverse modes but is agnostic about additional massive worldsheet excitations. The axion therefore provides an example in which lattice spectra reveal a degree of freedom absent from the minimal Goldstone EFT.

Nonetheless, several aspects of the infrared dynamics of confining strings and related extended objects remain poorly understood. Firstly, the coupling between worldsheet modes and the surrounding bulk is not part of the EST, even though flux tubes are embedded in theories with bulk excitations, such as glueballs. Secondly, string thermodynamics is much less developed than the low-lying spectrum, despite being governed by the same theory. Thirdly, for domain walls generated by spontaneous symmetry breaking (SSB), one expects a relation between the emergent wall and defect data of the critical theory, but no general map from defect CFT data to the fluctuating worldsheet theory is known. These three questions define the main directions pursued, to different degrees, in this thesis.

[1] Which should not be confused with the QCD axion.

The numerical laboratory used in this thesis is the 3D Ising model. It is simple enough to be studied numerically with high precision, while still yielding a nontrivial interacting conformal field theory at criticality, a massive phase away from criticality, and domain-wall sectors selected by boundary conditions. Studying these sectors, both numerically and analytically, provides a controlled way to test effective descriptions of strongly coupled quantum field theory.

The first direction is a toroidal domain-wall numerical setup yielding high precision free energy measurements, used to extract intrinsic EST Wilson coefficients from a microscopic lattice model. Compared with open-string observables, such as Polyakov-loop correlators, this avoids boundary Wilson coefficients that enter at lower order. It is also easier to measure than an excited-state spectrum and probes a less explored thermodynamic regime of EST. Moreover, varying the torus modulus increases the sensitivity to higher-order non-universal couplings. The main drawback is that corrections previously derived for ground-state energies must be generalized to the torus partition function.

In addition, our analysis clarifies two technical points that are important for quantitative comparisons with Monte Carlo data: firstly, the EST fixes the normalization of the toroidal domain-wall partition function; secondly, the divergent perturbative expansion in inverse powers of the area is not well suited for numerical fits at the typical physical sizes accessible in simulations. The latter issue is mitigated by leveraging the low-energy integrability of the EST, using the thermodynamic Bethe ansatz to compute the spectrum from the phase shift. With it, we obtain a perturbative expansion of the free energy only in the Wilson coefficients, while the dependence on the area is kept non-perturbatively.

The determination of γ_3 serves two purposes. First, it provides a precise measurement of the leading non-universal worldsheet coefficient. Second, when combined with bootstrap constraints on worldsheet scattering amplitudes, it probes possible short-distance scenarios for the worldsheet dynamics [16, 17]. For example, if the short-distance worldsheet dynamics is dominated by the axionic resonance, then $\gamma_3 > 0$. A negative value would therefore exclude the axion-dominated scenario.

The second direction concerns the coupling between worldsheet degrees of freedom and bulk excitations. In a confining theory, a flux tube does not exist as a completely isolated object. It is embedded in a bulk theory with other modes, most notably Yang-Mills glueballs. At sufficiently low energies, integrating out these modes only renormalizes the Wilson coefficients of the EST, such that their effect is visible only indirectly. Keeping the lightest bulk field explicit makes it possible to identify the observables in which the wall-bulk coupling appears at leading order.

This EFT has a restricted domain of applicability. It is not a generic effective description of the full confined phase, because no simple Lagrangian-level counting parameter uniformly suppresses all couplings between the flux tube and the bulk modes. In particular, the would-be parameter $m^2/\sigma \sim 10$ is not small; see the lattice results in table 34 of [18]. A known exception is compact $U(1)$ gauge theory in three dimensions, where such a hierarchy can be parametrically realized [19]. We therefore restrict attention to infrared observables with $p_\parallel^2 \ll \sigma$ for which the leading contribution is dominated by exchange of the lightest bulk mode. The aim is to identify this class of observables, test the resulting predictions with Monte Carlo data, and provide a starting point for a systematic treatment of bulk-worldsheet couplings.

The third direction concerns domain walls generated by spontaneous symmetry breaking, which is how the string-like objects studied in this thesis are realized on the lattice. These domain walls are not fundamental degrees of freedom. They emerge in the symmetry-broken phase, where boundary conditions or symmetry twists select a sector dominated, at large volume, by a single domain wall. From this perspective, the domain wall is an extended infrared object generated along the RG flow

away from the symmetry twisted sector of the critical theory. Existing work on defect CFTs and RG domain walls suggests that critical defect data and emergent extended objects may be related, but no general framework is known that maps the conformal data of the original defect to the worldsheet dynamics of the fluctuating wall. The strategy pursued here is more limited. We track the domain-wall free energies and bulk correlation functions along the RG flow.

However, several ingredients required for a complete infrared description of the confined phase remain poorly understood. They are not addressed in this thesis, but they define important directions for future work. The first is string breaking. Once dynamical matter is present, the flux tube is no longer asymptotically stable as it can mix with hadronic states and decay into shorter flux tubes or bulk particles. This process does not fit within the standard framework of an isolated long-string EFT, as it needs a paradigm in which the number and topology of string segments can change. The question is becoming increasingly timely in view of recent progress in quantum simulation, where real-time string breaking has been observed in (2+1)-dimensional gauge-theory settings [20].

A second missing ingredient is the dynamics of junctions in string networks, which is required for an infrared description of hadrons beyond the mesonic sector. These directions are beginning to attract renewed attention, such as in recent work on baryonic confining-string junction dynamics [21, 22], but they are not yet part of a unified effective framework for flux-tube networks in generic hadrons. A complete description would have to treat worldsheet fluctuations, bulk couplings, string breaking, and junction dynamics within a common language.

We now turn to the conventions, methods, and organization of the thesis.

(Not so) Brief overview of the thesis

Most of the work in this thesis is performed in Euclidean signature, since the relevant lattice observables are free energies and Euclidean correlation functions. The Euclidean EST used here should be understood as the Wick rotation of the Lorentzian long-string theory. The local operator expansion and its Wilson coefficients are common to the two descriptions, but the observables targeted in each signature differ. Partition functions and thermodynamic quantities are naturally Euclidean, whereas phase shifts, unitarity, and bootstrap constraints refer to the Lorentzian worldsheet theory. Comparisons between the two are meaningful because they involve the same Wilson coefficients, analytically continued between signatures.

Methodologically, the thesis combines analytical and numerical work. The analytical results developed in the following chapters are tested, whenever possible, against dedicated Monte Carlo simulations of the 3D Ising model. This numerical focus leads us to specialize many constructions to three dimensions and, in some cases, to $\mathbb{Z}_2$-symmetric systems, where clean lattice observables are available. These restrictions are often practical rather than conceptual. The same ideas should extend to four-dimensional theories or to other microscopic models, although such extensions may require nontrivial adaptations of the observables, algorithms, or lattice setup.

All simulation code used in this thesis was developed specifically for the problems at hand. The Monte Carlo implementations were written in C++ with OpenMP parallelization by the author and collaborators, with most of the code written by the author. Bash scripts were used to manage production runs and job submissions, while Python was used for data processing, statistical analysis, fitting, and figure generation.

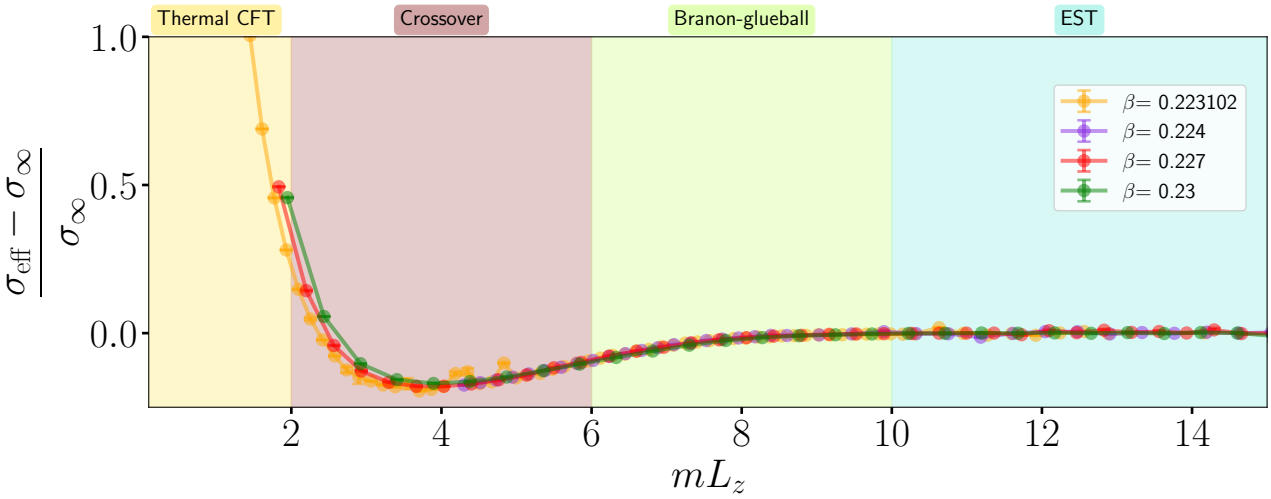


Figure 1 Domain wall effective string tension as a function of the transverse size, shown through $(\sigma_{\text{eff}} - \sigma_\infty)/\sigma_\infty$ versus mL_z, for several values of β. The shaded regions indicate the qualitative regimes discussed in the text. At small mL_z, the system is controlled by the thermal critical regime. At intermediate sizes the data pass through a crossover region, followed by a regime where the leading finite-L_z corrections are governed by the coupling between the fluctuating domain wall and the lightest bulk excitation. At larger mL_z, these effects become exponentially suppressed and the isolated-domain-wall EST description is recovered.

Fig. 1 summarizes the regimes studied in the thesis through the infinite domain-wall effective string tension as a function of the physical transverse size, mL_z. At large mL_z, the system is described by the isolated-wall EST and becomes independent of the transverse size, corresponding to the plateau. The leading corrections to this plateau are exponentially suppressed and motivated the branon-glueball analysis. At small mL_z, the behaviour is governed by the thermal 3D Ising CFT. The intermediate region, near the minimum of the curve, is less understood. It remains unclear whether a unified effective description can capture the crossover between critical defect physics, bulk excitations, and the emergent worldsheet theory.

The thesis is organized as follows. Chapter 1 reviews the effective theory of isolated long strings, from the symmetry-based Goldstone description to modern scattering-based, bootstrap, and finally lattice developments. The chapter also fixes the boundary of the standard string framework. It identifies which observables are described by the Goldstone EFT alone and which ones require additional worldsheet or bulk degrees of freedom. Chapter 2 reviews the Monte Carlo methods used in the numerical part of the work and presents the two-level flat-histogram bias developed to measure free-energy differences with high precision. This algorithm is used in Chapters 3 and 5.

The original results of the thesis are contained in Subsec. 2.4.2 and Chapters 3, 4, and 5. Chapter 3 develops a toroidal domain-wall setup for extracting intrinsic worldsheet data without boundary contamination. The main observable is the toroidal domain-wall free energy, from which we determine the first non-universal EST coefficient, γ_3, and compare it with S-matrix bootstrap constraints.

Chapter 4 extends the infrared description by coupling the fluctuating wall to the lightest massive excitation of the ambient bulk theory. This chapter introduces the corresponding renormalized worldsheet-bulk coupling and derives its consequences for finite-transverse-volume corrections, bulk one-point and two-point functions in the presence of the wall, and particle-wall scattering amplitudes in the controlled low parallel momentum regime. These predictions are then tested in the 3D Ising model.

Chapter 5 studies the $\mathbb{Z}_2$-twisted sector of the 3D Ising universality class at criticality. The main observable is the sector free-energy difference between periodic and antiperiodic boundary conditions on $T_L^2 \times S_{L_z}^1$, from which we extract the symmetry-twisted thermodynamic Casimir difference $\Delta_{\mathbb{Z}_2} = 0.327(2)$. The finite-aspect-ratio dependence determines the thermal screening mass through the dimensionless combination $\kappa_{\text{eff}} = m_{\text{scr}} L_z = 0.71(4)$ and isolates the lowest $\mathbb{Z}_2$-odd energy gap on the transverse torus, $E_\sigma L_z = \kappa_\sigma = 1.230(3)$.

References

[1] Kenneth G. Wilson. "Confinement of Quarks." In: *Physical Review D* 10.8 (Oct. 15, 1974), pp. 2445–2459. DOI: 10.1103/PhysRevD.10.2445.

[2] F. Bissey et al. "Gluon Flux-Tube Distribution and Linear Confinement in Baryons." In: *Physical Review D* 76.11 (Dec. 27, 2007), p. 114512. DOI: 10.1103/PhysRevD.76.114512.

[3] Geoffrey F. Chew and S. C. Frautschi. "Principle of Equivalence for All Strongly Interacting Particles within the S-Matrix Framework." In: *Physical Review Letters* 7.10 (Nov. 15, 1961), pp. 394–397. DOI: 10.1103/PhysRevLett.7.394.

[4] R. Dolen, D. Horn, and C. Schmid. "Finite-Energy Sum Rules and Their Application to πN Charge Exchange." In: *Physical Review* 166.5 (Feb. 25, 1968), pp. 1768–1781. DOI: 10.1103/PhysRev.166.1768.

[5] G. Veneziano. "Construction of a Crossing-Simmetric, Regge-behaved Amplitude for Linearly Rising Trajectories." In: *Il Nuovo Cimento A (1965-1970)* 57.1 (Sept. 1, 1968), pp. 190–197. ISSN: 1826-9869. DOI: 10.1007/BF02824451.

[6] L. Susskind. "Dual-Symmetric Theory of Hadrons.—I." In: *Il Nuovo Cimento A (1965-1970)* 69.3 (Oct. 1, 1970), pp. 457–496. ISSN: 1826-9869. DOI: 10.1007/BF02726485.

[7] Martin Lüscher and Peter Weisz. "Quark Confinement and the Bosonic String." In: *Journal of High Energy Physics* 2002.07 (Aug. 2002), p. 049. ISSN: 1126-6708. DOI: 10.1088/1126-6708/2002/07/049.

[8] Michele Caselle, Martin Hasenbusch, and Marco Panero. "String Effects in the 3d Gauge Ising Model." In: *Journal of High Energy Physics* 2003.01 (Feb. 2003), p. 057. ISSN: 1126-6708. DOI: 10.1088/1126-6708/2003/01/057.

[9] K. Jimmy Juge. "Fine Structure of the QCD String Spectrum." In: *Physical Review Letters* 90.16 (2003). DOI: 10.1103/PhysRevLett.90.161601.

[10] Michele Caselle, Michele Pepe, and Antonio Rago. "Static Quark Potential and Effective String Corrections in the (2+1)-d SU(2) Yang-Mills Theory." In: *Journal of High Energy Physics* 2004.10 (Nov. 2004), p. 005. ISSN: 1126-6708. DOI: 10.1088/1126-6708/2004/10/005.

[11] Michele Caselle, Martin Hasenbusch, and Marco Panero. "On the Effective String Spectrum of the Tridimensional 2 Gauge Model." In: *Journal of High Energy Physics* 2006.01 (Jan. 2006), p. 076. ISSN: 1126-6708. DOI: 10.1088/1126-6708/2006/01/076.

[12] Andreas Athenodorou, Barak Bringoltz, and Michael Teper. "Closed Flux Tubes and Their String Description in D =3+1 SU(N) Gauge Theories." In: *Journal of High Energy Physics* 2011.2 (Feb. 8, 2011), p. 30. ISSN: 1029-8479. DOI: 10.1007/JHEP02(2011)030.

[13] Bastian B. Brandt. "Spectrum of the Open QCD Flux Tube and Its Effective String Description I: 3d Static Potential in SU(N = 2, 3)." In: *Journal of High Energy Physics* 2017.7 (July 4, 2017), p. 8. ISSN: 1029-8479. DOI: 10.1007/JHEP07(2017)008.

[14] Sergei Dubovsky, Raphael Flauger, and Victor Gorbenko. "Evidence from Lattice Data for a New Particle on the Worldsheet of the QCD Flux Tube." In: *Physical Review Letters* 111.6 (Aug. 9, 2013), p. 062006. DOI: 10.1103/PhysRevLett.111.062006.

[15] Sergei Dubovsky and Victor Gorbenko. "Towards a Theory of the QCD String." In: *Journal of High Energy Physics* 2016.2 (Feb. 3, 2016), p. 22. ISSN: 1029-8479. DOI: 10.1007/JHEP02(2016)022.

[16] Adwait Gaikwad, Victor Gorbenko, and Andrea L. Guerrieri. "QCD Worldsheet Axion from the Bootstrap." In: *Journal of High Energy Physics* 2024.1 (Jan. 17, 2024), p. 90. ISSN: 1029-8479. DOI: 10.1007/JHEP01(2024)090.

[17] Joan Elias Miró, Andrea L. Guerrieri, Aditya Hebbar, João Penedones, and Pedro Vieira. "Flux Tube S-Matrix Bootstrap." In: *Physical Review Letters* 123.22 (Nov. 27, 2019), p. 221602. DOI: 10.1103/PhysRevLett.123.221602.

[18] Andreas Athenodorou and Michael Teper. "SU(N) Gauge Theories in 3+1 Dimensions: Glueball Spectrum, String Tensions and Topology." In: *Journal of High Energy Physics* 2021.12 (Dec. 13, 2021), p. 82. ISSN: 1029-8479. DOI: 10.1007/JHEP12(2021)082.

[19] Ofer Aharony, Netanel Barel, and Tal Sheaffer. *Effective Strings in QED_3*. Feb. 18, 2025. DOI: 10.48550/arXiv.2412.01313. arXiv: 2412.01313 [hep-th].

[20] Daniel González-Cuadra et al. "Observation of String Breaking on a (2 + 1)D Rydberg Quantum Simulator." In: *Nature* 642.8067 (June 2025), pp. 321–326. ISSN: 1476-4687. DOI: 10.1038/s41586-025-09051-6.

[21] Zohar Komargodski and Siwei Zhong. *The Baryon Junction and String Interactions*. July 4, 2024. DOI: 10.48550/arXiv.2405.12005. arXiv: 2405.12005 [hep-th].

[22] Michele Caselle, Nicodemo Magnoli, Dario Panfalone, and Lorenzo Verzichelli. *The Mass of the Baryon Junction: A Lattice Computation in 2 +1 Dimensions*. Nov. 2, 2025. DOI: 10.48550/arXiv.2508.00608. arXiv: 2508.00608 [hep-lat].

Chapter 1

Overview of the Effective String Theory

This chapter reviews the effective string theory (EST), which provides the theoretical starting point for this thesis. It discusses its historical origin, the symmetry-based construction of the long-string EFT, and it introduces the modern integrability-based viewpoint used later to perform computations. The language in this chapter reflects the literature, which is focused on confining strings. Nonetheless, the same EFT applies to the domain wall studied below. The microscopic origins differ, but their infrared symmetry structure is the same.

The history of string descriptions in QFT and hadronic physics contains two closely intertwined lines of development that eventually acquired rather different physical interpretations. The first originated in the dual-resonance program. Veneziano's 1968 amplitude [1] was introduced as a model of hadronic scattering with narrow resonances and approximately linear Regge trajectories. This framework soon acquired a geometric interpretation in terms of one-dimensional extended objects, with the relativistic area action given in published form by Goto [2]. During the 1970s, this line of development moved away from hadronic phenomenology toward a theory of fundamental strings. A decisive step was the recognition by Yoneya [3] and by Scherk and Schwarz [4] that the massless spin-two state of the closed string could be associated with gravity. Subsequent developments, including Polyakov's worldsheet path-integral formulation [5] and the Green–Schwarz anomaly-cancellation mechanism [6], established string theory as a candidate framework for quantum gravity and unification rather than as a phenomenological model of hadrons.

A second, historically intertwined but physically distinct line developed from the study of confinement in non-Abelian gauge theories. Nielsen and Olesen's vortex solutions [7] provided an early field-theoretic realization of string-like flux tubes, while Wilson's lattice formulation [8] gave a precise connection between confinement and an area law for large Wilson loops. Nambu [9], Mandelstam [10], and 't Hooft [11] further developed the picture in which confinement is associated with the formation of chromoelectric flux tubes. The modern effective-string viewpoint emerged more explicitly with the work of Lüscher, Symanzik and Weisz [12] and Lüscher [13], who showed that the long-wavelength fluctuations of a confining flux tube lead to universal infrared corrections, and was subsequently developed into a systematic effective-field-theory framework, notably by Polchinski and Strominger

[14]. Although this development remained historically connected to fundamental string theory, its physical interpretation is different: in EST the string is not a fundamental object propagating in a critical target space, but an extended excitation generated dynamically within an ordinary quantum field theory.

EST starts from the sharp separation between the microscopic origin of confinement and the infrared dynamics of a long flux tube. The key observation is that an infinitely long flux tube breaks translations in the transverse directions and therefore supports Goldstone modes [13]. Their long-distance dynamics can then be organized as an EFT constrained by nonlinearly realized spacetime symmetries and expanded in derivatives, or equivalently in inverse powers of the string length [14, 15]. This viewpoint is already visible in the long-string analysis of Lüscher, Symanzik, and Weisz [12], and especially in Lüscher's derivation of the universal inverse-length correction to the static potential, whose coefficient is fixed by the number of massless degrees of freedom, $D-2$, and by the worldsheet boundary conditions [13].

1.1. Long flux tubes as effective Goldstone theories

The aim of this section is to construct the long-string EFT directly from its symmetry-breaking pattern. We first identify the light worldsheet degrees of freedom and the symmetries acting on them. In static gauge, the effective action is then obtained by writing local operators built from the transverse fields X^i and their derivatives that are invariant under the manifest unbroken symmetries, and by imposing the broken target-space rotations through their nonlinear realization on X^i [15]. Equivalently, before gauge fixing, the same EFT can be organized geometrically in terms of reparametrization-invariant scalars constructed from the embedding [15].

Consider a straight string embedded in D-dimensional Euclidean space. For definiteness, take the classical configuration to extend along the x^2 direction, with x^1 denoting Euclidean time. In the infinite-length limit, the choice of the (x^1, x^2)-plane as the worldsheet breaks the Euclidean group down to the subgroup that preserves this plane

$$SO(D) \times \mathbb{R}^D \to SO(2) \times SO(D-2) \times \mathbb{R}^2. \tag{1.1}$$

The unbroken symmetries are translations along the worldsheet, rotations in the longitudinal plane, and rotations in the transverse space. The broken generators are the transverse translations and the rotations that mix longitudinal and transverse directions [16].

The low-energy worldsheet theory contains only $D-2$ independent massless fields, which in static gauge are identified with the transverse displacements of the string. The mismatch with the naive Goldstone counting familiar from internal symmetries is a standard feature of spontaneously broken spacetime symmetries [17].

In the language of [17], redundancies occur when the action of the broken generators, T^a, on the order parameter $\phi(r)$, admits non-trivial solutions

$$c_a(r)\, T^a \langle \phi(r) \rangle = 0. \tag{1.2}$$

For a flat string, this redundancy is encoded in the spacetime algebra. The spontaneous breaking of transverse translations P_i and mixed rotations $J_{\beta i}$ might naively suggest an independent Goldstone

field for each broken generator. However, these fields are not independent. Because a worldvolume translation P_β acting on a broken rotation generates a broken transverse translation, schematically

$$[P^\alpha, J_{\beta i}] = \delta_{\alpha\beta} P_i, \tag{1.3}$$

the Goldstone associated with $J_{\beta i}$ can be eliminated through an inverse Higgs constraint. It is then expressed in terms of derivatives of the transverse displacement field X_i, which is the Goldstone associated with the broken translations P_i.

The inverse-Higgs reduction fixes the basic structure of the effective theory. The physical infrared fields are the $D-2$ Goldstone modes X^i associated with the broken transverse translations. Transverse translation invariance acts as the shift symmetry

$$X^i(\xi) \to X^i(\xi) + a^i, \tag{1.4}$$

so the local action can depend on X^i only through derivatives. The manifest unbroken $SO(2) \times SO(D-2)$ symmetry determines how the worldsheet and transverse indices may be contracted, while the broken rotations impose additional constraints through their nonlinear action on X^i. Equivalently, in a gauge-independent formulation the action depends only on the geometry of the embedded surface rather than on its absolute position in flat target space [13, 15].

Before gauge fixing, the broken rotations act as ordinary target-space Lorentz transformations of the embedding coordinates. After fixing the worldsheet reparametrization invariance, a broken Lorentz transformation must in general be accompanied by a compensating reparametrization to preserve the gauge condition. As a result, the broken rotations act nonlinearly on the transverse Goldstone fields X_i. This imposes constraints absent in a generic two-dimensional EFT of $D-2$ shift-symmetric scalars [1], and it strongly restricts the allowed operators. The explicit form of this realization depends on the gauge choice and is discussed in Sec. 1.1.4.

No detailed microscopic input has been used so far. The Goldstone modes are fixed by the symmetry-breaking pattern of the long-string vacuum, while locality and the existence of a separation of scales allow their interactions to be organized in a derivative expansion. The first predictions of EST are therefore universal: they do not depend on whether the string arises in Yang-Mills theory, in a spin system, or in any other theory supporting a stable long string. The practical consequence is that, to leading order, any sufficiently long string is governed by $D-2$ free massless bosons. Hence, their zero-point energy, the first universal correction to the classical string energy, is the famous Lüscher term.

There are, however, two important infrared subtleties. First, since the worldsheet theory is two-dimensional and the transverse modes are massless, an infinitely long string does not have a sharply defined transverse position. Its transverse fluctuations grow at large distances. This does not invalidate the effective description, but it complicates its interpretation. The infrared theory describes a rough, fluctuating surface around a chosen plane, not a rigid localized object. Second, this construction is agnostic about additional massive worldsheet excitations, which are integrated out in the strict long-distance EFT and contribute only through the renormalization of its Wilson coefficients. Nonetheless, they may become visible at the intermediate length scales accessible in lattice simulations. Their existence is therefore a dynamical question, to be decided by matching to experimental/numerical

[1] Generic two-dimensional shift-symmetric scalar EFTs exist. They are just not, in general, Goldstone theories of spontaneously broken internal symmetries in two dimensions.

data.

Before turning to explicit computations, we first discuss the gauge choices commonly used to organize the EST.

1.1.1. Gauge choices

A gauge choice is not a conceptual necessity, but it is usually the simplest way to organize computations. The Nambu-Goto and Polyakov descriptions are classically equivalent, since eliminating the auxiliary worldsheet metric in the Polyakov action gives the geometric area action. Quantum mechanically, however, the two formulations organize the theory differently and make different symmetries, constraints, and potential anomalies manifest. These are not competing microscopic definitions of the string, but are merely different organizations of the same infrared expansion, provided anomalies, counterterms, and field redefinitions are treated consistently. In practice, the literature mainly uses three related viewpoints: the orthogonal/conformal-gauge formulation [14], Polyakov-like formulations with an auxiliary worldsheet metric [18], and static gauge [15].

The first viewpoint is the orthogonal, or conformal, gauge [14, 16, 19]. In this one fixes the worldsheet reparametrization freedom so that the induced metric is locally conformal, making the residual conformal structure of the worldsheet manifest. In non-critical target-space dimension, as is the case here for $D = 3 \neq 26$, however, the naive conformal-gauge Nambu-Goto theory has a Weyl anomaly, as the central charge of the embedding fields does not cancel the conformal ghosts. As a fundamental string theory this would be inconsistent, but in EST, which is an EFT, one instead requires conformal invariance only order by order in the long-string expansion. The Weyl anomaly is then compensated by additional terms in the effective action, beginning with the Polchinski–Strominger term, whose coefficient is fixed by the target-space dimension rather than by microscopic dynamics.

A second viewpoint introduces an auxiliary intrinsic worldsheet metric and works in a Polyakov-like formalism. This restores worldsheet covariance and allows one to classify operators in a manifestly gauge-invariant way [18]. Conceptually, this has the clear advantage that the effective action can be discussed without committing too early to a particular gauge fixing, and the organization of operators becomes cleaner. From a practical point of view, however, this comes at the price of additional redundancy.

For the purposes of this thesis, static gauge will be the default choice because the physical degrees of freedom are manifest, with the transverse displacements X^i as the only independent fields. This is also the natural description of the domain-wall systems studied below, where the wall is represented as a height field over a reference plane. In this gauge the derivative expansion becomes an ordinary local expansion in X^i and their derivatives, making it convenient for constructing the effective action, discussing universality, and identifying boundary operators. The price is that target-space symmetry is not manifest. Rotations mixing longitudinal and transverse directions are realized nonlinearly, so Lorentz invariance must be imposed as a constraint on the allowed operators and coefficients [15, 20].

In static gauge, fluctuations of the embedding along the worldsheet directions are removed using worldsheet reparametrization invariance by identifying the longitudinal target-space coordinates with the worldsheet coordinates,

$$X^\alpha(\xi) = \xi^\alpha, \qquad \alpha = 1, 2. \tag{1.5}$$

The embedding then takes the form

$$X^\mu(\xi) = \big(\xi^1, \xi^2, X^i(\xi)\big), \qquad i = 3, \dots, D. \tag{1.6}$$

leaving the transverse fields $X_i(\xi)$ as the independent physical degrees of freedom. These fields are the Goldstone modes associated with the broken transverse translations and describe local displacements of the string relative to the reference plane [2].

The static-gauge and orthogonal-gauge descriptions are physically equivalent, but the equivalence is not completely automatic. The agreement of the leading corrections to the long-string spectrum is therefore a nontrivial consistency check. It shows that the apparent differences between the two descriptions are differences of organization rather than physical content, once regularization, nonlinear Lorentz symmetry, and field redefinitions are treated consistently [14, 16, 19].

1.1.2. Lüscher term

Historically, the Lüscher term was one of the first concrete indications that a long confining flux tube behaves as a string [13]. In modern language, the Lüscher term is the Casimir energy of the $D-2$ transverse massless modes on the worldsheet, and is therefore universal. We reproduce the derivation in the EFT language here both because of its historical importance and because it provides the simplest illustration of low-energy universality.

Consider a long string of length R, stretched along the ξ^2 direction. In Euclidean signature, we take the worldsheet time to have extent L, $\xi^1 \in [0, L]$. [3] The symmetry analysis above determines the leading action. The zero-derivative term is the classical free-energy cost proportional to the worldsheet area, while transverse shift symmetry forbids a potential for X^i. At two-derivative order, $SO(2)\times SO(D-2)$ invariance leaves a unique quadratic kinetic term. The leading effective action is therefore

$$S_{\text{eff}} = \sigma LR + \frac{\sigma}{2}\int d^2\xi \partial_\alpha X^i \partial_\alpha X^i, \qquad i = 3, \dots, D, \tag{1.7}$$

The path integral is Gaussian and yields

$$Z(L,R) \propto e^{-\sigma LR}\left[\det(-\partial^2)\right]^{-\frac{D-2}{2}}, \tag{1.8}$$

where $-\partial^2$ is the scalar Laplacian on the worldsheet. The ground state energy is extracted from the large L behaviour,

$$Z(L,R) \sim e^{-LE_0(R)}, \qquad L \to \infty. \tag{1.9}$$

To evaluate the partition function, we expand the transverse fields in eigenmodes of the spatial Laplacian,

$$X^i(\xi_1, \xi_2) = \sum_{n=1}^{\infty} X_n^i(\xi_1)\sin(\omega\xi_2), \tag{1.10}$$

[2] The fields $X^i(\xi)$ are target-space coordinate fields in the transverse directions. For small fluctuations around a flat reference plane they coincide with normal displacements at leading order, but for a generic curved embedding the local normal directions are field-dependent

[3] The notation in this section differs from that used in Chapter 3. Here the cylinder has a distinguished Euclidean time extent L and a spatial string length R, so it is useful to keep the two directions notationally separate. In Chapter 3 the worldsheet is a torus associated with a domain wall, and the two wrapped directions are treated symmetrically, so they are denoted by L_1 and L_2.

with a set of harmonic oscillators with frequencies ω_n. The zero-point energy is therefore

$$E_0(R) = \sigma R + \frac{D-2}{2}\sum_n \omega_n. \tag{1.11}$$

The Lüscher term is the regularized value of this Casimir energy, where the spectrum ω_n is determined by the boundary conditions. For an open string with fixed endpoints, the transverse fields obey Dirichlet boundary conditions,

$$X^i(\xi^1, 0) = X^i(\xi^1, R) = 0, \tag{1.12}$$

and $\omega_n = \frac{\pi n}{R}$, with $n \in \mathbb{N}$. Thus

$$E_0^{\text{open}}(R) = \sigma R + \frac{D-2}{2}\frac{\pi}{R}\sum_{n=1}^{\infty} n = \sigma R - \frac{\pi(D-2)}{24R}, \tag{1.13}$$

where

$$\sum_{n=1}^{\infty} n = \zeta(-1) = -\frac{1}{12}. \tag{1.14}$$

Higher-derivative interactions generate terms starting at R^{-3}.

Analogously, for a closed string the Casimir energy is

$$E_0^{\text{closed}}(R) = \sigma R - \frac{\pi(D-2)}{6R}. \tag{1.15}$$

The coefficient is four times larger than in the open string case because periodic boundary conditions give momenta in units of $2\pi/R$, and both left- and right-moving excitations contribute.

The leading theory is thus fixed by the Goldstone content and already gives the universal $1/R$ correction. The next question is how strongly symmetry and consistency constrain the subleading terms. We will approach this in several complementary ways: first through open-closed duality of the finite-volume partition function, then directly through the nonlinear realization of spacetime symmetry in static gauge, and finally through a geometric formulation of the worldsheet action.

1.1.3. Open-closed duality

Finite worldsheet partition functions are constrained not only by local symmetry, but also by consistency between different channel decompositions. For the open string cylinder, this condition is open-closed duality. The same cylinder amplitude can be written either as a trace over open string states of length R propagating for Euclidean time L or as a closed string exchange amplitude between boundary states separated by Euclidean distance R. In quantum field theory this is not merely a formal rewriting. It imposes nontrivial constraints on the spectrum, on the allowed boundary terms, and on the normalization of the cylinder partition function [21, 22].

A closely related idea will reappear later in this thesis for toroidal domain walls. There the finite worldsheet has no boundary, and the relevant consistency condition is not open-closed duality of the cylinder, but modular invariance of the torus partition function.

Open-closed duality is highly restrictive. In particular, the authors of [21] used it to show that the would-be correction of order $1/R^2$ to the open string ground state energy is absent, and that the terms

at order $1/R^3$ are not arbitrary but, in $D = 3$, are fixed. Thus open-closed duality turns the EST into more than a typical EFT as it imposes global consistency conditions on the finite-volume theory.

Schematically, the derivation goes as follows. The cylinder partition function can be written in the open string channel as

$$Z_{\rm cyl}(R, L) = {\rm Tr}_{\rm open} e^{-LH_{\rm open}(R)} = \sum_n w_n e^{-LE_n(R)}, \tag{1.16}$$

where R is the separation between the endpoints and L is the Euclidean time extent, w_n may depend on R but not on L. At leading order, the $D-2$ transverse fields are free massless bosons on a strip. This gives

$$Z_0(R, L) = e^{-\sigma LR}\eta(q)^{-(D-2)}, \qquad q = e^{-\pi L/R}. \tag{1.17}$$

Using

$$\eta(\tau)^{-(D-2)} = q^{-\frac{D-2}{24}} \prod_{n=1}^{\infty}(1-q^n)^{-(D-2)}, \tag{1.18}$$

this becomes

$$Z_0(R, L) = \sum_{N=0}^{\infty} d_N \exp\left[-L\left(\sigma R + \frac{\pi}{R}\left(N - \frac{D-2}{24}\right)\right)\right], \tag{1.19}$$

from which we can read the spectrum

$$E_N(R) = \sigma R + \frac{\pi}{R}\left(N - \frac{D-2}{24}\right), \tag{1.20}$$

and where d_N are the degeneracies generated by

$$\prod_{n=1}^{\infty}(1-q^n)^{-(D-2)} = \sum_{N=0}^{\infty} d_N q^N. \tag{1.21}$$

The same cylinder partition function can also be interpreted in the closed string channel. Introducing

$$\tau = \frac{iL}{2R}, \qquad q = e^{2\pi i\tau}, \tag{1.22}$$

the modular transformation $\tau \to \tilde{\tau} = -1/\tau$ maps $q \to \tilde{q} = e^{-4\pi R/L}$. Using the property

$$\eta(\tau) = (-i\tau)^{-1/2}\eta(-1/\tau), \tag{1.23}$$

we get

$$Z_0(R, L) = e^{-\sigma RL}\eta(\tau)^{-(D-2)} = e^{-\sigma RL}\left(\frac{L}{2R}\right)^{\frac{D-2}{2}} \eta(\tilde{\tau})^{-(D-2)}. \tag{1.24}$$

We now ask whether a correction of order $1/R^2$ to the open string energies is allowed. The leading kinetic term contains two derivatives and produces the $1/R$ contribution to the open-string energy. A bulk correction at order $1/R^2$ would require a local scalar with effectively one additional derivative, but no such three-derivative bulk operator is compatible with the symmetries. The required additional power of 1/R can instead arise from restricting a two-derivative operator to the one-dimensional

boundary, leading to the term written below.

$$S_{\rm b} = b \int_{\partial\Sigma} d\xi^0 \partial_2 X^i \partial_2 X_i. \tag{1.25}$$

Its expectation value in the free theory gives a correction to the cylinder partition function of the form [13]

$$Z_{\rm cyl} = Z_0 \left[1 + \lambda_b \frac{L}{R^2} E_2(q) + O(R^{-3})\right], \tag{1.26}$$

where λ_b is proportional to the boundary coupling b, and E_2 is the Eisenstein series of weight two; see app. A for a review of the Eisenstein series properties. Since at large R

$$E_2(q) = 1 + O(q), \tag{1.27}$$

this term would produce corrections of order $1/R^2$ to the open string energy levels.

The obstruction becomes clear only after transforming to the closed string channel. The anomalous modular transformation of E_2 gives

$$E_2(\tau) = \tau^{-2} E_2(-1/\tau) + \frac{6i}{\pi}\tau^{-1}. \tag{1.28}$$

For $\tau = iL/(2R)$, this implies

$$\frac{L}{R^2} E_2(q) = -\frac{4}{L} E_2(\tilde{q}) + \frac{12}{\pi R}. \tag{1.29}$$

The second term is the problem. A closed-channel decomposition has the form

$$Z_{\rm cyl}(R, L) = \langle B | e^{-R H_{\rm closed}(L)} | B \rangle = \sum_m |\langle B|m\rangle|^2 e^{-R\widetilde{E}_m(L)}, \tag{1.30}$$

where the overlap coefficients may depend only on L, the spatial size in this channel. The only allowed R-dependence is linear in R, arising from corrections to the closed-string energies, since these appear multiplied by R in the exponent. Such terms can therefore be reinterpreted as perturbative corrections to the closed-string ground-state energy. Thus, there is no allowed closed-channel interpretation of a term proportional to $1/R$, implying that $b = 0$. The next order computation shows that there are no free parameters at order $1/R^3$, in $D = 3$, and just one in $D = 4$.

The absence of the $1/R^2$ correction is the first nontrivial consequence of open-closed duality. A term allowed by locality and symmetry is removed by the requirement that the same cylinder amplitude admit a consistent closed string channel interpretation [21, 22]. We now show that the same putative leading correction is excluded locally by the nonlinearly realized spacetime symmetry.

1.1.4. Higher-order bulk terms

We now derive locally, from the static-gauge EFT, the constraints on the subleading bulk interactions that were encountered above through open-closed duality. The aim is also to determine at which derivative order genuinely new microscopic information can first enter the bulk action. The construction follows the standard EFT logic.

One first writes the most general local bulk worldsheet Lagrangian compatible with locality, the

unbroken $SO(D-2)$ transverse rotations, Euclidean invariance on the worldsheet, parity[4] and constant shifts

$$X^i(\xi) \to X^i(\xi) + a^i, \qquad a^i = \text{constant}. \tag{1.33}$$

One then removes redundant terms in the action due to integrations by parts and field redefinitions. Finally, one imposes the nonlinear realization of the broken rotations that mix worldsheet and transverse directions. In the static gauge this last step fixes the first higher-derivative bulk terms to their Nambu-Goto values and sharply reduces the space of admissible operators at each order [15, 19, 20].

To make the construction explicit, consider the action through four-derivative order. At order zero, there is the classical action term, since the shift symmetry forbids undifferentiated X^i. At order two, the leading bulk action is the standard action for $D-2$ massless bosons

$$S_2 = \frac{\sigma}{2} \int d^2\xi \, \partial_\alpha X^i \partial^\alpha X_i. \tag{1.34}$$

At the next order, terms quadratic in second derivatives are allowed by the manifest symmetries, for example

$$\int d^2\xi \, \partial_\alpha \partial_\beta X^i \partial^\alpha \partial^\beta X_i, \qquad \int d^2\xi \, (\partial^2 X^i)^2. \tag{1.35}$$

However, these terms are redundant as bulk operators. Up to integrations by parts,

$$\int d^2\xi \, \partial_\alpha \partial_\beta X^i \partial^\alpha \partial^\beta X_i = \int d^2\xi (\partial^2 X^i)^2, \tag{1.36}$$

where boundary terms are ignored in the bulk classification. The remaining operator is proportional to the square of the leading equation of motion, $\partial^2 X^i = 0$. Equivalently, it can be removed by the field redefinition

$$X^i \to X^i + a\partial^2 X^i, \tag{1.37}$$

under which δS_2 is, up to boundary terms,

$$\delta S_2 = -\sigma a \int d^2\xi (\partial^2 X^i)^2. \tag{1.38}$$

Thus the coefficient of the four-derivative operator in eq. (1.35) can be shifted arbitrarily by a field redefinition, and it is not part of the physical bulk operator basis.

After removing such redundancies, the parity-even four-derivative bulk Lagrangian density can be

[4] Parity is not, *a priori,* a symmetry of the effective string theory. The effective action must instead respect the discrete symmetries of the microscopic theory and of the particular string or domain wall sector under consideration. For a codimension-one object, the choice of transverse normal is an orientation convention. Reversing this normal gives

$$n^\mu \to -n^\mu, \qquad K_{ab} \to -K_{ab}, \tag{1.31}$$

because the extrinsic curvature is linear in n^μ.

For a domain wall produced by the spontaneous breaking of a $\mathbb{Z}_2$ symmetry, this normal reversal has a microscopic interpretation. The two sides of the wall correspond to the two degenerate vacua. Acting with the $\mathbb{Z}_2$ symmetry exchanges these vacua, and therefore reverses the convention that defines the orientation of the wall. The geometric surface is the same, but the normal vector changes sign. The domain-wall effective action must therefore be invariant under

$$K_{ab} \to -K_{ab}. \tag{1.32}$$

Thus, terms containing an odd number of extrinsic curvatures are excluded.

written as

$$\mathcal{L}_4 = c_2 \left(\partial_\alpha X^i \partial^\alpha X_i\right)^2 + c_3 \left(\partial_\alpha X^i \partial_\beta X_i\right) \left(\partial^\alpha X^j \partial^\beta X_j\right). \tag{1.39}$$

At this stage c_2 and c_3 are arbitrary, but they will be fixed by imposing the nonlinear realization of target-space rotations. Consider an infinitesimal rotation mixing a worldsheet direction α with a transverse direction i. In static gauge, with the convention used here, its action on the transverse fields is [5]

$$\delta X^i = \epsilon^i_\alpha \xi^\alpha + \epsilon^j_\alpha X_j \partial^\alpha X^i. \tag{1.41}$$

The first term is the inhomogeneous shift induced by the broken rotation, while the second term is the compensating diffeomorphism required to preserve the static gauge. We denote the rotations as δ_0 and the compensating diffeomorphism δ_1.

The variation of the quadratic Lagrangian under δ_0 is a total derivative,

$$\delta_0 \left(\frac{1}{2} \partial_\beta X^i \partial_\beta X_i\right) = \epsilon^i_\beta \partial_\beta X_i. \tag{1.42}$$

The first nontrivial constraint at this order comes from requiring the variation of the four-derivative terms under δ_0 to cancel the variation of the quadratic term under δ_1. Define

$$A \equiv \partial_\gamma X^k \partial_\gamma X_k, \qquad B \equiv \left(\partial_\gamma X^k \partial_\delta X_k\right) \left(\partial^\gamma X^l \partial^\delta X_l\right). \tag{1.43}$$

Then

$$\delta_0 A = 2\epsilon^i_\alpha \partial^\alpha X_i, \qquad \delta_0 B = 4\epsilon^i_\alpha \partial_\beta X_i \partial^\alpha X^j \partial^\beta X_j. \tag{1.44}$$

Therefore,

$$\delta_0 \mathcal{L}_4 = 4c_2 \left(\partial X \cdot \partial X\right) \epsilon^i_\alpha \partial^\alpha X^i + 4c_3 \epsilon^i_\alpha \partial_\beta X_i \partial^\alpha X^j \partial^\beta X_j. \tag{1.45}$$

On the other hand, when acting on the kinetic term, the nonlinear part of the transformation gives, modulo total derivatives,

$$\delta_1 \left(\frac{1}{2} \partial_\beta X^i \partial^\beta X_i\right) = -\frac{1}{2} \left(\partial X \cdot \partial X\right) \epsilon^i_\alpha \partial^\alpha X_i + \epsilon^i_\alpha \partial_\beta X_i \partial^\alpha X^j \partial^\beta X_j. \tag{1.46}$$

Requiring $\delta\mathcal{L} = 0$ at fourth derivative order yields $\delta_0 \mathcal{L}_4 + \delta_1 \mathcal{L}_2 = 0$

$$\begin{cases} 4c_2 - \frac{1}{2} = 0, \\ 4c_3 + 1 = 0 \end{cases} \implies (c_2, c_3) = \left(\frac{1}{8}, -\frac{1}{4}\right). \tag{1.47}$$

Thus the four-derivative bulk terms contain no new microscopic data as their coefficients are fixed by the nonlinear realization of spacetime symmetry.

[5] In static gauge, $X^\beta(\xi) = \xi^\beta$. An infinitesimal rotation in the (α, i)-plane gives $\delta_{\rm rot} X^\alpha = -\epsilon X^i$ and $\delta_{\rm rot} X^k = \epsilon \delta^{ki} \xi^\alpha$. To preserve the gauge condition, this must be accompanied by a worldsheet reparametrization $\delta_{\rm diff} X^\mu = -\zeta^\beta \partial_\beta X^\mu$ with $\zeta^\beta = -\epsilon X^i \delta^\beta_\alpha$. Therefore $\delta_{\rm diff} X^k = \epsilon X^i \partial_\alpha X^k$, and the gauge-fixed transformation is

$$\delta X^k = \epsilon \delta^{ki} \xi^\alpha + \epsilon X^i \partial_\alpha X^k. \tag{1.40}$$

The overall sign depends on the conventions for ϵ and the infinitesimal reparametrization.

The general structure of the bulk effective action is therefore

$$S_{\text{bulk}} = \sigma \int d^2\xi \left[1 + \frac{1}{2}\partial_\alpha X^i \partial^\alpha X_i + \sum_{n\geq 2} \mathcal{L}_{2n} \right], \tag{1.48}$$

where $\mathcal{L}_{2n}$ denotes the contribution with $2n$ worldsheet derivatives. At each order, the problem is reduced to a finite EFT task: construct all operators allowed by the manifest symmetries, remove redundancies, and impose the nonlinear realization of the broken spacetime symmetries. This procedure is systematic and can be carried out to arbitrary order.[6]

1.1.5. Boundary terms

For open strings, the effective action is not exhausted by bulk worldsheet terms. The boundary EFT depends on the physical nature of the endpoints. In the setup considered here, the flux tube ends on static external sources. The endpoints are prescribed and the transverse worldsheet fields therefore obey Dirichlet boundary conditions. Neumann boundary conditions instead describe endpoints that are free to move transversely and lead to a different boundary EFT [22]. Neither setup should be identified directly with a physical meson containing dynamical quarks, whose endpoints can recoil, carry additional quantum numbers, mix with other hadronic states, and allow the flux tube to break.

The EFT must therefore distinguish operators integrated over the interior of the worldsheet, S_{bulk}, from operators localized on its boundary, S_{bdy}. The latter encode short-distance physics near the sources and give additional finite-size corrections to observables such as the static potential or Polyakov-loop correlators. These boundary terms carry independent non-universal Wilson coefficients and are not determined by the bulk worldsheet action alone. This distinction is essential when one wants to extract intrinsic worldsheet Wilson coefficients, since boundary operators enter at lower order than the first intrinsic non-universal bulk coefficient. This is one reason for focusing on toroidal domain walls, where boundary contributions are absent, in Chapter 3. It is nevertheless useful to determine the order at which boundary effects first enter.

Let τ denote Euclidean time and let $r \in [0, R]$ parameterize the string. For fixed endpoints, the transverse fields obey Dirichlet boundary conditions,

$$X^i(\tau, 0) = X^i(\tau, R) = 0. \tag{1.49}$$

The boundary action must be organized as a derivative expansion compatible with the symmetries preserved by the endpoints.

Again, some operators allowed by the manifest symmetries are nevertheless forbidden by the nonlinear realization of target-space Lorentz symmetry. For example, a putative two-derivative boundary term of the form [7]

$$\int_{\partial\Sigma} d\tau \partial_r X^i \partial_r X_i \tag{1.50}$$

where $\partial_r X^i$ characterizes the angle at which the flux tube approaches the boundary, is not compatible with the full nonlinear Lorentz symmetry. Under a rotation mixing the string direction r with a

[6] By a sufficiently motivated individual.

[7] This is the same term excluded by Lüscher using the open-closed duality, thus we already know it is not allowed. Nonetheless, it is pedagogical to understand why it is excluded based on symmetry arguments.

transverse direction, the endpoint slope transforms inhomogeneously,

$$\delta(\partial_r X^i) = \epsilon^i + \cdots , \tag{1.51}$$

such that the variation of the operator is proportional to

$$\int_{\partial\Sigma} d\tau \epsilon^i \partial_r X_i, \tag{1.52}$$

which is not a total derivative and cannot be canceled by any lower-order boundary term. Its coefficient must therefore vanish. This is consistent with the absence of a $1/R^2$ correction found above from open-closed duality, now derived locally from the nonlinear realization of spacetime symmetry.

The first nontrivial Lorentz-invariant Dirichlet boundary term instead appears at higher derivative order. Consider the normalized normal boundary vector

$$n^\mu = \frac{(0, 1, v^i)}{\sqrt{1+v^2}}, \quad v^i \equiv \partial_r X^i \tag{1.53}$$

and its time variation

$$\partial_\tau n^\mu = \frac{(0, 0, \partial_\tau \partial_r X^i)}{\sqrt{1+v^2}} - \frac{(0, 1, v^i)}{(1+v^2)^{3/2}} v \cdot \partial_\tau v^i. \tag{1.54}$$

Then, the simplest Lorentz invariant term is $\partial_\tau n^\mu \partial_\tau n_\mu$, reproducing the leading term in [23]

$$S_{b_2} = b_2 \int_{\partial\Sigma} d\tau \left[\frac{\partial_\tau \partial_r X \cdot \partial_\tau \partial_r X}{1 + \partial_r X \cdot \partial_r X} - \frac{(\partial_\tau \partial_r X \cdot \partial_r X)^2}{(1 + \partial_r X \cdot \partial_r X)^2} \right]. \tag{1.55}$$

Geometrically, it is the square of the covariant variation, along the endpoint worldline, of the unit vector tangent to the worldsheet and normal to the boundary. It measures changes in the direction with which the string leaves the endpoint.

Expanding at small slope gives

$$S_{b_2} = b_2 \int_{\partial\Sigma} d\tau \partial_\tau \partial_r X^i \partial_\tau \partial_r X^i + \cdots , \tag{1.56}$$

where the coefficient b_2 is the first non-universal boundary coupling for an open string with fixed endpoints. Its contribution to the open string spectrum scales as [22]

$$\Delta E_{\text{bdy}}(R) \sim \frac{b_2}{\sigma^2 R^4}. \tag{1.57}$$

1.2. Nambu-Goto as the minimal geometric completion

The preceding construction organized the long-string EFT directly in static gauge and used the nonlinear spacetime symmetries to constrain its coefficients. We now introduce a complementary geometric organization of the same universal interactions. This makes their relation to the Nambu-Goto action manifest and provides a geometric basis for classifying the first non-universal corrections. The leading reparametrization-invariant functional is the worldsheet area, giving the Nambu-Goto action. For a

domain wall in the 3D Ising model, this area dependence also has a simple microscopic interpretation: its energy is proportional to the number of frustrated bonds.

For simplicity, from now on, we focus on the $D = 3$ case. Let $X^a(\xi)$, with $a = 1, \ldots, 3$, denote the embedding of the worldsheet into Euclidean spacetime, with metric G_{ab}, and let

$$h_{\alpha\beta} \equiv \partial_\alpha X^a \partial_\beta X^b G_{ab} \tag{1.58}$$

be the induced metric on the worldsheet. If one requires locality and worldsheet reparametrization invariance, the leading geometric term is the worldsheet area functional,

$$S_{\rm NG} = \sigma \int d^2\xi \sqrt{\det h_{\alpha\beta}}. \tag{1.59}$$

In this sense, the Nambu-Goto action is the minimal geometric completion[8] of the leading long-string effective theory: it resums the interactions fixed by the induced worldsheet geometry into the simplest reparametrization-invariant action containing no derivatives of the induced metric [15, 16].

In static gauge, the induced metric becomes

$$h_{\alpha\beta} = \delta_{\alpha\beta} + \partial_\alpha X \partial_\beta X, \tag{1.60}$$

and expanding the square root using

$$\sqrt{\det(1+A)} = 1 + \frac{1}{2}\mathrm{Tr}A + \frac{1}{8}\big(\mathrm{Tr}A\big)^2 - \frac{1}{4}\mathrm{Tr}(A^2) + O(A^3), \qquad A_{\alpha\beta} = \partial_\alpha X \partial_\beta X \tag{1.61}$$

yields

$$S_{\rm NG} = \sigma \int d^2\xi \left[1 + \frac{1}{2}\partial_\alpha X \partial_\alpha X + \frac{1}{8}\left(\partial_\alpha X \partial_\alpha X\right)^2 - \frac{1}{4}\left(\partial_\alpha X \partial_\beta X\right)\left(\partial_\alpha X \partial_\beta X\right) + O(\partial^6)\right]. \tag{1.62}$$

The quadratic term is the expected action for the transverse Goldstone mode. The nontrivial point is that the four-derivative coefficients coincide with those fixed by the nonlinear realization of spacetime symmetry in eq. (1.47). Thus the first interaction terms are not arbitrary. They are precisely the ones equivalent to Nambu-Goto.

The Nambu-Goto action therefore provides the simplest geometric realization of the universal long-string dynamics, obtained by retaining only the induced area term. A generic microscopic theory also generates additional reparametrization-invariant operators constructed, for example, from the extrinsic curvature and covariant derivatives of the embedding. Their Wilson coefficients contain new microscopic information and produce the first departures from the universal Nambu-Goto predictions.

The distinction is especially important at the quantum level. As a fundamental string theory, the bare Nambu-Goto action is not consistent in generic target-space dimension, reflected in the usual anomaly away from the critical dimension. As an effective description of a long confining string, this is not the relevant requirement.

[8] Here "completion" means a nonlinear geometric completion of the leading derivative expansion. It should not be confused with a UV completion. The Nambu-Goto action by itself is not a microscopic definition of a generic confining string, nor does it contain all operators allowed in the effective theory.

1.2.1. Beyond Nambu-Goto: geometric invariants and the end of universality

We now use the geometric formulation to determine where universality ends, namely to identify the first local operators whose coefficients are not fixed by the long-string symmetries. The candidate corrections are reparametrization-invariant scalars constructed from the induced metric, the extrinsic curvature, and covariant derivatives acting on them.

The question is not whether such terms are allowed, but at which order in the long string limit they first contribute. As usual in EFT, symmetry-allowed operators are expected to be generated unless forbidden by an additional principle. This point requires some care. The simplest intrinsic curvature invariant,

$$\int_\Sigma d^2\xi\sqrt{h}\mathcal{R}, \tag{1.63}$$

does not modify the local dynamics of a closed worldsheet, because in two dimensions it is topological. In dimensional regularization, however, such terms can still be retained by continuing the worldsheet dimension away from two, where they are no longer strictly topological and may enter as evanescent operators or counterterms.

Similarly, the operator

$$\int_\Sigma d^2\xi\sqrt{h}K^2, \qquad K \equiv h^{\alpha\beta}K_{\alpha\beta}, \tag{1.64}$$

where $K \equiv h^{\alpha\beta}\nabla_\alpha\partial_\beta X$ is the mean extrinsic curvature. Since $K = 0$ is the leading equation of motion, the K^2 operator can be removed by a field redefinition. Thus the first curvature invariants one can write are not necessarily the first physical corrections to the EST.

After the topological and redundant terms are removed, the first genuinely new bulk operators are built from higher powers of $K^i_{\alpha\beta}$, or from covariant derivatives of it, modulo integrations by parts, equations of motion, and geometric identities such as the Gauss-Codazzi relations.

In $D = 3$, there is only one transverse direction. This makes the geometric operator basis particularly constrained. The four- and six-derivative bulk terms are fixed to their Nambu-Goto values, and the first non-universal correction appears only at eight-derivative order. It may be written as

$$S_{\gamma_3} = 2\frac{\gamma_3}{\sigma}\int_\Sigma d^2\xi\sqrt{h}\left(K_{\alpha\beta}K^{\alpha\beta}\right)^2, \tag{1.65}$$

with the normalization of γ_3 chosen to match the normalization in the phase shift [24]. This is the geometric origin of the coefficient γ_3 used later in the thesis.

Expanding about a nearly flat worldsheet, the extrinsic curvature is [9]

$$K_{\alpha\beta} = \partial_\alpha \partial_\beta X + O(\partial X \partial^2 X), \tag{1.70}$$

and therefore

$$S_{\gamma_3} = 2\frac{\gamma_3}{\sigma} \int_\Sigma d^2\xi \, (\partial_\alpha \partial_\beta X \partial_\alpha \partial_\beta X)^2 + O(\partial^{10}). \tag{1.71}$$

The operator may also be represented using the intrinsic scalar curvature in codimension one, but this is not the most convenient definition. By the Gauss-Codazzi relation,

$$\mathcal{R} = K^2 - K_{\alpha\beta} K^{\alpha\beta}, \tag{1.72}$$

such that, using the leading equation of motion $K = 0$, one finds that $\mathcal{R}^2$ and K^4 are equivalent.

In $D > 3$ the situation is less restrictive. There are several transverse directions, and additional contractions of the extrinsic curvature and its covariant derivatives become independent. The identities that delay the first correction in $D = 3$ no longer remove all lower-order structures. The precise operator basis is therefore dimension-dependent. The EFT logic is, however, the same: construct all reparametrization-invariant geometric terms, remove topological and equation of motion redundancies, and identify the first coefficients not fixed by Nambu-Goto symmetry.

There is, however, an important subtlety. Each geometric invariant generates an infinite tower of static-gauge interactions when expanded in the transverse fluctuations. Therefore, terms at a fixed order in the inverse-length expansion can arise from different sources: tree-level contributions from higher-derivative invariants, loop corrections involving lower-order vertices, and mixed diagrams involving several operators. The power counting must track both the derivative order of the geometric invariant and the loop order at which its expanded vertices contribute.

This is one reason why it is often more efficient to reorganize the calculation in terms of the worldsheet scattering phase shift. At low energies, the universal long-string dynamics is integrable, with elastic factorized scattering, so the corresponding tower of perturbative contributions can be resummed into the phase shift rather than computed diagram by diagram.

1.3. Modern effective string theory: Integrability and the $T\bar{T}$ deformation

The classification of local operators in the derivative expansion can be complemented by a scattering-based description of the long-string dynamics. Once the infrared degrees of freedom are identified with

[9] The extrinsic curvature is the normal projection of the second covariant derivative of the embedding,

$$K^a_{\alpha\beta} = P^a{}_b \nabla_\alpha \partial_\beta X^b, \tag{1.66}$$

where

$$\nabla_\alpha \partial_\beta X^a = \partial_\alpha \partial_\beta X^a + \Gamma^a{}_{bc} \partial_\alpha X^b \partial_\beta X^c \tag{1.67}$$

and

$$P^a{}_b = \delta^a{}_b - \partial_\gamma X^a h^{\gamma\delta} \partial_\delta X_b \tag{1.68}$$

is the projector onto directions normal to the worldsheet. Thus

$$K^a_{\alpha\beta} = \left(\delta^a{}_b - \partial_\gamma X^a h^{\gamma\delta} \partial_\delta X_b\right) \partial_\alpha \partial_\beta X^b \tag{1.69}$$

Equivalently, instead of projecting, one can compute the Christoffels on the worldsheet.

the transverse Goldstone modes, one can ask what worldsheet S-matrix is generated by the allowed interactions and what this implies for possible UV completions. This formulation is also well suited to lattice applications, since simulations probe finite-volume spectra and partition functions more directly than local worldsheet interactions. At low energies the worldsheet scattering is integrable, and the thermodynamic Bethe ansatz (TBA) provides an exact relation between the scattering data and the finite-volume spectrum.

The central development was the realization that the worldsheet S-matrix associated with the Goddard-Goldstone-Rebbi-Thorn (GGRT)/Nambu-Goto theory spectrum, which gives the Nambu-Goto spectrum in the long-string setting considered here, is described by a pure phase shift [25, 26]. Later this was interpreted as the gravitational dressing [27], or $T\bar{T}$ deformation [27–30], an irrelevant integrable deformation of the free theory of massless bosons. Non-universal corrections can then be organized as deformations of this integrable phase shift. The integrability of the Goldstone-only GGRT worldsheet theory is special to $D = 3$ and $D = 26$, under the assumption that the only massless degrees of freedom are the massless modes [31].

In scattering language, the infinite tower of Nambu-Goto operators in static gauge is repackaged as a purely elastic two-body phase shift. For a left-moving and a right-moving massless excitation with Mandelstam invariant s, the universal phase shift is [10]

$$S_{\mathrm{GGRT}}(s) = e^{2i\delta_{\mathrm{GGRT}}(s)}, \qquad 2\delta_{\mathrm{GGRT}}(s) = \frac{\ell_s^2 s}{4}. \tag{1.73}$$

Then, Bethe quantization states that for a state with worldsheet momenta p_i on a circle R, the quantization conditions take the form

$$p_i R + \sum_{j\neq i} 2\delta(s_{ij}) = 2\pi n_i, \tag{1.74}$$

Here $s_{ij} = (p_i + p_j)^2$ is the Mandelstam invariant of the two-particle collision. For massless worldsheet excitations it vanishes for particles with the same handedness, while a left- and a right-moving excitation have nontrivial scattering. Each particle therefore accumulates the phase shifts associated with all particles of opposite handedness as it goes around the circle. Thus one can reconstruct the corresponding finite-volume spectrum, the GGRT spectrum. In comparison with lattice data for excited states this scattering-based organization can be more efficient than a direct large R expansion [25, 29, 32].

Alternatively, non-universal EST data can also be packaged as corrections to the GGRT phase shift. In three target-space dimensions, the minimal extension is

$$2\delta(s) = \frac{\ell_s^2 s}{4} + \gamma_3 \ell_s^6 s^3. \tag{1.75}$$

Using this phase shift, the TBA allows us to treat the γ_3 deformation perturbatively [11] while keeping the dependence on the worldsheet area non-perturbative. This avoids fitting directly with the asymptotic, generally divergent, large R expansion.

[10] Since the Goldstones are massless, left-left and right-right scattering is kinematically trivial.

[11] TBA by itself is non-perturbative in γ_3. Here it is used only perturbatively because we were forced to expand the equations order by order in γ_3 in order to solve them.

A notational convention should be made explicit. The same symbol γ_3 is used both for the coefficient of the geometric operator K^4 in the static-gauge effective action and for the coefficient of the s^3 term in the low-energy two-branon phase shift. This identification is meant at the order where the two descriptions are matched. It should not be interpreted as saying that the phase shift

$$2\delta(s) = \frac{\ell_s^2 s}{4} + \gamma_3 \ell_s^6 s^3 \tag{1.76}$$

is an exact resummation of the full $\gamma_3 K^4$ deformation. The GGRT phase shift is special. No analogous closed-form elastic completion is assumed for the K^4 interaction. Once the K^4 operator is expanded in static gauge, it generates higher-point vertices as well as corrections to higher powers in the elastic phase shift. At sufficiently high order it can also contribute to inelastic multiparticle processes. Thus the coefficients in the phase-shift expansion are physical combinations of Wilson coefficients in the effective action, not generally in a one-to-one correspondence with them. Conversely, an elastic phase shift in which only the s^3 correction is kept corresponds to a particular combination of Wilson coefficients, not to turning on only the geometric operator K^4 in the action.

The scattering formulation replaces the diagram-by-diagram expansion with a spectral computation based on the worldsheet S-matrix, and is the strategy used later to extract γ_3 from the numerical data.

1.3.1. The structure of the scattering amplitude

There are two distinct first-principles inputs controlling the low-energy worldsheet scattering amplitude. The first is the S-matrix bootstrap, which constrains the allowed coefficients in the low-energy expansion of the elastic Goldstone S-matrix, using basic physical principles described below. The second is the power counting for the first inelastic processes. Combining these inputs, the elastic amplitude may be written in terms of a complex low-energy phase shift,

$$2\delta_{\text{EST}}(s) = \frac{\ell_s^2 s}{4} + \gamma_3 \ell_s^6 s^3 + \gamma_5 \ell_s^{10} s^5 + \gamma_7 \ell_s^{14} s^7 + i\gamma_8 \ell_s^{16} s^8 + \mathcal{O}\left(s^9\right). \tag{1.77}$$

We now schematically derive the general form in eq. (1.77).

S-matrix bootstrap

Here we briefly review the derivation of the lower bound on γ_3 obtained in [24]. In $D = 3$ there is a single transverse Goldstone mode, so left-right elastic scattering is described by a single scalar function $S(s)$. Its low-energy expansion is

$$2\delta(s) = \frac{\ell_s^2 s}{4} + \gamma_3 \ell_s^6 s^3 + \mathcal{O}(s^5), \tag{1.78}$$

where $S(s) = e^{2i\delta(s)}$. The first term is the universal GGRT contribution, while γ_3 parametrizes the leading non-universal correction.

The bootstrap asks which values of γ_3 are compatible with analyticity, real analyticity, crossing symmetry, and unitarity of the two-dimensional S-matrix. Physically, analyticity encodes causality and

locality by allowing singularities only when physical intermediate states can go on shell, real analyticity follows from the Hermiticity of the underlying theory, and unitarity expresses conservation of probability, with any reduction of the elastic amplitude accounting for probability flowing into inelastic channels. Setting $\ell_s = 1$ temporarily, real analyticity and crossing imply

$$S(-s^*) = S(s)^*, \tag{1.79}$$

while unitarity on the physical cut requires

$$|S(s)| \leq 1, \qquad s > 0. \tag{1.80}$$

Together with analyticity, these conditions imply that $S(s)$ defines a holomorphic map from the upper half-plane to the unit disk. The Schwarz-Pick lemma can therefore be applied. For any z, w in the upper half-plane,

$$\left| \frac{S(z) - S(w)}{1 - \overline{S(w)} S(z)} \frac{z - \overline{w}}{z - w} \right| \leq 1. \tag{1.81}$$

Inserting the low-energy expansion, eq. (1.78), and expanding the Schwarz-Pick combination for small imaginary z and w, one finds

$$S^{(1)}(z|w) = -1 + \left(\frac{1}{96} + 8\gamma_3 \right) |zw| + \cdots . \tag{1.82}$$

Since $S^{(1)}$ must remain inside the unit disk, the first correction away from -1 must be non-negative. This gives

$$\frac{1}{96} + 8\gamma_3 \geq 0, \qquad \Longrightarrow \qquad \gamma_3 \geq \gamma_3^{\min} = -\frac{1}{768}. \tag{1.83}$$

The extremal solution saturating this bound is integrable and is identified with the massless Goldstino S-matrix associated with the flow from the tricritical Ising model to the critical Ising model [24]. This special solution should not be interpreted as generic: there is no reason for a microscopic confining string or domain wall to saturate the bound. In the following, $\gamma_3^{\min}$ will instead provide a useful normalization for the measured non-universal coupling.

Onset of particle production

Due to parity, the first inelastic channel is $2 \to 4$, and is generated by the same non-universal K^4 interaction that gives the real $\gamma_3 s^3$ correction to the elastic phase shift. Expanded in static gauge, this interaction also contains higher-point vertices. The leading operator in K^4 that generates particle production is

$$K^4 \supset \gamma_3 \ell_s^8 \left(\partial^2 X \right)^4 (\partial X)^2 \tag{1.84}$$

such that

$$\mathcal{M}_{2\to 4} \sim \gamma_3 \ell_s^8 p^{10} \sim \gamma_3 \ell_s^8 s^5, \tag{1.85}$$

up to numerical convention-dependent factors. Unitarity then relates the loss of elastic probability to the square of this production amplitude,

$$|S_{2\to2}|^2 + \sum_{n\geq4} P_{2\to n} = 1, \qquad P_{2\to4} \sim \frac{1}{s^2}|\mathcal{M}_{2\to4}|^2 \sim \gamma_3^2 \ell_s^{16} s^8. \tag{1.86}$$

Thus the first absorptive correction to the elastic phase shift appears at order s^8. The corresponding coefficient γ_8 receives a contribution of order γ_3^2. This is a power-counting statement, which may be spoiled by special integrable completions where higher-order terms cancel the associated particle production [12].

1.3.2. Thermodynamic Bethe ansatz for effective strings

Having understood the low-energy integrable structure, we now use the thermodynamic Bethe ansatz to derive the finite-volume spectrum from the worldsheet scattering phase shift. The application of TBA methods to effective strings and confining flux tubes was developed in [24–26, 29, 31, 34]. The γ_3 corrections will be studied in Chapter 3.

We work in units where

$$\sigma = 1, \qquad \ell_s = 1, \tag{1.87}$$

and restore dimensions in the main text by using

$$R = \sqrt{\sigma} L_2, \qquad \mathcal{A} = \sigma L_1 L_2, \qquad R^2 = \frac{\mathcal{A}}{u}. \tag{1.88}$$

GGRT spectrum

Since the worldsheet theory is massless, we explicitly distinguish right- and left-moving excitations. We now parameterize the physical momenta as p/R and q/R, with $p, q > 0$ dimensionless. For a right-left collision,

$$s = 4\frac{pq}{R^2}. \tag{1.89}$$

with phase shift

$$2\delta(s) = \frac{s}{4}. \tag{1.90}$$

Then, the TBA equations reduce to [13]

$$\epsilon_R(x) = x\left[1 + \frac{P_L^{(1)}}{R^2} + \frac{1}{R^2}\int_0^\infty \frac{dx'}{2\pi} \log\left(1 - e^{-\epsilon_L(x')}\right)\right], \tag{1.91}$$

with

$$x \equiv pR, \qquad P_R^{(1)} = \sum_l p_l, \tag{1.92}$$

[12] For a pedagogical example of how the absence of particle production recursively fixes the higher interactions in two-dimensional scalar theories, leading to the sinh-Gordon and sine-Gordon models, see the review [33].

[13] For brevity, we will show the equations for the right movers. The equation for the left movers is obtained by swapping L with R.

and where the sum is over all right movers. Plugging the ansatz suggested by eq. (1.91)

$$\epsilon_R(x) = c_R x, \tag{1.93}$$

into the TBA equations and using

$$\int_0^\infty \frac{dx}{2\pi} \log\left(1 - e^{-cx}\right) = -\frac{\pi}{12c}, \tag{1.94}$$

we obtain

$$c_R = 1 + \frac{P_L^{(1)}}{R^2} - \frac{\pi}{12 c_L R^2}. \tag{1.95}$$

Excited states are obtained by including physical worldsheet particles whose momenta satisfy the Bethe quantization condition around the spatial circle,

$$2\pi n_l = c_R p_l, \tag{1.96}$$

such that

$$P_R^{(1)} = \frac{2\pi k}{c_R}, \tag{1.97}$$

where

$$k = \sum_l n_l. \tag{1.98}$$

Equations (1.95) and (1.97) imply

$$c_R = 1 + \frac{2\pi}{c_L R^2}\left(k' - \frac{1}{24}\right), \tag{1.99}$$

$$c_L = 1 + \frac{2\pi}{c_R R^2}\left(k - \frac{1}{24}\right). \tag{1.100}$$

The TBA energy and momentum are given by

$$E_{k,k'} = R(c_R + c_L - 1), \qquad P_{k,k'} = R(c_R - c_L). \tag{1.101}$$

Finally, solving for c_R and c_L gives

$$E_{k,k'} = R\left[1 + \frac{4\pi}{R^2}\left(k + k' - \frac{1}{12}\right) + \frac{4\pi^2}{R^4}(k - k')^2\right]^{1/2}, \tag{1.102}$$

and

$$P_{k,k'} = \frac{2\pi(k - k')}{R}, \tag{1.103}$$

where we can verify explicitly that translations are preserved, as expected. This is the GGRT spectrum for one boson, obtained in the light cone quantization of the Polyakov action.

From eq. (1.98) we see that the degeneracy of the level k is the number of integer partitions of k, denoted by $p(k)$, and analogously for k'.

1.4. Lattice developments and the worldsheet axion

The development of EST was not driven only by formal progress on the worldsheet side. Lattice gauge theory provided increasingly precise evidence that long confining flux tubes are described by an effective string at large distances. Simulations of the static potential confirmed the linear term and the universal Lüscher correction, while later studies of closed-flux-tube spectra showed that many low-lying states are well approximated by the Nambu-Goto, or GGRT, prediction even at short lengths [21, 32, 35].

The same numerical progress also exposed the limitations of the minimal Goldstone description. In $(3+1)$-dimensional Yang-Mills theory, some closed string levels show structured deviations from the universal GGRT spectrum. The scattering-based formulation of EST made these deviations interpretable. Using approximate integrability and TBA methods, Dubovsky, Flauger, and Gorbenko argued that they provide evidence for an additional massive pseudoscalar excitation localized on the worldsheet, the worldsheet axion [36, 37]. More recent lattice studies have sharpened this picture [37].

This does not modify the universal infrared logic described above. EST describes the massless Goldstone modes required by broken transverse translations. Additional massive worldsheet excitations, when present, are non-universal. At energies below their mass, their effects are absorbed into Wilson coefficients of the Goldstone EFT. At energies where they are resolved, they must be included as explicit worldsheet degrees of freedom. Thus symmetry fixes the universal long-distance sector, while the non-universal spectrum of the worldsheet theory must be determined by matching to microscopic data.

The worldsheet axion shows why the symmetry analysis must be supplemented by microscopic data. The lattice calculation supplies finite-volume spectra, but these spectra become physically informative only once they are organized by the worldsheet theory. Conversely, the same data test the minimal Goldstone EFT and can reveal structures not required by symmetry alone. The worldsheet axion is therefore not an arbitrary field added to the effective action. It is a non-universal worldsheet excitation inferred from controlled deviations between lattice spectra and the universal GGRT/EST expectations. The numerical results that led to its discovery, taken from [36], are shown in fig. 1.1.

The same logic will be used below for the Ising domain wall. The effective description becomes quantitative only after it is matched to observables in a microscopic theory. Here the matching is performed using lattice Monte Carlo simulations of the 3D Ising model, which provide non-perturbative access to the free energies, partition-function ratios, and correlation functions used to test the effective string description.

Summary of the hierarchy The discussion above identifies the hierarchy of effects that will be used in the rest of the thesis. At the longest distances, the only active worldsheet degrees of freedom are the transverse Goldstone modes. Their free dynamics gives the universal Lüscher term. The first nonlinear corrections are still universal and are organized by the Nambu-Goto theory.

Beyond this universal sector, the structure depends on the geometry of the observable. For open strings, boundary operators introduce independent Wilson coefficients before the first intrinsic bulk coefficient can be isolated. The leading allowed boundary correction is conventionally denoted by b_2. Closed worldsheets avoid these boundary terms. In particular, for a toroidal worldsheet in $D = 3$, the first intrinsic non-universal correction is governed by the coefficient γ_3, multiplying the leading

quartic extrinsic curvature interaction. Massive worldsheet excitations are not included as explicit degrees of freedom in the strict infrared EST; if they are not resolved, their effects are encoded in the Wilson coefficients. If they become kinematically accessible, they must instead be treated as additional worldsheet states or as part of the microscopic dynamics matched onto the EST.

The next chapter introduces the Monte Carlo methods used for these measurements.

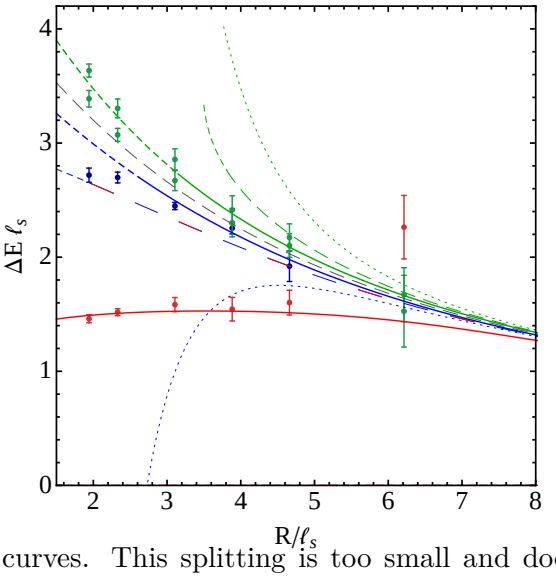


Figure 1.1. Plot taken from [36]. Finite-volume signature of the worldsheet axion. The figure shows the energy as a function of the closed-flux-tube length for the lowest states with one left-moving and one right-moving phonon in four-dimensional SU(3) Yang-Mills theory. In a phonons-only description, these states form the two-phonon band. They decompose into scalar (blue), pseudoscalar (red), and spin-two (green) representations of the transverse $O(2)$ symmetry. The GGRT/Nambu-Goto prediction, shown as the grey dashed curve, is that they are all degenerate. Universal relativistic-string corrections, dominated here by the Polchinski-Strominger interaction, split the different spin channels and the corresponding predictions are shown by the thin dashed curves. This splitting is too small and does not explain the pseudoscalar data. In particular, the red pseudoscalar level is not behaving as the ordinary pseudoscalar member of the two-phonon band. Introducing a massive pseudoscalar worldsheet field produces a resonant contribution to antisymmetric Goldstone scattering and smaller correlated shifts in the scalar and spin-two channels. The solid curves show the resulting axion-inclusive prediction.

References

[1] G. Veneziano. "Construction of a Crossing-Simmetric, Regge-behaved Amplitude for Linearly Rising Trajectories." In: *Il Nuovo Cimento A (1965-1970)* 57.1 (Sept. 1, 1968), pp. 190–197. ISSN: 1826-9869. DOI: 10.1007/BF02824451.

[2] Tetsuo Gotō. "Relativistic Quantum Mechanics of One-Dimensional Mechanical Continuum and Subsidiary Condition of Dual Resonance Model." In: *Progress of Theoretical Physics* 46.5 (Nov. 1, 1971), pp. 1560–1569. ISSN: 0033-068X. DOI: 10.1143/PTP.46.1560.

[3] Tamiaki Yoneya. "Connection of Dual Models to Electrodynamics and Gravidynamics." In: *Progress of Theoretical Physics* 51.6 (June 1, 1974), pp. 1907–1920. ISSN: 0033-068X. DOI: 10.1143/PTP.51.1907.

[4] J. Scherk and John H. Schwarz. "Dual Models for Non-Hadrons." In: *Nuclear Physics B* 81.1 (Oct. 25, 1974), pp. 118–144. ISSN: 0550-3213. DOI: 10.1016/0550-3213(74)90010-8.

[5] A. M. Polyakov. "Quantum Geometry of Bosonic Strings." In: *Physics Letters B* 103.3 (July 23, 1981), pp. 207–210. ISSN: 0370-2693. DOI: 10.1016/0370-2693(81)90743-7.

[6] Michael B. Green and John H. Schwarz. "Anomaly Cancellations in Supersymmetric D = 10 Gauge Theory and Superstring Theory." In: *Physics Letters B* 149.1 (Dec. 13, 1984), pp. 117–122. ISSN: 0370-2693. DOI: 10.1016/0370-2693(84)91565-X.

[7] H. B. Nielsen and P. Olesen. "Vortex-Line Models for Dual Strings." In: *Nuclear Physics B* 61 (Sept. 24, 1973), pp. 45–61. ISSN: 0550-3213. DOI: 10.1016/0550-3213(73)90350-7.

[8] Kenneth G. Wilson. "Confinement of Quarks." In: *Physical Review D* 10.8 (Oct. 15, 1974), pp. 2445–2459. DOI: 10.1103/PhysRevD.10.2445.

[9] Y. Nambu. "Strings, Monopoles, and Gauge Fields." In: *Physical Review D* 10.12 (Dec. 15, 1974), pp. 4262–4268. DOI: 10.1103/PhysRevD.10.4262.

[10] S. Mandelstam. "Vortices and Quark Confinement in Non-Abelian Gauge Theories." In: *Physics Letters B* 53.5 (Jan. 6, 1975), pp. 476–478. ISSN: 0370-2693. DOI: 10.1016/0370-2693(75)90221-X.

[11] G. 't Hooft. "On the Phase Transition towards Permanent Quark Confinement." In: *Nuclear Physics B* 138.1 (June 5, 1978), pp. 1–25. ISSN: 0550-3213. DOI: 10.1016/0550-3213(78)90153-0.

[12] M. Lüscher, K. Symanzik, and P. Weisz. "Anomalies of the Free Loop Wave Equation in the WKB Approximation." In: *Nuclear Physics B* 173.3 (Oct. 27, 1980), pp. 365–396. ISSN: 0550-3213. DOI: 10.1016/0550-3213(80)90009-7.

[13] M. Lüscher. "Symmetry-Breaking Aspects of the Roughening Transition in Gauge Theories." In: *Nuclear Physics B* 180.2 (Mar. 30, 1981), pp. 317–329. ISSN: 0550-3213. DOI: 10.1016/0550-3213(81)90423-5.

[14] Joseph Polchinski and Andrew Strominger. "Effective String Theory." In: *Physical Review Letters* 67.13 (Sept. 23, 1991), pp. 1681–1684. DOI: 10.1103/PhysRevLett.67.1681.

[15] Ofer Aharony and Zohar Komargodski. "The Effective Theory of Long Strings." In: *Journal of High Energy Physics* 2013.5 (May 23, 2013), p. 118. ISSN: 1029-8479. DOI: 10.1007/JHEP05(2013)118.

[16] Ofer Aharony and Matthew Dodelson. "Effective String Theory and Nonlinear Lorentz Invariance." In: *Journal of High Energy Physics* 2012.2 (Feb. 6, 2012), p. 8. ISSN: 1029-8479. DOI: 10.1007/JHEP02(2012)008.

[17] Ian Low and Aneesh V. Manohar. "Spontaneously Broken Spacetime Symmetries and Goldstone's Theorem." In: *Physical Review Letters* 88.10 (Feb. 25, 2002), p. 101602. DOI: 10.1103/PhysRevLett.88.101602.

[18] Simeon Hellerman, Shunsuke Maeda, Jonathan Maltz, and Ian Swanson. "Effective String Theory Simplified." In: *Journal of High Energy Physics* 2014.9 (Sept. 30, 2014), p. 183. ISSN: 1029-8479. DOI: 10.1007/JHEP09(2014)183.

[19] Ofer Aharony, Matan Field, and Nizan Klinghoffer. "The Effective String Spectrum in the Orthogonal Gauge." In: *Journal of High Energy Physics* 2012.4 (Apr. 11, 2012), p. 48. ISSN: 1029-8479. DOI: 10.1007/JHEP04(2012)048.

[20] Ofer Aharony and Eyal Karzbrun. "On the Effective Action of Confining Strings." In: *Journal of High Energy Physics* 2009.06 (June 2009), p. 012. ISSN: 1126-6708. DOI: 10.1088/1126-6708/2009/06/012.

[21] Martin Lüscher and Peter Weisz. "String Excitation Energies in SU(N) Gauge Theories beyond the Free-String Approximation." In: *Journal of High Energy Physics* 2004.07 (July 2004), p. 014. ISSN: 1126-6708. DOI: 10.1088/1126-6708/2004/07/014.

[22] Ofer Aharony and Matan Field. "On the Effective Theory of Long Open Strings." In: *Journal of High Energy Physics* 2011.1 (Jan. 2011), p. 65. ISSN: 1029-8479. DOI: 10.1007/JHEP01(2011)065. arXiv: 1008.2636 [hep-th].

[23] M. Billó, M. Caselle, F. Gliozzi, M. Meineri, and R. Pellegrini. "The Lorentz-invariant Boundary Action of the Confining String and Its Universal Contribution to the Inter-Quark Potential." In: *Journal of High Energy Physics* 2012.5 (May 28, 2012), p. 130. ISSN: 1029-8479. DOI: 10.1007/JHEP05(2012)130.

[24] Joan Elias Miró, Andrea L. Guerrieri, Aditya Hebbar, João Penedones, and Pedro Vieira. "Flux Tube S-Matrix Bootstrap." In: *Physical Review Letters* 123.22 (Nov. 27, 2019), p. 221602. DOI: 10.1103/PhysRevLett.123.221602.

[25] Sergei Dubovsky, Raphael Flauger, and Victor Gorbenko. "Solving the Simplest Theory of Quantum Gravity." In: *Journal of High Energy Physics* 2012.9 (Sept. 27, 2012), p. 133. ISSN: 1029-8479. DOI: 10.1007/JHEP09(2012)133.

[26] S. Dubovsky, R. Flauger, and V. Gorbenko. "Flux Tube Spectra from Approximate Integrability at Low Energies." In: *Journal of Experimental and Theoretical Physics* 120.3 (Mar. 1, 2015), pp. 399–422. ISSN: 1090-6509. DOI: 10.1134/S1063776115030188.

[27] Sergei Dubovsky, Victor Gorbenko, and Mehrdad Mirbabayi. "Asymptotic Fragility, near AdS2 Holography and $T\overline{T}$." In: *Journal of High Energy Physics* 2017.9 (Sept. 27, 2017), p. 136. ISSN: 1029-8479. DOI: 10.1007/JHEP09(2017)136.

[28] Andrea Cavaglià, Stefano Negro, István M. Szécsényi, and Roberto Tateo. "T$\overline{\text{T}}$-Deformed 2D Quantum Field Theories." In: *Journal of High Energy Physics* 2016.10 (Oct. 20, 2016), p. 112. ISSN: 1029-8479. DOI: 10.1007/JHEP10(2016)112.

[29] Michele Caselle, Davide Fioravanti, Ferdinando Gliozzi, and Roberto Tateo. "Quantisation of the Effective String with TBA." In: *Journal of High Energy Physics* 2013.7 (July 10, 2013), p. 71. ISSN: 1029-8479. DOI: 10.1007/JHEP07(2013)071.

[30] F. A. Smirnov and A. B. Zamolodchikov. "On Space of Integrable Quantum Field Theories." In: *Nuclear Physics B* 915 (Feb. 1, 2017), pp. 363–383. ISSN: 0550-3213. DOI: 10.1016/j.nuclphysb.2016.12.014.

[31] Patrick Cooper, Sergei Dubovsky, Victor Gorbenko, Ali Mohsen, and Stefano Storace. "Looking for Integrability on the Worldsheet of Confining Strings." In: *Journal of High Energy Physics* 2015.4 (Apr. 23, 2015), p. 127. ISSN: 1029-8479. DOI: 10.1007/JHEP04(2015)127.

[32] Andreas Athenodorou, Barak Bringoltz, and Michael Teper. "Closed Flux Tubes and Their String Description in D =3+1 SU(N) Gauge Theories." In: *Journal of High Energy Physics* 2011.2 (Feb. 8, 2011), p. 30. ISSN: 1029-8479. DOI: 10.1007/JHEP02(2011)030.

[33] Patrick Dorey. *Exact S-matrices*. Oct. 5, 1998. DOI: 10.48550/arXiv.hep-th/9810026. arXiv: hep-th/9810026.

[34] Patrick Dorey and Roberto Tateo. "Excited States by Analytic Continuation of TBA Equations." In: *Nuclear Physics B* 482.3 (Dec. 30, 1996), pp. 639–659. ISSN: 0550-3213. DOI: 10.1016/S0550-3213(96)00516-0.

[35] Martin Lüscher and Peter Weisz. "Quark Confinement and the Bosonic String." In: *Journal of High Energy Physics* 2002.07 (Aug. 2002), p. 049. ISSN: 1126-6708. DOI: 10.1088/1126-6708/2002/07/049.

[36] Sergei Dubovsky, Raphael Flauger, and Victor Gorbenko. "Evidence from Lattice Data for a New Particle on the Worldsheet of the QCD Flux Tube." In: *Physical Review Letters* 111.6 (Aug. 9, 2013), p. 062006. DOI: 10.1103/PhysRevLett.111.062006.

[37] Andreas Athenodorou, Sergei Dubovsky, Conghuan Luo, and Michael Teper. *Confining Strings and the Worldsheet Axion from the Lattice*. Dec. 16, 2025. DOI: 10.48550/arXiv.2411.03435. arXiv: 2411.03435 [hep-th].

Chapter 2

Lattice realization of the domain wall and Monte Carlo

Lattice Monte Carlo (MC) simulations provide the numerical input used throughout this thesis. This chapter defines the microscopic lattice ensembles, update algorithms, and estimators used to measure the observables analyzed later. The emphasis is not on MC methods in general, but on the specific problem of measuring partition-function ratios, free-energy differences, and correlation functions in periodic and $\mathbb{Z}_2$-twisted sectors.

The microscopic system used to realize the worldsheet in the numerical work is the 3D Ising model with boundary conditions chosen to be either periodic or $\mathbb{Z}_2$-twisted/antiperiodic. In the ordered phase but near the critical point, the twisted sector contains a domain wall wrapping the longitudinal directions. At criticality, the same construction defines a twisted-sector free energy difference, controlled by the thermodynamic Casimir difference. The lattice definition is common to both regimes, while the physical interpretation of the measured free-energy differences and correlation functions depends on the context.

The main numerical novelty of this work is the direct measurement of ratios of partition functions with different boundary conditions, with high precision. These ratios are essential because dividing by the periodic-sector partition function cancels the common bulk contributions, isolating the free-energy cost associated with the emergent domain wall. Independent Monte Carlo simulations can determine expectation values within a fixed ensemble, but they do not determine the normalization of the partition function. Therefore, the simulations below are performed in an extended configuration space, where the boundary coupling is promoted to a dynamical variable. The periodic and antiperiodic sectors then appear as subspaces of the extended configuration space. A flat-histogram method is used to interpolate between the two subspaces efficiently, allowing the desired free-energy difference to be reconstructed directly. We also considered a nonequilibrium Jarzynski-based reconstruction. Although the production measurements use the flat-histogram construction, the Jarzynski implementation, the methodological developments made, and the limitations of this approach are discussed below.

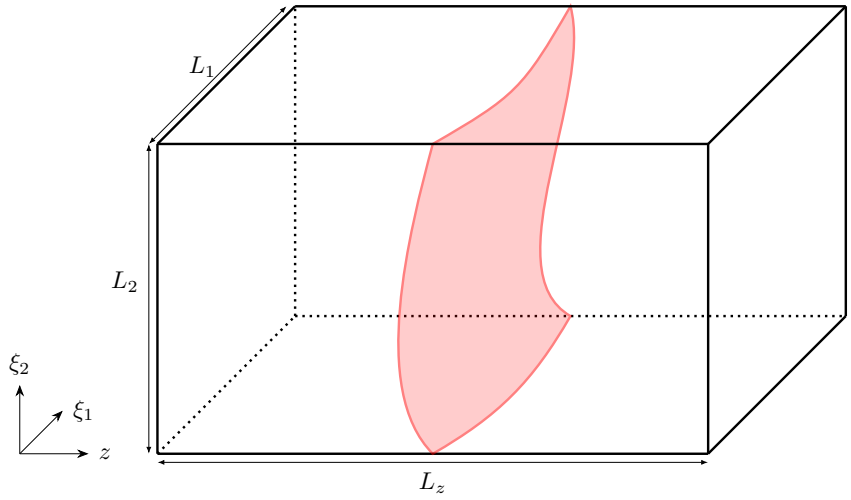


Figure 2.1 Schematic representation of the domain wall/worldsheet on a 3D torus. For 3D Ising, the boundary conditions are periodic along ξ_1 and ξ_2 and antiperiodic along z.

We begin by defining the lattice ensembles and observables that provide the microscopic starting point for the Monte Carlo measurements. For a general review of MC methods see [1, 2].

2.1. Lattice ensembles and observables

This subsection fixes the lattice model and notation used throughout the numerical part of the thesis. The microscopic system is a 3D Ising model on a lattice, with boundary conditions chosen to define different sectors of the theory.

2.1.1. Lattice model and boundary conditions

We consider Ising spins[1] $s_x = \pm 1$ on a 3D lattice with linear sizes L_1, L_2, L_z and periodic identifications. The partition function is

$$Z = \sum_{\{s_x=\pm 1\}} \exp\left(\beta \sum_{\langle xy\rangle} J_{xy} s_x s_y\right), \tag{2.1}$$

where the sum runs over nearest-neighbour bonds.

The couplings J_{xy} encode both the local interaction and the chosen boundary sector. In the periodic sector all bonds have $J_{xy} = 1$, while the antiperiodic sector is obtained by flipping the sign of the bonds crossing one plane orthogonal to the z-direction. We denote the corresponding partition functions by Z_{P} and Z_{AP}, respectively. The antiperiodic conditions force a domain wall wrapping the transverse directions [3–6]. At criticality, the same construction defines a $\mathbb{Z}_2$-twisted sector. L_1 and L_2 are the sizes of the directions parallel to the plane on which the coupling is modified, while L_z denotes the direction across that plane as shown in fig. 2.1. The corresponding transverse area is $A = L_1 L_2$. For square transverse geometries we drop the subscript, $L_1 = L_2 = L$.

The position of the flipped plane is conventional. By flipping contiguous planes of spins on one side of the frustrated plane, one moves the set of frustrated bonds to a different plane without changing the

[1] We use s instead of the standard σ to avoid confusion with the string tension.

partition function. The invariant information is therefore not the location of this plane, but the global boundary sector: the antiperiodic ensemble contains a non-trivial $\mathbb{Z}_2$ twist around the compact z-direction. It is important to distinguish this auxiliary twist defect from the physical domain wall. The twist defect is the chosen plane of flipped bonds, and its position is a convention. The domain wall, by contrast, appears in the ordered phase as an emergent dynamical object whose position fluctuates.

The relevant observable is the free-energy difference between sectors (i.e. the ratio of the two sector partition functions),

$$\Delta F = F_{\mathrm{AP}} - F_{\mathrm{P}} = -\log \frac{Z_{\mathrm{AP}}}{Z_{\mathrm{P}}}. \tag{2.2}$$

The periodic/antiperiodic sector construction is precisely the setting in which the extended-configuration-space and flat-histogram methods [7–9] become useful. This sector difference should not be identified blindly with the physical domain-wall free energy, as discussed in Chapter 3.

2.2. Markov chain Monte Carlo

The lattice observables introduced above are expectation values over an exponentially large configuration space. Direct summation is therefore impossible except for the smallest of lattices. Monte Carlo methods replace the exact sum by a sum over the relevant configurations, sampled directly from the desired equilibrium probability distribution. The resulting Markov chain is a numerical device. It is not a physical time evolution, as many different dynamics have the same stationary distribution and therefore produce the same equilibrium observables.

The freedom to choose different MC dynamics is both a blessing and a curse. On the one hand, the constraints are very weak: the chain must have the desired equilibrium distribution and must be able to explore the relevant configuration space. In practice, this is enforced through detailed balance, or the weaker condition of global balance, together with ergodicity. On the other hand, there is no general classification of all possible Monte Carlo dynamics, let alone a way of predicting the efficiency of an arbitrary algorithm. Efficiency is then empirical and must be tested through autocorrelation times, tunneling rates, and stability under changes of simulation parameters.

The choice of algorithm is therefore an integral part of the numerical analysis itself. Fortunately, for the 3D Ising model, we stand on the shoulders of giants, as highly efficient Monte Carlo algorithms are already available. The simulations in this thesis are therefore built from the established Monte Carlo toolkit and adapted to the specific ensembles and observables considered below.

Let us now recap Markov chain Monte Carlo, the conditions that guarantee its correctness, and how to test its efficiency. Next, we will discuss the MC dynamics used in this thesis.

2.2.1. Importance sampling

For an observable $\mathcal{O}$, the expectation value in an ensemble with action $S(C)$ is

$$\langle \mathcal{O} \rangle = \frac{1}{Z} \sum_C \mathcal{O}(C) e^{-S(C)}, \qquad Z = \sum_C e^{-S(C)}, \tag{2.3}$$

where C denotes a spin configuration. Importance sampling rewrites this average as an expectation value with respect to the Boltzmann probability

$$\pi(C) = \frac{e^{-S(C)}}{Z}. \tag{2.4}$$

The Monte Carlo estimator is then

$$\overline{\mathcal{O}} = \frac{1}{N} \sum_{n=1}^{N} \mathcal{O}(C_n), \tag{2.5}$$

where the configurations C_n are generated by the Markov chain whose stationary distribution is $\pi(C)$.

Importance sampling reduces variance by sampling the configurations that dominate the Boltzmann weight more often. Its efficiency, however, still depends on the Markov-chain dynamics. In this thesis, efficiency is improved mainly through cluster updates, which reduce critical slowing down, and through flat-histogram extended ensembles, which improve tunneling between boundary sectors.

2.2.2. Markov chains

A Markov chain is a stochastic process on the configuration space. Starting from a configuration C_n, the next configuration C_{n+1} is drawn with transition probability $P(C_n \to C_{n+1})$. Its defining property is that this probability depends only on the current configuration (i.e. the process is memoryless)

$$P(C_{n+1} = C' \mid C_n, C_{n-1}, \ldots, C_0) = P(C_{n+1} = C' \mid C_n) = P\left(C_n \to C_{n+1}\right). \tag{2.6}$$

Markov-chain Monte Carlo is especially useful for interacting lattice systems because the Boltzmann distribution is usually known only up to its normalization. Transition rules can be built from ratios of Boltzmann weights, where the unknown partition function cancels. This avoids the need for direct independent sampling from the full target distribution, which is generally impossible. Rejection sampling and independent importance sampling face the same obstruction. Without a proposal distribution close to the target measure, their efficiency deteriorates rapidly with volume.

The main advantage of Markov-chain Monte Carlo is that the dynamics of the sampler is itself a design choice. One is not restricted to drawing configurations in a fixed way and the transition rule can be engineered to move efficiently through the relevant regions of configuration space, overcome barriers, or decorrelate slow modes, while leaving the target distribution unchanged. The price is that successive configurations are correlated, with the strength of these correlations depending on the chosen dynamics.

For a Markov chain to sample the desired ensemble correctly, the target distribution must be stationary under the transition rule, and the chain must be ergodic so that it can explore all relevant regions of configuration space and converge independently of its initial state. Detailed balance is a simple sufficient condition for stationarity, though not a necessary one.

2.2.3. Detailed balance and ergodicity

A sufficient condition for a chosen distribution, $\pi(C)$, to be a stationary distribution of the Markov chain is detailed balance,

$$\pi(C)P(C \to C') = \pi(C')P(C' \to C) \qquad \forall C, C'. \tag{2.7}$$

Its interpretation is that the probability flux between any pair of configurations is balanced. Detailed balance is stronger than necessary as stationarity only requires global balance,

$$\sum_C \pi(C)P(C \to C') = \pi(C') \qquad \forall C', \tag{2.8}$$

but is in general extremely difficult to impose, as it requires summing over the full configuration space. In practice, detailed balance is usually imposed because it is a simple and robust way to construct correct update rules [1].

Stationarity alone is not sufficient. The chain must also be ergodic, meaning that every configuration with nonzero Boltzmann weight must be reachable from any other such configuration, after a finite number of steps.

2.2.4. Thermalization, autocorrelation, and statistical errors

Since Markov-chain sampling does not produce independent configurations, successive configurations retain short-time memory of one another. Hence, the initial part of any chain retains memory of the initial condition. The process of erasing the information about the initial condition is known as thermalization. The samples generated while thermalizing are discarded, with the cut chosen by monitoring the stability of representative observables, that is, until the variation of the observable is merely the statistical noise.

After thermalization, the chain samples the target ensemble, but the measurements are still correlated. Hence, it is essential that statistical errors be estimated through autocorrelation analysis or independent simulations, with the latter preferred. For a sequence of measurements $\mathcal{O}_n$, the normalized autocorrelation function is

$$\rho_{\mathcal{O}}(t) \equiv \frac{\langle (\mathcal{O}_n - \langle \mathcal{O} \rangle)(\mathcal{O}_{n+t} - \langle \mathcal{O} \rangle) \rangle}{\langle (\mathcal{O}_n - \langle \mathcal{O} \rangle)^2 \rangle}. \tag{2.9}$$

With this, we can define the corresponding integrated autocorrelation time

$$\tau_{\mathrm{int},\mathcal{O}} \equiv \frac{1}{2} + \sum_{t=1}^{\infty} \rho_{\mathcal{O}}(t), \tag{2.10}$$

where the $1/2$ is chosen such that the asymptotic variance of the sample mean goes as

$$\sigma^2_{\overline{\mathcal{O}}} \simeq \frac{2\tau_{\mathrm{int},\mathcal{O}}\, \sigma^2_{\mathcal{O}}}{N}. \tag{2.11}$$

Here N is the number of samples in a chain and $\sigma^2_{\mathcal{O}}$ is the variance of the observable $\mathcal{O}$ [1, 2].

Equivalently, autocorrelations reduce the effective number of independent samples by

$$N_{\text{eff}} \simeq \frac{N}{2\tau_{\text{int},\mathcal{O}}}, \tag{2.12}$$

meaning that adding every sample to the average or adding a sample every $2\tau_{\text{int},\mathcal{O}}$ Monte Carlo steps will produce results of equivalent quality, but error bars will be underestimated in the former.

In the uncorrelated limit, $\rho_{\mathcal{O}}(t > 0) = 0$, so that $\tau_{\text{int},\mathcal{O}} = \frac{1}{2}$, the usual central-limit result is recovered

$$\sigma^2_{\overline{\mathcal{O}}} = \frac{\sigma^2_{\mathcal{O}}}{N}. \tag{2.13}$$

Thus, the integrated autocorrelation time directly controls the computational and consequently monetary cost of the simulations. This is particularly important for expensive observables, such as correlation functions, where the cost of measurement can exceed the cost of sampling. In that regime, measuring too frequently only produces highly correlated data at high computational cost. Reducing $\tau_{\text{int},\mathcal{O}}$ is therefore essential. This motivates going beyond the generic Metropolis update and using the more efficient Wolff cluster algorithm, described below.

2.3. Monte Carlo updates

2.3.1. The Metropolis update

The simplest local update is the Metropolis update [10]. One proposes a change $C \to C'$, from a proposal distribution g (e.g. a single-spin flip or a change in an auxiliary variable), which is accepted with probability

$$p_{\text{acc}}(C \to C') = \min\left(1, e^{-[S(C')-S(C)]}\frac{g\,(C' \to C)}{g\,(C \to C')}\right). \tag{2.14}$$

The main advantage of the Metropolis update is its generality. It can be applied to any action for which the change in the action can be computed. This makes it useful not only for spin updates, but also for auxiliary variables such as the boundary coupling introduced below.

Its drawback is that, while easy to construct, samples are usually correlated. This is especially severe near criticality and in systems with free-energy barriers or collective modes. For this reason, the simulations in this thesis use Metropolis updates only when better updates are not available.

2.3.2. The Wolff cluster update

Wolff [11] is the main algorithm used in this thesis, in the measurements of both the free-energy differences and correlation functions. It updates collective degrees of freedom, known as clusters, and is much more efficient than local spin-flip updates, especially near criticality, in the sense described below.

Let us start by reviewing the periodic case. In the standard ferromagnetic Ising model, a Wolff update starts from a randomly chosen seed spin. Neighboring spins with the same orientation, meaning that a bond is satisfied, are added to the cluster with probability

$$p_{\text{add}} = 1 - e^{-2\beta J}. \tag{2.15}$$

After the cluster has been built, all spins in the cluster are flipped.

The same construction can be used in the presence of signed nearest-neighbour couplings J_{xy}. In the AP case, a bond is satisfied when

$$J_{xy}s_x s_y > 0. \tag{2.16}$$

Equivalently, the activation probability is

$$p_{xy} = \begin{cases} 1 - e^{-2\beta|J_{xy}|}, & J_{xy}s_x s_y > 0, \\ 0, & J_{xy}s_x s_y < 0. \end{cases} \tag{2.17}$$

Thus, across an antiperiodic plane, where $J_{xy} < 0$, the cluster connects anti-aligned rather than aligned spins. This gives a general implementation of Wolff updates when we promote the boundary coupling to a dynamical variable.

2.3.3. Algorithmic efficiency

Critical slowing down refers to the growth of Monte Carlo autocorrelation times near a second-order phase transition, where the diverging physical correlation length produces increasingly slow collective modes. Its severity depends strongly on the update algorithm. When Monte Carlo time is measured in sweeps, with one sweep corresponding to $V = L^d$ attempted local updates[2], it has been observed that the integrated autocorrelation time scales as

$$\tau_{\mathrm{int},\mathcal{O}} \sim L^{z_\mathcal{O}}. \tag{2.18}$$

The dynamical exponent $z_\mathcal{O}$ is observable dependent, and it measures the nontrivial growth of autocorrelations beyond the trivial volume cost of a sweep.

Unlike static critical exponents, the dynamical exponent is not a property of the static universality class alone. It depends on the Monte Carlo update and on the observable. For the single spin-flip updates in the 3D Ising universality class, one finds exponents $z_M = 2.04(3)$ and $z_E = 2.03(10)$[12] for the magnetization and energy, while a modern improved-model estimate gives $z_\chi = 2.0245(15)$ for the magnetic susceptibility [13]. For the Wolff update the effective exponent is much smaller. After converting cluster flips to sweep-equivalent Monte Carlo time, a representative estimate in the 3D Ising model is $z_E = 0.44(10)$ [14].

2.4. Free-energy differences

Markov-chain Monte Carlo determines expectation values from relative statistical weights only. The overall normalization Z cancels from the transition probabilities and is therefore invisible to the simulation, even though it is precisely what is needed to determine the free energy $F = -\log Z$. This matters here because the EST predictions involve free energies with a definite normalization, or equivalently partition-function ratios between specified ensembles. The domain wall free energy, minus the log of the ratio between periodic and antiperiodic boundary conditions, must therefore be measured directly, rather than reconstructed from independently normalized simulations [15, 16].

[2] For cluster updates, Monte Carlo time is measured in units normalized by the average cluster size, so that one sweep corresponds approximately to one attempted update per spin.

We therefore embed the periodic and antiperiodic sectors into a larger configuration space by promoting the coupling on a chosen plane to a dynamical variable. There are many possible choices for this extension (e.g. flipping the neighbour coupling on a pair at a time). We choose a uniform interpolation of the plane coupling, J, assigned to the bonds perpendicular to a fixed plane Σ.

For fixed J, define

$$e^{-F(J)} \equiv Z(J) \equiv \sum_{\{s\}} \exp\left[\beta \sum_{\langle xy \rangle} s_x s_y + \beta\,(J-1) \sum_{x \in \Sigma} s_x s_{x+\hat{n}_\Sigma}\right], \tag{2.19}$$

where the first sum is over all neighbours and the second sum over the links perpendicular to a plane. We take $J \in [-1, 1]$, whose endpoints correspond to the periodic and antiperiodic sectors,

$$F(1) = F_{\mathrm{P}}, \qquad F(-1) = F_{\mathrm{AP}}, \tag{2.20}$$

respectively. The desired sector free-energy difference is therefore

$$\Delta F = F_{\mathrm{AP}} - F_{\mathrm{P}}. \tag{2.21}$$

A flat-histogram method is then used to sample this auxiliary parameter efficiently. Once the bias has converged, the free-energy difference can be read off directly. This construction is well suited to the present problem for three reasons. First, it measures the sector ratio directly, avoiding an undetermined additive normalization in the free energy. Second, it uses a continuous interpolation between sectors, improving the tunneling between them. Third, it can be combined with the same Wolff updates used for the ordinary periodic ensemble.

The limitation is that the auxiliary coupling must itself be sampled, typically with a Metropolis update, introducing a slow degree of freedom into the Markov chain. In addition, a flat histogram in the auxiliary variable does not guarantee fast decorrelation of all relevant modes. Hidden autocorrelations may persist, so convergence to a statistically reliable flat histogram can be arbitrarily slow.

The method belongs to a broader class of approaches for measuring free-energy differences. The basic difficulty is old, and diverse strategies have been developed: free-energy perturbation [17], acceptance-ratio estimators [15], nonequilibrium work relations [18, 19], histogram reweighting [16], multicanonical sampling [7, 8], entropic sampling [20], Wang-Landau [9], transition-matrix methods [21, 22], and optimized broad-histogram or optimized multicanonical ensembles [23, 24].

The method used here is closest in spirit to the direct Monte Carlo measurement of the Ising interface tension in [3]. There, the simulation configuration space already included both periodic and antiperiodic boundary conditions, and the interface free energy was extracted by counting how many times each sector was visited. It also identified the main limitation of this approach. When the surface free energy becomes large, the antiperiodic sector becomes rare, and the statistics of boundary-sector changes deteriorates. It was suggested that this problem might be addressed by combining the method with multicanonical ideas, while noting that the naive introduction of a chemical potential for the antiperiodic sector does not solve the tunneling problem.

The flat-histogram construction used in this thesis can be viewed as a realization of this insight. Instead of biasing only the endpoint sectors, we introduce a dynamical plane coupling and reconstruct the free-energy profile as a function of this coupling. A purely binned bias, however, would still be inefficient at the volumes needed here, because the free-energy profile is extensive and varies smoothly

across the J-interval. The additional ingredient that makes our method practical is the two-level representation of the bias: a smooth continuous component captures the dominant variation, while a Wang-Landau histogram corrects the residual structure, without which we likely would not have achieved the required precision.

2.4.1. Bias reconstruction: the flat histogram sampling

Promoting the boundary coupling to a dynamical variable places the method in the class of expanded-ensemble or flat-histogram algorithms depending on the perspective, adapted here to an interpolating boundary coupling rather than to a temperature or bulk coupling [25, 26].

The extended partition function, including the flat-histogram bias, is

$$Z_{\text{ext}} = \int_{J_{\min}}^{J_{\max}} dJ\, e^{-F(J)-\omega(J)}, \tag{2.22}$$

where $\omega(J)$ is a bias potential we wish to determine. The corresponding marginal distribution of J is

$$P(J) \propto e^{-F(J)-\omega(J)}. \tag{2.23}$$

Here the auxiliary variable J is sampled with a flat measure, so there is no additional density-of-states factor, $\Omega(J) = 1$.

A flat distribution in J is obtained when the bias is the negative of the free energy

$$\omega(J) = -F(J) + \text{const.} \tag{2.24}$$

The free energy can then be reconstructed up to the additive constant corresponding to the unknown normalization discussed above.

In practice, the sampled interval is chosen slightly larger than the physical range $[-1, 1]$. This avoids extracting endpoint values from boundary bins and allows $F(\pm 1)$ to be obtained by interpolation of the reconstructed profile around those points.

The bias potential is determined with a Wang-Landau type flat-histogram procedure [9]. The interval in J is divided into bins. The simulation alternates between Wolff updates of the spins at fixed J and Metropolis proposals that change J. During the bias-construction stage, the histogram $H(J)$ is accumulated and the bias is updated whenever a bin is visited, including when the new bin is the same as the old bin. With the sign convention above, visiting bin i increases the bias in that bin by f

$$\omega(J_i) \to \omega(J_i) + f, \tag{2.25}$$

so that frequently visited bins become less favorable.

In the infinite sample size limit, the measured histogram is constant and

$$F(J) = -\omega(J) + \text{const.} \tag{2.26}$$

At finite refinement level, however, there are residual deviations from flatness. Once the bias is frozen, a production run is performed in the fixed extended ensemble, in which we measure the resulting histogram

$$P_{\text{meas}}(J) \propto e^{-F(J)-\omega_{\text{final}}(J)}, \tag{2.27}$$

which is used to correct the bias. The final estimator for the free-energy profile is therefore

$$F(J) = -\omega_{\text{final}}(J) - \log P_{\text{meas}}(J) + \text{const.} \tag{2.28}$$

Therefore, instead of continuing the Wang-Landau refinement until the update size f becomes negligible, we stop once the bias is accurate enough for the simulation to visit the full J-interval with reasonable probability. This is more efficient because, during the adaptive Wang-Landau stage, the transition kernel changes and hence the process does not have a fixed stationary distribution. Measurements accumulated during this stage are therefore unphysical. Once the bias is frozen, detailed balance is restored with respect to the fixed modified ensemble, and the residual deviations from a flat histogram provide a systematically improvable correction to the finite f bias.

The Wang-Landau refinement proceeds in stages. After each stage, the J-histogram is tested for flatness. In the implementation used here, a stage is finished when

$$\frac{H_{\max} - H_{\min}}{\bar{H}} < 0.05 \tag{2.29}$$

and the relative neighbouring-bin variance is below 1%. The update size is then halved,

$$f \to \frac{f}{2}, \tag{2.30}$$

and the next refinement stage begins. We use 16 refinement stages in the simulations reported below, starting from $f = 0.1$.

The flatness of the marginal J-histogram is a necessary convergence check, but it is not sufficient. The auxiliary coupling J is a collective variable coupled to an entire plane of spins, and its autocorrelation can be much longer than that of local observables. This is particularly visible beyond the antiperiodic endpoint, $J \lesssim -1$, where the simulation can tunnel slowly between different interface configurations even when the marginal histogram in J appears flat. In practice this limits how far the sampled interval can be extended beyond the relevant endpoint. This does not affect the endpoint reconstruction directly, because the region outside $[-1, 1]$ is used only to improve the interpolation near $J = \pm 1$.

As the boundary coupling is varied, the domain-wall sector changes qualitatively. This change is visible, for example, in fig. 3.5 of [27]. For $1 \geq J \geq 0$, the defect plane is not frustrated, and the system is in the periodic sector. No domain wall exists. For $-1 < J < 0$, the plane contains frustrated bonds, but their magnitude is smaller than that of the bulk bonds. In this regime the domain wall is attracted to the defect plane, because placing the wall on top of the defect reduces the energetic cost of the spin flip. The probability distribution for the wall position is then localized near the defect and decays rapidly away from it. At $J = -1$, the antiperiodic point is reached. The position of the flipped plane is then arbitrary, as the physical domain wall is no longer pinned to it. Its center-of-mass position is therefore uniformly distributed along the transverse direction. For $J < -1$, the defect bonds are stronger than the bulk bonds, and the wall is instead repelled from the defect plane.

The large autocorrelation times observed for $J < -1$ are likely caused by this reorganization of the domain-wall distribution. Close to $J = -1$, the defect-induced potential is weak, with a strength roughly set by $A\beta|J+1|$. When the simulation crosses into $J < -1$, the defect changes from attracting the wall to repelling it. The relevant slow process is then not a local change in bond energy, but a global rearrangement of the wall-position distribution.

2.4.2. Continuous plus residual flat-histogram bias

The flat-histogram implementation used in this thesis differs from the standard Wang-Landau construction in the parametrization of the bias potential. The standard method stores the bias as a purely binned function, derived from the histogram in J. This is sufficient in principle, but it becomes inefficient for the present problem.

The free-energy profile is extensive in the domain-wall area and varies smoothly over the J-interval. A purely binned bias must therefore approximate a large smooth contribution by a piecewise-constant function. At large volume, the bias can vary appreciably across a single bin unless the J-binning is made very fine.

Refining the binning is not cost-free, however. At fixed Monte Carlo steps/CPU time, increasing the number of bins reduces the average number of samples per bin. For an approximately flat histogram, the mean bin occupation scales as N_{MC}/N_J. Thus, the error of a bin, and hence of the corresponding free-energy estimate, increases with the number of bins

$$\delta F_i \sim \sqrt{\frac{2\tau_i N_J}{N_{\mathrm{MC}}}}, \tag{2.31}$$

where τ_i is the integrated autocorrelation time of the bin-occupation estimator.

To mitigate this problem, we use a two-level representation of the bias. Instead of storing $\omega(J)$ only as a binned function, we split it into a discrete and a continuous part

$$\omega(J) = \Delta\omega_i + bJ + cJ^2, \tag{2.32}$$

where i is the bin containing J. The coefficients b and c describe the dominant smooth component, while $\Delta\omega_i$ stores only the residual binned correction. The continuous part is extracted from preliminary Wang-Landau runs, and it changes very little after the first iterations. This procedure is a problem-specific acceleration of flat-histogram sampling, related in spirit to optimized broad-histogram and optimized multicanonical schemes [23, 24]. This method is systematically improvable by considering higher-order polynomials or orthogonal function bases.

The expectation is that this construction can be generalized case by case. For a given interpolation, a simple family of continuous bias functions should often capture the dominant smooth free-energy profile, leaving only a small residual correction for the flat-histogram procedure.

In the 3D Ising model, the continuous piece is well approximated by a quadratic function of J, with a binned contribution that can be several orders of magnitude smaller than the leading smooth component. Fig. 2.2 shows a difference of two orders of magnitude between the two contributions for moderate lattice sizes $\sim 64^2 \times 32$ in the ordered phase, $\beta = 0.23$.

The decomposition is used in the Metropolis update of the plane coupling as follows. For a proposal $J \to J'$, we identify the corresponding bins $i \to i'$, and the bias difference is then

$$\omega(J') - \omega(J) = \Delta\omega_{i'} - \Delta\omega_i + b(J' - J) + c\left(J'^2 - J^2\right). \tag{2.33}$$

The residual binning is refined when necessary. If, after a refinement stage, the residual bias changes too sharply between neighbouring bins, the number of bins is increased and $\Delta\omega_i$ is interpolated onto the

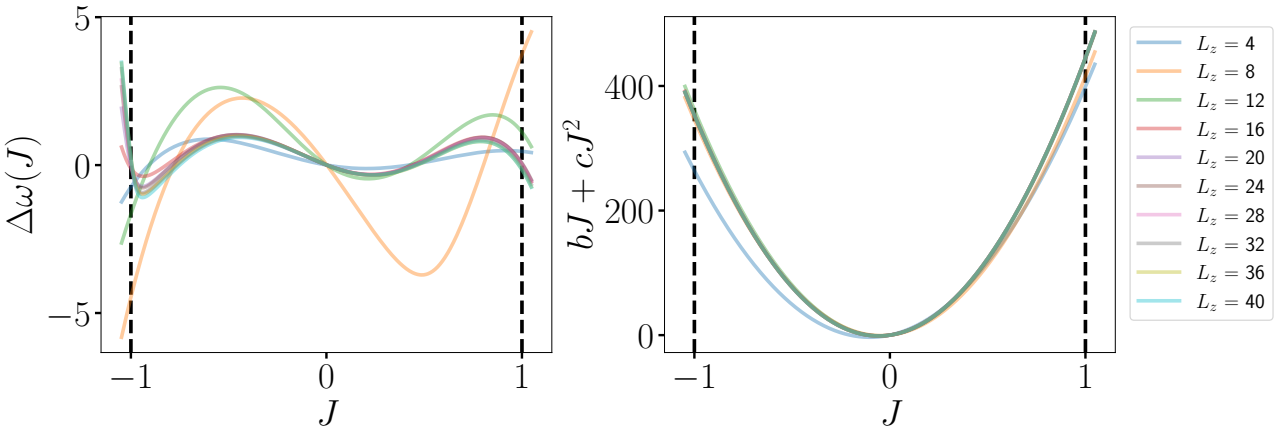


Figure 2.2 Discrete **(left)** and continuous **(right)** contributions to $\omega(J)$ for square domain walls of size 64^2 and $\beta = 0.23$, with 512 bins.

finer grid. This preserves the smooth continuous approximation while keeping the residual histogram sufficiently resolved.

2.4.3. Jarzynski method

Inspired by the application of non-equilibrium methods to lattice theory in [19], the first strategy we tried for measuring the free-energy difference between boundary sectors was based on the Jarzynski equality [18]. The basic idea is appealing. Instead of sampling an equilibrium ensemble that interpolates between the two endpoints, one drives the system out of equilibrium along a prescribed path in an extended configuration space, and extracts the equilibrium free-energy difference from the distribution of the work performed along this path. The method is closely related to the Crooks fluctuation theorem [28], and has become a standard tool in nonequilibrium free-energy estimation, especially in molecular simulations and single-molecule pulling experiments [29–32].

In the present problem the path is a sequence of values of the boundary coupling, $J_0, J_1, \ldots, J_N$, interpolating between the periodic and antiperiodic sectors. Starting from an equilibrium configuration at J_0, the coupling is changed step by step. After each change, a prescribed number of Monte Carlo updates is performed at the new value of J. For a trajectory Γ, the dimensionless work is

$$W[\Gamma] = \sum_{n=0}^{N-1} \left[S_{J_{n+1}}(s_n) - S_{J_n}(s_n) \right], \tag{2.34}$$

where s_n is the configuration before the change from J_n to J_{n+1}. The Jarzynski equality then gives

$$e^{-\Delta F} = \left\langle e^{-W} \right\rangle, \tag{2.35}$$

where the average is over independent realizations of the nonequilibrium path. This formulation gives considerable freedom. Since the intermediate configurations need not be equilibrium samples, one can tune the protocol, including the step size.

The comparison between forward and reverse transformations provides a useful diagnostic of the

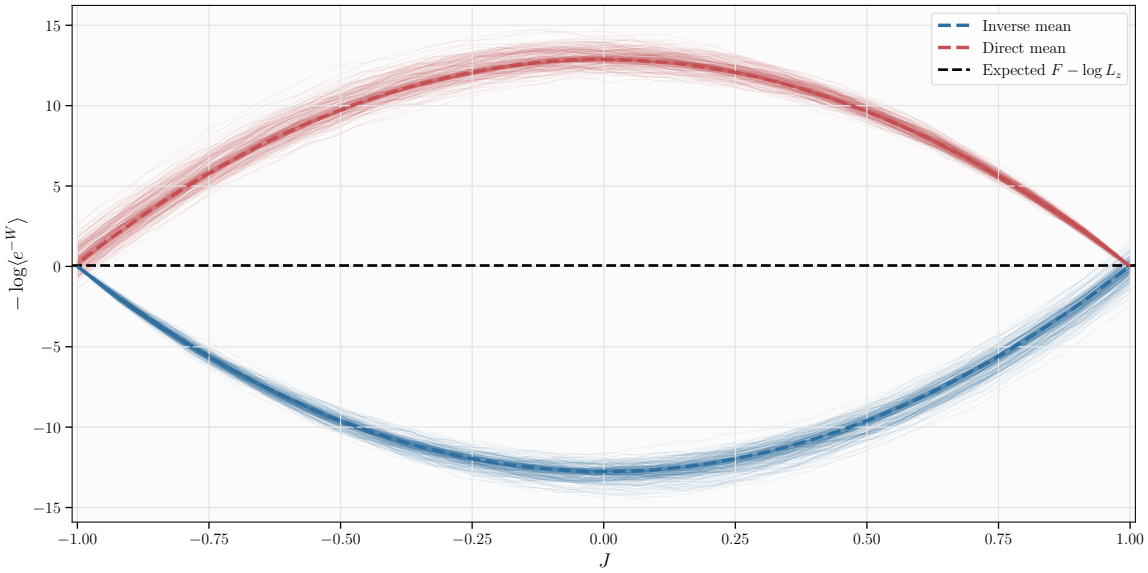


Figure 2.3 Nonequilibrium Jarzynski estimates for free energy interpolating between boundary sectors, for $V = 18^2 \times 96$ and $\beta = 0.223102$ with 1000 steps. The coupling J parametrizes the path between the periodic and antiperiodic ensembles. The plotted quantity is the cumulative estimator $-\log\langle e^{-W}\rangle$, shown for forward and reverse paths. Thin curves denote individual realizations and thick dashed curves their averages. The latter should match the sum of the data shown in fig. 2.2.

systematic bias associated with irreversible driving. By Jensen's inequality,

$$\Delta F \leq \langle W\rangle_{\text{fwd}}, \tag{2.36}$$

while applying the same argument to the reverse process gives

$$-\langle W\rangle_{\text{back}} \leq \Delta F. \tag{2.37}$$

Thus, the forward and reverse mean works bracket the desired free-energy difference. For sufficiently large samples, the width of this bracket gives a useful measure of the systematic bias induced by irreversible driving. Fig. 2.3 shows several realizations of a nonequilibrium protocol, both in the forward and backward directions.

The main difficulty is that the exact estimator is controlled by the exponential average $\langle e^{-W}\rangle$. For fast protocols, or for large systems, this average can be dominated by rare trajectories with unusually small dissipated work, which can be exponentially hard to sample [33, 34]. In practice, this produced large finite-sample biases unless the protocol was made sufficiently slow, at which point the computational cost became comparable to, or worse than, equilibrium methods.

An improvement is to use cluster updates during the nonequilibrium protocol, like Wolff. The motivation was to reduce autocorrelations and improve equilibration along the path. This does not change the Jarzynski identity, provided the update at each value of J preserves the corresponding equilibrium distribution. It only changes the nonequilibrium dynamics used to generate the work ensemble. Figure 2.4 compares the distributions of the Jarzynski weights e^{-W} obtained with SSF and Wolff updates. The two algorithms give comparable central values, but their tails differ substantially. In both the forward and reverse transformations, the Wolff distribution has a much more strongly suppressed tail, whereas SSF produces broader tails extending to larger values of e^{-W}.

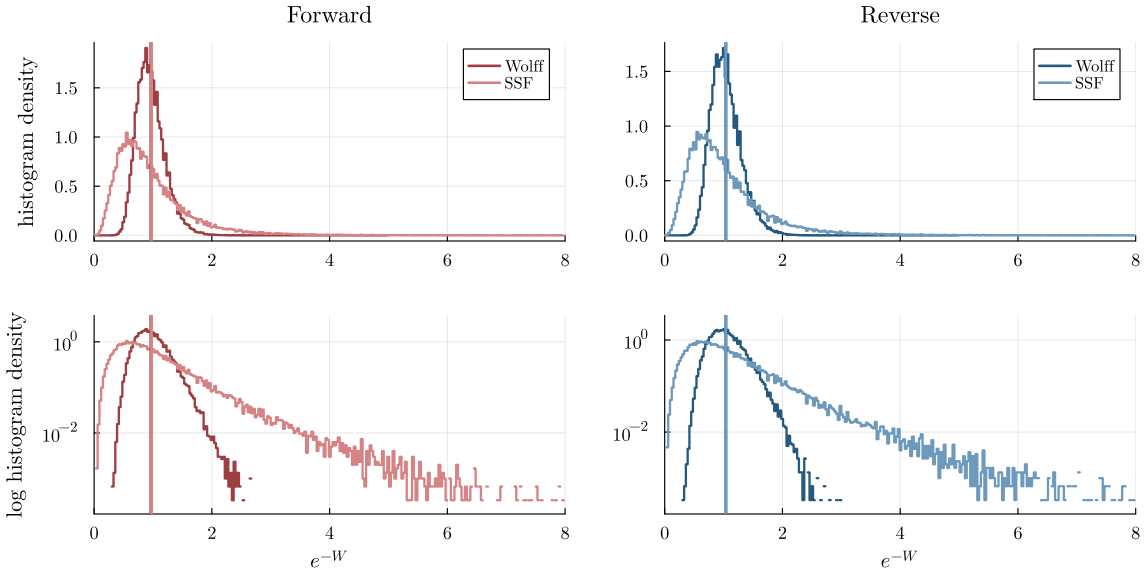


Figure 2.4 Histograms of the Jarzynski weights e^{-W} for the forward and reverse transformations, comparing Wolff and SSF updates for $V = 3^2 \times 9$, $\beta = 0.223102$, 200 transition steps and 10^5 Monte Carlo samples. The upper panels show the probability densities on a linear scale, while the lower panels show the same distributions on a logarithmic scale in order to expose the tails. Vertical lines indicate the sample means. For this data set the SSF distributions have substantially broader tails than the corresponding Wolff distributions, implying larger fluctuations of the exponential-work estimator and stronger sensitivity to rare events.

A improvement is to decompose the transformation into several smaller nonequilibrium estimates. Instead of estimating the full ratio $Z(J_N)/Z(J_0)$ in one step, one introduces intermediate couplings and writes

$$\frac{Z(J_N)}{Z(J_0)} = \prod_{k=0}^{N-1} \frac{Z(J_{k+1})}{Z(J_k)} = \prod_{k=0}^{N-1} e^{-\Delta F_k}. \tag{2.38}$$

Each factor can then be estimated with a Jarzynski protocol restricted to the smaller interval $J_k \to J_{k+1}$,

$$e^{-\Delta F_k} = \left\langle e^{-W_k} \right\rangle_k, \qquad \Delta F = \sum_{k=0}^{N-1} \Delta F_k. \tag{2.39}$$

The motivation is that neighbouring ensembles overlap much better than the two endpoint sectors. This suppresses the heavy tails of the work distributions, making the exponential averages substantially less sensitive to rare trajectories. The staged estimator therefore replaces one poorly behaved non-equilibrium average by a product of many better-conditioned ones.

The limitation is that this improvement is obtained only if each factor is estimated with the correct initial distribution. For the ratio $Z(J_{k+1})/Z(J_k)$, the corresponding subprotocol must start from configurations thermalized at J_k. If one instead records increments along a single non-equilibrium path and averages them level by level, the configurations at intermediate J_k are not distributed according to the equilibrium ensemble at that coupling. The resulting product is then no longer a sequence of exact Jarzynski estimates. Making the staged construction exact requires either thermalizing the starting ensemble for every small interval or running sufficiently slow protocols that the system remains close to equilibrium along the path. Both options consume much of the efficiency gained by splitting the transformation into many levels.

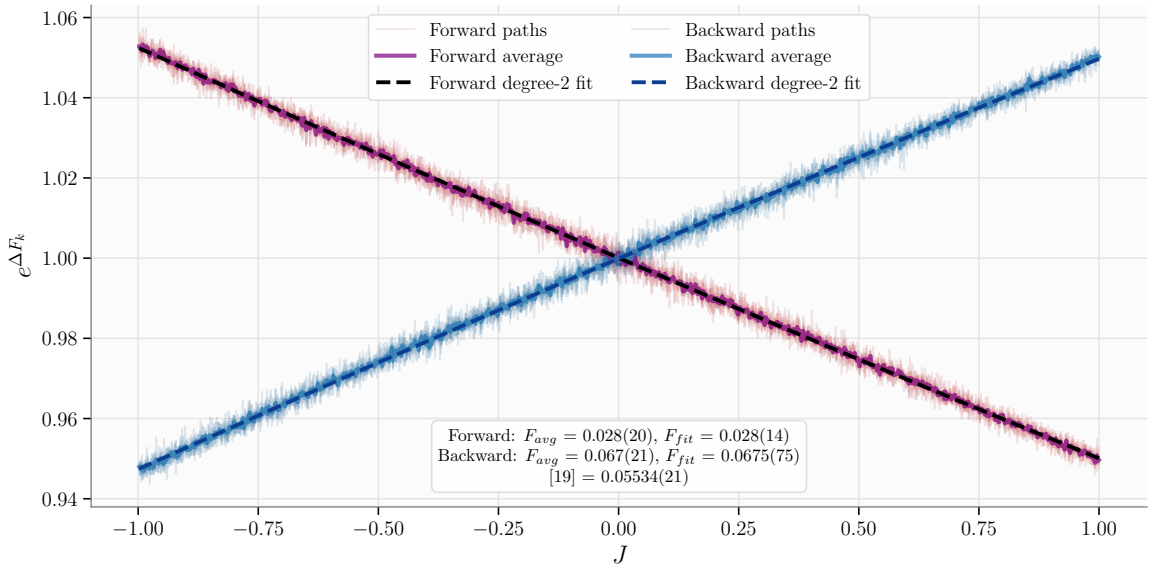


Figure 2.5 Multilevel Jarzynski estimate of the free-energy difference between boundary sectors. The coupling J parametrizes the interpolation path, and the vertical axis shows the incremental factors $e^{\Delta F_k}$ entering the staged product estimator. Thin transparent lines are individual paths, solid lines are averages over paths, and dashed lines are quadratic fits used to smooth the factors before multiplying them. The forward and backward mean works, shown in the inset, provide upper and lower bounds on the free-energy difference, respectively, as follows from Jarzynski's equality via Jensen's inequality. Although the staged decomposition improves the overlap of neighbouring steps, it does so at the cost of introducing statistical noise.

A putative improvement would be to replace the single transformation by a sequence of intermediate couplings, following the same general motivation as multistep work methods such as [35]. One particularly simple implementation would be an explicitly staged equilibrium calculation. For each interval $J_k \to J_{k+1}$, one could run an independent simulation thermalized at J_k, measure the work or action difference associated with changing the coupling to J_{k+1}, and use this to estimate the local ratio $Z(J_{k+1})/Z(J_k)$. In the instantaneous switching limit this is the standard free-energy perturbation estimator [36]. If both neighbouring ensembles are sampled, the appropriate bidirectional equilibrium estimator is Bennett's acceptance ratio [15]. Later work connected this estimator to nonequilibrium work relations and maximum-likelihood estimators based on forward and reverse transformations [31]. The natural extension to many intermediate ensembles is MBAR [37]. This strategy has the important advantage that all intervals can be simulated independently, and the overlap problem is reduced because neighbouring ensembles are much closer than the two endpoint sectors.

For the final measurements, however, we retained the flat-histogram method. Although staging improves the overlap between neighbouring ensembles, each interval requires a separate equilibration and error analysis and, more importantly, splitting the path in coupling space does not remove slow collective modes such as the motion or reorganization of the domain wall.

2.5. Observables: Continuum/Lattice correspondence

We briefly review the definition of the microscopic operators, the optimal strategy for measuring correlation functions, and the relation between lattice observables and their continuum counterparts.

2.5.1. Microscopic operators

In the antiperiodic sector, we need to be careful about the definition of the lattice operators. For the spin field, a naive correlator $\langle s(0)s(x)\rangle_{\mathrm{AP}}$ depends on the chosen position of the defect plane, which is not physical. To remove this dependence, we insert a compensating $\mathbb{Z}_2$ line between the two spins,

$$G_s^{\mathrm{def}}(x) \equiv \Big\langle s(0)\eta(x,0)s(x)\Big\rangle_{\mathrm{AP}}, \qquad \eta(x,0) = \pm 1, \tag{2.40}$$

where $\eta(x,y) = -1$ iff the shortest lattice path from x to y crosses the defect plane. Equivalently, η parallel transports the spin operator through the $\mathbb{Z}_2$-twisted background. At long distances the correlator reduces to $\langle s\rangle^2$, the disconnected contribution, times a sign determined by the relative position of the wall with respect to the operator insertions.

By contrast, the energy operator is $\mathbb{Z}_2$-even, so no compensating η-line is required between two energy insertions. However, its lattice definition must still respect the fact that the defect plane is a gauge choice for the twist. For a bond operator, the defect-invariant local energy is built from the signed coupling

$$\epsilon_{xy} \propto J_{xy} s_x s_y. \tag{2.41}$$

As before, using $s_x s_y$ without the factor J_{xy} would introduce an artificial dependence on the chosen position of the flipped plane. With the signed definition, the energy operator measures only the local cost associated with the physical wall rather than the defect.

2.5.2. Connection between lattice and continuum

The matching to the continuum effective description is performed at the level of long-distance observables, not at the level of microscopic lattice operators.

These fields are not canonically normalized continuum fields. Near the scaling limit, a lattice operator admits a schematic expansion in continuum operators with the same quantum numbers,

$$O_x^{\mathrm{lat}} \longrightarrow \sum_a \mathcal{N}_a \mathcal{O}_a(x), \tag{2.42}$$

where the coefficients $\mathcal{N}_a$ depend on the microscopic definition of O_x^{lat}. They are non-universal matching coefficients. At long distances, the lightest continuum operator controls the decay or scaling form of the correlators, while the coefficients $\mathcal{N}_a$ map the MC normalization to CFT normalization

$$\langle \mathcal{O}(r)\mathcal{O}(0)\rangle^{\mathrm{conn}} \underset{rm_{\mathcal{O}}\to\infty}{\simeq} \frac{\mathcal{N}_{\mathcal{O}}^2}{4\pi}\frac{e^{-m_{\mathcal{O}}r}}{r}. \tag{2.43}$$

The critical scaling of $\mathcal{N}_{\mathcal{O}}$ can be determined as follows. Consider the lattice correlator at distance $r = 1/m$,

$$\langle \mathcal{O}(r = 1/m)\mathcal{O}(0)\rangle_{\mathrm{P}}^{\mathrm{conn}} \sim m\mathcal{N}_{\mathcal{O}}^2 \tag{2.44}$$

Now let us compare this with the UV CFT prediction,

$$\langle \mathcal{O}(r)\mathcal{O}(0)\rangle^{\mathrm{conn}} \sim a^{2\Delta_{\mathcal{O}}}\langle \mathcal{O}_{\mathrm{CFT}}(r)\mathcal{O}_{\mathrm{CFT}}(0)\rangle = \frac{a^{2\Delta_{\mathcal{O}}}}{r^{2\Delta_{\mathcal{O}}}}, \tag{2.45}$$

where a denotes the lattice spacing. Comparing the two predictions at $r = 1/m$,

$$\mathcal{N}_{\mathcal{O}}^2 \sim a\,(am)^{2\Delta_{\mathcal{O}}-1} = at^{\nu(2\Delta_{\mathcal{O}}-1)}, \tag{2.46}$$

where we used $ma \sim t^{\nu}$ with $t = (T_c - T)/T_c$ and $\Delta_\epsilon = 3 - 1/\nu$.

2.5.3. Correlation functions

For a lattice operator $\mathcal{O}$, the expectation value is the sum over configurations

$$\langle \mathcal{O} \rangle = \frac{1}{Z} \sum_{\{s\}} \mathcal{O}[\{s\}] e^{-S[\{s\}]}, \tag{2.47}$$

and the corresponding connected two-point function is

$$G_{\mathcal{O}}(x, y) = \langle \mathcal{O}_x \mathcal{O}_y \rangle - \langle \mathcal{O}_x \rangle \langle \mathcal{O}_y \rangle. \tag{2.48}$$

On a finite translationally invariant lattice, the signal-to-noise ratio is increased by averaging over all translations

$$G_{\mathcal{O}}(r) = \frac{1}{V} \sum_{x} \left[\langle \mathcal{O}_{x+r} \mathcal{O}_x \rangle - \langle \mathcal{O} \rangle^2 \right], \tag{2.49}$$

where the lattice volume is $V = L_1 L_2 L_z$. When the boundary sector singles out the z-direction, correlators are often organized according to their separation along directions parallel or perpendicular to the modified plane.

The translational average is a discrete autocorrelation and can therefore be evaluated with a fast Fourier transform, reducing the computational complexity from V^2 to $V \log V$. Defining

$$\widetilde{\mathcal{O}}_k = \sum_x e^{-ik\cdot x} \mathcal{O}_x, \tag{2.50}$$

one obtains

$$C_{\mathcal{O}}(r) = \frac{1}{V} \mathcal{F}^{-1} \left[\widetilde{\mathcal{O}}_k \widetilde{\mathcal{O}}_k^* \right](r). \tag{2.51}$$

The Monte Carlo estimator is obtained by averaging $C_{\mathcal{O}}(r)$ over many MC samples and independent simulations.

When a connected correlator is needed, it is constructed from the full correlator by subtracting the corresponding one-point contribution,

$$G_{\mathcal{O}}(r) = \langle C_{\mathcal{O}}(r) \rangle - \langle \mathcal{O} \rangle^2, \tag{2.52}$$

where $\langle O \rangle$ is computed from the source MC samples. Equivalently, one may compute the autocorrelation of the fluctuation field $\delta\mathcal{O}_x = \mathcal{O}_x - \langle \mathcal{O} \rangle$. The subtraction must, however, use the ensemble one-point function. Subtracting the spatial average separately on each configuration removes the zero-momentum mode and defines a different finite-volume estimator.

Alternatively, for sufficiently large volumes, the disconnected contribution is estimated from the large distance plateau of the full two-point function,

$$\langle C_{\mathcal{O}}(r) \rangle \xrightarrow{|r|\to\infty} \langle \mathcal{O} \rangle^2, \tag{2.53}$$

provided the separation is large compared with the correlation length, such that finite-volume/image effects are controlled.

References

[1] A. Sokal. "Monte Carlo Methods in Statistical Mechanics: Foundations and New Algorithms." In: *Functional Integration: Basics and Applications*. Ed. by Cecile DeWitt-Morette, Pierre Cartier, and Antoine Folacci. Boston, MA: Springer US, 1997, pp. 131–192. ISBN: 978-1-4899-0319-8. DOI: 10.1007/978-1-4899-0319-8_6.

[2] M. E. J. Newman, G. T. Barkema, M. E. J. Newman, and G. T. Barkema. *Monte Carlo Methods in Statistical Physics*. Oxford, New York: Oxford University Press, Feb. 11, 1999. 490 pp. ISBN: 978-0-19-851797-9.

[3] Martin Hasenbusch. "Direct Monte Carlo Measurement of the Surface Tension in Ising Models." In: *Journal de Physique I* 3.3 (Mar. 1, 1993), pp. 753–765. ISSN: 1155-4304, 1286-4862. DOI: 10.1051/jp1:1993160.

[4] Michele Caselle, Martin Hasenbusch, and Marco Panero. "High Precision Monte Carlo Simulations of Interfaces in the Three-Dimensional Ising Model: A Comparison with the Nambu-Goto Effective String Model." In: *Journal of High Energy Physics* 2006.03 (Mar. 2006), p. 084. ISSN: 1126-6708. DOI: 10.1088/1126-6708/2006/03/084.

[5] Marco Billó, Michele Caselle, and Livia Ferro. "The Partition Function of Interfaces from the Nambu-Goto Effective String Theory." In: *Journal of High Energy Physics* 2006.02 (Feb. 2006), p. 070. ISSN: 1126-6708. DOI: 10.1088/1126-6708/2006/02/070.

[6] M. Hasenbusch and K. Pinn. "The Interface Tension of the Three-Dimensional Ising Model in the Scaling Region." In: *Physica A: Statistical Mechanics and its Applications* 245.3 (Nov. 1, 1997), pp. 366–378. ISSN: 0378-4371. DOI: 10.1016/S0378-4371(97)00314-2.

[7] Bernd A. Berg and Thomas Neuhaus. "Multicanonical Algorithms for First Order Phase Transitions." In: *Physics Letters B* 267.2 (Sept. 12, 1991), pp. 249–253. ISSN: 0370-2693. DOI: 10.1016/0370-2693(91)91256-U.

[8] Bernd A. Berg and Thomas Neuhaus. "Multicanonical Ensemble: A New Approach to Simulate First-Order Phase Transitions." In: *Physical Review Letters* 68.1 (Jan. 6, 1992), pp. 9–12. DOI: 10.1103/PhysRevLett.68.9.

[9] Fugao Wang and D. P. Landau. "Efficient, Multiple-Range Random Walk Algorithm to Calculate the Density of States." In: *Physical Review Letters* 86.10 (Mar. 5, 2001), pp. 2050–2053. DOI: 10.1103/PhysRevLett.86.2050.

[10] Nicholas Metropolis, Arianna W. Rosenbluth, Marshall N. Rosenbluth, Augusta H. Teller, and Edward Teller. "Equation of State Calculations by Fast Computing Machines." In: *The Journal of Chemical Physics* 21.6 (June 1, 1953), pp. 1087–1092. ISSN: 0021-9606. DOI: 10.1063/1.1699114.

[11] Ulli Wolff. "Collective Monte Carlo Updating for Spin Systems." In: *Physical Review Letters* 62.4 (Jan. 23, 1989), pp. 361–364. DOI: 10.1103/PhysRevLett.62.361.

[12] S. Wansleben and D. P. Landau. "Monte Carlo Investigation of Critical Dynamics in the Three-Dimensional Ising Model." In: *Physical Review B* 43.7 (Mar. 1, 1991), pp. 6006–6014. DOI: 10.1103/PhysRevB.43.6006.

[13] Martin Hasenbusch. "Dynamic Critical Exponent z of the Three-Dimensional Ising Universality Class: Monte Carlo Simulations of the Improved Blume-Capel Model." In: *Physical Review. E* 101.2–1 (Feb. 2020), p. 022126. ISSN: 2470-0053. DOI: 10.1103/PhysRevE.101.022126. PMID: 32168572.

[14] P. Tamayo, R. C. Brower, and W. Klein. "Single-Cluster Monte Carlo Dynamics for the Ising Model." In: *Journal of Statistical Physics* 58.5 (Mar. 1, 1990), pp. 1083–1094. ISSN: 1572-9613. DOI: 10.1007/BF01026564.

[15] Charles H Bennett. "Efficient Estimation of Free Energy Differences from Monte Carlo Data." In: *Journal of Computational Physics* 22.2 (Oct. 1, 1976), pp. 245–268. ISSN: 0021-9991. DOI: 10.1016/0021-9991(76)90078-4.

[16] Alan M. Ferrenberg and Robert H. Swendsen. "New Monte Carlo Technique for Studying Phase Transitions." In: *Physical Review Letters* 61.23 (Dec. 5, 1988), pp. 2635–2638. DOI: 10.1103/PhysRevLett.61.2635.

[17] B. Widom. "Some Topics in the Theory of Fluids." In: *The Journal of Chemical Physics* 39.11 (Dec. 1, 1963), pp. 2808–2812. ISSN: 0021-9606. DOI: 10.1063/1.1734110.

[18] C. Jarzynski. "Nonequilibrium Equality for Free Energy Differences." In: *Physical Review Letters* 78.14 (Apr. 7, 1997), pp. 2690–2693. DOI: 10.1103/PhysRevLett.78.2690.

[19] Michele Caselle, Gianluca Costagliola, Alessandro Nada, Marco Panero, and Arianna Toniato. "Jarzynski's Theorem for Lattice Gauge Theory." In: *Physical Review D* 94.3 (Aug. 12, 2016), p. 034503. DOI: 10.1103/PhysRevD.94.034503.

[20] Jooyoung Lee. "A New Monte Carlo Algorithm: Entropic Sampling." In: *Physical Review Letters* 71 (1993), pp. 211–214. DOI: 10.1103/PhysRevLett.71.211.

[21] Jian-Sheng Wang, Tien Kiat Tay, and Robert H. Swendsen. "Transition Matrix Monte Carlo Reweighting and Dynamics." In: *Physical Review Letters* 82.3 (Jan. 18, 1999), pp. 476–479. DOI: 10.1103/PhysRevLett.82.476.

[22] M. Fitzgerald, R. R. Picard, and R. N. Silver. "Monte Carlo Transition Dynamics and Variance Reduction." In: *Journal of Statistical Physics* 98.1 (Jan. 1, 2000), pp. 321–345. ISSN: 1572-9613. DOI: 10.1023/A:1018635108073.

[23] Simon Trebst, David A. Huse, and Matthias Troyer. "Optimizing the Ensemble for Equilibration in Broad-Histogram Monte Carlo Simulations." In: *Physical Review E* 70.4 (Oct. 4, 2004), p. 046701. DOI: 10.1103/PhysRevE.70.046701.

[24] J. Viana Lopes, Miguel D. Costa, J. M. B. Lopes dos Santos, and R. Toral. "Optimized Multicanonical Simulations: A Proposal Based on Classical Fluctuation Theory." In: *Physical Review E* 74.4 (Oct. 5, 2006), p. 046702. DOI: 10.1103/PhysRevE.74.046702.

[25] A. P. Lyubartsev, A. A. Martsinovski, S. V. Shevkunov, and P. N. Vorontsov-Velyaminov. "New Approach to Monte Carlo Calculation of the Free Energy: Method of Expanded Ensembles." In: *The Journal of Chemical Physics* 96.3 (Feb. 1, 1992), pp. 1776–1783. ISSN: 0021-9606. DOI: 10.1063/1.462133.

[26] E. Marinari and G. Parisi. "Simulated Tempering: A New Monte Carlo Scheme." In: *Europhysics Letters* 19.6 (July 1992), p. 451. ISSN: 0295-5075. DOI: 10.1209/0295-5075/19/6/002.

[27] David Capitão Lima. "High Precision Measurements of Interfaces' Free Energy." In: (Dec. 14, 2022). DOI: 10.34626/xr1d-4508.

[28] Gavin E. Crooks. "Entropy Production Fluctuation Theorem and the Nonequilibrium Work Relation for Free Energy Differences." In: *Physical Review E* 60.3 (Sept. 1, 1999), pp. 2721–2726. DOI: 10.1103/PhysRevE.60.2721.

[29] Gerhard Hummer and Attila Szabo. "Free Energy Reconstruction from Nonequilibrium Single-Molecule Pulling Experiments." In: *Proceedings of the National Academy of Sciences* 98.7 (Mar. 27, 2001), pp. 3658–3661. DOI: 10.1073/pnas.071034098.

[30] Christopher Jarzynski. "Equalities and Inequalities: Irreversibility and the Second Law of Thermodynamics at the Nanoscale." In: *Annual Review of Condensed Matter Physics* 2.1 (Mar. 1, 2011), pp. 329–351. ISSN: 1947-5454, 1947-5462. DOI: 10.1146/annurev-conmatphys-062910-140506.

[31] Michael R. Shirts, Eric Bair, Giles Hooker, and Vijay S. Pande. "Equilibrium Free Energies from Nonequilibrium Measurements Using Maximum-Likelihood Methods." In: *Physical Review Letters* 91.14 (Oct. 2, 2003), p. 140601. DOI: 10.1103/PhysRevLett.91.140601.

[32] Christoph Dellago and Gerhard Hummer. "Computing Equilibrium Free Energies Using Non-Equilibrium Molecular Dynamics." In: *Entropy* 16.1 (Jan. 2014), pp. 41–61. ISSN: 1099-4300. DOI: 10.3390/e16010041.

[33] Jeff Gore, Felix Ritort, and Carlos Bustamante. "Bias and Error in Estimates of Equilibrium Free-Energy Differences from Nonequilibrium Measurements." In: *Proceedings of the National Academy of Sciences* 100.22 (Oct. 28, 2003), pp. 12564–12569. DOI: 10.1073/pnas.1635159100.

[34] Christopher Jarzynski. "Rare Events and the Convergence of Exponentially Averaged Work Values." In: *Physical Review E* 73.4 (Apr. 5, 2006), p. 046105. DOI: 10.1103/PhysRevE.73.046105.

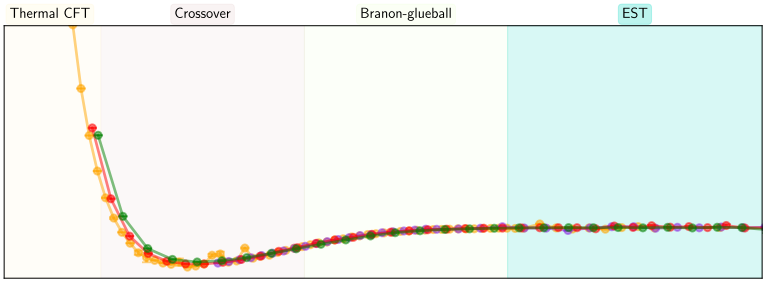
[35] Ignacia Echeverria and L. Mario Amzel. "Estimation of Free-Energy Differences from Computed Work Distributions: An Application of Jarzynski's Equality." In: *The Journal of Physical Chemistry B* 116.36 (Sept. 13, 2012), pp. 10986–10995. ISSN: 1520-6106. DOI: 10.1021/jp300527q.

[36] Robert W. Zwanzig. "High-Temperature Equation of State by a Perturbation Method. I. Nonpolar Gases." In: *The Journal of Chemical Physics* 22.8 (Aug. 1, 1954), pp. 1420–1426. ISSN: 0021-9606. DOI: 10.1063/1.1740409.

[37] Michael R. Shirts and John D. Chodera. "Statistically Optimal Analysis of Samples from Multiple Equilibrium States." In: *The Journal of Chemical Physics* 129.12 (Sept. 28, 2008), p. 124105. ISSN: 1089-7690. DOI: 10.1063/1.2978177. PMID: 19045004.

Chapter 3

Effective string theory on a torus: the 3D Ising domain wall



The results presented in this chapter are based on [1], where we studied a toroidal domain wall free energy in the 3D Ising model using effective string theory (EST). The aim is to extract intrinsic worldsheet data from a finite-volume observable free of boundary contamination. The chapter therefore has two roles: it determines the string tension from the large-area regime and then uses the torus free energy to measure the leading non-universal worldsheet coefficient, γ_3. Constructing the effective string tension plot was the starting point for much of the work developed in this thesis.

3.1. Summary

As reviewed in Chapter 1, in three target spacetime dimensions the long string action is unusually constrained. After removing topological terms and operators proportional to the leading equations of motion, the first independent non-universal bulk operator appears at eight-derivative order. With the Euclidean conventions used in this thesis, the action is

$$S = \int_\Sigma d^2\xi \sqrt{h} \left[\frac{1}{\ell_s^2} + 2\gamma_3 \ell_s^2 K^4 + O(\ell_s^4) \right], \tag{3.1}$$

where

$$h_{\alpha\beta} = \partial_\alpha X^\mu \partial_\beta X^\nu G_{\mu\nu}, \qquad K^4 = \left(K^\mu_{\alpha\beta} K^{\alpha\beta}_\mu \right)^2, \qquad K^\mu_{\alpha\beta} = \nabla_\alpha \partial_\beta X^\mu. \tag{3.2}$$

Here ξ^α, with $\alpha = 1, 2$, are worldsheet coordinates, $G_{\mu\nu}$ is the target-space metric, which we take to be the Euclidean metric, and ℓ_s is the string length, defined by $\ell_s^2 \equiv 1/\sigma$, where σ is the string tension. The Wilson coefficients are normalized so that the branon two-to-two phase shift takes the form

$$2\delta(s) = \frac{\ell_s^2 s}{4} + \gamma_3 \ell_s^6 s^3 + \mathcal{O}\left(s^5\right). \tag{3.3}$$

The main observable is the free energy of a rectangular toroidal domain wall with side lengths L_1 and L_2. We denote the dimensionless area, the EST counting parameter, by $\mathcal{A} \equiv L_1 L_2 \sigma$. We parameterize the generic torus by $\tau = \alpha + iu$.

The EST prediction for the torus free energy is then

$$F(\tau) = F_{\mathrm{U}}(\tau) - \gamma_3 \mathcal{A} \frac{\sum_{k,k',s,s'} e^{2\pi i \alpha (k-k')} p(k,s) p(k',s') \Delta\varepsilon_{k,k',s,s'} \varepsilon_{k,k'} K_0(\mathcal{A}\varepsilon_{k,k'})}{\sum_{k,k'} e^{2\pi i \alpha (k-k')} p(k) p(k') \varepsilon_{k,k'} K_1(\mathcal{A}\varepsilon_{k,k'})} + \mathcal{O}\left(\gamma_3^2 \mathcal{A}^{-5}\right) \tag{3.4}$$

$$= F_{\mathrm{U}}(\tau) - \frac{\gamma_3}{\mathcal{A}^3} \frac{2\pi^6}{225} (\tau - \bar{\tau})^4 E_4(\tau) E_4(-\bar{\tau}) + O(\gamma_3 \mathcal{A}^{-4}) + \mathcal{O}\left(\gamma_3^2 \mathcal{A}^{-5}\right). \tag{3.5}$$

where E_4 is the holomorphic Eisenstein series of weight four, and F_{U} is universal and follows from the GGRT theory. The first line is the TBA result, while the second is the perturbative path integral computation.

For numerical comparisons, it is important not to rely directly on the large-area expansion in eq. (3.5). That expression is the first term of an asymptotic expansion in inverse powers of $\mathcal{A}$, and the accessible Monte Carlo data lie in a regime where it is not sufficiently controlled. We therefore use a thermodynamic Bethe ansatz formulation based on the low-energy integrable worldsheet theory defined by the phase shift in eq. (3.3). In this approach the expansion is performed perturbatively in the Wilson coefficients, but the dependence on the area is kept non-perturbatively. Expanding this TBA result at large area reproduces the perturbative path-integral result in eq. (3.5).

The microscopic test is performed in the broken phase of the 3D Ising model. Antiperiodic boundary conditions in one direction select a sector containing a domain wall, schematically represented in fig. 3.1, while periodic boundary conditions give us the reference for the bulk physics. The domain-wall free energy is obtained from the corresponding free-energy difference. See Chapter 2 for a review of the MC methods and a detailed explanation of the microscopic model. We measure this quantity with

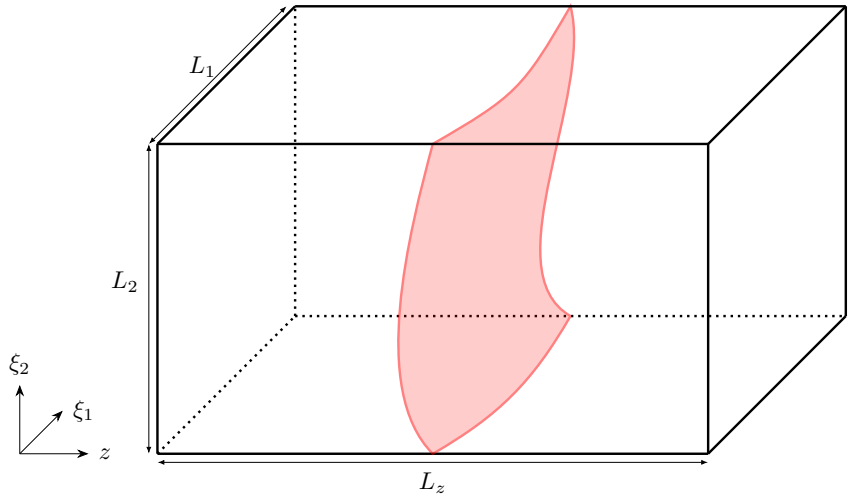


Figure 3.1 Schematic representation of the domain wall/worldsheet on a 3D torus. For 3D Ising, the boundary conditions are periodic along ξ_1 and ξ_2 and antiperiodic along z.

the two-level flat-histogram bias introduced in subsec. 2.4.2, using the extended configuration space that includes the plane coupling J discussed there.

Of special interest is the normalization of the partition function, which has been claimed to depend on the microscopic theory and hence to constitute an additional fit parameter. We find that our prediction for the normalization matches the MC data. Thus, the obtained lattice data are well described by two physical parameters: the string tension and γ_3. We find

$$\frac{\gamma_3}{|\gamma_3^{\min}|} = -0.82(15), \qquad \gamma_3 = -0.00106(18). \tag{3.6}$$

The fitted value is compatible with previous estimates and lies closer to the lower bound obtained from the worldsheet S-matrix bootstrap [2]. As discussed in sec. 1.3, γ_3 has slightly different meanings depending on whether we define it from the static gauge action or from the phase shift.

3.2. Effective string theory on a toroidal worldsheet

We review the EST in Chapter 1. Here we extend it from the long string to the large domain wall. The simulations discussed below are for square domain walls with no twist, but keeping τ explicit is useful because it makes the modular structure of the answer explicit.

3.2.1. Universal contribution and Gaussian normalization

We describe the universal partition function as a quantum-mechanical sum over string states. We foliate the toroidal worldsheet along the ξ^1 direction, so that L_2 is the length of the spatial closed string and L_1 is the Euclidean propagation time. Foliating in the orthogonal direction gives an equivalent expression with $\tau \to -1/\tau$.

We start by assuming the GGRT closed string spectrum in three target-space dimensions. There are several equivalent ways to justify this starting point. The same spectrum can be obtained from the $T\bar{T}$ deformation of the free boson that generates Nambu-Goto [3]; from light-cone quantization of the

Polyakov action [4]; or from the TBA spectrum associated with the integrable theory with the linear phase shift [5], as reviewed in subsec. 1.3.2. The left- and right-moving oscillator levels are denoted by k and k', and have energy

$$E_{k,k'} = \sigma L_2 \mathcal{E}_{k,k'} = \sigma L_2 \sqrt{1 + \frac{4\pi u}{\mathcal{A}} \left(k + k' - \frac{1}{12} \right) + \left(\frac{2\pi u (k - k')}{\mathcal{A}} \right)^2} \tag{3.7}$$

with degeneracies $p(k)$ and $p(k')$, where $p(k)$ is the number of integer partitions of k.

The string has two kinds of degrees of freedom: the center of mass degrees of freedom of a particle in a space with one less dimension, and the internal degrees of freedom. Thus, we can treat it as a particle with the rest mass depending on the internal excitations

$$m_{k,k'}^{\text{GGRT}} \equiv \sigma L_2 \mathcal{E}_{k,k'}. \tag{3.8}$$

The center of mass of the wall carries transverse momentum p_z. The full energy of a given state is

$$E_{k,k',p_z} = \sigma L_2 \sqrt{\mathcal{E}_{k,k'}^2 + \left(\frac{p_z}{\sigma L_2} \right)^2}. \tag{3.9}$$

In order to be careful about the normalization of the partition function, let us first keep L_z finite with periodic boundary conditions,

$$e^{ip_z z} = e^{ip_z (z + L_z)} \qquad \Rightarrow \qquad p_z = \frac{2\pi n}{L_z}, \qquad n \in \mathbb{Z}. \tag{3.10}$$

In the infinite transverse volume limit the sum becomes

$$\sum_n \longrightarrow \frac{L_z}{2\pi} \int dp_z. \tag{3.11}$$

Thus, the universal partition function is

$$Z_{\text{U}}(\tau = iu) = \text{Tr} e^{-L_1 H} = \frac{L_z}{2\pi} \int dp_z \sum_{k,k'=0}^{\infty} p(k) p(k') e^{-L_1 E_{k,k',p_z}}. \tag{3.12}$$

where the integral over p_z can be done exactly

$$Z_{\text{U}}(iu) = \left(\frac{\sigma \mathcal{A} L_z^2}{\pi^2 u} \right)^{1/2} \sum_{k,k'=0}^{\infty} p(k) p(k') \mathcal{E}_{k,k'} K_1 \left(\mathcal{A} \mathcal{E}_{k,k'} \right). \tag{3.13}$$

K_1 is a modified Bessel function.

3.2.1.1. Large area expansion

The large-area expansion of the partition function can be derived using the approach outlined in app. A of [6]. By expanding both $\mathcal{E}_{k,k'}$ and K_1 we obtain [1]

$$Z_{\mathrm{U}} = e^{-\mathcal{A}} \left(\frac{\sigma L_z^2}{2\pi u}\right)^{\frac{1}{2}} \sum_{k,k'} p(k)p(k') \left(1 + \sum_{n=1}^{\infty} \frac{f_n(k,k')}{\mathcal{A}^n}\right) e^{2\pi i\tau\left(k-\frac{1}{24}\right)} e^{-2\pi i\bar{\tau}\left(k'-\frac{1}{24}\right)}, \tag{3.14}$$

where $f_n(k,k')$ are polynomials in k and k'

$$f_1(k,k') = \frac{\pi^2 u^2}{72}(24k-1)\left(24k'-1\right) + \pi u\left(k'+k-\frac{1}{12}\right) + \frac{3}{8} \tag{3.15}$$

$$f_2(k,k') = \frac{\pi^4(1-24k)^2u^4\left(1-24k'\right)^2}{10368} - \frac{\pi^3u^3}{864}(24k-1)\left(12k'+12k-1\right)\left(24k'-1\right) \tag{3.16}$$

$$+ \frac{\pi^2u^2}{4}\left(\left(k-k'\right)^2 - 3\left(k'+k-\frac{1}{12}\right)^2\right) - \frac{3\pi u}{8}\left(k'+k-\frac{1}{12}\right) - \frac{15}{128}. \tag{3.17}$$

The $f_n(k,k')$ can be replaced by differential operators with respect to τ or $\bar{\tau}$ acting on the exponential

$$Z_{\mathrm{U}} = e^{-\mathcal{A}} \left(\frac{\sigma L_z^2}{2\pi u}\right)^{\frac{1}{2}} \left(1 + \sum_{n=1}^{\infty} \frac{f_n\left(\frac{\partial_\tau}{2\pi i}, -\frac{\partial_{\bar{\tau}}}{2\pi i}\right)}{\mathcal{A}^n}\right) Z_0, \tag{3.18}$$

where we define Z_0 as

$$Z_0 \equiv \sum_k p(k) e^{2\pi i\tau\left(k-\frac{1}{24}\right)} \sum_{k'} p(k') e^{-2\pi i\bar{\tau}\left(k'-\frac{1}{24}\right)} = \eta^{-1}(q)\eta^{-1}(\bar{q}). \tag{3.19}$$

η is the Dedekind eta function and $q \equiv e^{2\pi i\tau}$.

For a general torus modulus $\tau = \alpha + iu$, the trace is twisted by an insertion of the worldsheet momentum, such that each state receives a phase $e^{2\pi i\alpha(k-k')}$. In the large-area expansion this combines naturally with the Boltzmann factor into the standard torus weights

$$e^{2\pi i(\alpha+iu)(k-1/24)} e^{-2\pi i(\alpha-iu)(k'-1/24)}. \tag{3.20}$$

In order to find a closed expression for the partition function at each order in $1/\mathcal{A}$, we require the following properties of the Dedekind eta functions and holomorphic Eisenstein series [7]

$$q\partial_q\eta^{-1}(q) = -\eta^{-1}(q)\frac{E_2(q)}{24} \tag{3.21}$$

$$q\partial_q E_2(q) = \frac{E_2(q)^2 - E_4(q)}{12} \tag{3.22}$$

$$q\partial_q E_4(q) = \frac{E_2(q)E_4(q) - E_6(q)}{3} \tag{3.23}$$

$$q\partial_q E_6(q) = \frac{E_2(q)E_6(q) - E_4(q)^2}{2}. \tag{3.24}$$

[1] At this stage, although $\tau = iu = -\bar{\tau}$, we treat τ and $\bar{\tau}$ as independent variables.

Finally, we can compute the large-area expansion of the free energy

$$F_{\mathrm{U}} = -\log Z_{\mathrm{U}} = \mathcal{A} - \frac{1}{2}\log\left(\frac{\sigma i}{\pi(\tau-\bar{\tau})}L_z^2\right) + 2\log|\eta(\tau)| + \sum_{n=1}^{\infty}\frac{g_n(\tau,\bar{\tau})}{\mathcal{A}^n} \tag{3.25}$$

with

$$g_1 = -\frac{\pi^2(\tau-\bar{\tau})^2}{288}|E_2|^2 + \frac{i\pi(\tau-\bar{\tau})}{48}\mathrm{Re}E_2 + \frac{3}{8}$$

$$\begin{aligned} g_2 = &-\frac{\pi^4(\tau-\bar{\tau})^4}{41472}\left(\mathrm{Re}\left[E_4(\tau)E_2(-\bar{\tau})^2\right] - |E_4|^2\right) + \frac{i\pi^3(\tau-\bar{\tau})^3}{3456}\mathrm{Re}\left[E_4(\tau)E_2(-\bar{\tau})\right] \\ &+ \frac{\pi^2(\tau-\bar{\tau})^2}{1152}\left(3|E_2|^2 + \mathrm{Re}E_4\right) - \frac{i\pi(\tau-\bar{\tau})}{32}\mathrm{Re}E_2 - \frac{3}{16} \end{aligned}$$

where all the holomorphic Eisenstein series are evaluated at $\tau \equiv \alpha + iu$, unless explicitly stated otherwise. Recalling that $E_{2n}\left(-\frac{1}{\tau}\right) = \tau^{2n}E_{2n}(\tau)$, except for $n=1$ for which $E_2\left(-\frac{1}{\tau}\right) = \tau^2 E_2(\tau) + \frac{6\tau}{\pi i}$, the modular invariance of the above coefficients can be explicitly checked. The coefficients g_n are fixed order by order by the same expansion procedure and can be computed to any order needed.

For square worldsheets, $\tau = i$, the first terms of the universal free energy are

$$F_{\mathrm{U}}(i) = \mathcal{A} + 0.391594\ldots - \frac{1}{2}\log(\sigma L_z^2) - \frac{0.250000\ldots}{\mathcal{A}} + \frac{0.014107\ldots}{\mathcal{A}^2} + \frac{0.131398\ldots}{\mathcal{A}^3} + O(\mathcal{A}^{-4}). \tag{3.26}$$

The universal partition function has a Hagedorn singularity at small area. The critical area is

$$\mathcal{A}_H = \begin{cases} \dfrac{\pi u}{3}, & u \geq 1, \\ \dfrac{\pi}{3u}, & u \leq 1. \end{cases} \tag{3.27}$$

For rectangular tori this condition is equivalent to requiring the GGRT ground-state energy to remain real. It should therefore be interpreted as a putative lower bound on the area range in which the Nambu-Goto/GGRT effective description can be valid, not as a criterion for validity. The description necessarily fails below this bound, but it may fail at larger areas.

3.2.1.2. Partition function normalization

To make contact with the path-integral perspective, we now isolate the leading Gaussian factor. At large $\mathcal{A}$, expanding eq. (3.13) gives

$$Z_{\mathrm{U}}(\tau,\bar{\tau}) = \underbrace{e^{-\mathcal{A}}\left(\frac{i\sigma L_z^2}{\pi(\tau-\bar{\tau})}\right)^{1/2} Z_0(\tau,\bar{\tau})}_{\tilde{Z}_0}\left[1 + O(\mathcal{A}^{-1})\right]. \tag{3.28}$$

The prefactor in eq. (3.28) is fixed by the zero mode of the transverse wall position and should not be treated as an arbitrary normalization. This can be checked directly in the Gaussian path integral. We work in static gauge and rescale the coordinates so that the worldsheet has unit dimensionless area

and aspect ratio u,

$$\xi^1 \in [0, \sqrt{u}], \qquad \xi^2 \in [0, 1/\sqrt{u}], \tag{3.29}$$

and introduce the dimensionless field $\pi = \sqrt{\sigma} X$. We call π a branon. With these conventions the leading quadratic action is

$$S_0[\pi] = \frac{1}{2} \int d^2\xi \, \partial_\alpha \pi \partial_\alpha \pi, \tag{3.30}$$

and interactions are organized in inverse powers of $\mathcal{A} = \sigma L_1 L_2$.

The zero mode of π is excluded from the propagator, since it is the collective coordinate associated with translations of the wall in the transverse direction. Its contribution was already included in the normalization of the Gaussian partition function

$$\widetilde{Z}_0 = \left[\det{}' \left(-\frac{\Delta_{T^2}}{2\pi} \right) \right]^{-1/2} \sqrt{\sigma L_z^2}, \tag{3.31}$$

where the prime means that the zero mode is omitted. The determinant is evaluated using zeta-function regularization,

$$\log \det{}' D = -\frac{d}{ds} \zeta_D(s) \Big|_{s=0}, \qquad \zeta_D(s) = {\sum_n}' \lambda_n^{-s}. \tag{3.32}$$

Plugging the eigenvalues of the scalar Laplacian on the torus, one obtains

$$\zeta_{-\Delta_{T^2}/(2\pi)}(s) = \sum_{(m,n) \in \mathbb{Z}^2 \setminus (0,0)} \left(\frac{2\pi |m + n\tau|^2}{\tau_2} \right)^{-s}. \tag{3.33}$$

The analytic continuation of this real Eisenstein series, together with Kronecker's limit formula [7] gives

$$\widetilde{Z}_0 = \left(\frac{i\sigma L_z^2}{\pi(\tau - \bar{\tau})} \right)^{1/2} |\eta(\tau)|^{-2}. \tag{3.34}$$

The Gaussian calculation reproduces the leading factor in eq. (3.28). In particular, the transverse zero mode fixes the area-independent normalization of the torus partition function, so the free-energy fits below do not require an additional arbitrary constant.

3.2.2. Leading non-universal correction

We now compute the leading non-universal correction to the torus free energy that depends on the first non-universal Wilson coefficient γ_3. We do this in two ways. The first, based on the path integral, is perturbative in γ_3 and organized as a large-area expansion. Later, this result will be reproduced as the large area limit of the finite area TBA expression, which is only perturbative in the coefficients of the phase shift.

3.2.2.1. Path integral approach

At large area, the extrinsic curvature reduces to

$$K_{\alpha\beta} = n_\mu \partial_\alpha \partial_\beta X^\mu = \frac{\partial_\alpha \partial_\beta X}{\sqrt{1 + \partial_\gamma X \partial^\gamma X}} = \partial_\alpha \partial_\beta X + O(\partial X \partial^2 X). \tag{3.35}$$

Therefore the leading contribution of the K^4 operator to the free energy is obtained from the quartic insertion

$$V_{\gamma_3}[\pi] = -\frac{2\gamma_3}{\mathcal{A}^3} \int d^2\xi \left(\partial_\alpha \partial_\beta \pi \partial_\alpha \partial_\beta \pi\right)^2 . \tag{3.36}$$

To first order in γ_3, the free-energy correction is

$$F_{\gamma_3} = \langle V_{\gamma_3} \rangle_0 + O(\gamma_3^2), \tag{3.37}$$

where the expectation value is taken in the Gaussian theory defined by eq. (3.30).

For a rectangular torus, the zero mode subtracted propagator is

$$G(\xi, \xi') = \frac{1}{4\pi} \sum_{(m,n)\in\mathbb{Z}^2\setminus(0,0)} \frac{\exp\left[2\pi i m(\xi^1 - \xi'^1)/\sqrt{u} + 2\pi i n \sqrt{u}(\xi^2 - \xi'^2)\right]}{\pi |m + iun|^2/u}, \tag{3.38}$$

and it is useful to define

$$G_{\alpha\beta\gamma\delta}(0) \equiv \partial_\alpha \partial_\beta \partial'_\gamma \partial'_\delta G(\xi, \xi')\big|_{\xi=\xi'} . \tag{3.39}$$

Wick contractions of eq. (3.36) give

$$F_{\gamma_3} = -\frac{4\gamma_3}{\mathcal{A}^3} \left[G_{1111}(0)^2 + 6G_{1122}(0)^2 + G_{2222}(0)^2\right] . \tag{3.40}$$

The remaining task is to define the coincident-point sums

$$\begin{aligned} G_{1111}(0) &\propto \sum_{(m,n)\in\mathbb{Z}^2\setminus(0,0)} \frac{m^4}{m^2/u + n^2 u} \\ G_{1122}(0) &\propto \sum_{(m,n)\in\mathbb{Z}^2\setminus(0,0)} \frac{n^2 m^2}{m^2/u + n^2 u} \\ G_{2222}(0) &\propto \sum_{(m,n)\in\mathbb{Z}^2\setminus(0,0)} \frac{n^4}{m^2/u + n^2 u} \end{aligned}$$

in a regularization compatible with the torus symmetries.

Following [8] $G_{1111}(0)$ and $G_{2222}(0)$ can be reduced to analytic continuations of Eisenstein-type series. For the rectangular torus, define

$$F_s(iu) = \sum_{(m,n)\in\mathbb{Z}^2\setminus(0,0)} \frac{n^s}{m^2/u + n^2 u}. \tag{3.41}$$

Since F_s converges for $\Re(s) < 0$, we can sum over m to obtain

$$F_s\left(iu\right) = 2\pi\zeta\left(1-s\right) + 4\pi\sum_{n=1}^{\infty}\frac{n^{s-1}}{\left(e^{2\pi nu}-1\right)}. \tag{3.42}$$

The sum converges for any s. After analytic continuation one finds

$$F_s(iu) = -\pi\frac{E_s(iu)}{\zeta(s)}\zeta(1-s), \tag{3.43}$$

where E_s is the holomorphic Eisenstein series. The two values needed for the leading γ_3 correction are

$$F_2(iu) = \frac{1}{2\pi}E_2(iu), \qquad F_4(iu) = -\frac{3}{4\pi^3}E_4(iu). \tag{3.44}$$

The mixed derivative term is reduced to the same class of sums by rewriting it in terms of powers of m and n, together with the analytically continued real Eisenstein series

$$G^s_{1122}(0) = \frac{1}{2}\left[\underbrace{\sum_{(m,n)\in\mathbb{Z}^2\setminus(0,0)}\frac{\left(n^{s/2}/u + m^{s/2}u\right)^2}{m^2/u + n^2u}}_{E_{-s}} - G^s_{1111}\left(0\right) - G^s_{2222}\left(0\right)\right]. \tag{3.45}$$

The part proportional to E_s vanishes when evaluated at $s = -1$, by the functional relation of the real analytic Eisenstein series

$$E_{-s+1}(\tau) = \frac{E_s(\tau)\Gamma(s)}{\Gamma(-s+1)}, \tag{3.46}$$

and the fact that the only pole of E_s is at $s = 1$.

Substituting these regularized sums into eq. (3.40) gives the leading non-universal correction for a rectangular torus,

$$F_{\gamma_3}(iu) = -\frac{32\gamma_3\pi^6}{225\,\mathcal{A}^3}u^4E_4(iu)^2 + O(\mathcal{A}^{-4}). \tag{3.47}$$

For a square torus, $u = 1$, this becomes

$$F_{\gamma_3}(i) = -\frac{\gamma_3}{\mathcal{A}^3}\frac{\Gamma(1/4)^{16}}{3200\pi^6} + O(\mathcal{A}^{-4}). \tag{3.48}$$

The result can be written in modular-invariant form for a general torus modulus τ as:

$$F_{\gamma_3}(\tau) = -\frac{\gamma_3}{\mathcal{A}^3}\frac{2\pi^6}{225}(\tau-\bar{\tau})^4E_4(\tau)E_4(-\bar{\tau}) + O(\mathcal{A}^{-4}). \tag{3.49}$$

The γ_3 contribution is the first term in the EST torus free energy that depends on microscopic worldsheet data. All lower-order terms are universal and are fixed by the GGRT theory, hence the string tension. As a check, taking the long-string limit $L_1 \to \infty$ at fixed L_2, the free energy is dominated by the closed string ground state energy,

$$\Delta E_0 = \lim_{L_1\to\infty}\frac{F_{\gamma_3}(L_1,L_2)}{L_1} = -\frac{32\pi^6}{225}\frac{\sqrt{\sigma}\gamma_3}{\left(\sqrt{\sigma}L_2\right)^7} + \cdots, \tag{3.50}$$

in agreement with the known large L_2 correction to the closed string spectrum in [2].

The perturbative computation has two important limitations. First, it captures only the leading large-area contribution linear in γ_3 while extending the path-integral calculation to higher orders rapidly leads to increasingly complicated multi-sums. Second, the analytic regularization of these sums does not keep the nonlinearly realized target-space symmetry manifest and, as in related zeta-function regularizations of the static-gauge theory, may require non-covariant intermediate counterterms [9]. This motivates the TBA formulation used in the next subsection.

3.3. Non-universal free energy from the thermodynamic Bethe ansatz

We now compute the finite-volume spectrum using TBA. The expansion remains perturbative in γ_3, but the dependence on the area $\mathcal{A}$ is kept unexpanded. In this form, universal finite-area effects are retained exactly within the TBA description, while the first non-universal correction is treated perturbatively.

The only additional input needed is the spectrum itself. The trace formula used for the GGRT contribution, eq. (3.13), depends only on this spectrum and therefore generalizes directly to the TBA-corrected case. We review the excited state TBA for GGRT in subsec. 1.3.2. Here, we just consider the extension to γ_3.

The computation of the partition function presented in sec. 3.2 can be generalized to arbitrary spectrum. Let I denote a set of quantum numbers characterizing the worldsheet spectrum, with degeneracy $p(I)$, and let

$$m_I = \sigma L_2 \mathcal{E}_I \tag{3.51}$$

be the corresponding rest mass, where ε_I is the dimensionless energy determined using TBA. As before, including the transverse center-of-mass momentum p_z, the energy is

$$E_{I,p_z} = \sigma L_2 \sqrt{\mathcal{E}_I^2 + \left(\frac{p_z}{\sigma L_2}\right)^2}. \tag{3.52}$$

After taking the transverse-volume continuum limit, the partition function becomes

$$Z = \left(\frac{\sigma L_z^2 \mathcal{A}}{\pi^2 u}\right)^{1/2} \sum_I p(I) \mathcal{E}_I K_1(\mathcal{A}\mathcal{E}_I). \tag{3.53}$$

3.3.1. Spectrum

We work in units in which $\sigma = 1$ inside the TBA equations and define the dimensionless spatial length

$$\mathcal{R} = \sqrt{\sigma} L_2 = \sqrt{\frac{\mathcal{A}}{u}}. \tag{3.54}$$

The two-to-two phase shift is

$$2\delta(s) = \frac{s}{4} + \gamma_3 s^3. \tag{3.55}$$

The cubic term gives additional x^3-dependent terms in the pseudoenergies, making the TBA equations significantly harder to solve. Thus we expand around $\gamma_3 = 0$. The linearized TBA equation for the

right-movers becomes

$$\epsilon_R(x) = x\left[1 + \frac{P_L^{(1)}}{R^2} + \frac{1}{R^2}\int_0^\infty \frac{dx'}{2\pi}\log\left(1 - e^{-\epsilon_L(x')}\right)\right] + \gamma_3 x^3\left[\frac{64P_L^{(3)}}{R^6} + \frac{96}{\pi R^6}\int_0^\infty dx'\, x'^2\log\left(1 - e^{-\epsilon_L(x')}\right)\right], \tag{3.56}$$

where

$$P_L^{(3)} = \sum_j q_j^3. \tag{3.57}$$

For brevity, we will only show the equations for the right movers. The left-moving equation is obtained by exchanging $R \leftrightarrow L$.

To solve perturbatively, expand all relevant quantities in γ_3

$$\epsilon_R(x) = c_R^{(1,0)}x + c_R^{(1,1)}x\gamma_3 + c_R^{(3,1)}x^3\gamma_3 + O(\gamma_3^2), \tag{3.58}$$

$$p_l = p_l^{(0)} + \gamma_3 p_l^{(1)} + O(\gamma_3^2), \tag{3.59}$$

$$P_R^{(1)} = P_R^{(1,0)} + \gamma_3 P_R^{(1,1)} + O(\gamma_3^2) \tag{3.60}$$

$$P_R^{(3)} = P_R^{(3,0)} + O(\gamma_3) \tag{3.61}$$

where $P_R^{(3)}$ is kept only at first order because it always appears multiplied by γ_3.

The zeroth-order equations are those of the GGRT spectrum. At linear order in γ_3, the excited state condition and the TBA yield the following set of equations

$$0 = c_R^{(1,0)}P_R^{(1,1)} + c_R^{(1,1)}P_R^{(1,0)} - c_R^{(3,1)}P_R^{(3,0)} \tag{3.62}$$

$$c_R^{(1,1)} = \frac{P_L^{(1,1)}}{R^2} + \frac{\pi c_L^{(1,1)}}{12\left(c_L^{(1,0)}\right)^2 R^2} + \frac{\pi^3 c_L^{(3,1)}}{30\left(c_L^{(1,0)}\right)^4 R^2} \tag{3.63}$$

$$c_R^{(3,1)} = -\frac{64P_L^{(3,0)}}{R^6} - \frac{32\pi^3}{15\left(c_L^{(1,0)}\right)^3 R^6}. \tag{3.64}$$

The terms proportional to π^3 come from

$$\int_0^\infty dx\, x^2\log(1 - e^{-cx}) = -\frac{\pi^4}{45c^3}. \tag{3.65}$$

The energy to this order is

$$E = R\left(c_R^{(1,0)} + c_L^{(1,0)} + \gamma_3 c_R^{(1,1)} + \gamma_3 c_L^{(1,1)} - 1\right) + O(\gamma_3^2). \tag{3.66}$$

Plugging the solutions of eqs. (3.62), (3.63), and (3.64) into the energy yields

$$E_{k,k',s,s'} = R\left[\mathcal{E}_{k,k'} - \frac{32\pi^6\gamma_3}{225R^8}\frac{(240s+1)(240s'+1)}{\mathcal{E}_{k,k'}\left[\left(\mathcal{E}_{k,k'}+1\right)^2 - \frac{\pi^2}{R^4}(k-k')^2\right]^3}\right] + O(\gamma_3^2), \tag{3.67}$$

k	s	$p\,(k,s)$
0	0	1
1	1	1
2	$(2,8)$	$(1,1)$
3	$(3,9,27)$	$(1,1,1)$
4	$(4,10,16,28,64)$	$(1,1,1,1,1)$
5	$(5,11,17,29,35,65,125)$	$(1,1,1,1,1,1)$
$\vdots$	$\vdots$	$\vdots$
8	$(8,14,20,26,\mathbf{32},38,44,56,62,68,\cdots,512)$	$(1,1,1,1,\mathbf{2},1,1,1,1,1,\cdots,1)$,

Table 3.1. Allowed values of s for each k and the corresponding degeneracies. The bold values highlight the first degenerate state $8 = 2+2+2+2 = 3+1+1+1+1+1$.

where $\mathcal{E}_{k,k'}$ is the GGRT result. The γ_3 deformation is more refined than a correction depending only on k and k'. It depends on how a given oscillator level is partitioned among modes. For a partition of k, $\{n_\ell\}$, define

$$s = \sum_\ell n_\ell^3, \qquad k = \sum_\ell n_\ell. \tag{3.68}$$

The degeneracy of the state, denoted by $p(k,s)$, counts the number of partitions of k with fixed value of s. Its generating function is

$$\mathcal{G}(x,z) = \prod_{m=1}^{\infty} \frac{1}{1-x^m z^{m^3}} = \sum_{k,s} p(k,s) x^k z^s. \tag{3.69}$$

The ordinary partition number is recovered by summing over s

$$p(k) = \sum_s p(k,s). \tag{3.70}$$

The degeneracies are shown in tab. 3.1.

Thus the spectrum entering the torus partition function can be written as

$$\mathcal{E}_{k,k',s,s'} = \mathcal{E}_{k,k'} - \gamma_3 \Delta\mathcal{E}_{k,k',s,s'} + O(\gamma_3^2), \tag{3.71}$$

with

$$\Delta\mathcal{E}_{k,k',s,s'} = \frac{2048\pi^6 u^4}{225\mathcal{A}^3} \frac{(240s+1)(240s'+1)}{\mathcal{E}_{k,k'}\left[\left(\mathcal{E}_{k,k'}+1\right)^2 - \frac{\pi^2 u^2}{\mathcal{A}^2}(k-k')^2\right]^3}. \tag{3.72}$$

For $k = k' = s = s' = 0$, it gives the finite R correction to the ground state energy,

$$E_0(R) = R\left[\sqrt{1-\frac{\pi}{3R^2}} - \gamma_3 \frac{32\pi^6}{225R^8} \frac{1}{\sqrt{1-\frac{\pi}{3R^2}}\left(\sqrt{1-\frac{\pi}{3R^2}}+1\right)^6}\right] + O(\gamma_3^2). \tag{3.73}$$

Its large R expansion reproduces the known long-string correction proportional to γ_3 [2].

Substituting eq. (3.71) into the general trace formula and expanding to first order in γ_3 gives

$$Z = Z_{\mathrm{U}} + \gamma_3 Z_{\gamma_3} + O(\gamma_3^2). \tag{3.74}$$

Equivalently, the free energy can be written as

$$F = F_{\mathrm{U}} + \gamma_3 \mathcal{F}^{\mathrm{TBA}}_{\gamma_3} + O(\gamma_3^2), \tag{3.75}$$

where

$$\mathcal{F}^{\mathrm{TBA}}_{\gamma_3}(\mathcal{A}, u) = -\mathcal{A} \frac{\sum_{k,k',s,s'} p(k,s)p(k',s')\Delta\mathcal{E}_{k,k's,s'}\mathcal{E}_{k,k'}K_0(\mathcal{A}\mathcal{E}_{k,k'})}{\sum_{k,k'} p(k)p(k')\mathcal{E}_{k,k'}K_1(\mathcal{A}\mathcal{E}_{k,k'})}. \tag{3.76}$$

Equation (3.76) is used in the numerical fits. The full correction $\gamma_3 \mathcal{F}^{\mathrm{TBA}}_{\gamma_3}$ is linear in γ_3, while $\mathcal{F}^{\mathrm{TBA}}_{\gamma_3}$ keeps the dependence on $\mathcal{A}$ unexpanded and converges exponentially. This improved convergence is the main practical advantage over the direct path-integral expansion.

3.3.2. Partition function and its large-area expansion

As in the GGRT spectrum, we can define a generating function for the large-area expansion, $Z^{(0)}_{\gamma_3}$, from

$$\begin{aligned} Z_{\gamma_3}(\tau = \alpha + iu) = \frac{32\pi^6 u^4}{225\mathcal{A}^3} \frac{\sqrt{\sigma L_z^2}}{\sqrt{2\pi u}} e^{-\mathcal{A}} \sum_{n=0} \frac{t_n\left(\frac{\partial_\tau}{2\pi i} + \frac{1}{24}, -\frac{\partial_{\bar\tau}}{2\pi i} + \frac{1}{24}\right)}{\mathcal{A}^n} \\ \times \sum_{k,k',s,s'} (240s+1)p(k,s)(240s'+1)p(k',s') e^{2\pi i\tau(k-1/12)} e^{-2\pi i\bar\tau(k'-1/12)} \end{aligned}$$

where

$$Z^{(0)}_{\gamma_3}(\tau) \equiv \left| q^{-1/24} \sum_{k,s} (240s+1)p(k,s)q^k \right|^2, \qquad q = e^{2\pi i\tau}. \tag{3.77}$$

The sum over the string modes can be computed using $\mathcal{G}$, defined in eq. (3.69), by noticing that

$$\sum_{k,s} sp(k,s)q^k = \frac{\partial}{\partial z}\mathcal{G}(q,z)\Big|_{z=1} = \left(\prod_{m=1}^{\infty} \frac{1}{1-q^m}\right) \sum_{m=1}^{\infty} \frac{m^3 q^m}{1-q^m}. \tag{3.78}$$

The standard identity

$$E_4(\tau) = 1 + 240 \sum_{m=1}^{\infty} \frac{m^3 q^m}{1-q^m} \tag{3.79}$$

then gives

$$q^{-1/24} \sum_{k,s} (240s+1)p(k,s)q^k = \frac{E_4(\tau)}{\eta(\tau)}. \tag{3.80}$$

Therefore

$$Z^{(0)}_{\gamma_3}(\tau) = \left| \frac{E_4(\tau)}{\eta(\tau)} \right|^2. \tag{3.81}$$

It follows that the large-area expansion of the TBA result begins with the path-integral result in eq. (3.47).

The next term in the large-area expansion is also fixed by the same TBA computation. For a general modulus $\tau = \alpha + iu$, one finds

$$\mathcal{F}^{\mathrm{TBA}}_{\gamma_3}(\tau) = -\frac{32\pi^6}{225\mathcal{A}^4}\Bigg[u^4|E_4|^2\mathcal{A} + \frac{\pi^2 u^6}{72}|7E_2E_4 - 8E_6|^2 + \frac{7\pi u^5}{12}\left(8\,\mathrm{Re}[E_4(\tau)E_6(-\bar{\tau})] - 7|E_4|^2\mathrm{Re}\,E_2\right) - \frac{u^4}{8}|E_4|^2 \tag{3.82}$$

$$+ O(\mathcal{A}^{-1})\Bigg], \tag{3.83}$$

where all holomorphic Eisenstein series without explicit argument are evaluated at τ. For the square tori used in the simulations this reduces to

$$\mathcal{F}^{\mathrm{TBA}}_{\gamma_3}(i) = -\frac{32\pi^6}{225\mathcal{A}^3}E_4(i)^2\left[1 - \frac{13}{2\mathcal{A}} + O(\mathcal{A}^{-2})\right]. \tag{3.84}$$

The TBA provides a finite-area resummation of the contribution linear in γ_3, using an integrable worldsheet description whose phase shift agrees with the EST to this order. For the terms needed below, it is sufficient to keep the leading and subleading large area contributions proportional to γ_3. Beyond linear order in γ_3, however, this description is not complete. At order γ_3^2, particle production, violations of factorized scattering, and additional higher-derivative Wilson coefficients can contribute.

3.3.3. Higher order corrections

The extension of the TBA computation to higher-order Wilson coefficients, γ_n, is straightforward, but meaningful only in the regime where the phase shift remains real (i.e. before integrability is lost, effectively only $n = 3, 5, 7$ [2]). The general result is

$$\Delta\mathcal{E}_{k,k',s,s'} = -2^{6n-1}\pi^{2n}\zeta(-n)^2\frac{\left(1 + \frac{2}{\zeta(-n)}s_n\right)\left(1 + \frac{2}{\zeta(-n)}s'_n\right)}{R^{2+2n}\mathcal{E}_{k,k'}\left(\left(\mathcal{E}_{k,k'} + 1\right)^2 - \frac{4\pi^2\left(k - k'\right)}{R^4}\right)^n}, \tag{3.85}$$

where s_n is now given by $s_n \equiv \sum_l n_l^n$, still restricted to $k = \sum_l n_l$, and the correction to the partition function is

$$\gamma_n Z_{\gamma_n} = -\frac{1}{2}\left(4^n\pi^n\zeta(-n)\right)^2\frac{\sqrt{\sigma L_z^2}}{\sqrt{2\pi u}}e^{-\mathcal{A}}\frac{u^{n+1}}{\mathcal{A}^n}\gamma_n\left(\left|\frac{E_{n+1}\left(\tau\right)}{\eta\left(\tau\right)}\right|^2 + \mathcal{O}(\mathcal{A}^{-n-1})\right). \tag{3.86}$$

[2] This statement is restricted to the elastic real phase-shift approximation used here. It should not be read as a statement about the full effective string theory, where higher Wilson coefficients and inelastic effects can appear.

3.4. MC simulations

This section outlines the strategy leading to the main result, namely the measurement

$$\gamma_3(0) = -0.82(15)|\gamma_3^{\min}| = -0.00106(18), \tag{3.87}$$

where $\gamma_3^{\min}$ is the bootstrap lower bound [2].

The simulation setup and MC methods are discussed in Chapter 2. This section is organized as follows. In subsec. 3.4.1 we show that multiple domain walls are strongly suppressed and argue for the dilute gas of interfaces picture. Subsec. 3.4.2 explains our strategy for extracting the string tension. The measurements themselves are presented and validated by determining the critical exponent $\nu = 0.6298(1)$, with a precision comparable to dedicated Monte Carlo studies, which reported $\nu = 0.62991(9)$ [10]. In subsec. 3.4.3 we determine the area-independent contribution to the free energy, the normalization of the partition function. Although sometimes regarded as model dependent, we show that for the 3D Ising model it agrees with the universal prediction of effective string theory, i.e. the normalization in eq. (3.34). Subsec. 3.4.4 describes how γ_3 is extracted from the numerical data and discusses possible sources of systematic uncertainty. Finally, in sec. 3.5 we measure finite-transverse-volume corrections to the string tension and argue they cannot be explained by considering the EST in finite transverse volume.

3.4.1. A dilute gas of domain walls versus a single domain wall

A major source of systematic uncertainty is our limited knowledge of the microscopic dynamics, specifically, how many domain walls are present and how they interact, as the boundary conditions only control the oddness of the number of domain walls. This uncertainty affects the relation between the domain wall free energy and the ratio of partition functions. Two common assumptions are employed in the literature: a single domain wall

$$F = -\ln\left(\frac{Z_{\mathrm{AP}}}{Z_{\mathrm{P}}}\right), \tag{3.88}$$

or a dilute gas of non-interacting/weakly interacting domain walls [11]

$$F = -\ln\left(\frac{1}{2}\ln\left(\frac{1+Z_{\mathrm{AP}}/Z_{\mathrm{P}}}{1-Z_{\mathrm{AP}}/Z_{\mathrm{P}}}\right)\right). \tag{3.89}$$

Figure 3.2 shows that the two predictions agree for all but the smallest domain wall areas, $(L_x, L_y) = (8, 8)$, implying that the free energy is sufficiently large to suppress additional domain walls. Because the dilute-gas free energy is transverse volume-independent, even for small areas likely with multiple domain walls, it suggests that domain walls indeed do not interact strongly with each other. Thus, we should be able to isolate the $\mathcal{A}^{-3}$ non-universal term controlled by γ_3.

3.4.2. The string tension

Determining the string tension is complicated by our ignorance of the area at which γ_3 corrections become larger than the statistical noise. The measured free energy is fitted to eq. (3.13) with the

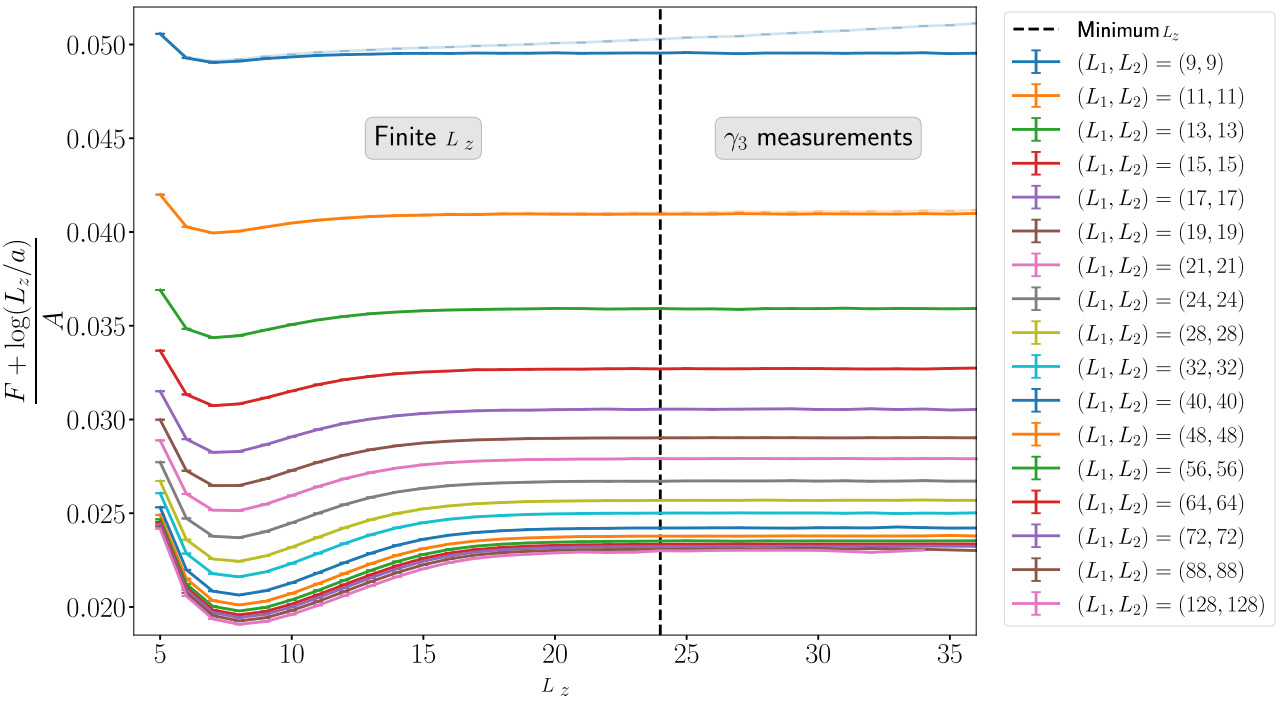


Figure 3.2 Comparison of the free energy estimates obtained from the dilute-gas picture (eq. (3.89), solid lines) and the single-domain wall picture (eq. (3.88), translucent lines). The two predictions coincide except for the smallest domain wall areas, indicating that additional domain walls are strongly suppressed. Simulations were performed at $\beta = 0.23$; error bars are often smaller than the line width. The vertical dashed line separates the data used for studying finite-transverse-volume effects (left) from the data used to determine γ_3 (right). The same qualitative behaviour is observed at all simulated temperatures. For clarity, only half of the measured areas are shown.

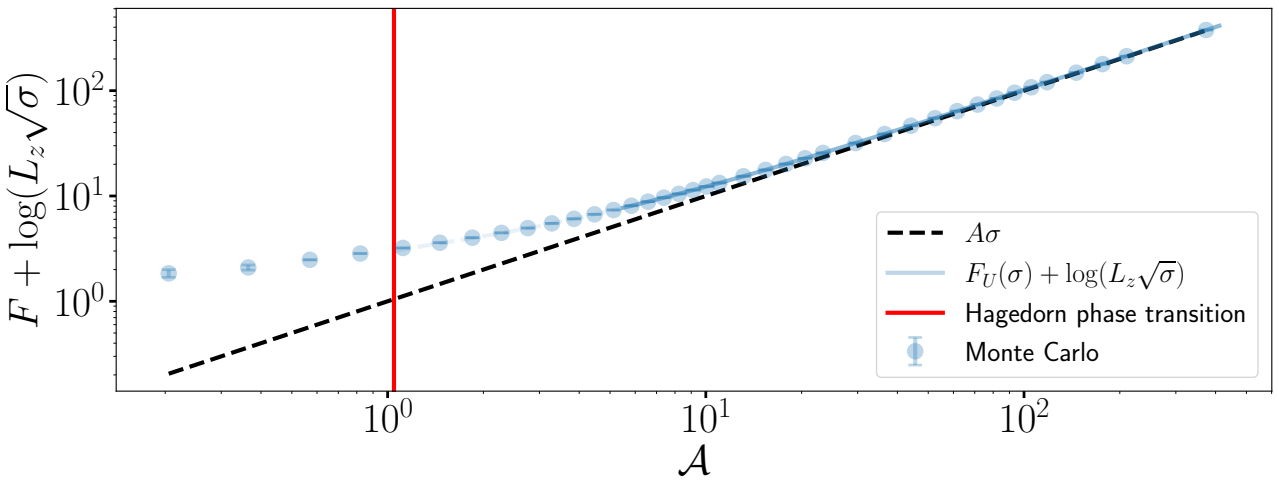


Figure 3.3 Free energy versus domain wall area. The black dashed line shows the leading linear term; the solid blue curve is the universal contribution of the partition function.

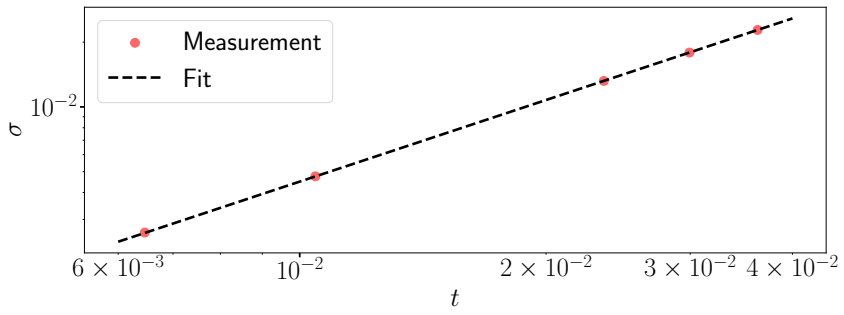


Figure 3.4 String tension versus reduced temperature (log-log scale).

β	σ
0.223102	0.0026062(12)
0.224	0.0047567(10)
0.227	0.0132004(25)
0.2285	0.0178901(14)
0.23	0.0227944(20)

Table 3.2. Measured string tensions. Statistical errors only.

string modes truncated at ~ 400. [3]

To reduce statistical errors, we average the free energy, after subtracting the $\log(L_z)$ contribution, over all transverse sizes above the threshold indicated by the vertical line in fig. 3.2. This threshold depends trivially on the single length scale of the system as the collapse in fig. 3.9 shows.

As a first step we fit only data with sufficiently large areas (typically $\mathcal{A} > 20$) to minimize a putative contamination, at the cost of degraded statistics. To optimize the fit range, which we have no way of knowing *a priori*, we proceed iteratively:

1. compute the difference between the data and the universal prediction;
2. identify the minimum area where this difference falls below the numerical uncertainty (typically $\mathcal{A} \approx 8$);
3. refit using this smaller cutoff area and verify that the deviations are smaller than the statistical uncertainty in the fitted domain. [4]

The fit quality is illustrated in fig. 3.3 and the deviations are shown in fig. 3.7. All quoted string tensions follow this procedure (Table 3.2). From the temperature dependence $\sigma \sim t^{2\nu}$, excluding the first data point we obtain $\nu = 0.6298(1)$, in good agreement with the bootstrap result $\nu = 0.629971(4)$ [12] and state-of-the-art Monte Carlo simulations $\nu = 0.62991(9)$ [10].

As a further check of the string-tension extraction, we fit the subleading corrections to the critical scaling form. Using the conformal-bootstrap values of $\nu = 0.62997097(12)$ [13] and $\theta = 0.5226(4)$ [14], as an external input, we fit

$$\sigma = \sigma_0 t^{2\nu} \left(1 + a t^{\theta} + b t\right), \qquad t = \beta - \beta_c. \tag{3.90}$$

The fitted coefficient can therefore be compared directly with the high-precision determination of [15].

Fig. 3.5 shows

$$\frac{\sigma}{\sigma_0 t^{2\nu}} = 1 + a t^{\theta} + b t. \tag{3.91}$$

The fitted correction agrees well with the literature result over the range of couplings used here. The individual coefficients a and b are correlated, and the mismatch with the earlier determination of the

[3] Even for very small areas ($\mathcal{A} \sim 1.1\,\mathcal{A}_{\text{crit}}$) fewer modes would likely suffice, but retaining a large cutoff is numerically inexpensive.

[4] Extending the fit range reduces the statistical error on σ, which tightens the error on the difference. We therefore increased the lower cut if necessary.

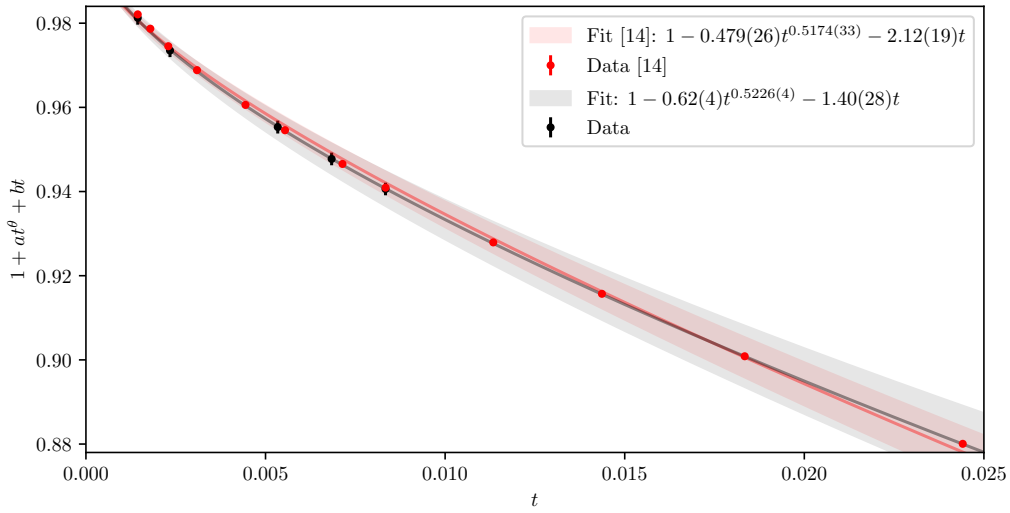


Figure 3.5 Subleading correction to the critical scaling of the domain-wall string tension. The plotted quantity is the correction factor multiplying the leading behaviour $\sigma = \sigma_0 t^{2\nu}$, with $t = \beta - \beta_c$. The two curves agree well over the fitted range.

subleading correction is largely due to the less precise value of the critical exponent $\theta = 0.5174(33)$ available at the time. The MC results are nevertheless compatible with the literature determination, up to small shifts attributable to using the exact expression in eq. (3.13) in the fit rather than its large-area expansion.

3.4.3. Area-independent contribution

With the string tension σ fixed, we define the area-independent part of the free energy

$$c_0 \equiv \lim_{\mathcal{A}\to\infty} \left[F(\mathcal{A}) - \mathcal{A} + \log(L_z\sqrt{\sigma})\right] \tag{3.92}$$

as represented in fig. 3.6.

For large areas the data coincide with the effective-string prediction, eq. (3.34),

$$-c_0 = -\frac{1}{2}\log\left(\frac{1}{2\pi u}\right) + 2\log|\eta(iu)|\,, \tag{3.93}$$

after the L_z-dependent term is removed. Allowing c_0 to float in the fit yields the same value, suggesting that the normalization is universal—contrary to the expectations in [6, 16]. Fixing c_0 therefore removes a fit parameter and significantly sharpens the fit of the EST parameters.

3.4.4. Measuring γ_3

As explained before, we do not use the asymptotic expansion, eq. (3.49), to fit the Monte Carlo data. If one nevertheless performs that fit, one obtains $\gamma_3 = -0.90(10)|\gamma_3^{\min}|$, where $\gamma_3^{\min} = -1/768$ is the lower bound obtained with the S-matrix bootstrap [2]. This result lies within 1σ of saturating the bootstrap bound and is in clear tension with the value reported by the authors in [17]. We do not expect the bound to be saturated in the case of a domain wall in the 3D Ising model, because the

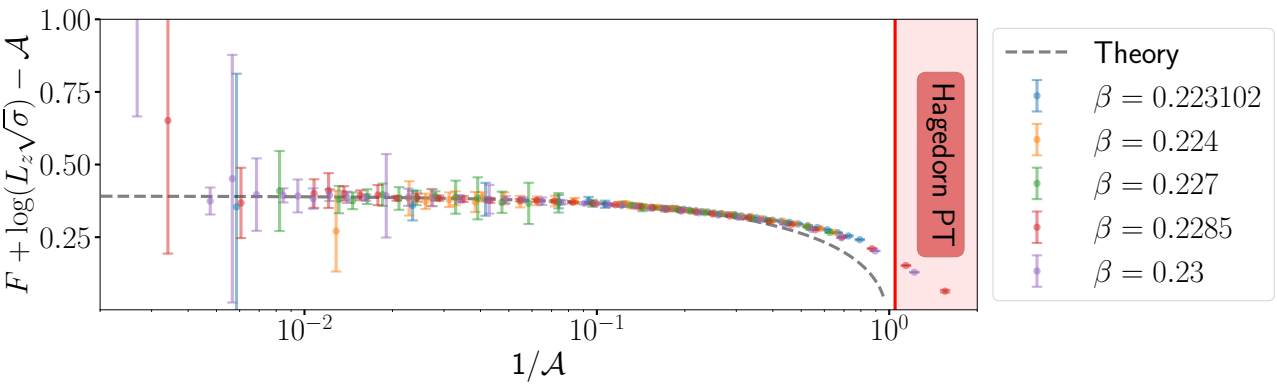


Figure 3.6 Measurement of $c_0 \equiv \lim_{\mathcal{A}\to\infty} F(\mathcal{A}) - \mathcal{A} + \log(L_z\sqrt{\sigma})$, for multiple temperatures. The dashed line is the universal contribution in eq. (3.13). Non-universal effects close to the Hagedorn transition are visible.

bound corresponds to a specific integrable theory, namely the Goldstino S-matrix describing the flow from tricritical Ising to free fermions [2].

We extract γ_3 from the combination

$$F_{\rm MC} = F_{\rm U} + \gamma_3^{\rm MC}\mathcal{F}_{\gamma_3}^{\rm TBA} + \mathcal{O}\left(\gamma_3^2\right) \Longrightarrow \gamma_3^{\rm MC} \equiv \frac{F_{\rm MC} - F_{\rm U}}{\mathcal{F}_{\gamma_3}^{\rm TBA}} + \mathcal{O}\left(\gamma_3^2\right). \tag{3.94}$$

Here $F_{\rm U}$ is obtained by numerically evaluating the first term in eq. (3.13) up to string level 400. We used the string tension measured in subsec. 3.4.2. $\gamma_3^{\rm MC}$ is shown in fig. 3.7. There is only a narrow window in area where the $\mathcal{A}^{-3}$ scaling is identifiable.

We also investigate the temperature (i.e. distance to the critical point) dependence of γ_3. The EST description becomes exact only in the critical continuum limit, where continuum symmetries are restored. However, at fixed dimensionless area $\mathcal{A}$, the size of the domain wall in lattice units diverges as we approach the critical point. Consequently, we must determine γ_3 at a finite distance from criticality and then extrapolate. The result of the extrapolation is shown in fig. 3.8, where γ_3 decreases monotonically as we approach the critical point. Performing a finite-size scaling analysis, we expect the leading correction to be controlled by $\theta = \omega\nu$, where $\omega = 0.82951(61)$ is the critical exponent of the leading irrelevant operator in the 3D Ising model [14]. Thus, the dependence on the reduced temperature is modeled as

$$\gamma_3(t) = \gamma_3(0) + at^{\omega\nu}, \tag{3.95}$$

where a is a fit parameter. Extrapolating to $t = 0$ yields

$$\gamma_3(0) = -0.82(10)|\gamma_3^{\rm min}| = -0.00106(13). \tag{3.96}$$

However, this fit is based on only three points and therefore does not robustly test the expected t-dependence near criticality, as systematic uncertainties are not fully controlled. As a diagnostic, we also perform a linear fit, which is indistinguishable (within errors) from the above over the available data, and obtain

$$\gamma_3(0) = -0.67(5)|\gamma_3^{\rm min}| = -0.00088(6). \tag{3.97}$$

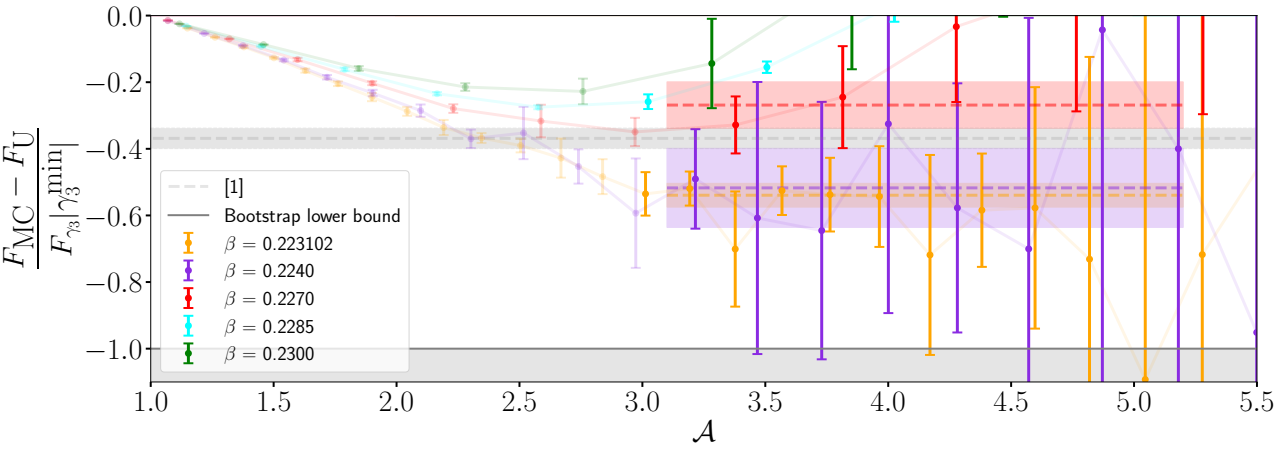


Figure 3.7 γ_3^{MC} as defined in eq. (3.94), normalized by the bootstrap lower bound, shown as a function of the area $\mathcal{A}$ for several inverse temperatures. Horizontal lines indicate the γ_3 value extracted from plateau fits. For $\beta = 0.23$ and $\beta = 0.2285$ it increases with $\mathcal{A}$ and no plateau is observed. For $\beta = 0.227$ the behaviour is unclear. For $\beta = 0.224$ and $\beta = 0.223102$, there are hints of a plateau, although it is not sharply defined due to large uncertainties. The data suggest that the continuum value lies between the finite-temperature estimates and the bootstrap lower bound, within the present systematics.

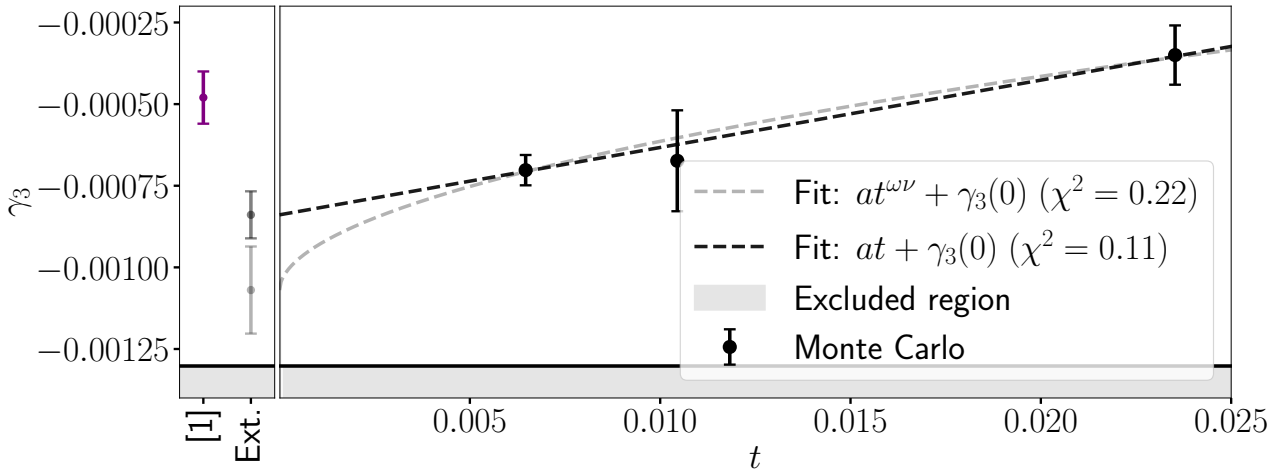


Figure 3.8 Extracted values of γ_3 versus reduced temperature. The black line is the bootstrap lower bound [2].

Taking the difference between the two extrapolations as an estimate of the systematic uncertainty, we quote

$$\gamma_3(0) = -0.82(15)|\gamma_3^{\min}| = -0.00106(20). \tag{3.98}$$

As β decreases toward criticality, the $\mathcal{A}$-dependence in fig. 3.7 evolves from a wedge-like profile at $\beta = 0.23$ (with no sign of saturation) to a decreasing curve that appears to level off into a plateau for $\beta = 0.224$ and $\beta = 0.223102$; the putative plateau is, however, only weakly resolved given the present uncertainties. At intermediate values ($\beta = 0.2285$–0.227), the behaviour is transitional and a plateau is not clearly identifiable.

A clear plateau emerges only sufficiently close to the critical point, where the EST description is expected to hold most cleanly. Further progress will likely require improved statistics in the mid-$\mathcal{A}$ regime, and data closer to criticality.

Higher-order Wilson coefficients can affect the determination of γ_3. These coefficients enter the asymptotic expansion in the area and they appear multiplied by increasingly large numerical factors. From eq. (3.86) we find that, for square domain walls,

$$\frac{Z_{\gamma_n}}{Z_{\gamma_3}} \sim \frac{\Delta\mathcal{E}^{(n)}_{0,0,0,0}}{\Delta\mathcal{E}^{(3)}_{0,0,0,0}} = \frac{225\ 4^{2n-3}\pi^{2n-6}\zeta(-n)^2}{\mathcal{A}^{2n-6}}, \tag{3.99}$$

which yields $\frac{25600\pi^4}{441\mathcal{A}^4}$ for $n = 5$. This ratio is smaller than 1 only when $\mathcal{A} \gtrsim 100$, well beyond the range of areas where our numerical precision is sufficient. This observation implies that, for γ_3 to remain the dominant contribution within the range of accessible areas, one must have $\gamma_5 \lesssim 10^{-3}\gamma_3$. This order of magnitude is also suggested by the S-matrix bootstrap bounds [2].

3.5. Effective string tension

While measuring γ_3, we identified a threshold in L_z above which the free energy becomes effectively independent of the transverse size. Rather than simply discarding the data below this threshold, we use them to probe finite-L_z effects associated with interactions between the domain wall and the lightest bulk excitation. These effects are studied in detail in Chapter 4. Here, we show that they cannot be accounted for by the EST of an isolated domain wall.

We begin by defining the effective string tension

$$\sigma_{\text{eff}}(L_z) \equiv \lim_{A\to\infty} \frac{F(\mathcal{A}, u, L_z; \sigma) + \log(L_z\sqrt{\sigma})}{A}. \tag{3.100}$$

The string tension used throughout the previous sections is its infinite-transverse-volume limit,

$$\sigma = \sigma_\infty \equiv \lim_{L_z\to\infty} \sigma_{\text{eff}}(L_z). \tag{3.101}$$

The EST itself can produce finite-L_z corrections to the free energy. We now show, however, that these corrections vanish in the infinite-area limit and therefore cannot account for the observed L_z-dependence of σ_{eff}.

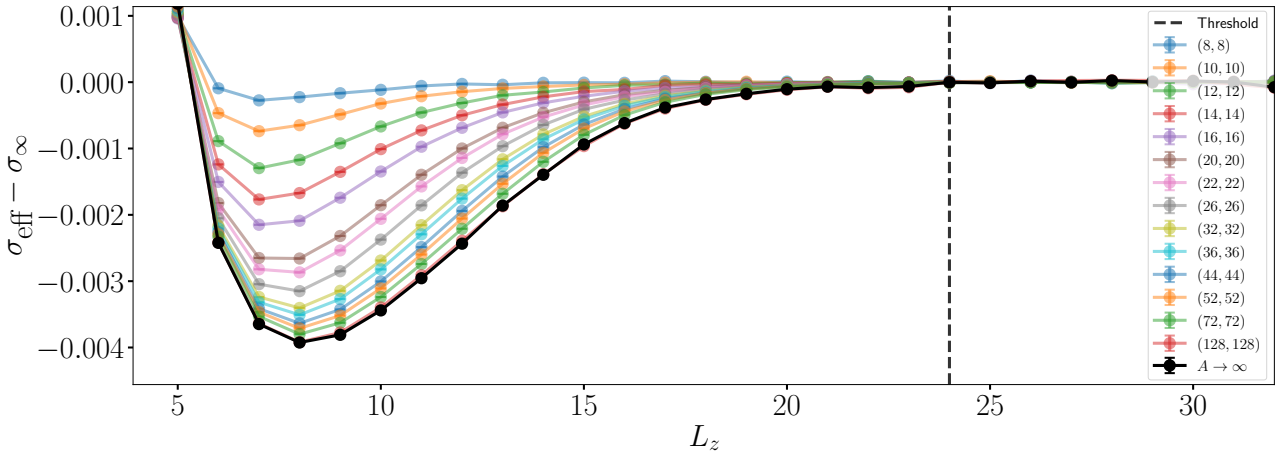


Figure 3.9 Difference between the effective string tension, defined in eq. (3.100), and its infinite-L_z value as a function of L_z, for $\beta = 0.23$. The vertical dashed line marks the threshold above which the data are used to determine γ_3. Colored curves correspond to finite domain-wall areas, increasing from top to bottom, while the black curve shows the extrapolation to infinite area.

Taking into account the winding ω around the compact dimension, the spectrum is [18]

$$\mathcal{E}_{k,k',n,\omega} = \sqrt{1 + \frac{4\pi}{\sigma L_2^2}\left(k + k' - \frac{1}{12}\right) + \left(\frac{2\pi\left(k - k' + n\omega\right)}{\sigma L_2^2}\right)^2 + \left(\frac{2\pi n}{\sigma L_2 L_z}\right)^2 + \left(\frac{L_z \omega}{L_2}\right)^2}. \tag{3.102}$$

In the large-area expansion the universal partition function becomes

$$Z_{\text{U}} = e^{-\mathcal{A}} \sum_{k,k',n,\omega} \sum_{\mu} \frac{h_\mu\left(k, k', n, \omega\right)}{\mathcal{A}^\mu} p(k) p(k') e^{2\pi i\left(\alpha(k-k'+n\omega) + ui\left(k+k' - \frac{1}{12} + \frac{\pi n^2}{\mathcal{L}_z^2} + \frac{\omega^2 \mathcal{L}_z^2}{4\pi}\right)\right)}. \tag{3.103}$$

where $\mathcal{L}_z = \sqrt{\sigma} L_z$. It can be verified that k, k', n, and ω appear in h_μ in specific combinations that allow the sum over them to be replaced by differential operators acting on Z_0

$$Z_0 \equiv \sum_{k,k',n,\omega} p(k) p(k') e^{2\pi i\left(\alpha(k-k'+n\omega) + ui\left(k+k' - \frac{1}{12} + \frac{\pi n^2}{\mathcal{L}_z^2} + \frac{\omega^2 \mathcal{L}_z^2}{4\pi}\right)\right)}. \tag{3.104}$$

Using

$$\begin{aligned} -\partial_u &= 2\pi\left(k + k' - \frac{1}{12}\right) + \frac{2\pi^2 n^2}{\mathcal{L}_z^2} + \frac{\omega^2 \mathcal{L}_z^2}{2} \\ -i\partial_\alpha &= 2\pi\left(k - k'\right) + 2\pi n\omega, \end{aligned}$$

the first three terms in h_μ take the following form

$$h_\mu\left(k, k', n, \omega\right) = \begin{pmatrix} 1 \\ 2u^2 \partial_\tau \partial_{\bar{\tau}} \\ 2u^3 \partial_\tau \partial_{\bar{\tau}} \left(u \partial_\tau \partial_{\bar{\tau}} + i\left(\partial_\tau - \partial_{\bar{\tau}}\right)\right) \\ \vdots \end{pmatrix} = \begin{pmatrix} 1 \\ 2u \mathcal{D}^{(1)}_{(0,0)}\left(\partial_\tau, \partial_{\bar{\tau}}\right) \\ 4u^2 \mathcal{D}^{(2)}_{(0,0)}\left(\partial_\tau, \partial_{\bar{\tau}}\right) \\ \vdots \end{pmatrix}, \tag{3.105}$$

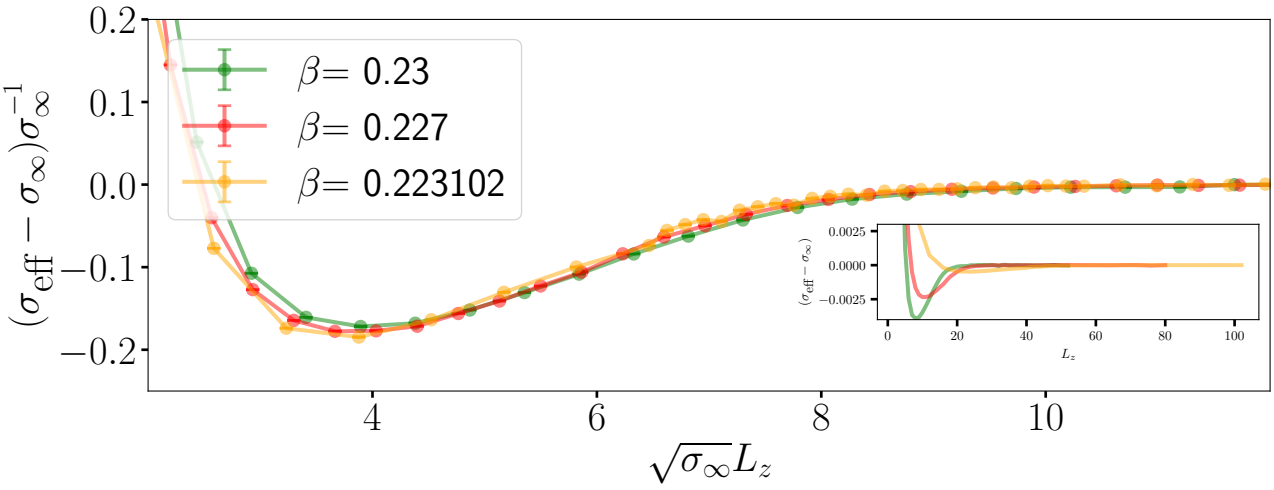


Figure 3.10 Rescaled string tension as a function of $\sqrt{\sigma_\infty} L_z$. We see that different temperatures collapse into the same curve in these rescaled variables. The inset displays the original data.

which we explicitly checked are the modular covariant derivatives, $\mathcal{D}^{(n)}_{(0,0)}$, that take a modular form of weight $(0,0)$ into a form of weight (n,n). Since u has weight $(-1,-1)$ and Z_0 has weight $(0,0)$, each coefficient in the large-area expansion is explicitly modular invariant. See [19–21] for a review.

Thus, we obtain

$$Z_U = e^{-\mathcal{A}} \sum_{n=0} \alpha_n \frac{u^n}{\mathcal{A}^n} \mathcal{D}^{(n)}_{(0,0)} \left(\partial_\tau, \partial_{\bar{\tau}}\right) Z_0, \tag{3.106}$$

where we made the area dependence explicit, and α_n are c-numbers. Thus, the finite-L_z corrections generated by the isolated-wall EST

$$\frac{F(A, L_z)}{A} = \sigma_\infty - \frac{\log\left(Z_0\left(A, L_z\right)\right)}{A} + \mathcal{O}\left(A^{-2}\right), \tag{3.107}$$

are suppressed by inverse powers of the area and vanish in the strict $\mathcal{A} \to \infty$ limit. Consequently,

$$\sigma^{\text{EST}}_{\text{eff}}(L_z) = \sigma_\infty, \tag{3.108}$$

is a prediction inconsistent with our data, as shown in fig. 3.9 and 3.10. We observe a trend opposite to the EST prediction: larger areas yield larger finite-transverse-volume corrections. In the curves shown, the area increases from top to bottom. We present data only for $\beta = 0.23$, which is, nonetheless, representative of all sampled temperatures.

In fig. 3.10, we argue that these corrections are universal. Measuring everything in units of the string tension, we see that different temperatures collapse into the same curve. In the continuum limit $\beta \to \beta_c$, this curve gives the string tension of a domain wall in the 3D Ising field theory. From the QFT perspective, this can be defined starting from the 3D Ising CFT on $\mathbb{R}^2 \times S^1$ with antiperiodic ($\mathbb{Z}_2$ flipping) boundary conditions along S^1, studied in Chapter 5, and turning on the ($\mathbb{Z}_2$ even) relevant deformation into the ferromagnetic phase.

References

[1] David Lima, J. M. Viana Parente Lopes, Jose Matos, and Joao Penedones. "Effective String Theory on a Torus: The 3d Ising Domain Wall." Oct. 2025. arXiv: 2510.15206 [hep-th].

[2] Joan Elias Miró, Andrea L. Guerrieri, Aditya Hebbar, João Penedones, and Pedro Vieira. "Flux Tube S-Matrix Bootstrap." In: *Physical Review Letters* 123.22 (Nov. 27, 2019), p. 221602. DOI: 10.1103/PhysRevLett.123.221602.

[3] Andrea Cavaglià, Stefano Negro, István M. Szécsényi, and Roberto Tateo. "T$\overline{\text{T}}$-Deformed 2D Quantum Field Theories." In: *Journal of High Energy Physics* 2016.10 (Oct. 20, 2016), p. 112. ISSN: 1029-8479. DOI: 10.1007/JHEP10(2016)112.

[4] P. Goddard, J. Goldstone, C. Rebbi, and C. B. Thorn. "Quantum Dynamics of a Massless Relativistic String." In: *Nuclear Physics B* 56.1 (May 21, 1973), pp. 109–135. ISSN: 0550-3213. DOI: 10.1016/0550-3213(73)90223-X.

[5] Sergei Dubovsky, Raphael Flauger, and Victor Gorbenko. "Solving the Simplest Theory of Quantum Gravity." In: *Journal of High Energy Physics* 2012.9 (Sept. 27, 2012), p. 133. ISSN: 1029-8479. DOI: 10.1007/JHEP09(2012)133.

[6] Marco Billó, Michele Caselle, and Livia Ferro. "The Partition Function of Interfaces from the Nambu-Goto Effective String Theory." In: *Journal of High Energy Physics* 2006.02 (Feb. 2006), p. 070. ISSN: 1126-6708. DOI: 10.1088/1126-6708/2006/02/070.

[7] Tom M. Apostol. *Modular Functions and Dirichlet Series in Number Theory*. Vol. 41. Graduate Texts in Mathematics. New York, NY: Springer, 1990. ISBN: 978-1-4612-6978-6 978-1-4612-0999-7. DOI: 10.1007/978-1-4612-0999-7.

[8] K. Dietz and T. Filk. "Renormalization of String Functionals." In: *Physical Review D* 27.12 (June 15, 1983), pp. 2944–2955. DOI: 10.1103/PhysRevD.27.2944.

[9] Sergei Dubovsky, Raphael Flauger, and Victor Gorbenko. "Effective String Theory Revisited." In: *JHEP* 09 (2012), p. 044. DOI: 10.1007/JHEP09(2012)044. arXiv: 1203.1054 [hep-th].

[10] Alan M. Ferrenberg and Robert H. Swendsen. "New Monte Carlo Technique for Studying Phase Transitions." In: *Physical Review Letters* 61.23 (Dec. 5, 1988), pp. 2635–2638. DOI: 10.1103/PhysRevLett.61.2635.

[11] Martin Hasenbusch. "Direct Monte Carlo Measurement of the Surface Tension in Ising Models." In: *Journal de Physique I* 3.3 (Mar. 1, 1993), pp. 753–765. ISSN: 1155-4304, 1286-4862. DOI: 10.1051/jp1:1993160.

[12] Filip Kos, David Poland, David Simmons-Duffin, and Alessandro Vichi. "Precision Islands in the Ising and O(N) Models." In: *Journal of High Energy Physics* 2016.8 (Aug. 4, 2016), p. 36. ISSN: 1029-8479. DOI: 10.1007/JHEP08(2016)036.

[13] Cyuan-Han Chang et al. "Bootstrapping the 3d Ising Stress Tensor." In: *JHEP* 03 (2025), p. 136. DOI: 10.1007/JHEP03(2025)136. arXiv: 2411.15300 [hep-th].

[14] Marten Reehorst. "Rigorous Bounds on Irrelevant Operators in the 3d Ising Model CFT." In: *Journal of High Energy Physics* 2022.9 (Sept. 21, 2022), p. 177. ISSN: 1029-8479. DOI: 10.1007/JHEP09(2022)177.

[15] Michele Caselle, Martin Hasenbusch, and Marco Panero. "High Precision Monte Carlo Simulations of Interfaces in the Three-Dimensional Ising Model: A Comparison with the Nambu-Goto Effective String Model." In: *Journal of High Energy Physics* 2006.03 (Mar. 2006), p. 084. ISSN: 1126-6708. DOI: 10.1088/1126-6708/2006/03/084.

[16] Michele Caselle, Gianluca Costagliola, Alessandro Nada, Marco Panero, and Arianna Toniato. "Jarzynski's Theorem for Lattice Gauge Theory." In: *Physical Review D* 94.3 (Aug. 12, 2016), p. 034503. DOI: 10.1103/PhysRevD.94.034503.

[17] Alberto Baffigo and Michele Caselle. "Ising String beyond the Nambu-Goto Action." In: *Physical Review D* 109.3 (Feb. 28, 2024), p. 034520. DOI: 10.1103/PhysRevD.109.034520.

[18] E. Beratto, M. Billò, and M. Caselle. "$T\overline{T}$ Deformation of the Compactified Boson and Its Interpretation in Lattice Gauge Theory." In: *Physical Review D* 102.1 (July 8, 2020), p. 014504. DOI: 10.1103/PhysRevD.102.014504.

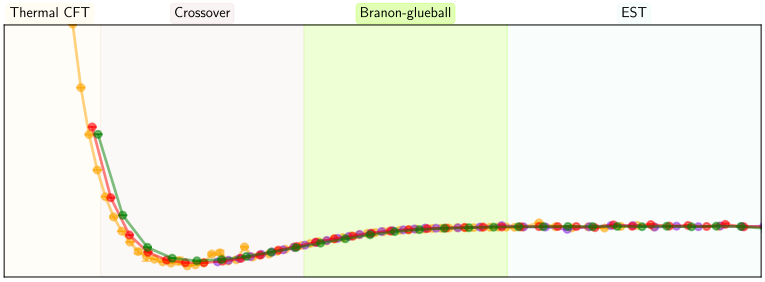
[19] Yunfeng Jiang. "A Pedagogical Review on Solvable Irrelevant Deformations of 2d Quantum Field Theory." In: *Communications in Theoretical Physics* 73.5 (May 1, 2021), p. 057201. ISSN: 0253-6102, 1572-9494. DOI: 10.1088/1572-9494/abe4c9. arXiv: 1904.13376 [hep-th].

[20] Ofer Aharony, Shouvik Datta, Amit Giveon, Yunfeng Jiang, and David Kutasov. "Modular Invariance and Uniqueness of $T\overline{T}$deformed CFT." In: *Journal of High Energy Physics* 2019.1 (Jan. 10, 2019), p. 86. ISSN: 1029-8479. DOI: 10.1007/JHEP01(2019)086.

[21] Eric D'Hoker and Justin Kaidi. *Lectures on Modular Forms and Strings*. Nov. 18, 2022. DOI: 10.48550/arXiv.2208.07242. arXiv: 2208.07242 [hep-th].

Chapter 4

Branon-Glueball interactions



The previous chapter treated the domain wall as an isolated effective string. Here we study observables that resolve the interaction between the fluctuating wall and massive bulk excitations. This chapter is based on [1], where this interaction was studied in the broken phase of the 3D Ising model using correlation functions and finite-transverse-volume effects.

4.1. Summary

The isolated-wall EST describes the Goldstone mode associated with broken transverse translations, and applies when bulk excitations are not resolvable. Some observables, however, are dominated by massive bulk propagation. We identify the kinematic regime in which this wall-bulk interaction can be described systematically. The central assumption is that the relevant long-distance behaviour is dominated by the lightest bulk scalar of mass m. The leading coupling to the wall is the pullback of the bulk field onto the fluctuating wall

$$S_{\rm int} = \lambda_0 \int d^2x_\parallel \sqrt{h}\phi\big(x_\parallel, \pi(x_\parallel)\big), \tag{4.1}$$

where $\pi(x_\parallel)$ is the transverse displacement of the wall and h is the induced metric. The form of this coupling is fixed by locality and reparametrization invariance, but we do not expect its coefficient to be universal. The EFT parameter is

$$\chi = \frac{m^2}{4\pi\sigma}. \tag{4.2}$$

The first result concerns the finite transverse-size correction to the wall free energy. For a wall wrapping a large transverse area and a compact perpendicular direction of length L_z, pure isolated EST predicts no L_z-dependence for the string tension, as discussed in sec. 3.5. The remaining possibility is that the leading L_z-dependence is a bulk effect. Wall fluctuations modify the naive massive-particle exchange, and the large mL_z prediction is

$$\frac{\sigma_{\rm eff}(L_z) - \sigma_\infty}{\sigma_\infty} \sim -\lambda^2 \frac{2^\chi \Gamma(\chi)}{8\pi} (mL_z)^\chi e^{-mL_z}. \tag{4.3}$$

The exponential e^{-mL_z} is due to the propagation of the lightest bulk particle around the compact transverse direction. The power $(mL_z)^\chi$ is the universal imprint of the fluctuating wall.

The same coupling λ controls the far transverse tail of wall-sector two-point functions. In the regime where the insertions are far away in the direction perpendicular to the wall, the correlator is dominated by the lightest bulk pole and receives the rough-wall enhancement

$$\delta G(x) \propto \lambda^2 (m|x_\parallel|)^{2\chi} \frac{|x_\perp|}{L_z} e^{-m|x_\perp|}. \tag{4.4}$$

Other observables are less universal. One-point functions and nearby-regime two-point functions depend on the microscopic operator used to probe the bulk, on its spectral density, and on the short-distance wall profile. For separations where the wall wandering is large compared with the microscopic wall width, the nearby two-point function is broadened by the Gaussian distribution, with a variance given by the relative wall displacement,

$$d^2(x_\parallel) = \Big\langle \big[\pi(x_\parallel) - \pi(0)\big]^2 \Big\rangle, \tag{4.5}$$

where π is the Goldstone.

The Monte Carlo tests are performed in the broken phase of the 3D Ising model with antiperiodic boundary conditions. The antiperiodic sector contains a fluctuating domain wall, while the periodic sector provides the corresponding bulk reference. The comparison requires care because the plane of

flipped bonds is only a representative of the global $\mathbb{Z}_2$ twist. It is not the physical wall. For the spin operator, which is $\mathbb{Z}_2$-odd, a compensating $\mathbb{Z}_2$ line removes the convention-dependent sign associated with the defect plane. For the energy operator, no such line is needed, but the operator must be defined using the signed bond energy so that it does not depend on the arbitrary position of the flipped plane.

The numerical results are consistent with an interaction of the type in eq. (4.1). The analysis goes as follows. The defect spin correlator gives a direct extraction of the wall variance and agrees with the free massless-boson prediction. With this input, the energy two-point function shows the expected near-wall Gaussian broadening, with the same variance determined from the spin correlator. The large-$x_\perp$ behaviour is also consistent with our predictions, although the evidence is weaker. With the available statistics, quantitative agreement is obtained only for $\beta = 0.3$.

The finite-L_z free-energy correction is more demanding. The measured effective tension approaches the isolated-wall plateau at large mL_z, and the sign and qualitative form of the correction agree with the bulk-exchange prediction. However, the asymptotic regime is reached slowly. Pre-asymptotic corrections remain important over the lattice sizes accessible in the simulations, so the free-energy data do not yet provide a precision determination of λ.

Wall fluctuations leave controlled, universal imprints on bulk observables. Wall roughness is not a subleading correction to the rigid-wall result. It changes the asymptotic form of finite-volume effects and correlation functions. At the same time, not every observable has a continuum interpretation. Some quantities are controlled by λ, while others retain non-universal dependence on microscopic operator data.

4.2. Effective field theory for particle-wall interactions

We consider a domain wall in three Euclidean dimensions, described at long distances by a single transverse Goldstone field. In static gauge the embedding is

$$X^\mu(x) = \big(x^1, x^2, \pi(x)\big), \tag{4.6}$$

where $x = (x^1, x^2) \equiv x_\parallel$ are coordinates along the wall and $\pi(x)$ is the transverse displacement.

At leading order in the long-distance expansion the worldsheet action is Gaussian,

$$S_{\mathrm{EST}} = \frac{\sigma}{2} \int d^2x \, \partial_\alpha \pi \, \partial_\alpha \pi + \cdots . \tag{4.7}$$

The ellipsis denotes higher-derivative worldsheet terms. They are not needed in this chapter, since the effects considered below are controlled by the leading rough-wall fluctuations.

The bulk theory is gapped. We denote by ϕ a scalar bulk operator that creates the lightest massive particle from the vacuum. Its two-point function admits the spectral representation

$$\langle \phi(x)\phi(0)\rangle_{\mathbb{R}^3} = \int_0^\infty ds \, \rho(s) \int \frac{d^3k}{(2\pi)^3} \frac{e^{ik\cdot x}}{k^2 + s}, \qquad \rho(s) = \delta(s - m^2) + \widetilde{\rho}(s), \tag{4.8}$$

where the continuum part has support above the next threshold. For observables controlled by long-distance bulk propagation, the leading asymptotic behaviour is determined by the isolated one-particle

pole at $s = m^2$, for which the bulk two-point function reduces to

$$\langle\phi(x)\phi(0)\rangle_{\mathbb{R}^3} \simeq \frac{e^{-m|x|}}{4\pi|x|}. \tag{4.9}$$

We will use this pole approximation for the finite-L_z correction to the wall free energy and, later, for the large-transverse-distance tail of the wall-sector two-point function. The correlation functions require somewhat more care, however. We will initially keep the full spectral density $\rho(s)$ as the one-point function and the near-wall regime of the two-point function depend on the complete spectral density and are therefore operator dependent. We will then show that, at sufficiently large $|\, x_\perp \,|$, the two-point function is again dominated by the lightest one-particle pole.

The leading interaction between the wall and the bulk scalar is the local coupling

$$S_{\rm int} = \lambda_0 \int d^2x\, \sqrt{h}\, \phi\big(x, \pi(x)\big), \tag{4.10}$$

where

$$h_{\alpha\beta} = \delta_{\alpha\beta} + \partial_\alpha\pi\, \partial_\beta\pi \tag{4.11}$$

is the induced metric on the wall. This is the lowest-order coupling compatible with worldsheet reparametrization invariance and Euclidean target-space symmetry. The coefficient λ_0 is a bare coupling. Physical long-distance observables will instead involve a renormalized dimensionless coupling, defined below.

4.2.1. Regime of validity

The interaction in eq. (4.10) should not be interpreted as a uniformly valid low-energy Lagrangian for all branon-glueball processes. In a generic confining or symmetry-broken theory, the lightest bulk mass is not parametrically below the string scale. A real-time bulk particle impinging on the wall with energy of order m can transfer momenta of order $m \sim \sqrt{\sigma}$ to the wall. Such a process probes the cutoff of the worldsheet derivative expansion.

The controlled observables considered here are different. They are dominated by bulk propagation with small momentum parallel to the wall. In Euclidean signature this corresponds to momenta of the form

$$p^\mu = \left(q, \pm i\sqrt{m^2 + q^2}\right), \qquad q \in \mathbb{R}^2, \qquad q^2 \ll m^2. \tag{4.12}$$

The bulk particle is nearly on shell, but the momentum carried along the wall [1] is small. This is the kinematic regime probed by finite transverse-volume effects and by the long-distance tails of wall-sector correlators. The EFT is therefore controlled not by a universal Lagrangian-level expansion parameter, but by the kinematic regime selected by the observables.

4.2.2. Wall fluctuations and Gaussian smearing

A central point in this chapter is that the wall cannot be treated as rigid. The branon field is massless in two dimensions, so its relative fluctuations grow logarithmically. For two points separated along

[1] In the Lorentzian theory, time is always one of the directions along the wall.

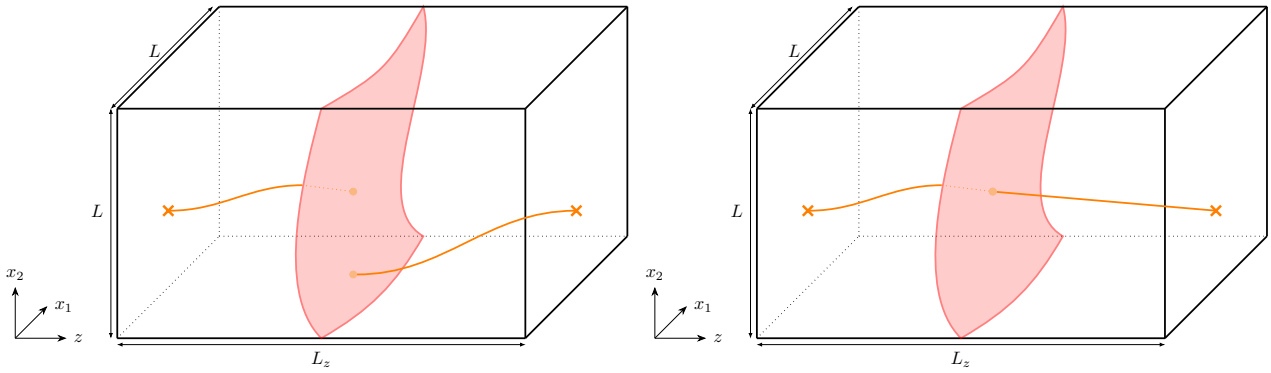


Figure 4.1 Left) diagrams contributing at $\mathcal{O}(\lambda^2)$ to the finite-L_z correction of the wall free energy for the linear coupling in eq. (4.1); right) diagrams contributing at $\mathcal{O}(\lambda_2)$ to the finite-L_z correction of the wall free energy for the quadratic coupling in eq. (4.31). The crosses show how the propagators are identified due to the periodic boundary conditions along the z direction.

the wall we define

$$d^2(x_\parallel) \equiv \left\langle \left[\pi(x_\parallel) - \pi(0)\right]^2 \right\rangle, \tag{4.13}$$

which on a large torus, approaches

$$d^2(x_\parallel) \simeq \frac{1}{\pi\sigma} \log \frac{|x_\parallel|}{r_0}, \tag{4.14}$$

where r_0 is a non-universal UV/lattice scale. The same scale appears below in the renormalized branon-glueball coupling.

The effect of wall fluctuations is most transparent in a convolution form. If

$$w = \pi(x_\parallel) - \pi(y_\parallel), \tag{4.15}$$

then the Gaussian branon theory gives

$$\left\langle \delta\big(w - \pi(x_\parallel) + \pi(y_\parallel)\big) \right\rangle_\pi = \frac{1}{\sqrt{2\pi d^2(x_\parallel - y_\parallel)}} \exp\left[-\frac{w^2}{2d^2(x_\parallel - y_\parallel)}\right]. \tag{4.16}$$

Averaging over the wall is therefore equivalent to smearing rigid-wall expressions by a Gaussian in the relative transverse displacement, using the

$$Y\left(\pi(x_\parallel) - \pi(y_\parallel)\right) = \int dw \frac{Y(w)}{\sqrt{2\pi d^2(x_\parallel - y_\parallel)}} \exp\left[-\frac{w^2}{2d^2(x_\parallel - y_\parallel)}\right]. \tag{4.17}$$

The Gaussian smearing is non-perturbative in the branon variance and generates the kinematic enhancement factors that appear below.

4.2.3. Finite transverse-volume correction to the wall tension

We first consider a toroidal wall of large area $A = L_1 L_2$, with a compact transverse direction of length L_z. The effective wall tension is defined by

$$\sigma_{\text{eff}}(L_z) = \lim_{A\to\infty} \frac{F(A, L_z)}{A}. \tag{4.18}$$

The leading contribution from the interaction eq. (4.10) appears at order λ_0^2. Subtracting the infinite-L_z contribution gives

$$\Delta F \simeq -\frac{\lambda_0^2}{2} \int d^2x\, d^2y \, \left[\langle\phi(x,\pi(x))\phi(y,\pi(y))\rangle_{L_z} - \langle\phi(x,\pi(x))\phi(y,\pi(y))\rangle_{\infty}\right], \tag{4.19}$$

where the subscripts indicate if the average is computed in finite or infinite volume. For large mL_z, the finite L_z propagator is described by the image expansion

$$G_{L_z}(x_\parallel, x_\perp) = \sum_{n\in\mathbb{Z}} G(x_\parallel, x_\perp + nL_z). \tag{4.20}$$

The leading correction comes from the nearest images, using $n = \pm 1$. Using translation invariance along the wall and the Gaussian smearing eq. (4.16), one obtains

$$\frac{\Delta F}{A} \simeq -\lambda_0^2 \int d^2r\, dw\, G(r, w + L_z) \frac{\exp[-w^2/(2d^2(r))]}{\sqrt{2\pi d^2(r)}}. \tag{4.21}$$

Given that $mL_z \gg 1$, we can expand the propagator

$$G\,(r, w + L_z) = \frac{e^{-m|x|}}{4\pi|x|}\,, \qquad |x| = \sqrt{r^2 + (w + L_z)^2} = L_z + w + \frac{r^2 + w^2}{2L_z} + \dots\,, \tag{4.22}$$

leading to

$$\frac{\Delta F}{A} \approx -\lambda_0^2 \frac{e^{-mL_z}}{4\pi L_z} \int dw e^{-mw} \int d^2r e^{-\frac{mr^2}{2L_z}} \frac{e^{-\dfrac{w^2}{2d^2(r)}}}{\sqrt{2\pi} d\,(r)}. \tag{4.23}$$

Notice that the integral is dominated by $r^2 \sim L_z/m$, which leads to $w^2 \sim d^2(r) \sim \frac{1}{\sigma} \ln L_z$. This is consistent with the approximations used above,$|r|, w \ll L_z$ and $mw^2 \ll L_z$. Integrating over w yields

$$\frac{\Delta F}{A} \approx -\lambda_0^2 \frac{e^{-mL_z}}{4\pi L_z} \int d^2r\, e^{-\frac{mr^2}{2L_z}} e^{\frac{1}{2}m^2 d^2(r)}\,. \tag{4.24}$$

Then, using the variance eq. (4.14), the integral over r can be done exactly,

$$\int d^2r e^{\frac{1}{2}m^2 d^2(r) - \frac{mr^2}{2L_z}} = 2\pi \int_{r_0}^{\infty} dr r (r/r_0)^{2\chi} e^{-\frac{mr^2}{2L_z}} \tag{4.25}$$

where $\chi \equiv \frac{m^2}{4\pi\sigma}$ is the parameter that controls the geometric enhancements and $\chi \to 0$ corresponds to the flat domain wall. We used r_0 as a UV cutoff for the integral over r. This is equivalent to

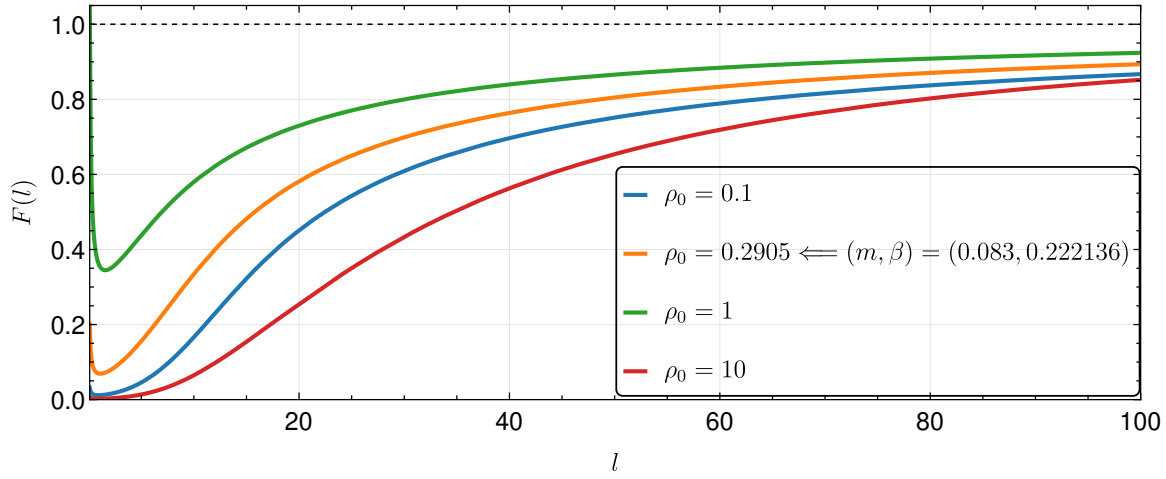


Figure 4.2 Numerical evaluation of $F(l)$ defined in eq. (4.30) for $\rho_0 = 0.1$, 0.2905, 1, 10. Both axes are truncated. The value $\rho_0 = 0.2905$ corresponds to the estimate of r_0 in eq. (4.97) in sec. 4.4; at the corresponding temperature, $ma = 0.083(4)$ with a the lattice spacing.

integrating only over the region where $d^2(r) > 0$.

Finally, we can write

$$\frac{\sigma_{\text{eff}}(L_z) - \sigma}{\sigma} = \lim_{A\to\infty} \frac{\Delta F}{\sigma A} \approx -\lambda^2 \frac{2^\chi \Gamma(\chi)}{8\pi} (mL_z)^\chi e^{-mL_z}\,, \qquad mL_z \gg 1\,, \tag{4.26}$$

where we introduced the renormalized dimensionless coupling

$$\lambda^2 \equiv \lambda_0^2 \frac{m}{\sigma^2} \frac{1}{(mr_0)^{2\chi}}\,. \tag{4.27}$$

As we shall see, this renormalized coupling will show up in other physical observables.

Equation (4.26) is asymptotic. At the values of mL_z accessible in the simulations, the approach to this limit is slow. It is useful to write

$$\frac{\sigma_{\text{eff}}(L_z) - \sigma}{\sigma} \simeq -\lambda^2 \frac{2^\chi \Gamma(\chi)}{8\pi} (mL_z)^\chi e^{-mL_z}\, \mathcal{F}(mL_z), \tag{4.28}$$

with

$$\lim_{\ell\to\infty} \mathcal{F}(\ell) = 1. \tag{4.29}$$

The function $\mathcal{F}$ contains power-law pre-asymptotic corrections from the same convolution integral. These corrections are numerically important and limit the precision with which λ can be extracted from the free energy alone. The approach to this asymptotic value is controlled by power-law corrections in inverse powers of l. Some of these corrections are encoded in eq. (4.23) and give

$$F(l) = \frac{\rho_0^{2\chi}}{\Gamma(1+\chi)(2l)^\chi} \int_{-\infty}^{\infty} dw \frac{e^{-\frac{w^2}{2}}}{\sqrt{2\pi}} \int_{\rho_0}^{\infty} d\rho \frac{\rho}{s} e^{l-s}\,, \qquad s^2 = \rho^2 + \left(l + w\sqrt{4\chi \ln\frac{\rho}{\rho_0}}\right)^2\,, \tag{4.30}$$

with $\rho_0 = mr_0$. The plot of $F(l)$ in fig. 4.2 shows that the asymptotic behaviour $F(l) \approx 1$ only sets in for rather large $l = mL_z \sim 30$.

The effective field theory may also contain an interaction of the form

$$\lambda_2 \int d^2x \sqrt{h} \phi^2(x, \pi(x)) \,. \tag{4.31}$$

The quadratic interaction therefore contributes to the free energy of the wall (see fig. 4.1) as

$$\Delta F \approx -\lambda_2 \int d^2x \left[\left\langle \phi(x,\pi(x))\, \phi(x,\pi(x)) \right\rangle_{L_z} - \left\langle \phi(x,\pi(x))\, \phi(x,\pi(x)) \right\rangle_{\infty} \right] \tag{4.32}$$

$$\approx -2\lambda_2 A G(0,0,L_z) = -A \frac{\lambda_2}{2\pi L_z} e^{-mL_z} \,. \tag{4.33}$$

We see that this is subleading with respect to eq. (4.26) at large L_z (although it has the same exponential dependence).

4.2.4. Particle scattering across the wall

The same coupling controls the low parallel momentum analytic structure of particle scattering off the wall. Consider a bulk particle with momentum decomposed as

$$p = (p_\parallel, p_\perp). \tag{4.34}$$

Parallel momentum is conserved by translation invariance along the wall. For on-shell particles the perpendicular momentum can either be transmitted or reflected,

$$p_\perp^{\text{out}} = p_\perp^{\text{in}} \qquad \text{or} \qquad p_\perp^{\text{out}} = -p_\perp^{\text{in}}. \tag{4.35}$$

Physical on-shell scattering at generic momenta lies outside the strict low-energy worldsheet EFT, but the amplitude is an analytic function of $s = -p^2$.

At leading order in λ_0, the transmission amplitude is

$$T(s) \simeq \lambda_0^2 \int d^2x\, e^{-ip_\parallel \cdot x} \left\langle e^{-ip_\perp [\pi(x) - \pi(0)]} \right\rangle . \tag{4.36}$$

Using the Gaussian variance,

$$\left\langle e^{-ip_\perp [\pi(x) - \pi(0)]} \right\rangle = \exp\left[-\frac{p_\perp^2}{2} d^2(x) \right], \tag{4.37}$$

and analytically continuing to the low-s regime, this gives

$$T(s) \simeq -\lambda^2 \frac{m}{16\pi} \frac{\Gamma(\chi)}{\Gamma(1-\chi)} \left(-\frac{s}{4m^2} \right)^{-\chi - 1}, \qquad |s| \ll m^2. \tag{4.38}$$

The same renormalized coupling λ that controls the finite- L_z correction also controls the low parallel momentum analytic structure of particle-wall scattering, reinforcing the idea that λ is the physical coupling.

The reflection amplitude is more subtle because it is sensitive to the wall's transverse zero mode. If the wall position is fixed or localized, reflection and transmission are generically of comparable size. If the zero mode is integrated over completely, translational averaging cancels the reflection amplitude.

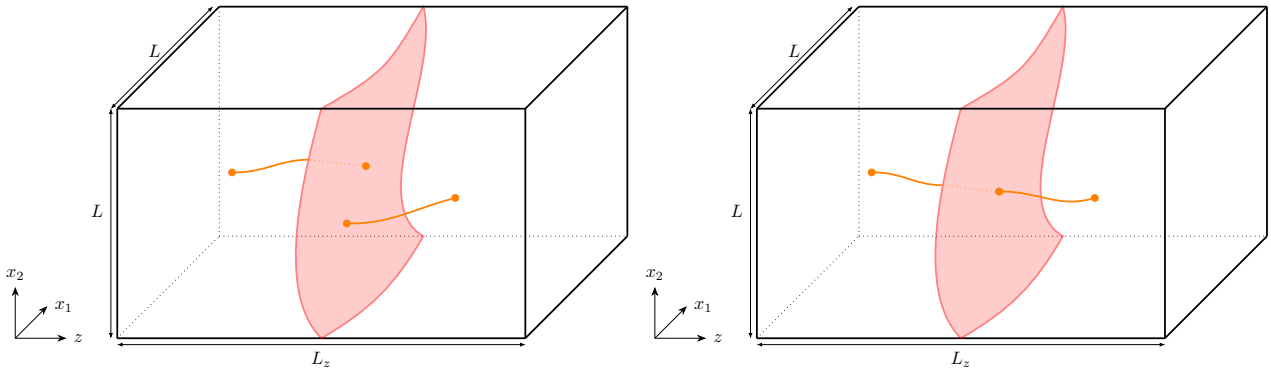


Figure 4.3 Left) diagrams contributing at $\mathcal{O}(\lambda^2)$ to the correction to the 2pt function for the linear coupling in eq. (4.1); right) diagrams contributing at $\mathcal{O}(\lambda_2)$ to the correction to the 2pt function for the quadratic coupling in eq. (4.31). The dots indicate the bulk operator insertions.

4.2.5. Correlation functions in the wall sector

Let us first consider the **one-point** function in the presence of the wall. At leading order in the coupling λ_0, the difference between antiperiodic and periodic boundary conditions is

$$\begin{aligned}\delta\langle\phi\rangle \equiv \langle\phi\rangle_{\rm AP} - \langle\phi\rangle_{\rm P} &= \lambda_0 \int d^2x \big\langle \phi(0)\,\phi(x,\pi(x))\big\rangle \\ &= \lambda_0 \int d^2x \int ds\rho(s) \int \frac{d^3k}{(2\pi)^3}\,\frac{e^{ik_\parallel\cdot x}}{k^2+s}\,\Big\langle e^{ik_\perp\pi(x)}\Big\rangle . \end{aligned} \tag{4.39}$$

The average over the zero mode π_0 of $\pi(x)$ leads to

$$\Big\langle e^{ik_\perp\pi(x)}\Big\rangle = \frac{1}{L_z}\int_0^{L_z} d\pi_0\, e^{-ik_\perp\pi_0}\Big\langle e^{ik_\perp\tilde\pi(x)}\Big\rangle = \frac{2\pi}{L_z}\,\delta(k_\perp)\Big\langle e^{ik_\perp\tilde\pi(x)}\Big\rangle = \frac{2\pi}{L_z}\,\delta(k_\perp)\,, \tag{4.40}$$

where we used $\pi(x) = \pi_0 + \tilde\pi(x)$. Performing the remaining d^2x integral then sets $k_\parallel = 0$, yielding

$$\delta\langle\phi\rangle = \frac{\lambda_0}{L_z}\int \frac{ds}{s}\rho(s)\,. \tag{4.41}$$

Thus, we conclude that the one-point function depends on the full spectral density of the operator, unlike the observables considered above that were dominated by the delta-function $\delta(s-m^2)$ corresponding to an on-shell single-particle state.

We next consider the connected **two-point** function in the wall background. The leading correction involves two insertions of the interaction vertex (see Fig. 4.3) and takes the form

$$\delta\langle\phi(0)\phi(x)\rangle \approx \frac{\lambda_0^2}{2}\int d^2x_1\, d^2x_2\,\big\langle \phi(0)\,\phi(x_1,\pi(x_1))\,\phi(x_2,\pi(x_2))\,\phi(x_\parallel,x_\perp)\big\rangle\,, \tag{4.42}$$

where $\delta\langle\ldots\rangle = \langle\ldots\rangle^{\rm conn}_{\rm AP} - \langle\ldots\rangle^{\rm conn}_{\rm P}$. Using Wick's theorem for the bulk field and keeping only the cross-contractions (linking 0 and x to the worldsheet insertions), the two such contractions cancel the explicit factor of 1/2. Writing the $\langle\phi\phi\rangle$ propagator in Fourier space and using $k = (k_\parallel, k_\perp)$, we

obtain

$$\delta\langle\phi(0)\phi(x)\rangle \approx \lambda_0^2 \int d^2x_1\, d^2x_2 \int ds_1\rho(s_1) \int ds_2\rho(s_2) \times \int \frac{d^3k}{(2\pi)^3}\frac{e^{ik_\parallel\cdot x_1}}{k^2+s_1}\int \frac{d^3k'}{(2\pi)^3}\frac{e^{ik'_\parallel\cdot(x_2-x_\parallel)-ik'_\perp x_\perp}}{(k')^2+s_2}\Big\langle e^{ik_\perp\pi(x_1)}\, e^{ik'_\perp\pi(x_2)}\Big\rangle. \tag{4.43}$$

The branon correlator gives

$$\Big\langle e^{ik_\perp\pi(x_1)}\, e^{ik'_\perp\pi(x_2)}\Big\rangle = \frac{2\pi}{L_z}\delta(k_\perp+k'_\perp)\Big\langle e^{ik_\perp[\pi(x_1)-\pi(x_2)]}\Big\rangle = \frac{2\pi}{L_z}\delta(k_\perp+k'_\perp)e^{-\frac{1}{2}k_\perp^2 d^2(x_1-x_2)}\,, \tag{4.44}$$

where the delta-function follows from averaging over the zero mode of π. It is now convenient to write $x_2 = x_1 + y$ and change to the integration variables y and x_1. Integrating over x_1 produces a delta function enforcing the conservation of parallel momentum,

$$\int d^2x_1\, e^{i(k_\parallel+k'_\parallel)\cdot x_1} = (2\pi)^2\delta^2(k_\parallel+k'_\parallel)\,. \tag{4.45}$$

Thus, we find

$$\delta\langle\phi(0)\phi(x)\rangle \approx \frac{\lambda_0^2}{L_z}\int d^2y \int ds_1\rho(s_1)\int ds_2\rho(s_2) \times \int \frac{d^3k}{(2\pi)^3}\frac{1}{k^2+s_1}\frac{e^{-ik_\parallel\cdot(y-x_\parallel)+ik_\perp x_\perp}}{k^2+s_2}e^{-\frac{1}{2}k_\perp^2 d^2(y)}\,. \tag{4.46}$$

Let us now consider the integral over $d^2k_\parallel$. Recall that the denominator $k^2+s_1 = k_\parallel^2+k_\perp^2+s_1$ and $k_\perp^2+s_1 > m^2$. Therefore, integrating over $k_\parallel$ produces a function of $(y-x_\parallel)^2$ that localizes $(y-x_\parallel)^2 \lesssim 1/m^2$. In practice, we can obtain the leading behaviour of this approximation simply by neglecting $k_\parallel$ in the denominators and using

$$\int \frac{d^2k_\parallel}{(2\pi)^2}e^{-ik_\parallel\cdot(y-x_\parallel)} = \delta^2(y-x_\parallel)\,. \tag{4.47}$$

Performing the integral over the parallel momentum gives

$$\delta\langle\phi(0)\phi(x)\rangle \approx \frac{\lambda_0^2}{L_z}\int ds_1\rho(s_1)\int ds_2\rho(s_2)\int\frac{dk_\perp}{2\pi}\frac{e^{ik_\perp x_\perp-\frac{1}{2}k_\perp^2 d^2(x_\parallel)}}{(k_\perp^2+s_1)(k_\perp^2+s_2)}\,. \tag{4.48}$$

Two limiting regimes are useful. For $md(x_\parallel)\gg 1$ and if $x_\perp$ is not too large, then the $k_\perp$ dependence in the denominator can be neglected, giving

$$\delta\langle\phi(0)\phi(x)\rangle \approx \frac{\lambda_0^2}{L_z}\left[\int\frac{ds}{s}\rho(s)\right]^2\frac{1}{\sqrt{2\pi d^2(x_\parallel)}}\exp\left[-\frac{x_\perp^2}{2d^2(x_\parallel)}\right]\,. \tag{4.49}$$

This regime is not universal, since it depends on the full spectral density of the correlator. For a fixed operator, however, the ratio

$$\frac{\delta\langle\phi(0)\phi(x)\rangle}{[\delta\langle\phi\rangle]^2} \approx \frac{L_z}{\sqrt{2\pi d^2(x_\parallel)}}\exp\left[-\frac{x_\perp^2}{2d^2(x_\parallel)}\right]\,, \tag{4.50}$$

is given by a universal Gaussian in $x_\perp$ with variance given by $d^2(x_\parallel)$.

Secondly, in the regime where $md(x_\parallel)$ is not too large and $1/m \ll |x_\perp| < L_z/2$, the integral over $k_\perp$ is dominated by the pole at $k_\perp^2 = -m^2$ and leads to

$$\delta\langle\phi(0)\phi(x)\rangle \approx \frac{\lambda_0^2}{L_z}\int \frac{dk_\perp}{2\pi}\frac{e^{ik_\perp x_\perp}}{\left(k_\perp^2+m^2\right)^2}e^{-\frac{1}{2}k_\perp^2 d^2(x_\parallel)} \tag{4.51}$$

$$\approx \frac{\lambda_0^2}{4m^2 L_z}e^{-m|x_\perp|}e^{\frac{1}{2}m^2d^2(x_\parallel)}|x_\perp|\,. \tag{4.52}$$

The validity of this approximation requires that $m|x_\perp| \gg m^2d^2(x_\parallel)$ so that the second exponential is a small correction to the first one. Notice that this is equivalent to $m|x_\perp| \ll \frac{x_\perp^2}{2d^2(x_\parallel)}$ which means that this approximation is valid when the prediction from eq. (4.49) is (exponentially) smaller. Finally, we can write

$$\delta\langle\phi(0)\phi(x)\rangle \approx \frac{\lambda^2 m}{64\pi^2\chi^2}\left(m|x_\parallel|\right)^{2\chi}\frac{|x_\perp|}{L_z}e^{-m|x_\perp|}\,, \qquad |x_\perp| \gg md^2(x_\parallel) \gg \frac{1}{m}\,, \tag{4.53}$$

where we used the effective coupling eq. (4.27). This is the third observable that is controlled by the coupling λ.

It is instructive to rederive the last formula without using Fourier space. We start from

$$\delta\langle\phi(0)\phi(x)\rangle \approx \lambda_0^2\int d^2x_1\,d^2x_2\,\left\langle\frac{e^{-m\sqrt{x_1^2+\pi(x_1)^2}}}{4\pi\sqrt{x_1^2+\pi(x_1)^2}}\frac{e^{-m\sqrt{(x_2-x_\parallel)^2+(x_\perp-\pi(x_2))^2}}}{4\pi\sqrt{(x_2-x_\parallel)^2+(x_\perp-\pi(x_2))^2}}\right\rangle\,, \tag{4.54}$$

where we assumed that $0 < \pi(x_1), \pi(x_2) < x_\perp$ and that the ϕ propagator is dominated by its large-distance behaviour. This approximation requires $m\pi(x_1) \gg 1$ and $m(x_\perp - \pi(x_1)) \gg 1$. In this case, the integral over x_1 is dominated by small values of x_1 and the integral over x_2 is dominated by x_2 close to $x_\parallel$. Therefore, we expand the square roots to the leading order in the denominator and keep a subleading term in the exponent,

$$\delta\langle\phi(0)\phi(x)\rangle \approx \lambda_0^2\int d^2x_1\,d^2x_2\,\left\langle\frac{e^{-m\pi(x_1)-m\frac{x_1^2}{2\pi(x_1)}}}{4\pi\,\pi(x_1)}\frac{e^{-m(x_\perp-\pi(x_2))-m\frac{(x_2-x_\parallel)^2}{2(x_\perp-\pi(x_2))}}}{4\pi(x_\perp-\pi(x_2))}\right\rangle\,. \tag{4.55}$$

Now we perform the Gaussian integrals over x_1 and x_2 assuming that $\pi(x_1) \approx \pi(0)$ and $\pi(x_2) \approx \pi(x_\parallel)$. This leads to

$$\delta\langle\phi(0)\phi(x)\rangle \approx \frac{\lambda_0^2}{4m^2}e^{-mx_\perp}\langle e^{-m(\pi(0)-\pi(x_\parallel))}\rangle \approx \frac{\lambda_0^2}{4m^2}e^{-mx_\perp}e^{\frac{1}{2}m^2d^2(x_\parallel)}\frac{x_\perp}{L_z}\,, \tag{4.56}$$

where we included the factor $x_\perp/L_z$ that represents the probability of the zero mode being between 0 and $x_\perp$ as we assumed. This matches precisely eq. (4.52) for $x_\perp > 0$.

4.2.6. Flux tube profile

In numerical studies of flux-tube profiles, one probes the flux tube by measuring the expectation value of a local bulk operator in the presence of two Polyakov loops. For a scalar operator $\mathcal{O}$, usually taken

to be $\mathrm{Tr}(F^2)$, the standard observable is

$$\rho_{\mathcal{O}}(x) = \frac{\langle P^\dagger P \mathcal{O}(x)\rangle}{\langle P^\dagger P\rangle} - \langle \mathcal{O}(x)\rangle\,. \tag{4.57}$$

Here $\rho_{\mathcal{O}}(x)$ is interpreted as the flux-tube profile. More precisely, one considers two straight Polyakov loops separated by a distance R. In the confining phase, the flux tube has a worldsheet bounded by the two Polyakov loops. The local operator is usually inserted at equal distance from the two loops, so that its position is characterized by the transverse distance y from the plane containing them. This type of observable has recently been studied in several complementary settings, including holographic large N constructions, compact QED_3, and lattice simulations of $2+1$-dimensional gauge theories [2–6].

We now compute the analogue of this observable in the EFT description of a fluctuating extended object. In the domain-wall setup the corresponding quantity is

$$\rho_{\mathcal{O}}(x) = \langle \mathcal{O}(x)\rangle_{\mathrm{AP}} - \langle \mathcal{O}(x)\rangle_{\mathrm{P}}\,. \tag{4.58}$$

If the wall zero mode is integrated over, this gives the correction to the integrated one point function discussed previously. To obtain a transverse profile, instead, the center of mass of the wall must be fixed. The EFT then computes the expectation value of the bulk operator at a fixed transverse distance from the fluctuating wall. Writing

$$\pi(z) = \pi_0 + \widetilde{\pi}(z), \qquad \langle \widetilde{\pi}(z)\rangle = 0, \tag{4.59}$$

and setting $\pi_0 = 0$, the leading contribution is

$$\rho_{\mathcal{O}}(x_\parallel, x_\perp) = \lambda_{\mathcal{O}} \int_\Sigma d^2z\, \left\langle G_{\mathcal{O}}\left(x_\parallel - z, x_\perp - \widetilde{\pi}(z)\right)\right\rangle_{\widetilde{\pi}} + O(\lambda_{\mathcal{O}}^2), \tag{4.60}$$

where $G_{\mathcal{O}}$ is the connected bulk two-point function of $\mathcal{O}$. Using the spectral representation of $G_{\mathcal{O}}$ and taking the wall to be infinitely extended, the integral over the worldsheet sets $k_\parallel = 0$. Therefore

$$\rho_{\mathcal{O}}(x_\perp) = \lambda_{\mathcal{O}} \int_0^\infty ds\, \rho_{\mathcal{O}}(s) \int \frac{dk_\perp}{2\pi}\, \frac{e^{ik_\perp x_\perp}}{k_\perp^2 + s} \exp\left[-\frac{k_\perp^2}{2}\left\langle \widetilde{\pi}(0)^2\right\rangle\right] + O(\lambda_{\mathcal{O}}^2). \tag{4.61}$$

Let us define

$$\left\langle \widetilde{\pi}(0)^2\right\rangle \equiv \Delta = \frac{C}{2\pi\sigma}. \tag{4.62}$$

Here C is a UV-sensitive dimensionless parameter as it depends both on the microscopic realization of the domain wall and on the microscopic operator used to probe it.

The transverse profile is therefore controlled by the smeared one-dimensional kernel

$$K(x; s, \Delta) = \int_{-\infty}^{\infty} \frac{dk}{2\pi}\, \frac{e^{ikx} e^{-\Delta k^2/2}}{k^2 + s}. \tag{4.63}$$

For $s > 0$ and $\Delta > 0$, this integral can be evaluated exactly:

$$K(x; s, \Delta) = \frac{e^{s\Delta/2}}{4\sqrt{s}} \left[e^{-\sqrt{s}|x|}\,\mathrm{erfc}\left(\sqrt{\frac{s\Delta}{2}} - \frac{|x|}{\sqrt{2\Delta}}\right) + e^{\sqrt{s}|x|}\,\mathrm{erfc}\left(\sqrt{\frac{s\Delta}{2}} + \frac{|x|}{\sqrt{2\Delta}}\right)\right]. \tag{4.64}$$

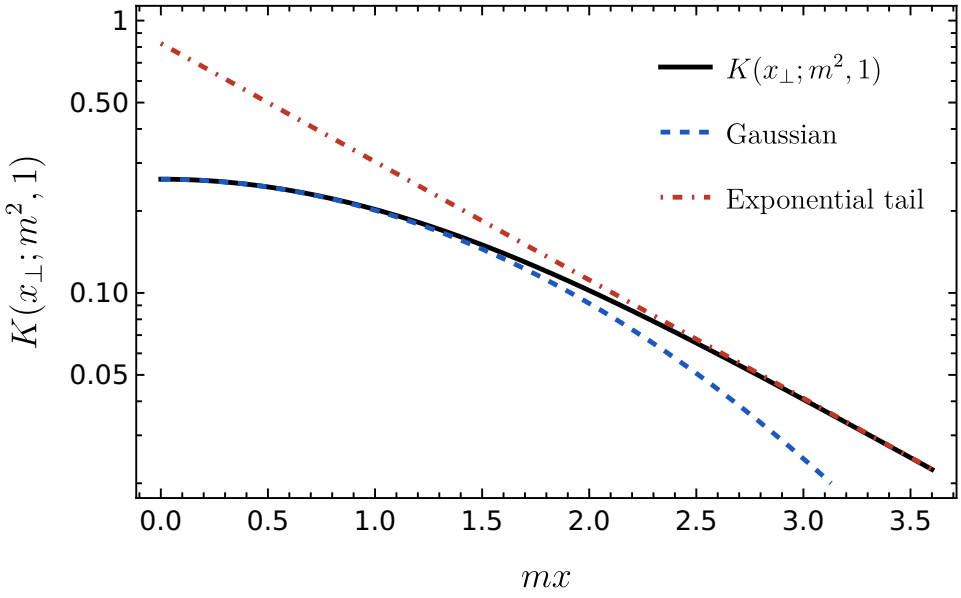


Figure 4.4 Single-pole transverse profile obtained from the exact kernel $K(x_\perp; m^2, 1)$. The resulting profile closely resembles those obtained in flux-tube profile studies [3, 4].

Thus, to leading order in the wall-bulk coupling,

$$\rho_{\mathcal{O}}(x_\perp) = \lambda_{\mathcal{O}} \int_0^\infty ds\, \rho_{\mathcal{O}}(s)\, K(x_\perp; s, \Delta) + O(\lambda_{\mathcal{O}}^2). \tag{4.65}$$

In the single-pole approximation, $\rho_{\mathcal{O}}(s)$ is replaced by the overlap with the lightest scalar state times $\delta(s - m^2)$, and the full transverse profile is simply proportional to $K(x_\perp; m^2, \Delta)$. For $\Delta = 1$, the profile shown in fig. 4.4 interpolates between a Gaussian at short distances and an exponential tail.

At large transverse separation,

$$K(x; s, \Delta) \sim \frac{e^{s\Delta/2}}{2\sqrt{s}}\, e^{-\sqrt{s}|x|}, \qquad |x| \gg \sqrt{\Delta}. \tag{4.66}$$

The exponential decay length is therefore fixed by the bulk mass scale $m = \sqrt{s}$, while the wall fluctuations only modify the normalization by the factor $e^{s\Delta/2}$, yielding

$$\rho_{\mathcal{O}}(x_\perp) \simeq \lambda_{\mathcal{O}} \frac{e^{-m|x_\perp|}}{2m} e^{\chi C}. \tag{4.67}$$

For an open flux tube of length R, the same formula gives

$$\langle \phi(0, y) \rangle_{\text{Pol}} - \langle \phi \rangle \simeq -\frac{\lambda_0}{2m} e^{-m|y|} e^{\frac{1}{2}m^2 \langle \pi^2(0) \rangle} = \text{const}\, R^\chi e^{-m|y|}, \tag{4.68}$$

where we used $\langle \pi^2(0) \rangle \simeq (2\pi\sigma)^{-1} \log(R/R_0)$ for the central variance of the flux tube [7, 8]. The scale R_0 is UV-sensitive and differs from r_0 in eq. (4.14) because it also receives contributions from the boundaries set by the Polyakov loops. Thus, while the EFT predicts the same exponential decay rate set by the bulk mass m, it also predicts a nontrivial enhancement of the amplitude with the Polyakov-loop separation, proportional to R^χ.

The Gaussian approximation obtained by matching $K(0)$ and $K''(0)$ is

$$K_{\mathrm{G}}(x) = K(0)\exp\left[-\frac{x^2}{2w^2}\right]. \tag{4.69}$$

with

$$K(0) = \frac{e^{s\Delta/2}}{2\sqrt{s}}\ \mathrm{erfc}\left(\sqrt{\frac{s\Delta}{2}}\right), \tag{4.70}$$

and

$$w^2 = \frac{K(0)}{\dfrac{1}{\sqrt{2\pi\Delta}} - sK(0)}. \tag{4.71}$$

Only in the limit $s\Delta \gg 1$ does this reduce to the naive smeared form

$$K_{\mathrm{G}}(x) \simeq \frac{1}{s\sqrt{2\pi\Delta}}\exp\left[-\frac{x^2}{2\Delta}\right]. \tag{4.72}$$

Let us now estimate the distance at which the profile crosses over from the Gaussian core to the exponential tail, in the single-pole regime, by comparing the logarithmic derivatives

$$\frac{d}{dx}\log K_{\mathrm{G}}(x) = -\frac{x}{w^2}, \qquad \frac{d}{dx}\log K_{\exp}(x) = -m. \tag{4.73}$$

Equating the two slopes gives

$$x_* = mw^2 = m\,\frac{K(0)}{\dfrac{1}{\sqrt{2\pi\Delta}} - m^2K(0)}. \tag{4.74}$$

The estimate x_* characterizes a crossover rather than a sharp transition. The exact kernel is smooth, and its logarithmic derivative approaches $-m$ only asymptotically. At small $s\Delta \ll 1$, $x_\star \sim \sqrt{\Delta\pi/2}$, while at large $s\Delta \gg 1$, $x_\star \sim \Delta\sqrt{s}$.

4.3. Geometric approximation for Ising correlators

The EFT construction above treats the wall as a fluctuating surface coupled to a continuum bulk field. For the Monte Carlo observables, in particular the $\mathbb{Z}_2$-odd observables that lie outside the EFT above, it is useful to formulate a complementary geometric thin-wall description. We then apply it to $\mathbb{Z}_2$-even correlators and recover the short-range Gaussian behaviour obtained in subsec. 4.2.5.

4.3.1. $\mathbb{Z}_2$-odd operators

In the ordered phase, far from the wall, the spin approaches

$$s \to \pm\langle s\rangle_{\mathrm{P}}, \tag{4.75}$$

with the sign determined by the magnetized domain. In the antiperiodic sector, which includes the sum over the wall zero mode,

$$\langle s\rangle_{\mathrm{AP}} = 0, \tag{4.76}$$

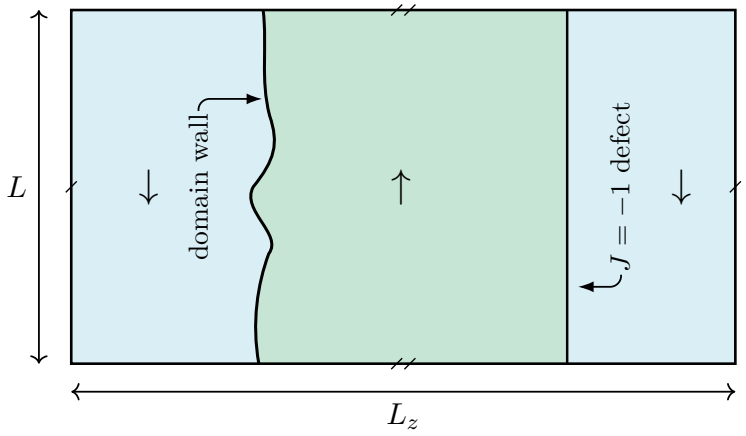


Figure 4.5 Schematic representation of a cut at fixed x (equivalently, at fixed y). Due to the periodic boundary conditions, the spins change sign at two locations: at the $J = -1$ defect and at the domain wall. In the text, as is customary, we will often refer to the former simply as the antiperiodic boundary condition, although here it is shown explicitly. The figure depicts only one possible simplified spin configuration, since all spins could be reversed, and clusters, which are typically present near the critical point, have been omitted for clarity. Only the domain wall carries a local excess of energy.

because a fixed point is equally likely to lie on either side of the fluctuating wall.

There are two surfaces at which the spin changes sign, see fig. 4.5. The first is the topological defect used to implement the antiperiodic boundary condition, namely the plane of flipped bonds. Its position is conventional. The second is the physical domain wall. We therefore use the defect-transported spin correlator defined in eq. (2.40), which removes the convention-dependent sign associated with the chosen representative of the $\mathbb{Z}_2$ twist.

At long distances, G_s^{def} reduces to $\langle s\rangle^2$ times the sign that records whether the two insertions lie in the same magnetized domain for a given wall configuration. Let

$$w = \pi(x_\parallel) - \pi(0). \tag{4.77}$$

Since the correlator is an ensemble average over wall configurations, its geometric prediction is obtained by averaging this configuration-dependent sign over the fluctuating wall. Averaging first over the zero mode $\pi(0)$, at fixed relative displacement w, gives

$$\big\langle \mathrm{sgn}\big(x_\perp - \pi(x_\parallel)\big)\mathrm{sgn}\big(-\pi(0)\big)\big\rangle_{\pi(0)} = \frac{L_z - 2|w - x_\perp|}{L_z}, \qquad |w - x_\perp| \le \frac{L_z}{2}. \tag{4.78}$$

The EST prediction is that the relative displacement w is Gaussian with variance $d^2(x_\parallel)$. Therefore

$$G_s^{\mathrm{def}}(x) = \langle s\rangle^2 \int dw\, \frac{\exp[-w^2/(2d^2(x_\parallel))]}{\sqrt{2\pi d^2(x_\parallel)}}\, \frac{L_z - 2|w - x_\perp|}{L_z}. \tag{4.79}$$

When $L_z \gg d(L/2)$, the integration range can be extended to the real line, yielding

$$\frac{G_s^{\mathrm{def}}(x)}{\langle s\rangle^2} \simeq 1 - \frac{2d(x_\parallel)}{L_z} f\left(\frac{|x_\perp|}{d(x_\parallel)}\right), \tag{4.80}$$

where

$$f(y) = y\,\mathrm{erf}\left(\frac{y}{\sqrt{2}}\right) + \sqrt{\frac{2}{\pi}}\,e^{-y^2/2}. \tag{4.81}$$

Equation (4.81) is a kinematic prediction of the rough-wall description and is independent of microscopic parameters apart from those entering $\langle \pi(x)\,\pi(0)\rangle$.

4.3.2. $\mathbb{Z}_2$-even operators

For $\mathbb{Z}_2$-even operators the defect plane does not induce a sign change. The representative case is the energy density ϵ. In the thin-wall description the wall-induced part of the energy density is localized near the wall core. For a fixed wall configuration, write

$$p_\epsilon\big(x_\perp - \pi(x_\parallel)\big) \equiv \langle \epsilon(x)\rangle_\pi - \langle\epsilon\rangle_{\mathrm{P}}, \tag{4.82}$$

the energy profile and define the corresponding integrated wall-core strength

$$T_\epsilon \equiv \int dx_\perp\, p_\epsilon(x_\perp). \tag{4.83}$$

By translational invariance in the antiperiodic sector, the one-point difference is the volume average of the profile,

$$\delta\langle\epsilon\rangle \equiv \langle\epsilon\rangle_{\mathrm{AP}} - \langle\epsilon\rangle_{\mathrm{P}} = \frac{T_\epsilon}{L_z}, \tag{4.84}$$

inspiring the identification

$$T_\epsilon = \lambda \int ds \frac{\rho(s)}{s}. \tag{4.85}$$

The relation factorizes the integrated profile into the wall-bulk coupling λ and an operator-dependent spectral integral. The coupling λ characterizes the interaction of the fluctuating wall with the bulk field, whereas the integral over $\rho(s)$ depends on the full spectral density of the operator and is therefore sensitive to its microscopic definition. Consequently, the integrated profile T_ϵ is not determined by λ alone. In particular, unlike observables dominated at long distances by the isolated one-particle pole at $s = m^2$, the one-point function receives contributions from the full spectral density and is generally UV sensitive. What is universal in eq. (4.84) is instead the kinematic $1/L_z$ dependence arising from delocalization of the wall zero mode.

For two-point functions, define the wall-induced connected difference

$$\delta G_\epsilon(x) \equiv \langle\epsilon(0)\epsilon(x)\rangle^{\mathrm{conn}}_{\mathrm{AP}} - \langle\epsilon(0)\epsilon(x)\rangle^{\mathrm{conn}}_{\mathrm{P}}. \tag{4.86}$$

In the thin-wall picture, the leading contribution comes from configurations in which both operator insertions overlap with the wall core. Using the same Gaussian approximation for the relative wall displacement,

$$\delta G_\epsilon(x) = \int dw\, \frac{e^{-w^2/(2d^2(x_\parallel))}}{\sqrt{2\pi d^2(x_\parallel)}} \int_0^{L_z} \frac{dz}{L_z}\, p_\epsilon(-z)\, p_\epsilon(x_\perp - z - w). \tag{4.87}$$

If the wall wandering is large compared with the wall thickness, $L_z \gg d(x_\parallel) \gg \xi = m^{-1}$, then the

profile can be replaced by its integrated strength, and

$$\delta G_\epsilon(x) \simeq \frac{T_\epsilon^2}{L_z} \frac{1}{\sqrt{2\pi d^2(x_\parallel)}} \exp\left[-\frac{x_\perp^2}{2d^2(x_\parallel)}\right]. \tag{4.88}$$

The same Gaussian broadening appears in the EFT expression in eq. (4.49). Again, the normalization is non-universal, but the transverse shape and its variance are fixed by wall fluctuations.

4.4. Monte Carlo simulations of domain walls in 3D Ising

The MC simulations use the setup described in Chapter 2, the Wolff algorithm described in subsec. 2.3.2 and the method for measuring correlation functions described in subsec. 2.5.3. We simulate lattices of volume $V = L^2 \times L_z$ in the symmetry-broken phase ($T < T_c$).

4.4.1. One-point functions

As discussed in subsec. 4.2.5, the wall-induced one-point shift is not universal. It depends on the chosen lattice discretization through the delta residue and through UV-sensitive contributions in the spectral density $\tilde{\rho}$. Using the lattice-to-continuum matching derived in subsec. 2.5.2, the overlap of the lattice energy operator with the lightest bulk state scales as

$$\mathcal{N}_\epsilon^2 \sim a(ma)^{2\Delta_\epsilon - 1} \sim a\, t^{\nu(2\Delta_\epsilon - 1)} \sim a\, t^{1.1498549(4)}, \tag{4.89}$$

using the values quoted in [9]. The numerical results are summarized in app. C.4; we find $\mathcal{N}_\epsilon(t) = 5.7(4)\sqrt{a}\, t^{0.56(1)}$.

A similar scaling estimate applies to the wall-core strength. The wall profile $p_\epsilon(x_\perp)$ is controlled by the same scaling dimension Δ_ϵ and, near criticality, takes the form $p_\epsilon(x_\perp) \sim (a/\xi)^{\Delta_\epsilon} h(x_\perp/\xi)$ with a universal scaling function h. Integrating over $x_\perp$ therefore gives $\mathcal{T}_{\rm lat} \equiv \int dx_\perp\, p_\epsilon(x_\perp) \sim a(\xi/a)^{1-\Delta_\epsilon}$, i.e.

$$\mathcal{T}_{\rm lat}(t) \sim a\, t^{\nu(\Delta_\epsilon - 1)} = a\, t^{0.26\ldots}, \tag{4.90}$$

again up to a non-universal prefactor and scaling corrections.

We then define the dimensionless combination

$$\tilde{\lambda}_0 \equiv \frac{\sqrt{m}\mathcal{T}_\epsilon^{\rm lat}}{\mathcal{N}_\epsilon} \sim t^0, \tag{4.91}$$

that remains finite when $t \to 0$.

We measure $\delta\langle\epsilon\rangle$ defined in eqs. (4.84) and (4.41), and convert it to $\tilde{\lambda}_0$ using eq. (4.91). Figure 4.6 plots $\tilde{\lambda}_0$ as a function of $\min(L, L_z)/\xi(t)$ for several transverse sizes L_z and wall areas $A = L^2$, so that the onset of finite-size effects is expressed directly in units of the bulk correlation length.

The data show that the leading L_z dependence of the one-point function is the kinematic factor $1/L_z$ predicted by eqs. (4.84) and (4.41). After this factor is removed through the definition of $\tilde{\lambda}_0$, the remaining variation with L_z is comparable to the error bars. In other words, the dominant transverse-size dependence is accounted for by zero-mode delocalization.

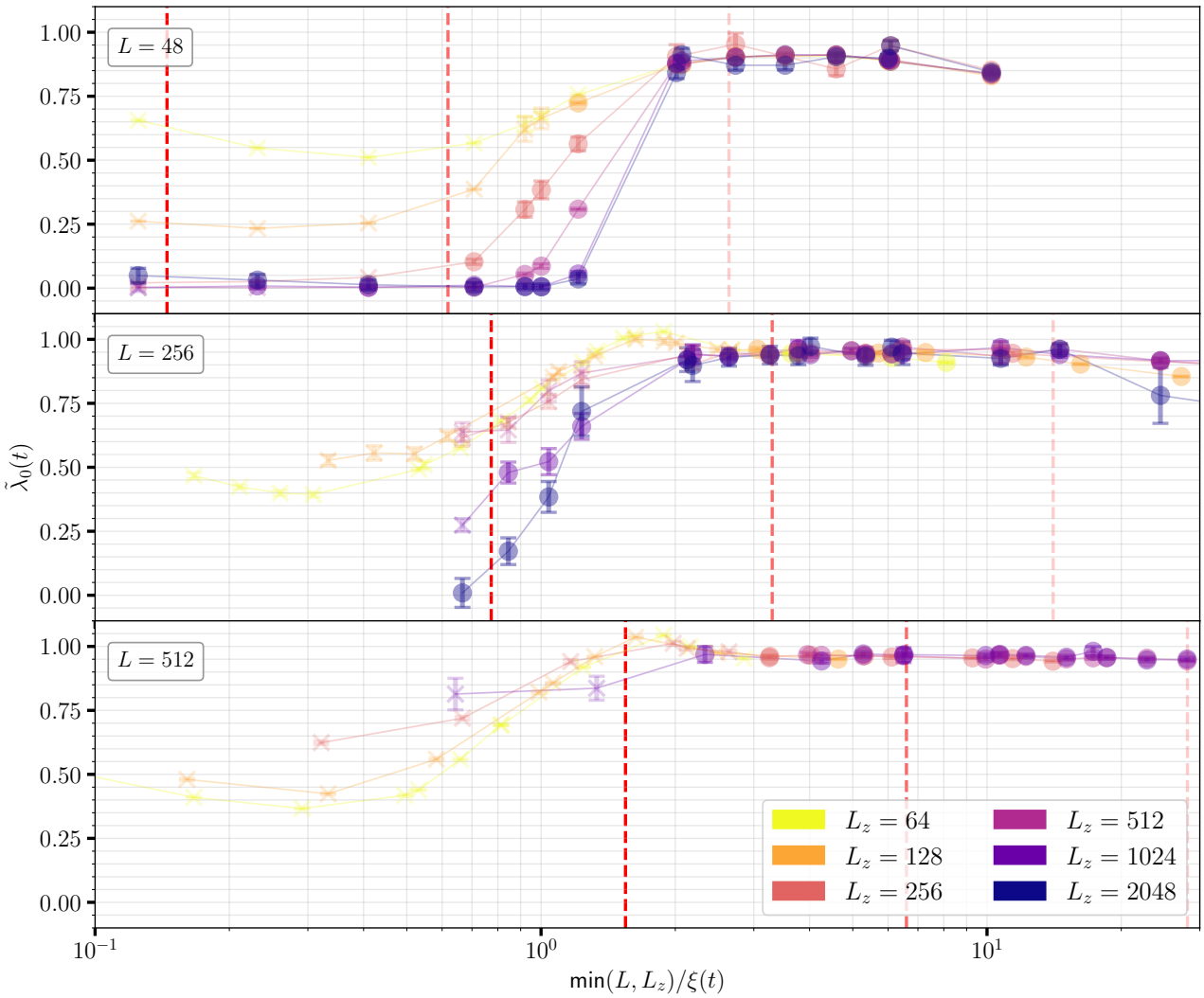


Figure 4.6 $\tilde{\lambda}_0$ extracted from the wall-induced one-point function, plotted against $\min(L, L_z)/\xi(t)$ for several domain-wall areas $A = L^2$ (panels) and transverse sizes L_z (colors). Crosses mark data with $L_z < 3\xi$, where transverse finite-size effects are expected. Vertical dashed lines indicate the reference locations corresponding to $t = 10^{-4}, 10^{-3}, 10^{-2}$ under the identification $\min(L, L_z) = L$, and are included only to provide a rough sense of the distance from criticality.

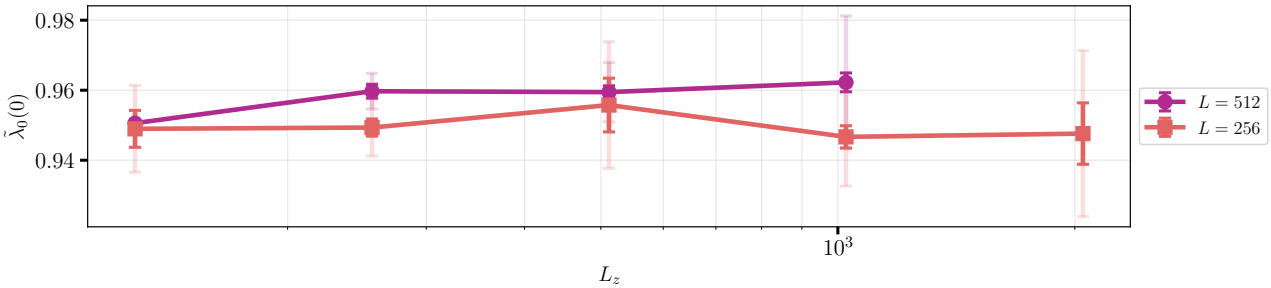


Figure 4.7 Volume dependence of $\tilde{\lambda}_0(0)$ (with $V = L^2 L_z$), obtained by averaging $\tilde{\lambda}_0(t)$ over the interval defined in the text. Dark error bars: statistical uncertainty of the average. Light error bars: max-min spread of $\tilde{\lambda}_0(t)$ over the averaging window. $L = 48$ is excluded because the interval is empty.

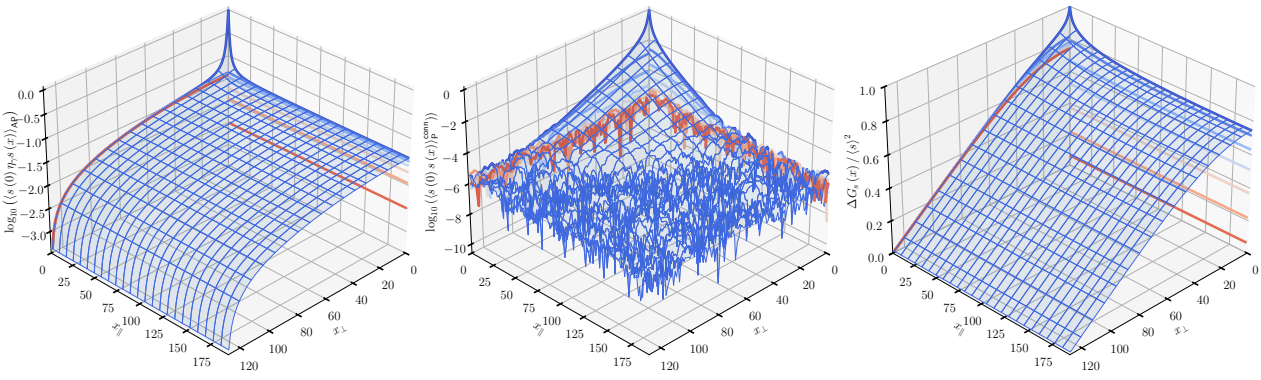


Figure 4.8 Spin-sector correlators at $\beta = 0.222136$ on $V = 384^2 \times 256$, shown as functions of $x = (x_\parallel, x_\perp)$ in log10 scale. Left: $\langle s(0)\,\eta_\gamma\,s(x)\rangle_{AP}$ defined in eq. (2.40). Middle: $\langle s(0)s(x)\rangle_{\mathrm{P}}^{\mathrm{conn}}$. Right: $\Delta G_s(x)$. Vertical planes show fixed-$x_\perp$ (or fixed-$x_\parallel$) slices of the surface.

As ξ becomes comparable to L, $\tilde{\lambda}_0$ decreases and eventually becomes consistent with zero. This is expected. Once $\sigma L^2 \sim 1$, the domain wall melts and the distinction between the antiperiodic and periodic sectors is washed out. Accessing the scaling regime therefore requires both $\sigma L^2 \gg 1$ and $mL_z \gg 1$.

In Chapter 3 we found that higher-derivative EST corrections are small once $\sigma A \gtrsim 30$. As a reference, at $t = 7 \times 10^{-3}$ (where $\xi \simeq 6$) one finds $\sigma A \simeq 4, 123, 492$ for $L = 48, 256, 512$, respectively; we therefore exclude $L = 48$ from the analysis. For $L = 256$ and $L = 512$, the lower end of the fitting window is set by $\sigma A \simeq 30$, corresponding to $t \simeq 1.6 \times 10^{-3}$ and $t \simeq 5.6 \times 10^{-4}$.

Fitting the largest volumes, $L = 512$ and $L_z \in [512, 1024]$, to $\tilde{\lambda}_0(t) = C\,t^{\alpha}$ over the interval $t \in [t_{\sigma A=30},\, t_{\xi=6}]$, with $t_{\xi=6} = 7 \times 10^{-3}$ and $L_z \gtrsim 3\xi$, we find α statistically consistent with zero. The analogous fit for the integrated wall-core amplitude gives

$$\mathcal{T}_\epsilon^{\mathrm{lat}}(t) = 2.6(2)\,t^{0.25(2)}, \tag{4.92}$$

in agreement with the scaling expected from eq. (4.90).

Finally, fig. 4.7 shows $\tilde{\lambda}_0$ averaged over this temperature window for each geometry. The dominant residual dependence is on the wall area, while the remaining L_z dependence is comparable to the error bars.

4.4.2. Two-point functions

We focus on $\beta = 0.222136$ ($\xi \sim 12$) and $V = 384^2 \times 256$. The qualitative behaviour is unchanged across our datasets provided $L, L_z \gg \xi \gg a$. We restrict to separations along the wall in a single direction, denoted $x_\parallel$.

4.4.2.1. $\mathbb{Z}_2$-odd operators

Eq. (4.80) predicts the shape of the normalized correlator difference $\Delta G_s(x)/\langle s\rangle^2$. For fixed $x_\parallel$ and $|x_\perp| \gg d(x_\parallel)$, it becomes approximately linear in $|x_\perp|$, and it vanishes at $|x_\perp| = L_z/2$. This behaviour is visible in the right panel of fig. 4.8.

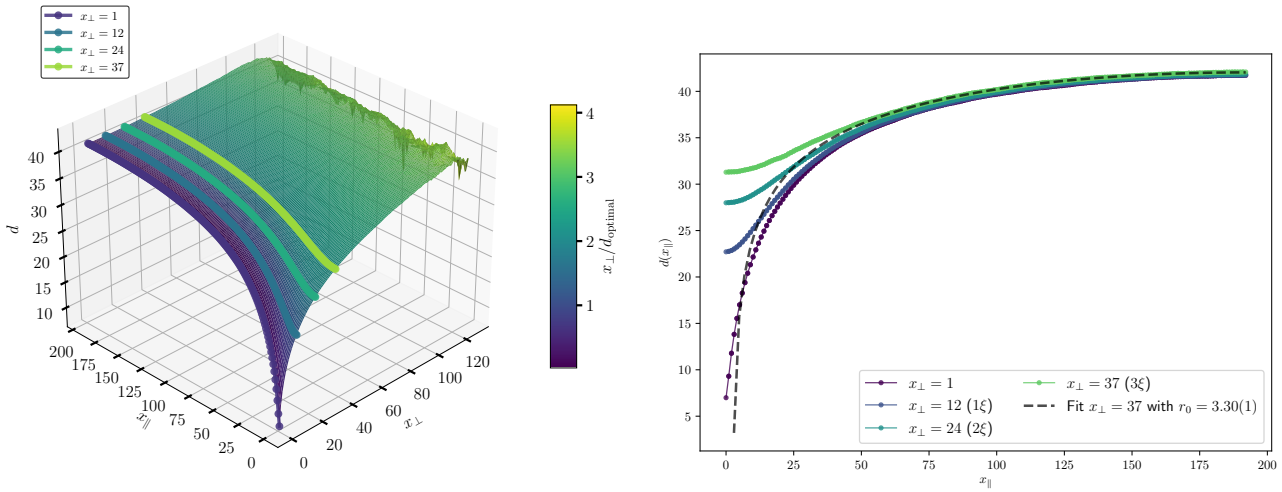


Figure 4.9 Extraction of the wall variance from the odd-sector correlator. Left: $d(x_\parallel, x_\perp)$ obtained by solving eq. (4.93) pointwise in $(x_\parallel, x_\perp)$. The highlighted curves are the fixed-$x_\perp$ slices shown in the right panel. Right: $d^2(x_\parallel)$ at selected transverse positions $x_\perp$ compared to the free massless-boson prediction on a torus, eq. (4.95); the fit determines the UV scale r_0 in eq. (4.97).

To extract $d(x_\parallel, x_\perp)$, we solve

$$\frac{\Delta G_s(x)}{\langle s\rangle^2} = 1 - \frac{2\,d(x_\parallel, x_\perp)}{L_z}\, f\!\left(\frac{|x_\perp|}{d(x_\parallel, x_\perp)}\right), \tag{4.93}$$

for $d(x_\parallel, x_\perp)$ for each value of $(x_\parallel, x_\perp)$. The results are shown in fig. 4.9. In the regime $L_z \gg |x_\perp|$ and $L_z \gg d(L/2)$, the extracted $d(x_\parallel, x_\perp)$ is only mildly dependent on $x_\perp$.

We compare the measured variance d to the free massless-boson prediction on a finite torus. We define $d^2(x_\parallel) \equiv \langle(\pi(x_\parallel) - \pi(0))^2\rangle$ by expanding the square and using point splitting,

$$d_L^2(x_\parallel) \equiv 2 \lim_{y\to 0}\left[\langle\pi(y)\pi(0)\rangle - \langle\pi(x_\parallel)\pi(0)\rangle + \frac{\alpha'}{2}\ln\frac{y^2}{r_0^2}\right]. \tag{4.94}$$

The logarithm subtracts the universal short-distance singularity of the free boson propagator, while the non-universal length scale r_0 parametrizes the remaining finite additive constant.

Using the free boson Green function on a torus [10], one obtains

$$d_L^2(x_\parallel) = 2\alpha' \ln\left[\frac{L}{\pi r_0}\left|\frac{\vartheta_1\!\left(\frac{\pi x_\parallel}{L}|q\right)}{\vartheta_1'(0|q)}\right|\right], \qquad q = e^{-\pi}, \qquad \alpha' = \frac{1}{2\pi\sigma}. \tag{4.95}$$

For fixed $x_\parallel$ and $L \to \infty$, this reduces to

$$d_L^2(x_\parallel) = 2\alpha' \ln\frac{|x_\parallel|}{r_0} + O\!\left(\frac{x_\parallel^2}{L^2}\right). \tag{4.96}$$

The dashed line in fig. 4.9 is obtained by fitting r_0 using $x_\parallel > 150$; the fit remains consistent down to

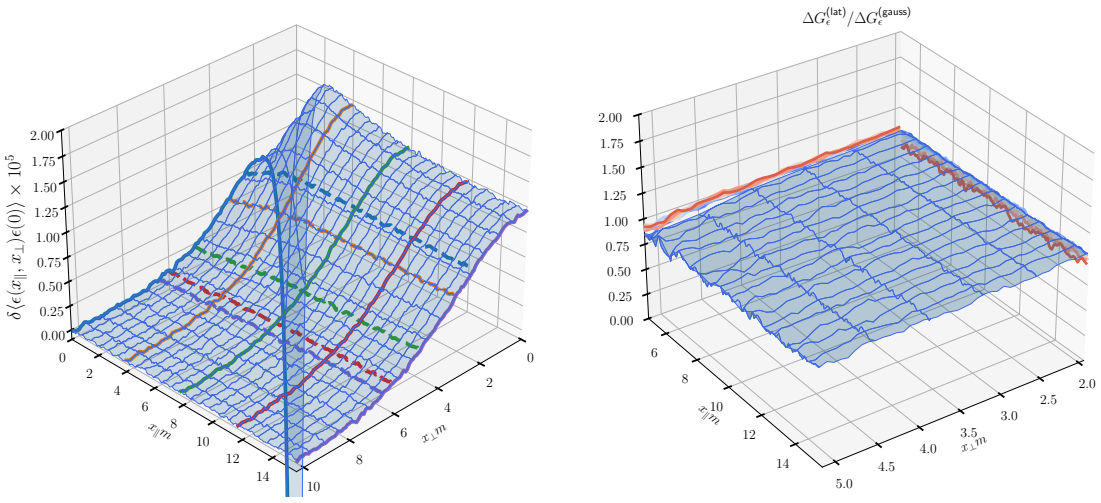


Figure 4.10 Even-sector energy correlator difference at $\beta = 0.222136$ on $V = 384^2 \times 256$. Left: $\Delta G_\epsilon(x) \equiv \langle\epsilon(0)\epsilon(x)\rangle^{\mathrm{conn}}_{\mathrm{AP}} - \langle\epsilon(0)\epsilon(x)\rangle^{\mathrm{conn}}_{\mathrm{P}}$. Solid lines denote the fixed-$x_\parallel$ cuts shown in left panel of fig. 4.11, while dashed lines denote the fixed-$x_\perp$ cuts shown in the left panel of fig. 4.12. Right: Comparison between MC data and the Gaussian prediction in eq. (4.88) and (4.50) for $x_\perp \in [2\xi, L_z/4]$ and $x_\parallel \gtrsim 5\xi$.

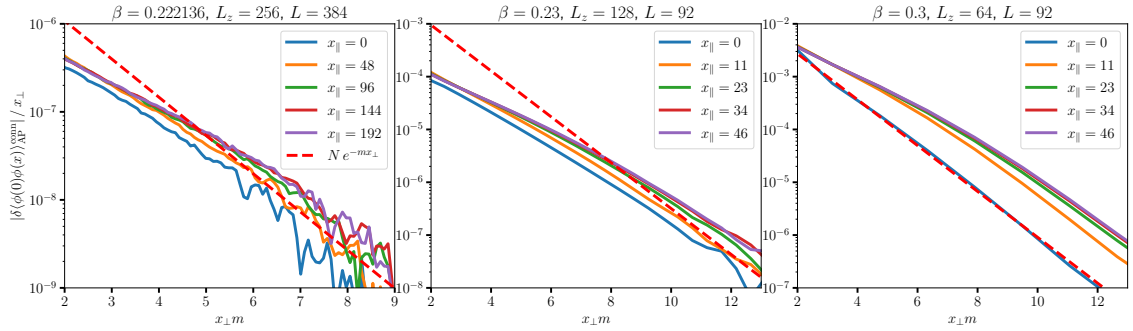


Figure 4.11 Long-distance regime of the even-sector correlator difference. We plot $|\delta\langle\epsilon(0)\epsilon(x_\parallel, x_\perp)\rangle|/|x_\perp|$ as a function of $m x_\perp$ for several $x_\parallel$ (legend) at the indicated β and volumes. Dashed lines show a reference exponential $\propto e^{-m x_\perp}$.

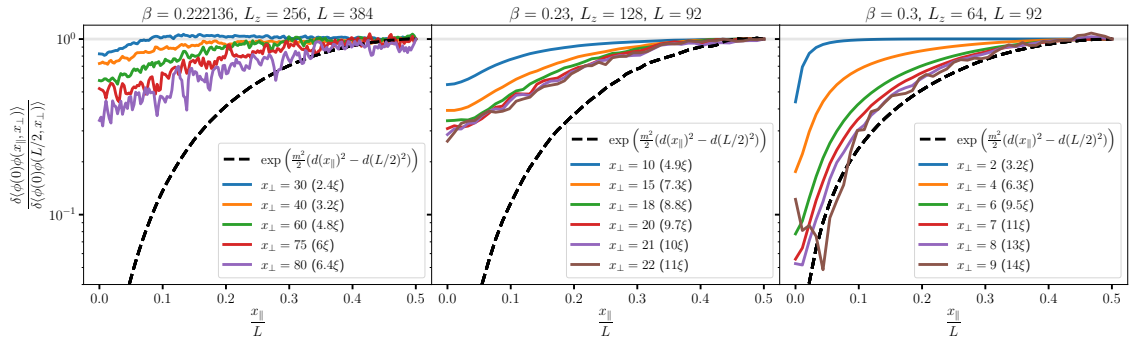


Figure 4.12 Test of the predicted $x_\parallel$ dependence in the long-distance regime. We plot $\delta\langle\epsilon(0)\epsilon(x_\parallel, x_\perp)\rangle/\delta\langle\epsilon(0)\epsilon(L/2, x_\perp)\rangle$ as a function of $x_\parallel/L$ for several $x_\perp$ (legend), at the indicated β and volumes. Dashed lines show the prediction for the $d^2(x_\parallel)$ extracted from the spin 2pt functions.

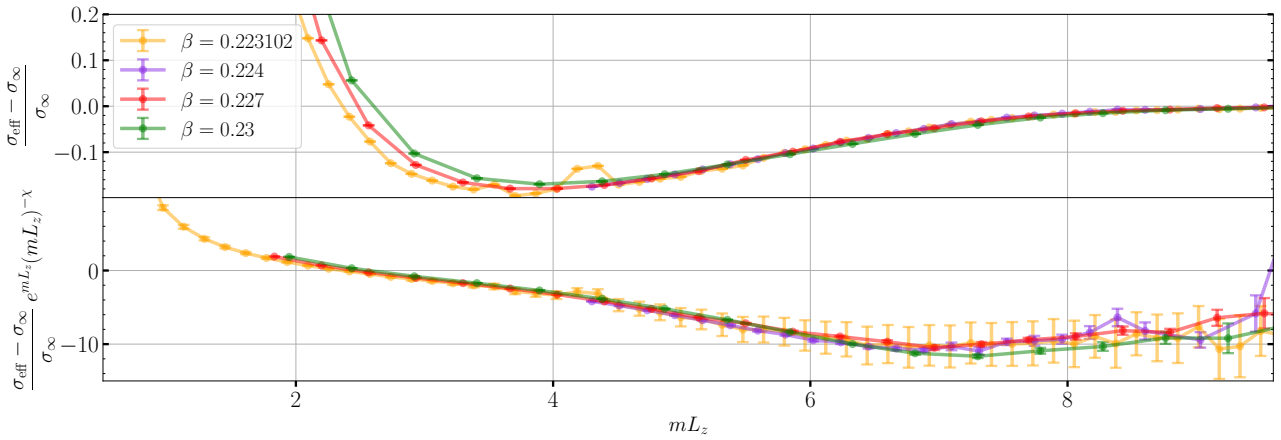


Figure 4.13 Finite-L_z shift of the effective string tension. Top: Monte Carlo data for $(\sigma_{\rm eff}(L_z) - \sigma_\infty)/\sigma_\infty$ at the indicated values of β. Bottom: the same data rescaled by $e^{mL_z}(mL_z)^{-\chi}$, with $\chi = m^2/(4\pi\sigma)$. For $mL_z \gtrsim 3$, the shift is negative and approximately follows the predicted leading dependence $-(mL_z)^\chi e^{-mL_z}$, while the residual drift in the lower panel shows that sizable pre-asymptotic corrections remain.

$|x_\parallel| \sim 50 \approx 4\xi$. For selected $x_\perp$ we obtain

$$r_0\big|_{x_\perp=1}^{V=384^2\times256} = 3.50(1)a, \qquad r_0\big|_{x_\perp=\xi}^{V=384^2\times256} = 3.49(1)a, \qquad r_0\big|_{x_\perp=2\xi}^{V=384^2\times256} = 3.43(1)a. \tag{4.97}$$

4.4.2.2. $\mathbb{Z}_2$-even operators

The left panel of fig. 4.10 shows $\Delta G_\epsilon(x_\parallel, x_\perp)$, i.e. the even-sector correlator difference (equivalently $\delta\langle\epsilon(0)\epsilon(x)\rangle$). The Gaussian profile predicted by the nearby-regime expression eq. (4.88) and (4.50) is visible in the fixed-$x_\parallel$ transverse slices shown in that panel: as a function of $x_\perp$, the correction is approximately Gaussian. To test this quantitatively, the right panel shows the ratio of the Monte Carlo data to the prediction of eqs. (4.88) and (4.50), so that agreement with the Gaussian form appears as a plateau near 1. The ratio remains close to 1 for $x_\perp \lesssim 5\xi \sim 60$ over the measured range of $x_\parallel$.

Fig. 4.11 compares $\delta\langle\epsilon(0)\epsilon(x)\rangle/|x_\perp|$ to the exponential falloff at large $x_\perp$ predicted by eq. (4.52). The overall coefficient is not extracted because the predicted $x_\parallel$ dependence cannot be cleanly resolved, as shown in fig. 4.12, where we plot

$$\frac{\delta\langle\epsilon(0)\epsilon(x_\parallel, x_\perp)}{\delta\langle\epsilon(0)\epsilon(L/2, x_\perp)} \approx e^{-\frac{1}{2}m^2\left(d^2(L/2) - d^2(x_\parallel)\right)}, \tag{4.98}$$

for several values of $x_\perp$. The decrease with $x_\perp$ is suggestive, but larger $x_\perp$ is required for a quantitative test. The dataset at $\beta = 0.3$ is closer to the predicted behaviour; however, despite being below the roughening transition, $\beta_c^{\rm R} = 0.40754(4)$ [11, 12], discretization effects are not under control there.

4.4.3. Free energies

We finally consider the finite-L_z dependence of the effective string tension. The free-energy difference is measured using the extended-ensemble flat-histogram method described in subsec. 2.4.2. We jointly

sample the spin configuration s and the plane coupling J, which interpolates between the periodic $J = 1$ and antiperiodic $J = -1$ sectors. The resulting reconstructed free energy gives directly

$$\Delta F_{\mathbb{Z}_2} = F(-1) - F(1) = -\log\left(\frac{Z_{\mathrm{AP}}}{Z_{\mathrm{P}}}\right) \tag{4.99}$$

The estimator gives the free-energy difference without reconstructing it from L_z derivatives or separately bulk-subtracted free energies.

A quantitative test of the asymptotic prediction is beyond the precision currently available for two reasons. First, the signal itself is exponentially small in the regime $mL_z \gg 1$ in which the asymptotic formula is derived. Second, even within the EFT, the approach to that regime is slow, as encoded in the pre-asymptotic factor $F(mL_z)$ introduced in eq. (4.28). The purpose of the present analysis is therefore limited. We ask whether the sign, scale, and qualitative L_z dependence of the Monte Carlo data are consistent with the predicted large L_z behaviour, but we do not attempt to extract λ from these data.

Figure 4.13 shows the Monte Carlo determination of

$$\frac{\sigma_{\mathrm{eff}}(L_z) - \sigma_\infty}{\sigma_\infty} \tag{4.100}$$

for four values of β, in the range where the extrapolation to infinite wall area is under control. Here σ_∞ denotes the large L_z limit of the effective string tension at fixed temperature. For $mL_z \gtrsim 3$, the shift is negative, as expected from the prediction of subsec. 4.2.3. Moreover, when plotted as a function of the scaling variable mL_z, the data for different β approximately collapse onto a common curve. This is consistent with the expectation that the leading dependence is governed by the universal combination $(mL_z)^\chi e^{-mL_z}$, with

$$\chi = \frac{m^2}{4\pi\sigma}\,. \tag{4.101}$$

The lower panel of fig. 4.13 shows the same data rescaled by the leading asymptotic kinematic factor,

$$e^{mL_z}(mL_z)^{-\chi}\,\frac{\sigma_{\mathrm{eff}}(L_z) - \sigma_\infty}{\sigma_\infty}\,. \tag{4.102}$$

If the asymptotic regime were already reached, this quantity would approach a constant proportional to $-\lambda^2$. Instead, the residual drift remains significant throughout the accessible range. This is expected. As already indicated by the numerical evaluation of the pre-asymptotic function $F(l)$ in subsec. 4.2.3, the convergence to the asymptotic form is slow. For the representative value of r_0 extracted from the two-point analysis, one finds $F(mL_z) \simeq 0.7$ even at $mL_z \simeq 30$. Sizeable corrections are therefore still present in the region accessible to the Monte Carlo simulation. Sufficient statistical precision to isolate λ would require reducing the present errors on σ_{eff} by many orders of magnitude — well beyond what is accessible with current simulation methods. At present, the free-energy observable is best viewed as supporting the sign and leading kinematic structure of the EFT prediction, but not as an independent precision probe of the coupling.

References

[1] J. M. Viana Parente Lopes, José Matos, and Joao Penedones. *Effective Strings and Particles Interacting in 3D: The Ising Model*. Apr. 9, 2026. DOI: 10.48550/arXiv.2604.08670. arXiv: 2604.08670 [hep-th].

[2] Michele Caselle, Elia Cellini, Alessandro Nada, Dario Panfalone, and Lorenzo Verzichelli. "Intrinsic Width of the Flux Tube as a Tool to Explore Confining Mechanisms in Lattice Gauge Theories." Jan. 2026. arXiv: 2601.19520 [hep-lat].

[3] Tommaso Canneti. "Flux Tube Profile from Holography: Finite Size and Strong Coupling Corrections." In: *JHEP* 04 (2026), p. 002. DOI: 10.1007/JHEP04(2026)002. arXiv: 2510.02442 [hep-th].

[4] Ofer Aharony, Netanel Barel, and Tal Sheaffer. *Effective Strings in QED_3*. Feb. 18, 2025. DOI: 10.48550/arXiv.2412.01313. arXiv: 2412.01313 [hep-th].

[5] Lorenzo Verzichelli, Michele Caselle, Elia Cellini, Alessandro Nada, and Dario Panfalone. "Intrinsic Width of the Flux Tube in 2+1 Dimensional Yang-Mills Theories." In: *42th International Symposium on Lattice Field Theory*. Mar. 2026. arXiv: 2603.05323 [hep-lat].

[6] Lorenzo Verzichelli, Michele Caselle, Elia Cellini, Alessandro Nada, and Dario Panfalone. "Intrinsic Width of the Flux Tube in 2+1 Dimensional Yang-Mills Theories." In: *PoS* LATTICE2024 (2025), p. 403. DOI: 10.22323/1.466.0403. arXiv: 2501.01740 [hep-lat].

[7] M. Luscher, G. Munster, and P. Weisz. "How Thick Are Chromoelectric Flux Tubes?" In: *Nuclear Physics B* 180 (1981), pp. 1–12. DOI: 10.1016/0550-3213(81)90151-6.

[8] M. Caselle, F. Gliozzi, Ulrika Magnea, and S. Vinti. "Width of Long Color Flux Tubes in Lattice Gauge Systems." In: *Nuclear Physics B* 460 (1996), pp. 397–412. DOI: 10.1016/0550-3213(95)00639-7. arXiv: hep-lat/9510019.

[9] Cyuan-Han Chang et al. "Bootstrapping the 3d Ising Stress Tensor." In: *Journal of High Energy Physics* 2025.3 (Mar. 18, 2025), p. 136. ISSN: 1029-8479. DOI: 10.1007/JHEP03(2025)136.

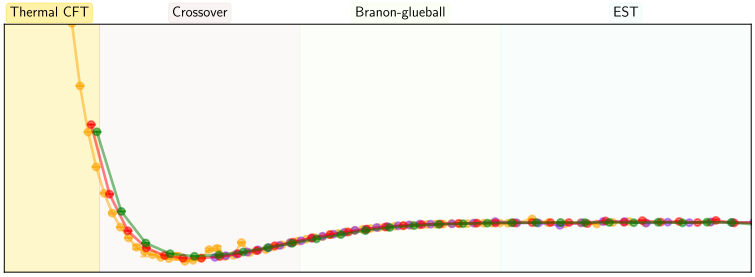
[10] Joseph Polchinski. *String Theory: Volume 1: An Introduction to the Bosonic String*. Vol. 1. Cambridge Monographs on Mathematical Physics. Cambridge: Cambridge University Press, 1998. ISBN: 978-0-521-63303-1. DOI: 10.1017/CBO9780511816079.

[11] M. Hasenbusch, S. Meyer, and M. Putz. "The Roughening Transition of the 3-D Ising Interface: A Monte Carlo Study." In: *Journal of Statistical Physics* 85 (1996), p. 383. DOI: 10.1007/BF02174211. arXiv: hep-lat/9601011.

[12] K. K. Mon, D. P. Landau, and D. Stauffer. "Interface Roughening in the Three-Dimensional Ising Model." In: *Physical Review B* 42.1 (July 1990), pp. 545–547. DOI: 10.1103/PhysRevB.42.545.

Chapter 5

Twisted Sectors in the thermal 3D Ising CFT



The preceding chapters studied the $\mathbb{Z}_2$-twisted sector in the ordered phase, where it is dominated at large volume by a fluctuating domain wall. At bulk criticality, the wall tension vanishes and the same twisted/untwisted partition-function ratio becomes a universal finite-volume observable of the 3D Ising CFT. This chapter is based on [1], where we study the universal information contained in this critical sector ratio.

5.1. Summary

Partition-function ratios between distinct global sectors are finite-volume observables of a lattice theory. At criticality they become symmetry-resolved compactification data of the underlying CFT. When the sector is defined by a global-symmetry twist, the ratio measures the response of the theory to a background symmetry holonomy, or equivalently to an invertible symmetry defect wrapping a non-contractible cycle. In this chapter we study such a sector ratio in the 3D Ising universality class. The simulations are performed on $T_L^2 \times S^1_{L_z}$. We study two limiting channels: the slab limit $R^2 \times S^1_{L_z}$ and the transverse-torus channel $T_L^2 \times R$. The two sectors are the untwisted periodic sector and the $\mathbb{Z}_2$-twisted antiperiodic sector.

We measure the twisted-sector free-energy difference using the extended-ensemble flat-histogram method described in subsec. 2.4.2. The plane coupling J interpolates between the periodic $J = 1$ and antiperiodic $J = -1$ sectors, and the reconstructed endpoint difference gives

$$\Delta F_{\mathbb{Z}_2} = F(-1) - F(1) = -\log\left(\frac{Z_{\mathrm{AP}}}{Z_{\mathrm{P}}}\right). \tag{5.1}$$

Thus, the sector free-energy difference is obtained directly, without separately determining the two partition functions.

We use this estimator to measure the symmetry-twisted free-energy difference in the 3D Ising slab at bulk criticality, and extract the corresponding thermodynamic Casimir difference directly, without bulk subtractions or numerical differentiation in L_z. Its output is nevertheless a sector difference, not an absolute thermodynamic Casimir amplitude. In each sector, the universal finite-volume part of the critical free energy is

$$f_\alpha(t, L_z) = L_z f_{\mathrm{bulk}}(t) + L_z^{-2}\Theta_\alpha(x), \qquad x = tL_z^{1/\nu}, \tag{5.2}$$

where α labels the boundary condition or global sector and Θ_α is universal [2–4]. The free-energy density difference then defines a symmetry-twisted thermodynamic Casimir difference $\Theta_\alpha(x) - \Theta_\beta(x)$. Extracting either absolute amplitude requires independent input for the other sector.

The 3D Ising universality class provides a useful benchmark for these strategies because several thermodynamic Casimir amplitudes and scaling functions are already known to high precision. Monte Carlo studies, often using improved realizations such as the Blume-Capel model, have determined $\Theta_\alpha(x)$ and the critical amplitudes $C_\alpha \equiv \Theta_\alpha(0)$ for several boundary conditions, including symmetry-breaking and ordinary/free surface universality classes. Periodic systems and slab corrections to scaling have also been studied numerically [5–11].

In the slab channel, the large-volume and large-aspect-ratio extrapolation gives the symmetry-twisted thermodynamic Casimir difference $\Delta_{\mathbb{Z}_2} = 0.327(2)$. The approach to this limit determines the thermal screening mass through the dimensionless combination $\kappa_{\mathrm{eff}} = m_{\mathrm{scr}} L_z = 0.71(4)$. In the opposite channel, where the transfer matrix acts on states quantized on the transverse torus, the same data isolate the lowest $\mathbb{Z}_2$-odd gap, giving $\kappa_\sigma = 1.230(3)$. Thus the sector ratio gives the Casimir difference in the slab limit, while its finite aspect-ratio corrections give selective access to symmetry-resolved finite-volume data.

An additional advantage of the sector difference is that it can suppress subleading corrections that would be present in the individual sectors. In the data analyzed here, some expected corrections are numerically unresolved, allowing the surviving finite-volume structures to be isolated more clearly.

Sec. 5.2 defines the twisted-sector free energy, its thermodynamic-limit density, and the expected critical corrections. Sec. 5.3.1 benchmarks the estimator in the critical two-dimensional Ising model. Sec. 5.3.2 gives the 3D result.

5.2. Twisted-sector free energy and scaling

Consider the 3D Ising model on $M = \mathbb{R}^2_{x,y} \times S^1_{L_z}$. A $\mathbb{Z}_2$ twist (AP sector) is implemented by inserting the global symmetry operator along the compact direction. The untwisted sector is denoted by P. On $\mathbb{R}^2 \times \mathbb{R}$ the corresponding defect plane can be removed by a spin flip on one side. On $\mathbb{R}^2 \times S^1_{L_z}$ it wraps a non-contractible cycle and defines a distinct global sector.

Hamiltonian quantization along z gives

$$Z_{\mathrm{P}} = \mathrm{Tr}_{\mathcal{H}}\big(e^{-L_z H}\big)\,, \qquad Z_{\mathrm{AP}} = \mathrm{Tr}_{\mathcal{H}}\big(S e^{-L_z H}\big)\,, \tag{5.3}$$

where S is the operator implementing the $\mathbb{Z}_2$ symmetry. We define

$$\Delta F_{\mathbb{Z}_2}(L_z) \equiv -\log\left(\frac{Z_{\mathrm{AP}}}{Z_{\mathrm{P}}}\right). \tag{5.4}$$

Its thermodynamic-limit free energy *per unit transverse area* is denoted by

$$\Delta f_{\mathbb{Z}_2}(L_z) \equiv \lim_{A\to\infty} \frac{\Delta F_{\mathbb{Z}_2}(L_z, A)}{A}, \tag{5.5}$$

where A denotes the transverse area, $A = L^2$ for the square defect used in the numerical simulations.

5.2.1. Scaling at criticality and corrections to scaling

Introduce a plane coupling J interpolating between the endpoint sectors: $J = 1$ is untwisted and $J = -1$ is $\mathbb{Z}_2$ twisted. For $F_J(L_z) \equiv -\log Z_J(L_z)$, differentiation with respect to L_z gives

$$\frac{\partial F_J}{\partial L_z} = \langle H \rangle_J. \tag{5.6}$$

On $M = \mathbb{R}^2 \times S^1_{L_z}$, transverse translations and rotations imply that the response to changing L_z is governed by the normal stress tensor,

$$\langle H \rangle_J = A \langle T_{zz} \rangle_J \qquad \Longrightarrow \qquad \frac{\partial}{\partial L_z}\left(\frac{F_J}{A}\right) = \langle T_{zz} \rangle_J. \tag{5.7}$$

At criticality, finite-size scaling gives the free energy per unit area as

$$f(J, L_z) = L_z f_{\mathrm{bulk}} + \frac{C_J}{L_z^2} + \sum_i \frac{\alpha_i(J)}{L_z^{2+\omega_i}} + \sum_{n\geq 1} \frac{\beta_n(J)}{L_z^{2+2n}} + \sum_m \frac{\gamma_m(J)}{L_z^{\hat{\Delta}_m}}, \tag{5.8}$$

where f_{bulk} is the J-independent bulk free-energy density per unit volume. C_J is the thermodynamic Casimir. The first sum runs over bulk irrelevant scalars with RG exponents $\omega_i > 0$. The second contains analytic corrections allowed by the symmetries, starting at L_z^{-4} in f (or L_z^{-5} in $\langle T_{zz} \rangle$). The

last sum would contain defect-local irrelevant operators; for example, a displacement operator with $\Delta = 3$ [12] would contribute as L_z^{-4} to $\langle T_{zz} \rangle$.

In our case and at the endpoint values $J = \pm 1$, the continuum partition functions are eq. (5.3), namely the untwisted and symmetry-twisted traces of the same bulk Hamiltonian. In the continuum, this endpoint sector is described by a global $\mathbb{Z}_2$ holonomy, equivalently by an invertible topological $\mathbb{Z}_2$ symmetry defect, or by a background $\mathbb{Z}_2$ gauge field for the ordinary 0-form symmetry with non-trivial holonomy along $S^1_{L_z}$ [13, 14]. Since this defect is topological, it does not carry a spectrum of defect-local irrelevant perturbations. The corrections retained below are therefore bulk irrelevant and analytic corrections associated with the lattice realization of the critical theory.

The sector free-energy density difference then takes the form

$$\Delta f_{\mathbb{Z}_2}(L_z) \equiv f(-1, L_z) - f(1, L_z) = \frac{1}{L_z^2} \left[\Delta_{\mathbb{Z}_2} + \sum_i \delta\alpha_i L_z^{-\omega_i} + \sum_{n \geq 1} \delta\beta_n L_z^{-2n} \right], \tag{5.9}$$

where $\Delta_{\mathbb{Z}_2} \equiv C_{-1} - C_1$ is the Casimir difference, not a conformal dimension, and $\delta\alpha_i, \delta\beta_n$ denote sector differences. In the 3D Ising class the leading bulk scalar correction is

$$\Delta f_{\mathbb{Z}_2}(L_z) = \Delta_{\mathbb{Z}_2} L_z^{-2} + \delta\alpha_1 L_z^{-2-\omega_1} + \mathcal{O}\left(L_z^{-4}\right), \tag{5.10}$$

with $\omega_1 = 0.82951(61)$ obtained with navigator-based numerical bootstrap [15]. The next irrelevant operator has $\omega_2 = 3.8956(43)$ obtained using extremal functionals [16].

5.3. Monte Carlo method and results

The Monte Carlo setup used in this chapter is the same as in Chapter 3. The microscopic model and flat-histogram bias construction are described in Chapter 2, so we do not repeat them here. The simulation may benefit from repeated visits to each bin; the reader probably does not.

5.3.1. Two-dimensional benchmark

Before the 3D analysis, we test the estimator where the answer is known: the critical two-dimensional Ising model on a torus of size $L \times L_z$, periodic along L and $\mathbb{Z}_2$-twisted along L_z. The theoretical predictions for this two-dimensional benchmark are reviewed in app. B.

Since the transverse direction is one-dimensional, we normalize the free-energy difference per unit length,

$$\Delta f_{\mathbb{Z}_2}(L_z, L) \equiv \frac{F_{\mathrm{AP}}(L, L_z) - F_{\mathrm{P}}(L, L_z)}{L}. \tag{5.11}$$

The critical two-dimensional theory gives, for $L \to \infty$ at fixed L_z,

$$\Delta f(L_z) = \frac{\pi}{4 L_z}, \tag{5.12}$$

so $\Delta f(L_z, L) L_z$ approaches $\pi/4$, up to finite-volume corrections at large q, which, for each L, corresponds to small L_z. This expectation is tested in fig. 5.1, where we plot $\Delta f(L_z, L)\, L_z$ for transverse sizes $L = 32, \ldots, 2048$. The data form a broad plateau near $\pi/4$.

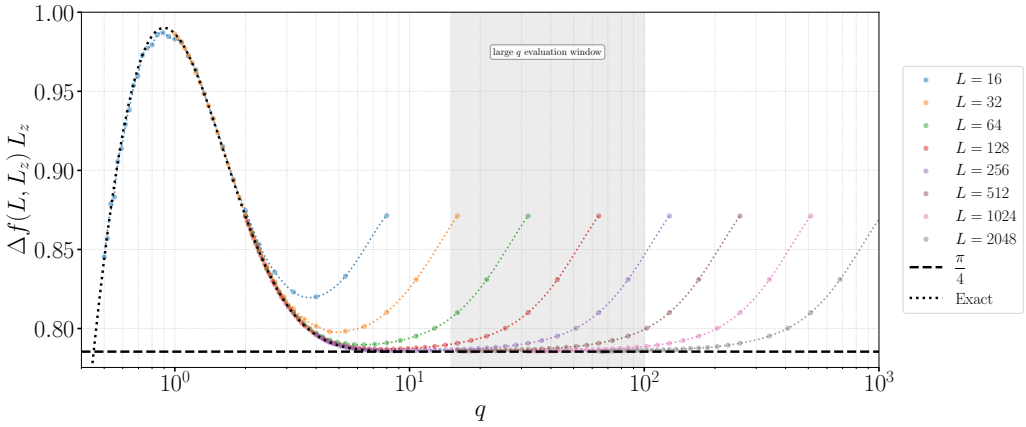


Figure 5.1 Two-dimensional benchmark of the flat-histogram estimator. The dimensionless difference $L_z \Delta f_{\mathbb{Z}_2}(L, L_z)$ is plotted against $q = L/L_z$ for several transverse sizes L. The dashed line is the conformal result $L_z \Delta f_{\mathbb{Z}_2} \to \pi/4$ at $q, L_z \to \infty$. The black dotted curve is the exact Ising torus result from the Jacobi-theta representation of the Virasoro characters [17]. Dashed curves are cubic interpolations in q at fixed L. The gray band marks the large-q window used below, to study finite-L effects. The deviations at small L_z/large-q are the lattice and finite-volume corrections discussed in the text.

5.3.1.1. Finite-volume corrections

Finite-volume corrections are discussed in app. B.1. With $q \equiv L/L_z$ and $t \equiv e^{-\pi q/4}$, the double asymptotic form is

$$\begin{aligned} L_z \Delta f_{\mathbb{Z}_2}(q, L_z) = & \frac{\pi}{4} + \frac{a_2}{L_z^2} + \frac{a_4}{L_z^4} + \mathcal{O}\left(L_z^{-6}\right) \\ & + \frac{1}{q}\left[t - \frac{1}{2}t^2 - \frac{5}{3}t^3\right] + \mathcal{O}\left(q^{-1}t^4\right) \\ & + \mathcal{O}\left(q^{-1}tL_z^{-2}\right), \end{aligned}$$

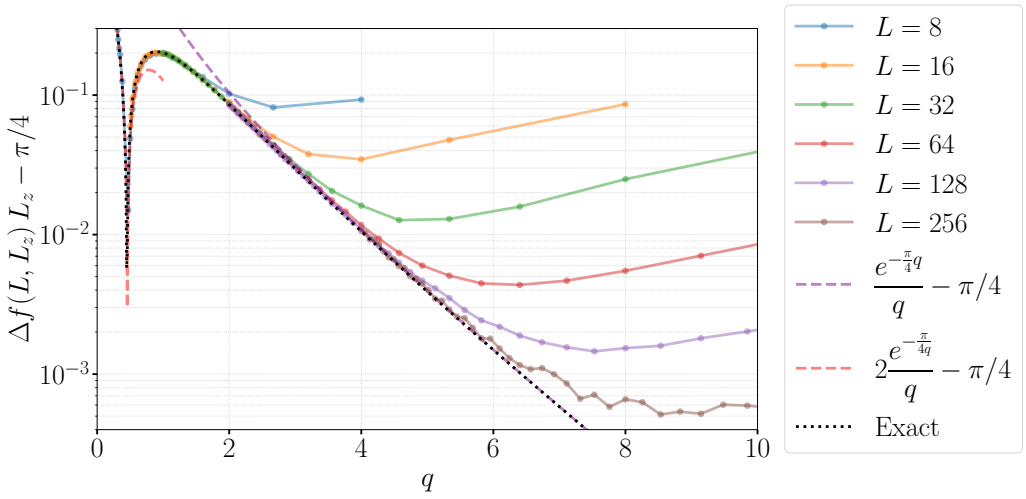


Figure 5.2 Finite-q corrections in the two-dimensional benchmark. The plot shows $L_z \Delta f_{\mathbb{Z}_2}(L, L_z) - \pi/4$ versus $q = L/L_z$. The dashed curves are the leading large-q and small-q exponential approximations. The exponential regime is visible only after the small-L_z lattice corrections are controlled.

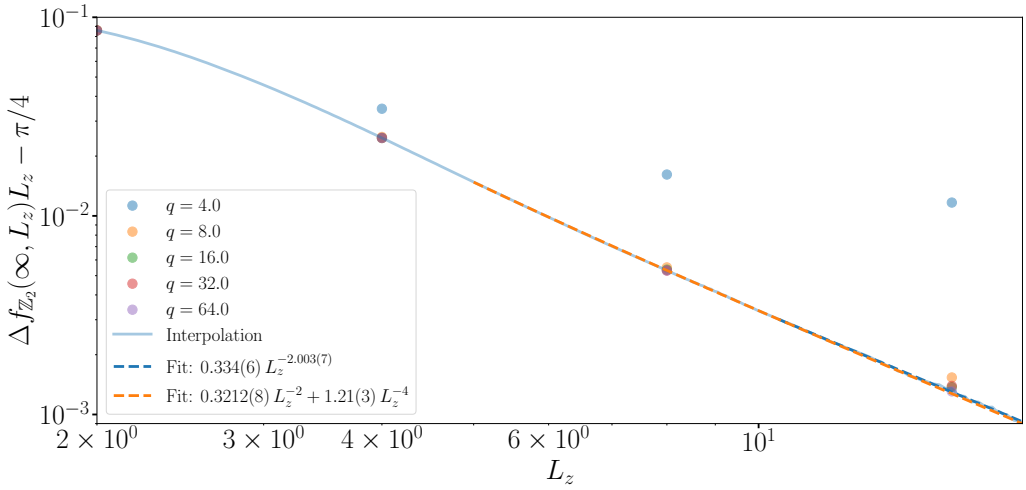


Figure 5.3 Large-q extrapolation at fixed L_z. For each $q \in [16, 100]$, the interpolation is evaluated and plotted versus L_z, as a single data set. This range makes exponential finite-q corrections negligible, as indicated by fig. 5.2. Raw data at aspect ratios with at least four values of L_z are also shown. The convergence from $q = 4$ to $q = 8$ and the stability at $q \gtrsim 16$ indicate that the interpolation is in the asymptotic regime.

where the $\mathcal{O}\left(q^{-1} t L_z^{-2}\right)$ term denotes omitted mixed corrections and a_n are unknown parameters.

The behaviour of $L_z \Delta f_{\mathbb{Z}_2}(L, L_z)$ is shown in fig. 5.1. The deviations from the asymptotic value have two origins. At fixed L_z, finite-L corrections are exponentially suppressed in L/L_z. They become visible only when L_z is increased at fixed transverse size, corresponding to small q. These are captured by the 2D Ising CFT in finite volume, see app. B, and shown as a dotted line in fig. 5.1.

At large q, the finite-q exponential corrections are negligible. The remaining deviations are lattice effects due to small L_z, which occur when $L_z \lesssim 10$. We analyze these corrections by extrapolating to infinite aspect-ratio at fixed L_z. In practice this means considering data with high enough $q \gtrsim 16$. Because only a few aspect ratios are available for several transverse sizes, we first interpolate the data in q at fixed L. We use a cubic interpolation to evaluate common aspect ratios. Fig. 5.3 shows the raw Monte Carlo data together with the interpolated large-q estimates for $q \in [16, 100]$. We fit these estimates with a free effective power and with the irrelevant-operator ansatz described in app. B. The free fit gives $\omega_{\text{eff}} = 2.003(7)$, consistent with a leading $1/L_z^2$ correction to $L_z \Delta f_{\mathbb{Z}_2}$. This is the scaling expected from the level-four irrelevant deformations of the isotropic square-lattice Ising model, $T^2 + \bar{T}^2$ and possibly $T\bar{T}$, although the latter is conjectured to be absent at criticality, at least for the nearest-neighbour square-lattice [18].

5.3.2. Three-dimensional analysis

The 3D measurement gives the sector free-energy difference per unit transverse area at finite transverse size, $\Delta f_{\mathbb{Z}_2}(L, L_z)$. We analyze the dimensionless combination

$$Y(L, L_z) \equiv L_z^2 \Delta f_{\mathbb{Z}_2}(L, L_z), \qquad q \equiv \frac{L}{L_z}. \tag{5.13}$$

The slab, $q \gg 1$, Casimir amplitude is obtained by taking both the infinite volume and aspect ratio

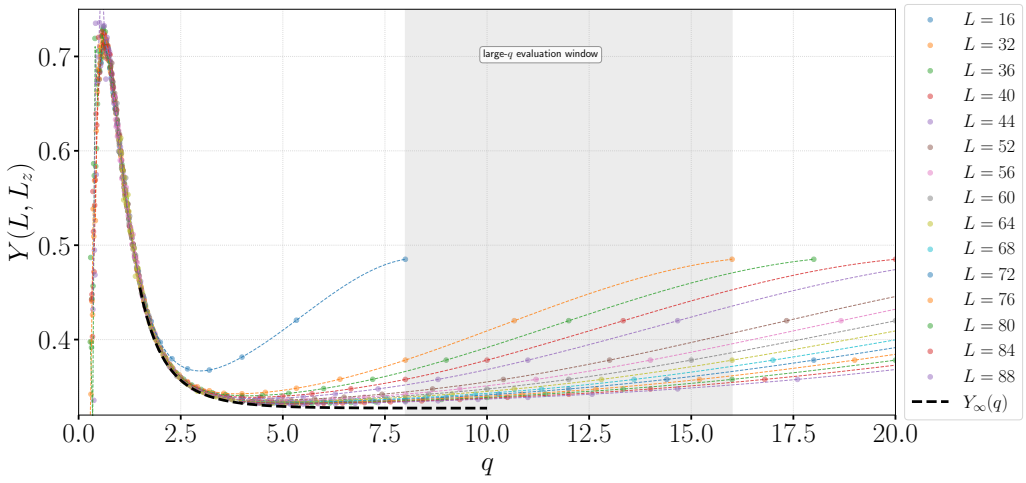


Figure 5.4 Raw finite-volume data for the 3D slab at $\beta = \beta_c = 0.221654626(5)$. The plot shows $Y(L, L_z) = L_z^2 \Delta f_{\mathbb{Z}_2}(L, L_z)$ versus $q = L/L_z$ for several transverse sizes L. Dashed curves are cubic interpolations in q at fixed L. The dashed black line is the infinite volume extrapolation. The gray band marks the large-q window used for the fixed-L_z diagnostic in fig. 5.5. Unlike the two dimensional case, there is no clear plateau.

limit. The two numerical orders of limits are expected to give the same result

$$\Delta_{\mathbb{Z}_2} = \lim_{q\to\infty} \lim_{L_z\to\infty} Y(qL_z, L_z) = \lim_{L_z\to\infty} \lim_{q\to\infty} Y(qL_z, L_z). \tag{5.14}$$

We use the large-q limit at fixed L_z as a diagnostic. In this regime the available data are close to the slab limit, and the remaining deviations are finite-L_z power corrections. This analysis identifies the correction terms used in the subsequent fixed-q infinite-volume extrapolation. The final estimate of $\Delta_{\mathbb{Z}_2}$ is obtained by first extrapolating to infinite volume at fixed q, to obtain $Y_\infty(q)$, and then studying the large-q behaviour. Taking the limits in this order is more stable because the approach of $Y_\infty(q)$ to the slab regime is exponentially suppressed in q, whereas large-q data at finite L_z approach the same limit with power corrections in L_z.

The raw data are shown in fig. 5.4. Unlike the two-dimensional case, finite-size effects are too large for the Casimir amplitude to be read off directly from a plateau. For each fixed transverse size, the data are interpolated as a function of q [1]. The interpolation compares different sizes at fixed aspect ratio and evaluates the large-q regime at fixed L_z. Fig. 5.4 omits pointwise error bars. The final uncertainty is estimated from the stability under fit windows and extrapolation ansätze, using the dense set of simulated volumes.

As in the two-dimensional benchmark, we use the large-q data at fixed L_z as a diagnostic of the slab regime. For each L_z, the interpolation is evaluated in the window $q \in [8, 16]$. In this range the estimates are stable under changes of q at fixed L_z, and the available raw data at fixed aspect ratios are consistent with the interpolated values. Fig. 5.5 shows the resulting large-q estimates as a function of L_z. This diagnostic is used to identify the correction powers that enter the subsequent fixed-q extrapolation.

[1] Repeating the full analysis with linear interpolation in q shifts the final value of $\Delta_{\mathbb{Z}_2}$ and κ by amounts smaller than the quoted uncertainties.

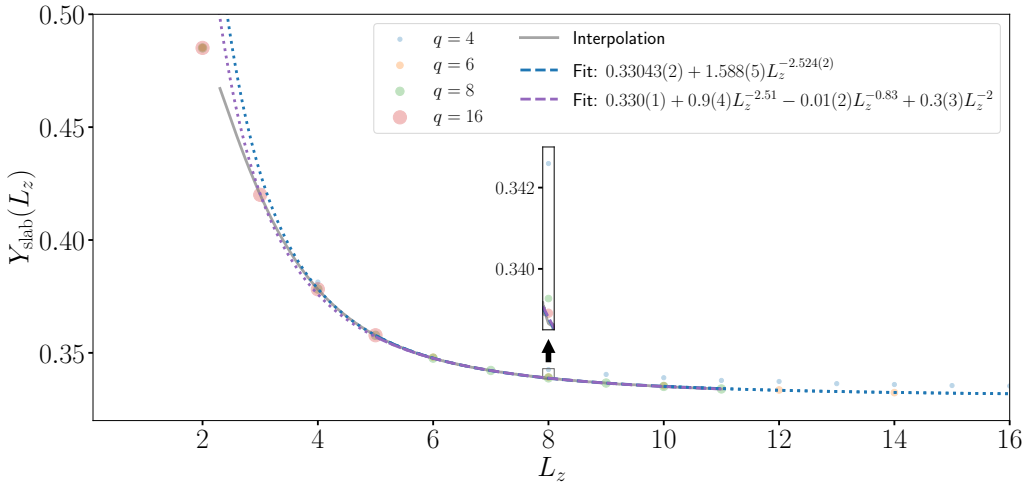


Figure 5.5 Large-q evaluation of the 3D slab data at fixed L_z. For each L_z, the interpolation is evaluated at $q = L/L_z \in [8, 16]$, where finite-q corrections are not visible within the statistical precision. The values are plotted versus L_z and show the finite-L_z approach to the slab Casimir amplitude. Raw data at fixed aspect ratios with several L_z values are also shown. A free power-law fit gives an effective exponent near 2.5; the second fit includes terms proportional to $L_z^{-(\Delta_{T'}-3)}$, $L_z^{-(\Delta_{\epsilon'}-3)}$, and L_z^{-2}. The uncertainties quoted in the fit labels are formal errors from the fit covariance matrix only; they do not include correlations, interpolation effects, or the systematic uncertainty from the extrapolation ansatz.

The resulting large-q values are fitted as a function of L_z. We compare two fit forms,

$$Y_{\mathrm{slab}}(L_z) = \Delta_{\mathbb{Z}_2} + aL_z^{-\omega_{\mathrm{eff}}}, \tag{5.15}$$

$$Y_{\mathrm{slab}}(L_z) = \Delta_{\mathbb{Z}_2} + a_{T'}L_z^{-(\Delta_{T'}-3)} + a_{\epsilon'}L_z^{-(\Delta_{\epsilon'}-3)} + bL_z^{-2} \tag{5.16}$$

The first fit is diagnostic. It determines the effective power visible over the available range. It gives $\omega_{\mathrm{eff}} \simeq 2.5$, close to the exponent of the leading non-conserved spin-two primary T'. This does not imply that lower powers are forbidden. Rather, it indicates that the ϵ' and L_z^{-2} sectors have small effective amplitudes in the sector difference over the fitted range. App. C discusses the allowed operators.

To understand why the scalar correction may be suppressed, it is useful to consider the related geometry $S^2 \times S^1$. In this case, radial quantization expresses the finite-volume trace directly in terms of CFT data; see app. C.3. The argument based on radial quantization does not determine the torus amplitudes relevant for the simulations, but it illustrates a general mechanism. In a sector difference, the scalar correction is controlled by the difference of scalar one-point coefficients, not by either coefficient separately. Thus, even if

$$L_z^{\Delta_{\epsilon'}}\langle\epsilon'\rangle_s \neq 0, \qquad s = \mathrm{AP}, \mathrm{P}, \tag{5.17}$$

the sector difference

$$L_z^{\Delta_{\epsilon'}}\left(\langle\epsilon'\rangle_{\mathrm{AP}} - \langle\epsilon'\rangle_{\mathrm{P}}\right) \tag{5.18}$$

can be small. In the trace interpretation, this suppression occurs because the leading vacuum contribution is common to the two sectors, while the difference is sensitive only to subleading parity-weighted states. The scalar correction proportional to $L_z^{-(\Delta_{\epsilon'}-3)}$ can therefore be smaller than a naive estimate based on the individual one-point functions would suggest.

By contrast, the leading nonconserved spin-two primary can couple directly to the tensor structure selected by the compact direction

$$Q_{\mu\nu} = n_\mu n_\nu - \frac{1}{3}\delta_{\mu\nu}. \tag{5.19}$$

There is no corresponding trace-level reason for the spin-two sector difference to be small. The same geometric selection rule also allows the leading even spin-four primary $C_{\mu\nu\rho\sigma}$, contracted with the symmetric-traceless part of $n_\mu n_\nu n_\rho n_\sigma$. Since $\Delta_C - 3 \simeq 2.02$, this correction is asymptotically larger than the T' correction. In practice it is difficult to separate this contribution from analytic L_z^{-2} corrections over the available range.

The second fit includes the leading correction sectors allowed by the 3D Ising CFT and by the slab geometry: the scalar ϵ' sector, the non-conserved spin-two sector, and an effective L_z^{-2} sector absorbing analytic and spin-four contributions. The fit amplitudes are highly correlated over the available L_z range. Thus, they do not yield a reliable determination of the subleading amplitudes.

The two fits are used to estimate the dependence of $\Delta_{\mathbb{Z}_2}$ on the choice of ansatz. Based on the results in fig. 5.5, we use the two extrapolation ansätze to obtain $Y_\infty(q)$. The spread between the two extrapolations is used as the systematic uncertainty associated with the finite-L_z ansatz.

The infinite volume extrapolations give the curves $Y_\infty(q)$ in fig. 5.6. The q interpolation is used only to compare transverse sizes at common aspect ratios. Interpolated points are not treated as independent data and are evaluated on a grid comparable in density to the original measurements.

We model the remaining corrections to the slab limit by the lightest screening state in the transverse channel, as discussed in app. C.1. The large-q fit uses

$$Y_\infty(q) = \Delta_{\mathbb{Z}_2} + 2\sqrt{\frac{\kappa}{2\pi}}q^{-3/2}e^{-\kappa q} + \cdots, \tag{5.20}$$

where $\kappa = m_{\mathrm{scr}}L_z$ is the dimensionless screening mass. The fitted value of κ is expected to correspond to $m_{\mathrm{scr}}L_z$ for the lightest thermal screening state that contributes to the sector difference, but an independent spectral measurement is needed for a direct identification. The factor $q^{-3/2}e^{-\kappa q}$ is the one-particle transverse-channel correction derived in app. C.1. Assuming no symmetry-protected degeneracy for the finite-volume ground state or the lightest screening state fixes the degeneracy factor in eq. (5.20). As a check, we replace the fixed coefficient $2\sqrt{\kappa/(2\pi)}$ in eq. (5.20) by a free amplitude. The fitted amplitude is compatible with the fixed normalization and leaves κ unchanged within the quoted uncertainty.

The CFT-motivated large-q fit is stable under changes of the lower cutoff $q_{\min}$. Fig. 5.7 shows weak variation of $\Delta_{\mathbb{Z}_2}$ over $q_{\min} \in [1.5, 8]$ [2]. The reduced χ^2_ν is nearly constant and below one, $\chi^2_\nu \simeq 0.3$-0.5. The stable values $\chi^2_\nu < 1$ suggest that the fit describes the data well and that the uncertainties propagated from the fixed-q extrapolation are conservative.

We take the CFT-motivated extrapolation as the central determination. Averaging its values over $q_{\min} \in [1.5, 6]$ gives

$$\Delta_{\mathbb{Z}_2} = 0.3274(1)_{\text{fit window}}, \tag{5.21}$$

where, as the residual fit-window uncertainty, we assigned half of the spread over this range,

$$\delta_{q_{\min}}\Delta_{\mathbb{Z}_2} = \frac{1}{2}\left[\max_{q_{\min}\in[1.5,6]}\Delta_{\mathbb{Z}_2} - \min_{q_{\min}\in[1.5,6]}\Delta_{\mathbb{Z}_2}\right] = 0.00012. \tag{5.22}$$

[2] For larger $q_{\min}$ the fits become unstable because the size of the fitted corrections approaches the statistical error.

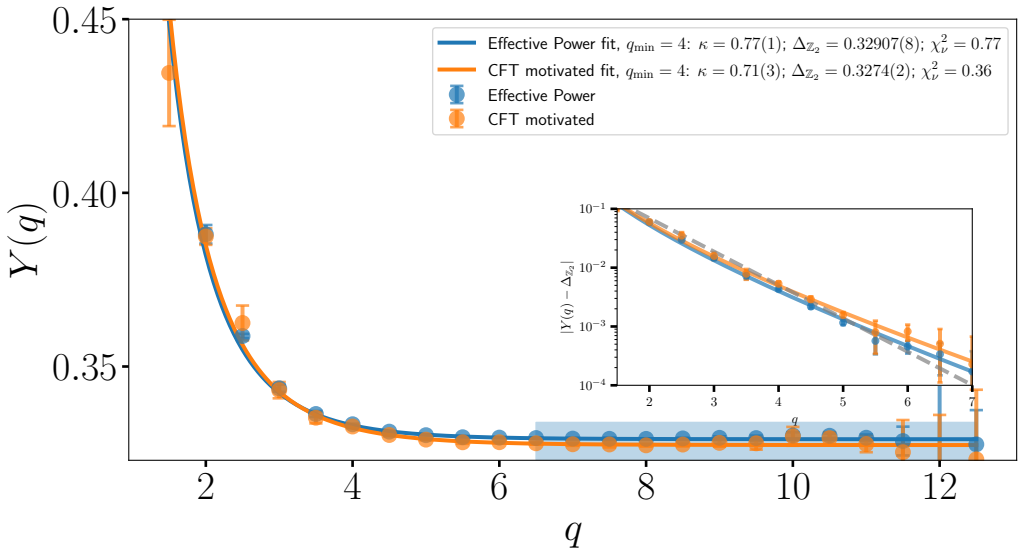


Figure 5.6 Large-q approach to the slab Casimir amplitude. The data are the large-volume estimates $Y_\infty(q)$ obtained at fixed aspect ratio after finite-L_z extrapolation. The horizontal asymptote is $\Delta_{\mathbb{Z}_2} = \lim_{q\to\infty} Y_\infty(q)$. The two curves correspond to the two finite-L_z extrapolation procedures and are fitted with the large-q correction in eq. (5.20). The inset subtracts the fitted $\Delta_{\mathbb{Z}_2}$. The spread between the two extrapolations is included in the systematic uncertainty. The fit-label errors are those of the representative $q_{\min} = 4$ fits. The final uncertainties are estimated from the $q_{\min}$ scan and from the spread between the two finite-L_z extrapolation procedures, as described in the text.

The dominant uncertainty comes from the finite-L_z extrapolation ansatz. We estimate it from the difference between the CFT-motivated and effective-power averages over the same $q_{\min}$ range,

$$\delta_{\text{ansatz}}\Delta_{\mathbb{Z}_2} = \left|\overline{\Delta}_{\text{eff}} - \overline{\Delta}_{\text{CFT}}\right| \sim 0.0017. \tag{5.23}$$

Thus our final result is

$$\Delta_{\mathbb{Z}_2} = 0.3274(1)_{q_{\min}}(17)_{\text{ansatz}}. \tag{5.24}$$

Combining the uncertainties into one conservative error bar gives

$$\Delta_{\mathbb{Z}_2} = 0.327(2), \tag{5.25}$$

consistent with the fixed-L_z large-q diagnostic.

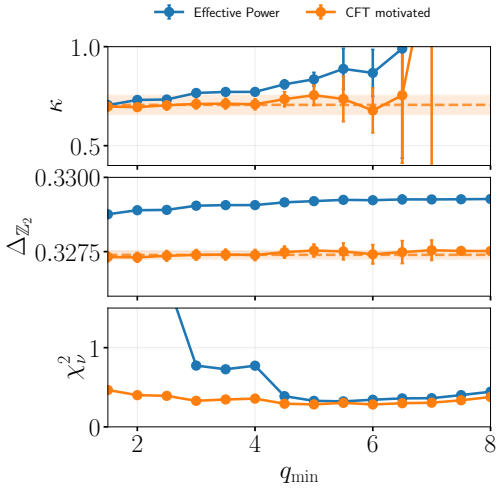
For the screening mass in units of $1/L_z$, only the CFT-motivated extrapolation is stable under changes of $q_{\min}$. Averaging over $q_{\min} \in [1.5, 6]$ and assigning half of the spread as the fit-window uncertainty gives

$$\kappa_{\text{eff}} = 0.71(4). \tag{5.26}$$

The fitted value of κ is expected to correspond to $m_{\text{scr}}L_z$ for the lightest thermal screening state that contributes to the sector difference, but an independent spectral measurement is needed for a direct identification. The quoted uncertainties come from changes of fit window and extrapolation ansatz.

Small-q channel

The raw data also test the opposite channel, $q = L/L_z \ll 1$. Whereas the large-q regime is controlled by the leading thermal screening state, the small-q regime treats the compact direction as the long



$q_{\min}$	κ (eff)	κ (CFT)	$\Delta_{\mathbb{Z}_2}$ (eff)	$\Delta_{\mathbb{Z}_2}$ (CFT)	χ^2_ν (eff)	χ^2_ν (CFT)
1.5	0.697(6)	0.69(2)	0.32871(6)	0.3273(2)	4.1	0.43
2	0.731(8)	0.69(2)	0.32889(7)	0.3273(2)	1.8	0.4
2.5	0.733(9)	0.70(2)	0.32890(7)	0.3274(2)	1.9	0.39
3	0.77(1)	0.71(2)	0.32905(7)	0.3274(2)	0.77	0.33
3.5	0.77(1)	0.71(3)	0.32907(8)	0.3274(2)	0.73	0.35
4	0.77(1)	0.71(3)	0.32907(8)	0.3274(2)	0.77	0.36
4.5	0.81(2)	0.73(4)	0.32916(8)	0.3275(2)	0.39	0.29
5	0.84(3)	0.75(5)	0.32920(9)	0.3275(2)	0.33	0.28
5.5	0.9(1)	0.7(1)	0.3292(1)	0.3275(3)	0.32	0.3
6	0.9(1)	0.7(1)	0.3292(1)	0.3274(3)	0.34	0.28

Figure 5.7 Stability of the final large-q extrapolation under variation of the lower fit cutoff $q_{\min}$. Left: dimensionless screening mass $\kappa = m_{\mathrm{scr}} L_z$, Casimir difference $\Delta_{\mathbb{Z}_2}$, and reduced chi-square χ^2_ν for the two finite-L_z extrapolation procedures used to construct $Y_\infty(q)$. Right: numerical values in the stable fit range. The labels "eff" and "CFT" denote the effective-power and CFT-motivated finite-L_z extrapolations. The difference between the two procedures is used as the systematic uncertainty. The shaded regions show the fit uncertainties of the central values quoted in the text.

transfer-matrix direction. The spectrum is that of the critical theory quantized on T^2_L.

The $\mathbb{Z}_2$ twist weights each finite-volume state by its $\mathbb{Z}_2$ parity. If the finite-volume ground state is unique and $\mathbb{Z}_2$ even, the leading ground-state contribution cancels in the sector difference. The first non-cancelling term is then the lightest $\mathbb{Z}_2$-odd state on the transverse torus. Thus

$$E_\sigma(L) - E_0(L) = \frac{\kappa_\sigma}{L} + \cdots , \tag{5.27}$$

and

$$Y\left(qL_z, L_z\right) \sim \frac{A_\sigma}{q^2} e^{-\kappa_\sigma / q} \tag{5.28}$$

The amplitude A_σ has a spectral interpretation. If the finite-volume ground state has degeneracy g_0 and the lightest odd level has degeneracy g_σ

$$A_\sigma = 2\,\frac{g_\sigma}{g_0}. \tag{5.29}$$

For the finite-volume geometry considered here, the ground state is expected to be unique, $g_0 = 1$, and the lowest $\mathbb{Z}_2$-odd state is expected to be nondegenerate. Hence $A_\sigma = 2$, with no symmetry-imposed degeneracy factor. We use this value to define the effective local estimator of the energy gap

$$\kappa^{\mathrm{eff}}_\sigma(q) = -q \log\left[\frac{q^2 Y(qL_z, L_z)}{A_\sigma}\right]. \tag{5.30}$$

If the small-q channel is dominated by a single $\mathbb{Z}_2$-odd state, $\kappa^{\mathrm{eff}}_\sigma(q)$ should approach a constant as $1/q \to \infty$. This is shown in Fig. 5.8, where the plateau is reached already for moderate values of $1/q$. Letting A_σ vary gives a value statistically compatible with 2. The deviations at small $1/q$ are due to

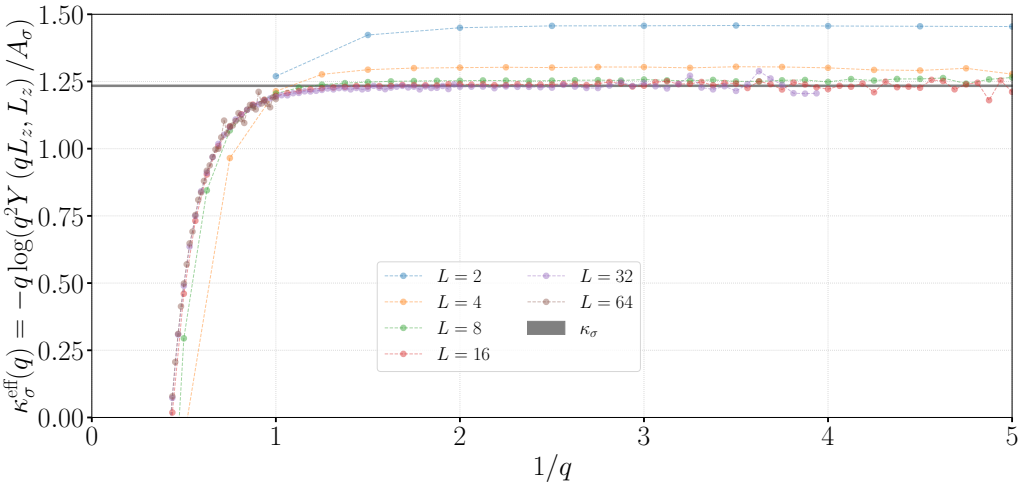


Figure 5.8 Small-q effective exponent in the 3D twisted-sector free-energy difference. The local estimator $\kappa_\sigma^{\mathrm{eff}}(q)$, defined in eq. (5.30), with $A_\sigma = 2$, is plotted versus $1/q$. Data from different transverse sizes collapse onto a common plateau. The horizontal line is the fitted value $\kappa_\sigma = 1.230(3)$, shown in fig. 5.9.

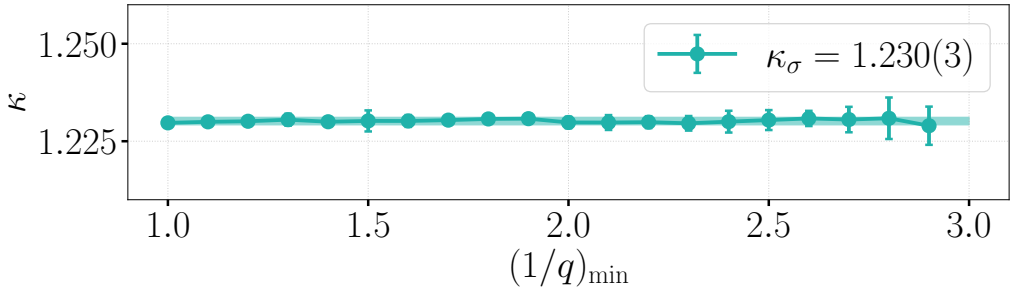


Figure 5.9 Stability of the small-q exponent in eq. (5.28), with $A_\sigma = 2$, under variation of the lower fit cutoff $(1/q)_{\mathrm{min}}$.

subleading odd states. We therefore extract the $\mathbb{Z}_2$-odd sector gap in the small-q channel by fitting

$$q^2Y(qL_z, L_z) = 2e^{-\kappa_\sigma/q} + A_{\sigma'}e^{-\kappa_{\sigma'}/q} \tag{5.31}$$

over several lower cutoffs in $1/q$, where $\kappa_{\sigma'}$ is the next $\mathbb{Z}_2$-odd energy gap and $A_{\sigma'}$ its degeneracy. With the current precision, the subleading parameters vary too widely with $(1/q)_{\mathrm{min}}$ for us to quote a meaningful result. Fig. 5.9 shows the stability of κ_σ under changes of $(1/q)_{\mathrm{min}}$. Averaging over the accepted range and taking half the variation over the averaging window as an error, we obtain

$$\kappa_\sigma = 1.230(3). \tag{5.32}$$

References

[1] José Matos. *Monte Carlo Reconstruction of Symmetry-Twisted Partition Function Ratios: The Critical 3D Ising*. June 30, 2026. DOI: 10.48550/arXiv.2607.00106. arXiv: 2607.00106 [hep-lat].

[2] Andrea Gambassi. "The Casimir Effect: From Quantum to Critical Fluctuations." In: *Journal of physics. Conference series* 161 (2009). Ed. by Gabriel Barton, Giovanni Carugno, Victor Dodonov, and Margarita Manko, p. 012037. DOI: 10.1088/1742-6596/161/1/012037. arXiv: 0812.0935 [cond-mat.stat-mech].

[3] Michael Krech. "The Casimir Effect in Critical Systems." In: WORLD SCIENTIFIC, July 1994. ISBN: 978-981-02-1845-4 978-981-4354-02-8. DOI: 10.1142/2434.

[4] H. W. Diehl. "The Theory of Boundary Critical Phenomena." In: *International Journal of Modern Physics B* 11 (1997), pp. 3503–3523. DOI: 10.1142/S0217979297001751. arXiv: cond-mat/9610143.

[5] Martin Hasenbusch. "Finite Size Scaling Study of Lattice Models in the Three-Dimensional Ising Universality Class." In: *Physical Review B* 82 (2010), p. 174433. DOI: 10.1103/PhysRevB.82.174433. arXiv: 1004.4486 [cond-mat.stat-mech].

[6] Andrea Bulgarelli, Michele Caselle, Alessandro Nada, and Marco Panero. "Casimir Effect in Critical O(N) Models from Nonequilibrium Monte Carlo Simulations." In: *Physical Review E: Statistical Physics, Plasmas, Fluids, and Related Interdisciplinary Topics* 112 (6 2025), p. 064126. DOI: 10.1103/lcvl-dgv4. arXiv: 2505.20403 [cond-mat.stat-mech].

[7] Martin Hasenbusch. "Thermodynamic Casimir Effect for Films in the Three-Dimensional Ising Universality Class: Symmetry-breaking Boundary Conditions." In: *Physical Review B* 82.10 (Sept. 2010), p. 104425. DOI: 10.1103/PhysRevB.82.104425.

[8] Martin Hasenbusch. "Thermodynamic Casimir Effect: Universality and Corrections to Scaling." In: *Physical Review B* 85.17 (May 2012), p. 174421. DOI: 10.1103/PhysRevB.85.174421.

[9] Martin Hasenbusch. "Thermodynamic Casimir Effect in Films: The Exchange Cluster Algorithm." In: *Physical Review E: Statistical Physics, Plasmas, Fluids, and Related Interdisciplinary Topics* 91.2 (Feb. 2015), p. 022110. DOI: 10.1103/PhysRevE.91.022110.

[10] Martin Hasenbusch. "Thermodynamic Casimir Forces between a Sphere and a Plate: Monte Carlo Simulation of a Spin Model." In: *Physical Review E: Statistical Physics, Plasmas, Fluids, and Related Interdisciplinary Topics* 87.2 (Feb. 2013), p. 022130. DOI: 10.1103/PhysRevE.87.022130.

[11] Alfred Hucht, Daniel Grüneberg, and Felix M. Schmidt. "Aspect-Ratio Dependence of Thermodynamic Casimir Forces." In: *Physical Review E: Statistical Physics, Plasmas, Fluids, and Related Interdisciplinary Topics* 83.5 (May 2011), p. 051101. DOI: 10.1103/PhysRevE.83.051101.

[12] Marco Billò, Vasco Gonçalves, Edoardo Lauria, and Marco Meineri. "Defects in Conformal Field Theory." In: *JHEP* 04 (2016), p. 091. DOI: 10.1007/JHEP04(2016)091. arXiv: 1601.02883 [hep-th].

[13] Davide Gaiotto, Anton Kapustin, Nathan Seiberg, and Brian Willett. "Generalized Global Symmetries." In: *JHEP* 02 (2015), p. 172. DOI: 10.1007/JHEP02(2015)172. arXiv: 1412.5148 [hep-th].

[14] Jun Maeda and Yuya Tanizaki. "Twisted Partition Functions as Order Parameters." In: *JHEP* 08 (2025), p. 128. DOI: 10.1007/JHEP08(2025)128. arXiv: 2505.16546 [hep-th].

[15] Marten Reehorst. "Rigorous Bounds on Irrelevant Operators in the 3d Ising Model CFT." In: *JHEP* 09 (2022), p. 177. DOI: 10.1007/JHEP09(2022)177. arXiv: 2111.12093 [hep-th].

[16] David Simmons-Duffin. "The Lightcone Bootstrap and the Spectrum of the 3d Ising CFT." In: *JHEP* 03 (2017), p. 086. DOI: 10.1007/JHEP03(2017)086. arXiv: 1612.08471 [hep-th].

[17] P. Di Francesco, P. Mathieu, and D. Senechal. *Conformal Field Theory*. Graduate Texts in Contemporary Physics. New York: Springer-Verlag, 1997. ISBN: 978-0-387-94785-3 978-1-4612-7475-9. DOI: 10.1007/978-1-4612-2256-9.

[18] Michele Caselle, Martin Hasenbusch, Andrea Pelissetto, and Ettore Vicari. "Irrelevant Operators in the Two-Dimensional Ising Model." In: *Journal of Physics A: Mathematical and General* 35 (2002), pp. 4861–4888. DOI: 10.1088/0305-4470/35/23/305. arXiv: cond-mat/0106372.

Chapter 6

Conclusions and Outlook

This thesis studied extended objects in the 3D Ising model, using the domain wall as a controlled laboratory for effective string theory. The main conclusion is that EST is highly predictive but not exhaustive. Some observables are governed by the isolated worldsheet theory, others probe massive bulk modes, and still others track the RG flow from critical finite-size data to the string tension of the massive phase.

The first main result concerns the torus free energy of a toroidal domain wall, which gives direct access to non-universal worldsheet data without boundary effects. The contribution linear in the leading non-universal coefficient γ_3 was computed using the thermodynamic Bethe ansatz while keeping the area dependence non-perturbative. Although the fully deformed equations are not presently tractable, the linear construction provides a stable fitting strategy for the Monte Carlo data and avoids the poor convergence of the divergent large-area expansion. The main quantitative result is the first non-universal worldsheet Wilson coefficient, $\gamma_3 = -0.00106(18)$, near the lower bound from the worldsheet S-matrix bootstrap.

The second result concerns observables for which the isolated-string description is incomplete. The difference between bulk correlation functions in the wall and vacuum sectors isolates the coupling of the fluctuating wall to the lightest massive bulk excitation. When the exchanged particle is nearly on shell and carries small momentum parallel to the wall, its propagation can be coupled systematically to the fluctuating wall position. The resulting expressions separate intrinsic bulk propagation from wall roughening, producing Gaussian broadening at short transverse distances and exponential bulk decay at larger distances.

The third result is methodological. The flat-histogram construction gives direct Monte Carlo access to ratios of partition functions in distinct global sectors by embedding the endpoint theories in a common enlarged configuration space. At criticality, these ratios define symmetry-resolved compactification data of the underlying CFT. For the 3D Ising model, the method determines the free-energy difference between the periodic and $\mathbb{Z}_2$-twisted sectors. Its slab limit yields the twisted-sector thermodynamic Casimir difference, while its finite-aspect-ratio dependence determines the thermal screening scale and the lowest $\mathbb{Z}_2$-odd transverse-torus gap. The same twist selects, in the broken phase and at large

volume, the sector dominated by a single fluctuating domain wall. Following its free energy away from criticality therefore connects symmetry-twisted CFT data to the tension of the emergent wall. The same sector construction consequently serves both as an effective-string observable in the broken phase and as a finite-volume probe of critical symmetry sectors. The main quantitative results are the twisted-sector thermodynamic Casimir difference, $\Delta_{\mathbb{Z}_2} = 0.327(2)$; the thermal screening scale, $\kappa_{\text{eff}} = m_{\text{scr}} L_z = 0.71(4)$; and the lowest $\mathbb{Z}_2$-odd energy gap on the transverse torus, $\kappa_\sigma = 1.230(3)$.

6.1. Extensions to $SU(N)$ and $3+1$ dimensions

The exact relation between the 3D Ising interface and a confining string is dimension-dependent. In three dimensions, the Ising model is dual to $\mathbb{Z}_2$ lattice gauge theory, and an Ising domain wall can be identified with a confining-string worldsheet in the dual theory, such as the worldsheet appearing in a Polyakov-loop correlator. This identification is possible because both objects are two-dimensional. It does not extend directly to higher dimensions: generalized Kramers-Wannier-Wegner duality maps a $\mathbb{Z}_2$ p-form theory in D dimensions to a $\mathbb{Z}_2$ $(D-p-2)$-form theory. The four-dimensional Ising model is therefore dual to a $\mathbb{Z}_2$ two-form gauge theory, whereas four-dimensional $\mathbb{Z}_2$ one-form gauge theory is self-dual. Preserving the Ising construction gives a 3D hypersurface. Preserving a two-dimensional string worldsheet instead requires studying a gauge theory directly.

A broader but weaker relation is provided by the Svetitsky-Yaffe conjecture. If the finite-temperature deconfinement transition of a $(d+1)$-dimensional gauge theory is continuous, its critical behaviour belongs to the universality class of a d-dimensional spin model whose global symmetry is the center of the gauge group. Thus, $SU(2)$ Yang-Mills theory in $3+1$ dimensions is related at criticality to the 3D Ising model [1], while $SU(3)$ Yang-Mills theory in $2+1$ dimensions is related to the two-dimensional three-state Potts model [2]. This correspondence supports comparisons of universal critical data, finite-size scaling functions, and conformal perturbation theory near deconfinement. It does not imply a microscopic equivalence between $SU(N)$ flux tubes and spin-model interfaces away from criticality, or equality of their non-universal effective-string coefficients.

Extending the analysis to $SU(N)$ requires studying the lattice gauge theory directly. Closed-string free energies, Polyakov-loop correlators, and finite-size corrections can then be used to determine the long-distance worldsheet data of genuine non-Abelian flux tubes. These must be distinguished from finite-temperature k-walls. An open confining flux tube is sourced by external color charges, whereas a closed winding flux tube is a source-free state carrying electric flux around a compact spatial direction. A k-wall is instead a codimension-one interface between deconfined vacua whose Polyakov loops differ by a center element z^k. It can be generated by boundary conditions selecting different center vacua or by a spatial 't Hooft defect implementing $P \mapsto z^k P$.

In three spacetime dimensions, a k-wall has the same dimension as a string worldsheet. Confining strings and k-walls provide two distinct realizations of the center structure of the same gauge theory. The former are electric-flux objects associated with the unbroken center one-form symmetry, while the latter are domain walls of the thermally reduced center symmetry in the deconfined phase. Studying both therefore provides a direct way to distinguish properties that follow solely from the infrared dynamics of a fluctuating extended object from those that depend on whether that object is a confining flux tube or an interface between distinct vacua. In particular, determining the leading non-universal coefficient γ_3 for both k-walls and confining strings would provide a quantitative test of how much

information about these distinct microscopic realizations survives in the non-universal worldsheet dynamics.

The exact confining-string interpretation is therefore specific to the $\mathbb{Z}_2$ theory considered here, with analogous constructions available for suitable 3D finite-Abelian spin/gauge dual pairs. Beyond this setting, the main transferable result is the finite-volume framework for isolating the contribution of the lightest bulk excitation to observables associated with a specified fluctuating defect. The same strategy can be applied to $SU(N)$ confining strings, k-walls, and higher-form defects once the corresponding microscopic object and its coupling to bulk excitations are identified.

6.2. Future directions

The results of this thesis suggest three main directions: refining measurements of intrinsic worldsheet dynamics, extending the description of worldsheet–bulk interactions, and connecting symmetry-twisted critical data to the massive domain-wall regime. Monte Carlo simulations are essential to this program because they provide microscopic systems in which these infrared assumptions can be tested non-perturbatively. This makes it possible to distinguish universal EST predictions from non-universal contributions determined by the underlying lattice theory.

The most direct continuation is to measure additional worldsheet finite-volume observables. Varying the full torus modulus, including its shear, would change the sensitivity to different terms in the EST expansion and provide further tests of the first non-universal coefficients. The cylinder limit offers a complementary channel in which the partition function becomes a thermal trace over worldsheet states. Its free energy could be used to extract an effective central charge and follow the transition between the infrared Goldstone theory and possible additional worldsheet degrees of freedom.

A more demanding objective is to resolve genuinely inelastic worldsheet effects. The TBA treatment used here starts from an elastic integrable theory and includes the leading non-universal interaction perturbatively. Generic EST interactions eventually generate particle production. Deviations of sufficiently precise torus free-energy data from the elastic prediction could therefore probe inelastic dynamics, although this would require substantially improved statistics and control over higher-order Wilson coefficients.

A central conceptual problem is to characterize how the $\mathbb{Z}_2$-twisted sector evolves from criticality into the ordered phase. At criticality, the twist is implemented by an invertible topological $\mathbb{Z}_2$ symmetry defect, equivalently by a background $\mathbb{Z}_2$ holonomy. Under the $\mathbb{Z}_2$-preserving relevant deformation into the ordered phase, the twist continues to define the same global symmetry sector, while at large volume this sector becomes dominated by a single non-topological interface with finite tension: the fluctuating domain wall. Following observables in the twisted sector along this flow could therefore relate symmetry-twisted CFT data to the wall tension, bulk screening masses, and worldsheet Wilson coefficients. Varying the aspect ratio and shear of the transverse torus would determine the moduli dependence of the twisted partition function and symmetry-resolved spectrum, while an independent measurement of the antiperiodic Casimir amplitude would separate the absolute sector amplitudes from their difference.

The endpoint-reconstruction method can also be generalized to other global symmetries. In an $O(N)$-invariant lattice model, for example, one could impose a compact-direction twist $g \in O(N)$ and measure Z_g/Z_1 directly. Analogous constructions may be possible for center and higher-form symmetries using background fluxes or holonomies. Such ratios would probe interface free energies, phase

structure, and symmetry-resolved compactification data, provided that the interpolating ensemble does not develop severe overlap, sign, or phase problems.

A related algorithmic objective is to estimate ratios of correlation functions directly across boundary sectors. In the branon–glueball problem, the relevant observable has the form

$$\frac{\langle \mathcal{O}(x_\parallel, x_\perp)\mathcal{O}(0)\rangle_{\mathrm{APBC}}}{\langle \mathcal{O}(x_\parallel, x_\perp)\mathcal{O}(0)\rangle_{\mathrm{PBC}}} = 1 + \frac{\lambda_0^2 \pi}{m^2} e^{-m\left(x_\perp - \sqrt{x_\perp^2 + x_\parallel^2}\right)} e^{\frac{1}{2}m^2 d^2(x_\parallel)} \frac{x_\perp \sqrt{x_\perp^2 + x_\parallel^2}}{L_z} + \cdots . \tag{6.1}$$

The apparently growing exponential results from normalization by the periodic correlator, which decays more rapidly in this kinematic regime. The ratio therefore isolates the wall-induced contribution and may be a better numerical target than the two correlators separately.

There is a two-dimensional precedent at the level of the underlying representation. In the Ising model, Kadanoff-Ceva disorder insertions are implemented by reversing the sign of the couplings crossed by a path on the dual lattice, whose endpoints define the disorder correlator [3]. This correlator is a ratio of partition functions and is mapped by Kramers-Wannier duality to an ordinary spin correlator of the dual Ising model. The corresponding dual correlation function can be sampled in an enlarged graph ensemble by worm algorithms, in which the two endpoints of an open graph are dynamical [4–6]. The open problem is to find variables in which the wall-induced contribution can likewise be sampled directly, instead of being extracted as a small difference between noisy observables.

The coupled wall–bulk EFT itself should also be systematized. A non-relativistic formulation in which the massive mode couples through vertex operators $e^{\pm im\pi}$ would clarify the power counting and determine which observables depend only on the leading wall–bulk coupling. It would also identify where additional short-distance coefficients enter.

The same EFT suggests a direct test in lattice gauge theory through measurements of the flux-tube profile. For a flux tube created by Polyakov loops, one can measure the expectation value of a local bulk operator, such as the action density, as a function of the transverse distance from the flux-tube plane. The full transverse dependence determines the profile, while its large-distance tail should be controlled by exchange of the lightest glueball, convolved with the rough transverse fluctuations of the string. Comparing this prediction with lattice data would test whether the wall–bulk coupling identified in the Ising model has a counterpart for genuine confining flux tubes.

Ordered phases with more than two vacua provide another extension. Clock models with $\mathbb{Z}_3$, $\mathbb{Z}_4$, or $\mathbb{Z}_6$ [1] symmetry and appropriately chosen boundary conditions can generate networks of domain walls meeting at junctions. These systems would provide controlled lattice analogues of flux-tube junctions and could test whether junctions carry localized degrees of freedom, how their energies depend on geometry, and which effective theory governs fluctuations of wall networks. Such configurations are analogues of static baryonic and multiquark flux-tube systems.

A more speculative possibility is to make the defect endpoints dynamical. Allowing the boundaries of the interpolating bond region to move would produce two particle worldlines coupled to an open domain wall. In Euclidean-time gauge, $x_a^0(\tau) = \tau$, the infrared action would schematically contain a

[1] The cases $n = 3, 4, 6$ are geometrically convenient because regular triangles, squares, and hexagons tile the plane, allowing a uniform lattice discretization of prisms with n equivalent lateral faces. Assigning the n ordered vacua cyclically to these faces forces the domain walls between adjacent vacua to meet along the prism axis, producing an n-wall junction.

worldsheet term, endpoint kinetic terms, direct endpoint interactions, and local boundary operators,

$$S_{\rm eff} = \sigma \int_\Sigma d^2\xi\sqrt{g} + \sum_{a=1}^{2} M_a \int d\tau\sqrt{1+\dot{\mathbf{x}}_a^2} + \int d\tau V(|\mathbf{x}_1-\mathbf{x}_2|) + S_{\rm bdy} + S_{\rm higher}. \tag{6.2}$$

In the heavy-endpoint limit this reduces to EST with fixed Dirichlet boundaries. For finite endpoint masses, the string length becomes a dynamical coordinate, $R(\tau) = |x_1(\tau) - x_2(\tau)|$, and integrating out the worldsheet at fixed R gives $V_{\rm eff}(R) = V(R) + \sigma R - \frac{\pi(D-2)}{24R} + \cdots$. This would provide a controlled model for the transition between fixed external sources and strings attached to dynamical particles.

The most ambitious direction is to revisit strong-coupling lattice YM expansions as possible microscopic surface descriptions of confining strings. These expansions naturally generate sums over constrained surfaces, but the surfaces contain thickness effects, self-intersections, contact interactions, and branching constraints. It remains unclear whether these weights can be reorganized into a controlled worldsheet theory whose infrared limit is EST. Understanding this relation would provide a microscopic route from a confining lattice theory to its effective string description, rather than introducing the worldsheet theory only at long distances.

6.3. Open questions

Several questions remain about confining flux tubes. The Goldstone sector of effective string theory gives a controlled asymptotic description, but does not determine its completion at the distances and geometries most relevant for gauge-theory observables. In practice, flux tubes are often longer than the bulk correlation length without being parametrically separated from it. In this regime, non-universal worldsheet coefficients, bulk dressing, and additional worldsheet degrees of freedom may remain numerically important.

One question is when massive worldsheet excitations must be retained explicitly. In the strict infrared, such modes can be integrated out and their effects are encoded in local higher-derivative operators. At the intermediate lengths probed by lattice spectra, however, the massive pseudoscalar observed on four-dimensional confining strings is resolved as an explicit unstable worldsheet resonance. It remains unclear which microscopic theories produce such modes, over what range an explicit description is required, and how their parameters match onto the Wilson coefficients of the Goldstone EFT.

A second question concerns the relation between worldsheet and bulk excitations. Standard EST integrates out massive bulk modes and encodes their effects in local Wilson coefficients. This is adequate for many asymptotic observables, but can fail for quantities sensitive to the transverse tube profile, finite transverse volume, or nearly on-shell bulk propagation. The distinction between an isolated-worldsheet EFT and an explicitly coupled worldsheet-bulk theory therefore determines which observables probe intrinsic string dynamics and which probe the embedding bulk theory.

The scope of universality in more general string sectors is also unresolved. Confinement involves not only closed strings, but also open and winding strings, junctions, and processes in which string topology changes. These introduce boundary coefficients, endpoint dynamics, junction structure, and mixing with non-string states. It remains unknown which features are fixed by symmetry and infrared consistency and which depend on microscopic dynamics.

Finally, the microscopic completion of EST remains obscure. Its infrared status as the Goldstone theory of a long string is secure, but it is unclear whether it admits an autonomous ultraviolet world-

sheet completion. Strong-coupling and random-surface representations suggest a microscopic surface description, yet they contain branching, self-intersections, contact interactions, and non-geometric weights. Whether these structures can be reorganized into a controlled worldsheet theory whose infrared limit is EST, or whether the only complete ultraviolet definition is the original bulk quantum field theory, remains open.

References

[1] Biagio Lucini, Michael Teper, and Urs Wenger. "Properties of the Deconfining Phase Transition in SU(N) Gauge Theories." In: *Journal of High Energy Physics* 2005.02 (Mar. 2005), p. 033. ISSN: 1126-6708. DOI: 10.1088/1126-6708/2005/02/033.

[2] Jack Liddle and Michael Teper. *The Deconfining Phase Transition in D=2+1 SU(N) Gauge Theories*. Mar. 14, 2008. DOI: 10.48550/arXiv.0803.2128. arXiv: 0803.2128 [hep-lat].

[3] Leo P. Kadanoff and Horacio Ceva. "Determination of an Operator Algebra for the Two-Dimensional Ising Model." In: *Physical Review B* 3.11 (June 1, 1971), pp. 3918–3939. DOI: 10.1103/PhysRevB.3.3918.

[4] Nikolay Prokof'ev and Boris Svistunov. "Worm Algorithms for Classical Statistical Models." In: *Physical Review Letters* 87.16 (Sept. 27, 2001), p. 160601. DOI: 10.1103/PhysRevLett.87.160601.

[5] Peter Hitchcock, Erik S. Sørensen, and Fabien Alet. "Dual Geometric Worm Algorithm for Two-Dimensional Discrete Classical Lattice Models." In: *Physical Review E* 70.1 (July 2, 2004), p. 016702. DOI: 10.1103/PhysRevE.70.016702.

[6] Ulli Wolff. "Simulating the All-Order Strong Coupling Expansion I: Ising Model Demo." In: *Nuclear Physics B* 810.3 (Apr. 1, 2009), pp. 491–502. ISSN: 0550-3213. DOI: 10.1016/j.nuclphysb.2008.09.033.

Appendix A

Modular functions and Eisenstein series

This appendix collects the conventions for the modular functions used in the torus computations of Chapter 3. We use the normalized holomorphic Eisenstein series. See [1] for a review.

Throughout,

$$q = e^{2\pi i \tau}, \qquad \tau \in \mathbb{H}. \tag{A.1}$$

The Dedekind eta function is

$$\eta(\tau) = q^{1/24} \prod_{n=1}^{\infty} (1 - q^n). \tag{A.2}$$

With this convention,

$$q\partial_q \eta^{-1}(\tau) = -\frac{E_2(\tau)}{24} \eta^{-1}(\tau). \tag{A.3}$$

For even weight $2k \geq 4$, define

$$G_{2k}(\tau) = \sum_{(m,n)\in\mathbb{Z}^2\setminus(0,0)} \frac{1}{(m+n\tau)^{2k}}. \tag{A.4}$$

This sum is absolutely convergent for $k \geq 2$. We use the normalized series

$$E_{2k}(\tau) = \frac{G_{2k}(\tau)}{2\zeta(2k)}. \tag{A.5}$$

Equivalently,

$$E_{2k}(\tau) = 1 - \frac{4k}{B_{2k}} \sum_{r=1}^{\infty} \sigma_{2k-1}(r) q^r \qquad \sigma_p(n) = \sum_{d|n} d^p. \tag{A.6}$$

In particular,

$$E_4(\tau) = 1 + 240 \sum_{n=1}^{\infty} \sigma_3(n) q^n, \qquad E_6(\tau) = 1 - 504 \sum_{n=1}^{\infty} \sigma_5(n) q^n. \tag{A.7}$$

The weight-two series is slightly different. The formal lattice sum

$$\sum_{(m,n)\in\mathbb{Z}^2\setminus(0,0)} \frac{1}{(m+n\tau)^2} \tag{A.8}$$

is not absolutely convergent, so E_2 is not obtained from the same unambiguous lattice sum as E_4 and E_6. With Eisenstein summation one defines

$$G_2(\tau) = \lim_{N\to\infty} \sum_{n=-N}^{N} \sum_{\substack{m\in\mathbb{Z} \\ (m,n)\neq(0,0)}} \frac{1}{(m+n\tau)^2}. \tag{A.9}$$

The normalized weight-two Eisenstein series is then

$$E_2(\tau) = \frac{G_2(\tau)}{2\zeta(2)} = \frac{3}{\pi^2} G_2(\tau), \tag{A.10}$$

or equivalently

$$E_2(\tau) = 1 - 24\sum_{r=1}^{\infty} \sigma_1(r) q^r. \tag{A.11}$$

The dependence on the summation prescription is reflected in the fact that E_2 is quasimodular rather than modular.

The Ramanujan identities used in Chapter 3 are

$$q\partial_q E_2 = \frac{E_2^2 - E_4}{12}, \qquad q\partial_q E_4 = \frac{E_2 E_4 - E_6}{3}, \qquad q\partial_q E_6 = \frac{E_2 E_6 - E_4^2}{2}. \tag{A.12}$$

These identities fix the normalization of the Eisenstein series used in the large-area expansion of the torus partition function. Under the modular S-transformation,

$$E_{2k}\left(-\frac{1}{\tau}\right) = \tau^{2k} E_{2k}(\tau), \qquad k \geq 2, \tag{A.13}$$

while

$$E_2\left(-\frac{1}{\tau}\right) = \tau^2 E_2(\tau) + \frac{6\tau}{\pi i}. \tag{A.14}$$

Equivalently,

$$E_2(\tau) = \tau^{-2} E_2\left(-\frac{1}{\tau}\right) + \frac{6i}{\pi\tau}. \tag{A.15}$$

The anomalous term is the standard quasimodular contribution. Despite this, the final free-energy coefficients combine into modular-invariant quantities.

The coincident-point sums appearing in the leading γ_3 correction are defined, for a rectangular torus $\tau = iu$, by

$$F_s(iu) = \sum_{(m,n)\in\mathbb{Z}^2\setminus(0,0)} \frac{n^s}{m^2/u + n^2 u}. \tag{A.16}$$

The sum is first defined where it converges and then analytically continued. After summing over m,

one obtains

$$F_s(iu) = 2\pi\zeta(1-s) + 4\pi \sum_{n=1}^{\infty} \frac{n^{s-1}}{e^{2\pi n u} - 1}. \tag{A.17}$$

For the two values needed in the thesis this gives

$$F_2(iu) = \frac{1}{2\pi} E_2(iu), \qquad F_4(iu) = -\frac{3}{4\pi^3} E_4(iu). \tag{A.18}$$

A useful check is the rectangular long-cylinder limit. For $\tau = \alpha + iu$,

$$q = e^{2\pi i \tau} = e^{-2\pi u} e^{2\pi i \alpha}. \tag{A.19}$$

Setting $\alpha = 0$ gives $\tau = iu$, and the normalized Eisenstein series approach their constant terms,

$$E_2(iu) = 1 - 24e^{-2\pi u} + O(e^{-4\pi u}), \tag{A.20}$$

$$E_4(iu) = 1 + 240e^{-2\pi u} + O(e^{-4\pi u}), \tag{A.21}$$

$$E_6(iu) = 1 - 504e^{-2\pi u} + O(e^{-4\pi u}). \tag{A.22}$$

In the same limit,

$$\eta(iu) = e^{-\pi u/12} \left(1 + O(e^{-2\pi u})\right). \tag{A.23}$$

For a general complex modulus $\tau = \alpha + iu$, the anti-holomorphic sector is written using $-\bar{\tau}$, which also lies in the upper half-plane. Since the Fourier coefficients of E_{2k} are real,

$$E_{2k}(-\bar{\tau}) = \overline{E_{2k}(\tau)}. \tag{A.24}$$

With these conventions, the leading non-universal correction to the torus free energy is

$$F_{\gamma_3}(\tau) = -\frac{\gamma_3}{\mathcal{A}^3} \frac{2\pi^6}{225} (\tau - \bar{\tau})^4 E_4(\tau) E_4(-\bar{\tau}) + O(\mathcal{A}^{-4}). \tag{A.25}$$

For a rectangular torus, $\tau = iu$, this becomes

$$F_{\gamma_3}(iu) = -\frac{32\gamma_3\pi^6}{225\,\mathcal{A}^3} u^4 E_4(iu)^2 + O(\mathcal{A}^{-4}). \tag{A.26}$$

Finally, one should distinguish the holomorphic Eisenstein series used above from the real analytic Eisenstein/Epstein zeta function appearing in the Gaussian determinant. The determinant computation uses the spectral zeta function of the scalar Laplacian on the torus and Kronecker's limit formula, leading to

$$\widetilde{Z}_0 = \left(\frac{i\sigma L_z^2}{\pi(\tau - \bar{\tau})}\right)^{1/2} |\eta(\tau)|^{-2}. \tag{A.27}$$

This fixes the zero-mode normalization of the torus partition function and is separate from the holomorphic E_2, E_4, E_6 identities used to organize the large-area expansion and the γ_3 correction.

References

[1] Eric D'Hoker and Justin Kaidi. *Lectures on Modular Forms and Strings*. Nov. 18, 2022. DOI: 10.48550/arXiv.2208.07242. arXiv: 2208.07242 [hep-th].

Appendix B

Two-dimensional Ising

In two dimensions the $\mathbb{Z}_2$-twisted thermodynamic Casimir difference is exact. See [1–3] for details. Consider the Ising CFT on a rectangular torus $T^2 = S^1_L \times S^1_{L_z}$, with L the length of the defect and L_z the thermal circle size. Set

$$\tau = i\frac{L}{L_z}, \qquad q = e^{2\pi i\tau} = e^{-2\pi L/L_z}. \tag{B.1}$$

For a non-anomalous $\mathbb{Z}_2$ symmetry, two equivalent torus amplitudes are

$$Z^{(\mathbb{Z}_2)}(\tau,\bar\tau) = \mathrm{Tr}_{\mathcal{H}}\left(Sq^{L_0-c/24}\bar q^{\bar L_0-c/24}\right), \qquad Z_{\mathbb{Z}_2}(\tau,\bar\tau) = \mathrm{Tr}_{\mathcal{H}_{\mathbb{Z}_2}}\left(q^{L_0-c/24}\bar q^{\bar L_0-c/24}\right), \tag{B.2}$$

related by the operator that implements the $\mathbb{Z}_2$-symmetry. The first is the twisted trace in the ordinary Hilbert space. The second is the partition function in the $\mathbb{Z}_2$-twisted Hilbert space. To analyze the large-L_z limit, it is useful to exchange the two torus cycles. In the exchanged channel, the measured free-energy difference is identified with the lowest gap in the $\mathbb{Z}_2$-twisted Hilbert space. The modular S transformation exchanges the two torus cycles, relating the amplitudes,

$$Z_{\mathbb{Z}_2}(\tau,\bar\tau) = Z^{(\mathbb{Z}_2)}\left(-\frac{1}{\tau},-\frac{1}{\bar\tau}\right). \tag{B.3}$$

Thus, inserting the symmetry line along one cycle is equivalent to quantizing on the Hilbert space twisted along the other cycle.

For the Ising minimal model, $c = 1/2$, and the three Virasoro primaries have weights

$$\mathbf{1}:\ h=\bar h=0, \qquad \epsilon:\ h=\bar h=\frac{1}{2}, \qquad \sigma:\ h=\bar h=\frac{1}{16}. \tag{B.4}$$

The diagonal modular-invariant partition function is

$$Z_{\mathbf{1}}(\tau,\bar\tau) = Z^{(\mathbf{1})}(\tau,\bar\tau) = |\chi_0|^2 + |\chi_{1/2}|^2 + |\chi_{1/16}|^2, \tag{B.5}$$

while insertion of the $\mathbb{Z}_2$ symmetry line gives

$$Z^{(\mathbb{Z}_2)}(\tau,\bar{\tau}) = |\chi_0|^2 + |\chi_{1/2}|^2 - |\chi_{1/16}|^2. \tag{B.6}$$

The minus sign is due to the odd $\mathbb{Z}_2$ charge of the spin field.

Under the modular S transformation, the characters mix as

$$\chi_i\left(-\frac{1}{\tau}\right) = \sum_j S_{ij}\chi_j(\tau) \qquad \text{with} \qquad S = \frac{1}{2}\begin{pmatrix} 1 & 1 & \sqrt{2} \\ 1 & 1 & -\sqrt{2} \\ \sqrt{2} & -\sqrt{2} & 0 \end{pmatrix}, \tag{B.7}$$

where the basis is $(\mathbf{1}, \epsilon, \sigma)$. This transformation keeps $Z_{\mathbf{1}}$ invariant, up to $\tau \to -1/\tau$ and acting on $Z^{(\mathbb{Z}_2)}$ gives

$$Z_{\mathbb{Z}_2}(\tau,\bar{\tau}) = \chi_0\bar{\chi}_{1/2} + \chi_{1/2}\bar{\chi}_0 + |\chi_{1/16}|^2. \tag{B.8}$$

The lightest state in $\mathcal{H}_{\mathbb{Z}_2}$ is therefore the σ primary, with

$$(h_0^{\mathbb{Z}_2}, \bar{h}_0^{\mathbb{Z}_2}) = \left(\frac{1}{16}, \frac{1}{16}\right). \tag{B.9}$$

Since the untwisted vacuum has $h_0^{\mathbf{1}} = \bar{h}_0^{\mathbf{1}} = 0$, the free energy density is

$$\Delta f(L_z) = E_0^{\mathbb{Z}_2} - E_0^{\mathbf{1}} = \frac{\pi}{4L_z}, \tag{B.10}$$

where we used that for a state with conformal weights $(h, \bar{h})$, the general cylinder energy is

$$E(h,\bar{h}) = \frac{2\pi}{L_z}\left(h + \bar{h} - \frac{c}{12}\right). \tag{B.11}$$

B.1. Finite-volume corrections

B.1.1. Lattice corrections and irrelevant operators

At finite-L_z, lattice realizations receive corrections from irrelevant operators allowed by the microscopic symmetries and the $\mathbb{Z}_2$-twisted ensemble. In two dimensions this structure is simple: the critical Ising theory has only the Virasoro primaries $\mathbf{1}, \sigma, \epsilon$, so critical corrections come from irrelevant operators in their conformal families.

For a bulk perturbation by an operator of scaling dimension Δ_i,

$$S_{\text{lat}} = S_{\text{CFT}} + \lambda_i \int d^2x \mathcal{O}_i(x) \tag{B.12}$$

the correction to the cylinder energy density scales as

$$\delta\Delta f_i(L_z) \sim L_z^{1-\Delta_i}. \tag{B.13}$$

Equivalently, the correction to the dimensionless free energy difference is

$$\delta\left[L_z\Delta f(L_z)\right] \sim L_z^{-(\Delta_i-2)}. \tag{B.14}$$

The $\mathbb{Z}_2$-twisted sector is equivalent to the insertion of a topological $\mathbb{Z}_2$ defect line. The line position is not physical, since it can be moved by deforming the seam. Moreover, the ensemble selects a torus cycle but not its orientation. Since global $\mathbb{Z}_2$ symmetry is preserved, $\mathbb{Z}_2$-odd insertions are absent from the free-energy difference. In particular,

$$\left\langle \int d^2x\sigma(x) \right\rangle_{\mathrm{AP}} = \left\langle \int d^2x\sigma(x) \right\rangle_{\mathrm{P}} = 0. \tag{B.15}$$

A nonzero one-point profile of σ requires a pinned interface, an oriented interface, or an explicitly symmetry-breaking field. That is not the unpinned AP partition function used here. Reflection-odd or odd-spin insertions are excluded for the same reason.

The energy operator is the leading $\mathbb{Z}_2$-even, symmetry-allowed operator. It is the relevant thermal perturbation,

$$t \int d^2x\epsilon(x), \qquad \Delta_\epsilon = 1. \tag{B.16}$$

It measures detuning from criticality, not an irrelevant finite-size correction. This effect is not expected here because the critical coupling of the two-dimensional Ising model is exact.

The leading irrelevant operators are dimension-four fields in the identity family. A convenient basis is

$$T\bar{T}, \qquad T^2 + \bar{T}^2, \tag{B.17}$$

with the usual quasi-primary subtractions in the chiral level-four operators understood. The operator $T\bar{T}$ is a rotational scalar. The combination $T^2 + \bar{T}^2$ has spin four and it is not invariant under continuous rotations, but only under the $\pi/2$ rotations of the square lattice. Both operators have $\Delta = 4$ and generate corrections of the form

$$L_z \Delta f(L_z) = \frac{\pi}{4} + \frac{a_2}{L_z^2} + \frac{a_4}{L_z^4} + \cdots . \tag{B.18}$$

The coefficient a_2 is nonuniversal. It can receive contributions from the scalar perturbation $T\bar{T}$ and from the lattice anisotropy $T^2 + \bar{T}^2$, unless one coefficient vanishes by improvement, integrability, or cancellation.

B.1.2. Exponential corrections from the cylinder spectrum

The leading finite-L corrections can also be written explicitly. These corrections are controlled by the spectrum of the CFT on a circle of circumference L_z

$$Z_s = g_{0,s} e^{-LE_{0,s}(L_z)} \left[1 + \sum_i r_{i,s} e^{-L(E_{i,s}(L_z) - E_{0,s}(L_z))} \right], \tag{B.19}$$

where $E_{i,s}$ are the excited-state energies with $E_{0,s}$ the ground-state, $g_{0,s}$ is the ground-state degeneracy, and $r_{i,s}$ are relative degeneracies, $g_{i,s}/g_{0,s}$, all in the sector s. The exponential corrections are controlled by the gaps

$$m_{i,s} = E_{i,s} - E_{0,s}. \tag{B.20}$$

Under radial quantization $\mathbb{R}^2 \sim \mathbb{R} \times S^1$, the thermal, or screening, masses of the theory compactified

on the circle of size L_z are related to the 2D Ising CFT data

$$\kappa_{i,s}/L_z \equiv m_{i,s} = 2\pi\left(\Delta_{i,s} - \Delta_{0,s}\right)/L_z. \tag{B.21}$$

The finite-L corrections are therefore

$$L_z\Delta f\left(q\right) = 2\pi\left(\Delta_{0,\mathbb{Z}_2} - \Delta_{0,\mathbf{1}}\right) + \frac{1}{q}\left(\log\frac{1+\sum_i r_{i,\mathbf{1}}e^{-\kappa_{i,1}q}}{1+\sum_i r_{i,\mathbb{Z}_2}e^{-\kappa_{i,\mathbb{Z}_2}q}} - \log\left(\frac{g_{0,\mathbb{Z}_2}}{g_{0,\mathbf{1}}}\right)\right). \tag{B.22}$$

The first excitation in the periodic sector is the spin primary, with $\Delta_\sigma = h_\sigma + \bar{h}_\sigma = \frac{1}{8}$, such that the leading periodic-sector gap is

$$\kappa_{1,\mathbf{1}} = 2\pi\left(\Delta_{\sigma,\mathbf{1}} - \Delta_{0,\mathbf{1}}\right) = \frac{\pi}{4}, \qquad r_{1,\mathbf{1}} = 1. \tag{B.23}$$

In the $\mathbb{Z}_2$-twisted Hilbert space, eq. (B.8), the ground state is σ, with $\Delta_{0,\mathbb{Z}_2} = \frac{1}{8}$, and the first excited state has scaling dimension $\Delta_{1,\mathbb{Z}_2} = 1/2$ and has relative degeneracy $r_{1,\mathbb{Z}_2} = 2$. The corresponding gap is

$$\kappa_1^{\mathbb{Z}_2} = \frac{3\pi}{4}. \tag{B.24}$$

Defining $t \equiv e^{-\pi q/4}$, the large-q form is

$$L_z\Delta f(q) = \frac{\pi}{4} + \frac{1}{q}\left[\log(1+t+\cdots) - \log(1+2t^3+\cdots)\right] \sim \frac{\pi}{4} + \frac{1}{q}\left(t - \frac{1}{2}t^2 - \frac{5}{3}t^3\right) + \mathcal{O}\left(q^{-1}t^4\right). \tag{B.25}$$

B.1.3. Mixed terms

Combining both limits, the double asymptotic expansion is

$$L_z\Delta f(L_z, L) = \frac{\pi}{4} + \frac{a_2}{L_z^2} + \frac{a_4}{L_z^4} + \cdots + \frac{1}{q}\left[t - \frac{1}{2}t^2 - \frac{5}{3}t^3 - \frac{1}{4}t^4 + \cdots\right] + \delta_{\text{mix}}(L_z, q). \tag{B.26}$$

The mixed terms come from shifts of the finite-size gaps and coefficients induced by irrelevant perturbations

$$\kappa_{n,s}(L_z) = \kappa_{n,s} + \frac{\mu_{2,n,s}}{L_z^2} + \frac{\mu_{4,n,s}}{L_z^4} + \cdots, \tag{B.27}$$

so that

$$\frac{1}{q}e^{-\kappa_{n,s}(L_z)q} = e^{-\kappa_{n,s}q}\left(\frac{1}{q} - \frac{\mu_{2,n,s}}{L_z^2} + \frac{1}{L_z^4}\left(\frac{\mu_{2,n,s}^2 q}{2} - \mu_{4,n,s}\right) + \cdots\right), \tag{B.28}$$

and the leading mixed corrections have the schematic form

$$\delta_{\text{mix}}(L_z, q) = \frac{e^{-\kappa_{n,s}q}}{L_z^2}\left[-\mu_{2,n,s} + \frac{1}{L_z^2}\left(\frac{\mu_{2,n,s}^2 q}{2} - \mu_{4,n,s}\right) + \mathcal{O}(L_z^{-4})\right]. \tag{B.29}$$

These mixed terms are subleading unless the fit includes both intermediate L_z and intermediate q data, but they are allowed by the same irrelevant operators that generate the power corrections.

Appendix C

Three-dimensional finite volume corrections

This appendix repeats, for the 3D analysis, the separation of correction terms used in the two-dimensional benchmark. We restrict the discussion to the leading effects relevant for the fits. One-particle states in the transverse channel give the large-q exponential corrections, while irrelevant operators and analytic slab terms give the power-law corrections used in the fixed-aspect-ratio extrapolation.

C.1. One-particle transverse corrections

Quantize along one transverse direction of the box $L \times L \times L_z$, and denote the sector by $s = \mathrm{P}, \mathrm{AP}$. The partition function has the spectral form

$$Z_s = \mathrm{Tr}\, e^{-LH_s(L,L_z)} = e^{-LE_{0,s}(L,L_z)} g_{0,s} \left[1 + \sum_{k,n,p} r_{k,s} e^{-L\sqrt{m_{k,s}^2 + p^2 + (2\pi n/L_z)^2}} + \cdots \right], \tag{C.1}$$

where $r_{k,s} = g_{k,s}/g_{0,s}$. For large transverse size, the sum over momentum p in the second transverse direction can be replaced by an integral. Defining

$$M_{k,n,s}^2 \equiv m_{k,s}^2 + \left(\frac{2\pi n}{L_z} \right)^2, \tag{C.2}$$

the one-particle corrections are

$$Z_s = e^{-LE_{0,s}(L,L_z)} g_{0,s} \left[1 + \frac{L}{\pi} \sum_{k,n} r_{k,s} M_{k,n,s} K_1(LM_{k,n,s}) + \cdots \right]. \tag{C.3}$$

At criticality the screening masses scale as $m_{k,s} = \kappa_{k,s}/L_z$. Setting $q = L/L_z$ gives

$$M_{k,n,s} K_1(LM_{k,n,s}) \sim \frac{1}{L_z} \sqrt{\frac{\pi}{2q}}\, K_{k,n,s}^{1/2} e^{-qK_{k,n,s}}, \qquad K_{k,n,s}^2 = \kappa_{k,s}^2 + 4\pi^2 n^2. \tag{C.4}$$

Thus one-particle states generate exponential corrections in q. Keeping only the lightest channel in each sector,

$$F_s = LE_{0,s}(L, L_z) - \log g_{0,s} - r_{0,s} q^{1/2} e^{-\kappa_s q} + \cdots . \tag{C.5}$$

Because the transverse box is square, the finite-L correction to the ground-state energy gives a second contribution. Write

$$E_{0,s}(L, L_z) = E_{0,s} - \frac{1}{\pi} \sum_{k,n} g_{k,s} M_{k,n,s} K_1(L M_{k,n,s}) + \cdots , \tag{C.6}$$

from expanding eq. (C.3) at large volume at fixed ratio. Thus, the full correction is

$$F_s = LE_{0,s} - \log g_{0,s} - \frac{L}{\pi} \sum_{k,n} (g_{k,s} + r_{k,s}) M_{k,n,s} K_1(L M_{k,n,s}) + \cdots , \tag{C.7}$$

and the dimensionless free-energy density becomes

$$F_s(q) = C_s - \frac{\log g_{0,s}}{q^2} - (g_{1,s} + r_{1,s}) \sqrt{\frac{\kappa_s}{2\pi q^3}} e^{-\kappa_s q} + \cdots . \tag{C.8}$$

and the sector difference

$$Y(q) = \Delta_{\mathbb{Z}_2} - \left(g_{1,\mathrm{AP}} + r_{1,\mathrm{AP}}\right) \sqrt{\frac{\kappa_{\mathrm{AP}}}{2\pi q^3}} e^{-q\kappa_{\mathrm{AP}}} + (g_{1,\mathrm{P}} + r_{1,\mathrm{P}}) \sqrt{\frac{\kappa_{\mathrm{P}}}{2\pi q^3}} e^{-q\kappa_{\mathrm{P}}} - \frac{1}{q^2} \log\left(\frac{g_{0,\mathrm{AP}}}{g_{0,\mathrm{P}}}\right) .$$

C.2. Slab power corrections

At fixed L_z, the limit $q = L/L_z \to \infty$ defines the slab free-energy density. As discussed in sec. 5.2, its large-L_z expansion is

$$Y(L_z) = \Delta_{\mathbb{Z}_2} + \sum_i a_i L_z^{-\omega_i} + \sum_{n \geq 1} b_n L_z^{-2n} + \cdots . \tag{C.9}$$

The first sum contains corrections from irrelevant perturbations of the critical theory. The second contains analytic slab corrections. We will now detail what can appear in these sums.

The first sum follows from perturbing the 3D Ising CFT by local irrelevant operators,

$$S_{\mathrm{lat}} = S_{\mathrm{CFT}} + \sum_i \lambda_i \int d^3x \, \mathcal{O}_i(x). \tag{C.10}$$

At first order, only operators whose integrated insertion is invariant under the symmetries of the AP-P observable can contribute. The unpinned AP and P partition functions preserve the global Ising spin flip. Thus $\mathbb{Z}_2$-odd bulk primaries, such as σ, σ', and odd tensor primaries, are absent from corrections to $F_{\mathrm{AP}} - F_{\mathrm{P}}$. Moreover, since the 1pt functions are integrated, descendants are projected out.

The leading $\mathbb{Z}_2$-even scalar irrelevant perturbation is

$$\epsilon', \qquad \omega_{\epsilon'} = \Delta_{\epsilon'} - 3 \simeq 0.82951(61), \tag{C.11}$$

from [1]. This is the leading ordinary bulk correction to scaling. The relevant thermal scalar ϵ is also

symmetry-allowed, but its coefficient is the detuning from the critical coupling, and should be absent given the precision with which β_c is known.

Spinful primaries can contribute only if the geometry supplies an invariant tensor with the same spin. In the present slab geometry, the compact direction and the defect plane select an axis but not an orientation. The background is invariant under $n_\mu \to -n_\mu$. Therefore only tensors even in n_μ are available. In particular, there is no invariant vector with which to contract a spin-one primary, so spin-one one-point functions are forbidden, unless an additional reflection-odd structure is introduced[1].

The first allowed tensor structure is the traceless spin-two combination

$$Q_{\mu\nu} = n_\mu n_\nu - \frac{1}{3}\delta_{\mu\nu}. \tag{C.12}$$

The leading nonconserved $\mathbb{Z}_2$-even spin-two primary can therefore contribute through

$$Q^{\mu\nu}T'_{\mu\nu}, \qquad \omega_{T'} = \Delta_{T'} - 3 \simeq 2.50915(44). \tag{C.13}$$

This contribution is allowed by the slab geometry and by the anisotropy introduced by the defect. The leading even spin-4 primary gives another possible contribution,

$$C_{\mu\nu\rho\sigma}, \qquad \omega_C = \Delta_C - 3 \simeq 2.022665(28), \tag{C.14}$$

from [3]. One source of the spin-four structure is geometric. Both the antiperiodic direction and the rectangular slab distinguish the compact axis. The second is the cubic lattice, whose microscopic anisotropy supplies a spin-four tensor even when the continuum slab geometry is rotationally symmetric in the transverse plane.

C.3. Sector difference of $\mathbb{Z}_2$-even one-point functions

We now discuss why some one-point functions may be smaller than expected.

The one-point functions of $\mathbb{Z}_2$-even operators need not be identical in the periodic and antiperiodic sectors. Nonetheless, they may be arbitrarily close. Consider the theory on $S^2_L \times S^1_{L_z}$ and quantize on S^2_L. This differs from the transverse T^2 used in the simulations, but it illustrates why sector differences can be smaller than the corresponding one-point functions in the individual sectors.

The periodic partition function is

$$Z_{\mathrm{P}} = \mathrm{Tr}\, e^{-L_z H}, \tag{C.15}$$

whereas the antiperiodic partition function inserts the Ising spin-flip operator S,

$$Z_{\mathrm{AP}} = \mathrm{Tr}\, S e^{-L_z H}. \tag{C.16}$$

For a scalar operator $\mathcal{O}$,

$$\langle \mathcal{O} \rangle_{\mathrm{P}} = \frac{1}{Z_{\mathrm{P}}} \mathrm{Tr}\left(\mathcal{O} e^{-L_z H}\right), \qquad \langle \mathcal{O} \rangle_{\mathrm{AP}} = \frac{1}{Z_{\mathrm{AP}}} \mathrm{Tr}\left(\mathcal{O} S e^{-L_z H}\right). \tag{C.17}$$

[1] This exclusion is also not expected to hide a low-lying correction. There is no known $\mathbb{Z}_2$-even spin-one primary in the 3D Ising CFT. If such a primary exists, existing bounds place it at $\Delta > 5$ [2]. Moreover, it is not clear that the lightest $\mathbb{Z}_2$-even vector, if present, would have the reflection parity required to couple to an oriented defect structure.

Choose energy eigenstates that simultaneously diagonalize S, $S|i\rangle = \eta_i|i\rangle$, with $\eta_i = \pm 1$. Using $E_i = \Delta_i/L$ and defining $C_{\mathcal{O}ii} \equiv \langle i\,|\mathcal{O}|\,i\rangle$ gives

$$L^{\Delta_\mathcal{O}}\langle\mathcal{O}\rangle_{\rm P} = \frac{\sum_i e^{-\Delta_i/q} C_{\mathcal{O}ii}}{\sum_i e^{-\Delta_i/q}}, \qquad L^{\Delta_\mathcal{O}}\langle\mathcal{O}\rangle_{\rm AP} = \frac{\sum_i \eta_i e^{-\Delta_i/q} C_{\mathcal{O}ii}}{\sum_i \eta_i e^{-\Delta_i/q}}, \tag{C.18}$$

Therefore

$$L^{\Delta_\mathcal{O}}\left(\langle\mathcal{O}\rangle_{\rm P} - \langle\mathcal{O}\rangle_{\rm AP}\right) = \sum_i e^{-\Delta_i/q} C_{\mathcal{O}ii}\left(\frac{1}{Z_{\rm P}} - \frac{\eta_i}{Z_{\rm AP}}\right). \tag{C.19}$$

In the small-q limit the lowest states dominate. Assuming a unique $\mathbb{Z}_2$-even vacuum with $\Delta_0 = 0$, define

$$\mathcal{E}(q) = \sum_{\eta_j=+1,\ j\neq 0} e^{-\Delta_j/q}, \qquad \Sigma(q) = \sum_{\eta_j=-1} e^{-\Delta_j/q}. \tag{C.20}$$

Then

$$Z_{\rm P} = 1 + \mathcal{E} + \Sigma, \qquad Z_{\rm AP} = 1 + \mathcal{E} - \Sigma, \tag{C.21}$$

and

$$\frac{1}{Z_{\rm P}} - \frac{\eta_i}{Z_{\rm AP}} = \begin{cases} -2\Sigma + \cdots, & \eta_i = +1, \\ 2 - 2\mathcal{E} + \cdots, & \eta_i = -1. \end{cases} \tag{C.22}$$

In this limit, the vacuum contribution is common to the two traces and cancels in the sector difference. Keeping only the lightest odd state, σ, gives

$$L^{\Delta_\mathcal{O}}\left(\langle\mathcal{O}\rangle_{\rm P} - \langle\mathcal{O}\rangle_{\rm AP}\right) = 2g_\sigma C_{\mathcal{O}\sigma\sigma} e^{-\Delta_\sigma/q} + \text{subleading exponentials}, \tag{C.23}$$

where g_σ is the degeneracy of the lightest odd level. Thus the scalar sector difference can be much smaller than the one-point coefficient in either sector. This supports the observation that ϵ' corrections in the slab analysis may be numerically smaller than further subleading corrections.

Large-q

The large-q limit of these expressions is more subtle than the small-q limit. Formally, one may introduce spectral moments

$$A_n \equiv \sum_j \Delta_j^n, \qquad B_n \equiv \sum_j \eta_j \Delta_j^n, \tag{C.24}$$

and expand the partition functions as

$$\sum_j e^{-\Delta_j/q} = A_0 - \frac{A_1}{q} + \frac{A_2}{2q^2} + O(q^{-3}), \tag{C.25}$$

with an analogous expression for the parity-weighted trace,

$$\sum_j \eta_j e^{-\Delta_j/q} = B_0 - \frac{B_1}{q} + \frac{B_2}{2q^2} + O(q^{-3}). \tag{C.26}$$

This gives a formal expansion in powers of $1/q$. However, these moments are not generally well defined as ordinary sums over the full CFT spectrum. Equivalently, they should be understood, if at all, as

regulated high-temperature limits of derivatives of the corresponding cylinder trace

$$A_n = \lim_{\beta\to 0}\left(-\frac{\partial}{\partial\beta}\right)^n \langle \mathbf{1}\rangle_{S^{d-1}\times S^1_\beta} \qquad B_n = \lim_{\beta\to 0}\left(-\frac{\partial}{\partial\beta}\right)^n \langle S\rangle_{S^{d-1}\times S^1_\beta}\,. \tag{C.27}$$

Moreover, even if such a regularization could be defined, the resulting observables would be sensitive to the UV completion of the microscopic model. In our simulations this UV completion is the lattice, not the CFT. The numerical coefficients extracted from a lattice $1/q$ expansion therefore cannot be interpreted as universal CFT data.

C.4. 3D Ising analysis

To determine the bulk inputs used in the main text, we analyze periodic connected two-point functions in the large-distance regime. For the energy operator, we fit

$$\langle \epsilon(r)\epsilon(0)\rangle_c \simeq \frac{\mathcal{N}_\epsilon^2}{4\pi}\,\frac{e^{-mr}}{r}, \tag{C.28}$$

implemented by fitting $r\langle \epsilon(r)\epsilon(0)\rangle_c$ on a log plot. The lower fit bound $r_{\min}$ is chosen such that the best-fit curve, extrapolated to slightly smaller separations, still agrees with the data for a few points beyond the fit window, indicating that residual short-distance and excited-state effects are subleading at $r \geq r_{\min}$. The upper bound $r_{\max}$ is taken as the largest separation before the signal becomes noise-dominated, always with $r_{\max} \lesssim L/4$ to avoid wrap-around effects.

In the symmetry-broken phase, spin and energy correlators are governed by the same lightest mass gap. In practice, however, the spin-spin correlator has a cleaner overlap with the lightest state, so we extract m from the spin channel and use eq. (C.28) only to determine $\mathcal{N}_\epsilon$. Since our goal is a robust input for the worldsheet analysis rather than a high-precision determination of bulk amplitudes, we use uncorrelated least-squares fits and quote statistical errors. As a basic robustness check, we repeat the fits with $r_{\min} \to r_{\min} \pm 1$ and, when useful, with a nearby $r_{\max}$; the resulting variation is negligible or comparable to the statistical uncertainty.

From these bulk two-point functions we obtain m and $\mathcal{N}_\epsilon$, while σ is taken from the free energy measurements for Chapter 3. The results are collected in table C.1. To convert $\mathcal{T}_\epsilon^{\text{lat}}$ to λ at the small reduced temperatures relevant for the one-point analysis, we need m and $\mathcal{N}_\epsilon$ for several temperatures close to the critical point. To reduce the number of dedicated simulations, we fit their temperature dependence and use the resulting interpolation. The results, in lattice units, $a = 1$, are

$$\mathcal{N}_\epsilon(t) = 5.7(4)t^{0.56(1)}, \tag{C.29}$$
$$\chi(t) = 0.79(1) - 0.15(30)t^{\omega\nu} + 1.7(1.0)t, \tag{C.30}$$
$$\sigma(t) = 1.515(2)t^{2\nu}\left(1 - 0.28(2)t^{\omega\nu} - 0.31(6)t\right), \tag{C.31}$$
$$m(t) = 3.832(1)t^{\nu}, \tag{C.32}$$

where $\nu = 0.62997097(12)$ [4], $\omega = 0.82951(61)$ [1].

param \ β	0.222136	0.223102	0.224	0.227	0.2285	0.23
m	0.083(4)	0.161(1)	0.2178(1)	0.3665(5)	0.4287(6)	0.4867(2)
σ [5]	–	0.0026062(12)	0.0047567(10)	0.0132004(25)	0.0178901(14)	0.0227944(20)
χ	–	0.791(9)	0.794(1)	0.810(2)	0.817(2)	0.827(1)
$\mathcal{N}_\epsilon$	0.0027(3)	0.0091(9)	–	–	–	0.07(1)

Table C.1. Bulk input parameters used in the analysis. The mass gap m is extracted from periodic spin-spin correlators, $\mathcal{N}_\epsilon$ from periodic energy-energy correlators, and σ is taken from Chapter 3. A dash indicates that the corresponding quantity was not extracted at that value of β. The quantity $\mathcal{N}_\epsilon$ is determined only for the subset of β values used in the quantitative matching tests and for a few additional points needed to fit its small-t extrapolation for the one-point analysis.

References

[1] Marten Reehorst. "Rigorous Bounds on Irrelevant Operators in the 3d Ising Model CFT." In: *JHEP* 09 (2022), p. 177. DOI: 10.1007/JHEP09(2022)177. arXiv: 2111.12093 [hep-th].

[2] Simão Meneses, João Penedones, Slava Rychkov, J. M. Viana Parente Lopes, and Pierre Yvernay. "A Structural Test for the Conformal Invariance of the Critical 3d Ising Model." In: *JHEP* 04 (2019), p. 115. DOI: 10.1007/JHEP04(2019)115. arXiv: 1802.02319 [hep-th].

[3] David Simmons-Duffin. "The Lightcone Bootstrap and the Spectrum of the 3d Ising CFT." In: *JHEP* 03 (2017), p. 086. DOI: 10.1007/JHEP03(2017)086. arXiv: 1612.08471 [hep-th].

[4] Cyuan-Han Chang et al. "Bootstrapping the 3d Ising Stress Tensor." In: *JHEP* 03 (2025), p. 136. DOI: 10.1007/JHEP03(2025)136. arXiv: 2411.15300 [hep-th].

[5] David Lima, J. M. Viana Parente Lopes, Jose Matos, and Joao Penedones. "Effective String Theory on a Torus: The 3d Ising Domain Wall." Oct. 2025. arXiv: 2510.15206 [hep-th].